

MAGNETISATION REVERSAL STUDIES OF PARTICULATE RECORDING MEDIA.

by

SHAUN ROBERT M^CCONOCHIE

A Thesis submitted in Partial Fulfilment of the Requirements of the University of
Central Lancashire for the Degree of Doctor of Philosophy.

at

Department of Physics, Astronomy and Mathematics
University of Central Lancashire
Preston PR1 2HE
March 1998

Supervisors:

Prof. P.R. Bissell
Dr. D. Parker
Dr. J. Gotaas

Abstract

Both an experimental investigation of the interaction effects within commercial particulate recording media and a numerical investigation of the reversal mechanism of particles within the media have been made. The particle systems investigated comprised three audio $\gamma\text{-Fe}_2\text{O}_3$ tapes, three audio CrO_2 tapes and a video metal particle tape.

An absolute measure of the interaction effects within particulate tapes has been investigated by comparing the measured properties of isolated particles taken from the medium with the measured bulk properties of the medium. The results indicated negative interactions for all the samples investigated except the video metal particle tape, which indicated positive interactions. However, ΔI plots for all the samples however, indicated negative interactions. This is contrary to the absolute interactions measured in the video metal particle tape. A possible explanation for this inconsistency was the presence of highly localised alignment of particles, "a chaining effect", within the metal particle system. This effect allows for increased system coercivity without removing the general negative interactions characteristic of all acicular particulate media.

A micromagnetic model was developed to study *typical* $\gamma\text{-Fe}_2\text{O}_3$ and CrO_2 particles measured experimentally in this study. Simulations were performed as a function of the applied field angle and the results compared to the experimental study. The simulations representing *typical* $\gamma\text{-Fe}_2\text{O}_3$ particles indicated reasonable agreement at the lower applied field angles, while poorer agreement was observed at larger applied field angles. The simulations representing a *typical* CrO_2 particle indicated reasonable agreement at the higher applied field angles, while poorer agreement was observed at low applied field angles. These inconsistencies for both types of particles investigated were accounted for by assumptions and simplifications within the model, particularly the absence of bulk crystalline imperfections, the degree of surface irregularities and the effect of an oversimplified particle shape.

The micromagnetic model developed was also used to investigate the effect of model parameters on the reversal mechanism of the $\gamma\text{-Fe}_2\text{O}_3$ particle simulation. It was found that the reversal mechanism was very sensitive to the size and shape of the model particle.

CONTENTS

Chapter One

MAGENETIC MATERIALS.

1.1 THE ORIGIN OF MAGNETISM	1
1.2 MAGNETIC UNITS	2
1.3 MAGNETIC DOMAINS	3
1.4 ANISOTROPY.....	4
1.4.1 <i>Shape anisotropy</i>	4
1.4.2 <i>Magnetocrystalline anisotropy</i>	6
1.4.3 <i>Mixed anisotropy</i>	8
1.5 DOMAIN WALL.....	8
1.6 THE SINGLE DOMAIN PARTICLE	10
1.6.1 <i>Coherent reversal</i>	10
1.6.2 <i>Incoherent reversal</i>	11
1.7 MAGNETIC INTERACTIONS IN PARTICULATE MEDIA.....	12
1.8 PARTICULATE RECORDING MEDIA	15

Chapter Two

MEASUREMENT OF THE PROPERTIES OF ISOLATED MAGNETIC PARTICLES: EXPERIMENTAL THEORY.

2.1 INTRODUCTION	20
2.2 SAMPLE PREPARATION.....	21
2.3 EXPERIMENTAL TECHNIQUES	22
2.4 MICROSCOPE	23
2.5 PULSED FIELD GENERATION	26
2.6 PULSED FIELD COIL	26
2.6.1 <i>Field Calculation</i>	28
2.6.2 <i>Field Calculation Uncertainty</i>	32
2.7 PULSED VOLTAGE SOURCE	33
2.8 CALIBRATION OF THE PULSED FIELD COILS.....	40
2.8.1 <i>Experimental calibration technique</i>	41
2.8.2 <i>Design, construction and characterisation of the orientation coils</i>	42
2.8.3 <i>Calibration of pulsed field coil OC11</i>	49

Chapter Three

MEASUREMENT OF THE INTRINSIC PROPERTIES OF THE INDIVIDUAL PARTICLES.

3.1 INTRODUCTION	51
3.2 SAMPLES	52
3.3 MEASUREMENT OF THE SWITCHING FIELD DISTRIBUTION OF AN ENSEMBLE OF PARTICLES	53
3.4 THE SWITCHING FIELD MEASUREMENT OF A PARTICLE AS A FUNCTION OF THE APPLIED FIELD ANGLE	59
3.5 THE REMANENT CURVE MEASURED FROM AN INDIVIDUAL PARTICLE	69
3.6 MEASUREMENT OF THE PHYSICAL DIMENSIONS OF THE PARTICLES	73

Chapter Four

BULK MEASUREMENTS AND ANALYSIS OF PARTICULATE MEDIA.

4.1 INTRODUCTION	80
4.2 HYSTERESIS MEASUREMENTS	81
4.3 REMANENCE CURVES.....	85
4.4 HENKEL PLOTS.....	88
4.5 IN-PLANE, EASY AXIS DISTRIBUTION MEASUREMENTS OF THE MEDIA.....	93
4.6 TRANSVERSE SUSCEPTIBILITY THEORY AND MEASUREMENTS.....	99
4.6.1 <i>The absolute magnetisation measurement of the samples</i>	101
4.7 EVALUATION OF THE OVERALL EASY AXIS DISTRIBUTIONS FOR THE SAMPLES	106

Chapter Five

DERIVATION AND ANALYSIS OF INTERACTION EFFECTS.

5.1 INTRODUCTION	111
5.2 MATHEMATICAL SIMULATION OF A MEDIA WITHOUT INTERACTIONS.....	112
5.3 NUMERICAL RESULTS AND ANALYSIS	116

Chapter six

NUMERICAL INVESTIGATION OF PARTICLES.

6.1 INTRODUCTION	125
6.2 STONER WOHLFARTH MODEL	126
6.3 THE CHAIN OF SPHERES MODEL.....	130
6.4 MICROMAGNETIC MODEL	134
6.4.1 <i>Co-ordinate system</i>	135
6.4.2 <i>Micromagnetic structure</i>	137
6.4.3 <i>Field terms</i>	139
6.4.4 <i>Dynamic calculations</i>	143
6.5 SIMULATION ALGORITHM.....	147
6.6 MICROMAGNETIC RESULTS AND DISCUSSION	149
6.6.1 <i>Simulations of a typical $\gamma\text{-Fe}_2\text{O}_3$ particle</i>	150
6.6.2 <i>The effect of model parameters on the $\gamma\text{-Fe}_2\text{O}_3$ particle simulation.</i>	156
6.6.3 <i>Simulations of a typical CrO_2 particle</i>	169

Chapter Seven

CONCLUSIONS AND FURTHER WORK.

7.1 CONCLUSIONS AND FURTHER WORK	172
BIBLIOGRAPHY.	177
APPENDIX A.	190
PUBLICATIONS.	192

ACKNOWLEDGEMENTS

I would like to thank the following who have supported my studies, and without whom it would have been a near impossible task to complete this work.

I would like to thank personally my supervisors Prof. Phil Bissell, Dr Dave Parker and Dr. Jim Gotass.

My family, especially my parents who have supported my studies for a very long time..... and now might expect me to leave home and support myself.

My fellow researcher, past and present, for making my time here very enjoyable. People who require a special mention are the table top footy bunch, Franck Schmidlin Paul Sollis, John Burgoyne and Martin Bellwood.

I would like to take this opportunity to save for posterity some moments I found particularly amusing.

The time Franck tried to solder the mains twice in as many minutes, while it was LIVE..

The time Nick and Alberto believed I found £30.00 of coppers under a magnet and then wanted their cut or they'd blag .

The time a certain John went on a holiday and only told his live in partner the night before, while we all knew a week before.

The time a researcher, at a congress, got locked in his room and had to relieve himself in a paper bin.

The time my sister, the teacher said that a thesaurus was a dinosaur.

The time Paul glued together Mattie's favourite reading material the RS catalogue, his favourite excuse to avoid work.

The time Mattie glued Paul's desk to the floor and his mug to the desk.

The time Martin compared his manhood with a particularly small bottle of beer and promptly got ridiculed.

One final note,

I'm Glad this is nearly over....

Chapter One

Magnetic materials.

1.1 The origin of magnetism

Magnetism is the result of the flow of charge, whether in an electric circuit or the motion of unpaired electrons within an atom. The magnetic moment generated from the quantised orbital motion of an electron around its nuclei is called the Bohr magneton and is the fundamental unit of magnetism.

The Bohr magneton is defined from an electron of mass M_e moving with a velocity v in a circular orbit of radius r . The orbital charge constitutes a current of magnitude,

$$i = \frac{e}{T} = \frac{ev}{2\pi r}, \quad (1-1)$$

where T is the period for a charge to complete an orbit. A current in a circular loop generates a magnetic field that is indistinguishable from that of a magnetic moment at a large distance away from the loop. The magnetic moment generated from a loop is given by

$$\mu = iA, \quad (1-2)$$

where A is the cross sectional area of the loop. Applying this definition for a moment to an orbiting electron and considering that angular momentum is quantised in units of $h/2\pi$, where h is Planck's constant, the lowest value of μ is given in the above equation and is called the Bohr magneton μ_B ($\mu_B = 9.27 \times 10^{-24} \text{ Am}^2$).

$$\mu_B = \frac{eh}{4\pi M_e}. \quad (1-3)$$

As well as the magnetic moment generated from orbital motion of unpaired electrons around the nucleus there exist two other sources, the moment generated from spin of the electron around its own axis and the moment generated from nucleus. The total moment of the atom is the vector sum of these moments, however, the contribution from the nucleus is insignificant when compared to the moment generated from the electrons.

In materials where the atoms have completely filled electrons orbits the moments generated from these electrons will tend to cancel each other, effectively reducing the total moment of the atom/material. For materials consisting of atoms with incompletely filled electron orbits the moment generated within these material can be large. As a consequence of these material characteristics there exist a number of possible descriptions of a materials magnetic characteristics.

1. The material can be Diamagnetic where the moment of the atoms within the material cancel each other out.
2. The material can be Antiferromagnetic, Ferrimagnetic, Paramagnetic or Ferromagnetic. These descriptions describe the conditions of a material having a net magnetic moment.

A full description of the various types of magnetic material can be found in the book by Crangle [1].

As the moment of a material is linked to its atomic structure, the alignment of the moments within a material can have some energy preferable direction. This preferred energy direction is described by the term anisotropy. The anisotropy of a material describes the easy axis directions for the moments to lie within a material. There exists a number of forms of anisotropy, these forms are discussed in later sections.

1.2 Magnetic units

There are currently three systems of units currently used in magnetism. These are CGS also known as the Gaussian system, the SI systems which are the Sommerfeld convention and the Kennelly convention [1-3].

The Gaussian system is commonly used throughout industry and research. However, there is now a tendency for research papers to be published in S.I. units, in the

convention known as the Sommerfeld. As it is more likely that this system will be increasingly used for research, it has been adopted in this thesis.

1.3 Magnetic domains

A domain is a region within a material where all magnetic moments are aligned. In order to explain the existence of aligned moments Weiss [4] proposed a mean (molecular) field theory. The theory extended the work by Langevin [5], who described paramagnetism based on classical Boltzmann statistics. The mean field proposed by Weiss described the effect of interatomic interactions. These interactions have the effect of causing neighbouring atomic moments to align parallel to one another. This mean field H_e within a domain is expressed as

$$H_e = \alpha M_s, \quad (1-4)$$

where M_s is the saturation magnetisation within the domain and α is the mean field constant. Weiss proposed another variation to his mean field approximation [6] that described an interaction field with nearest neighbour interactions only. This mean field approximation is represented by

$$\bar{H}_e = \sum_{\substack{\text{nearest} \\ \text{neighbours}}} \alpha_{ij} \bar{m}_j, \quad (1-5)$$

where α_{ij} is an interaction field constant between moments i and j . The model assumes that the interaction field constant is identical between all nearest neighbours and is equal to α . The interaction field constant can be used to model a ferromagnetic system with a positive α or an antiferromagnetic system with a negative α . An exchange energy E_i can be calculated between a moment \bar{m}_i and its adjacent moments \bar{m}_j by

$$E_i = -\mu_o \bar{m}_i \cdot \sum \alpha_{ij} \bar{m}_j, \quad (1-6)$$

where α_{ij} is the mean field constant between moments i and j . It can be postulated from the mean field proposed by Weiss that all moments would spontaneously align in a ferromagnetic material. This would be the case if there were no other contributions to the energy of the sample. The other contributing energy phenomena are the magnetostatic energy of a single domain, the domain wall energy and the anisotropy energy.

1.4 Anisotropy

The magnetic anisotropy of a material describes the energy of its moment for a particular orientation within the material. This energy dependence for a moment's orientation generates easy and hard axes for the moment to lie within the material; thus anisotropy acts like a force which pushes a moment into an energy favourable orientation. The easy axis of a moment is often referred to as its C-axis within the crystal structure. The sources of magnetic anisotropy are:

1. Magnetocrystalline anisotropy
2. Shape anisotropy
3. Stress anisotropy
4. Induced anisotropy
5. Exchange anisotropy

The anisotropy of magnetic particles within particulate media originate predominately from their shape and crystalline structure. These forms of anisotropy will be discussed in later sections. The other sources of anisotropy found in magnetism are described in the book by Cullity [7].

1.4.1 Shape anisotropy

In a magnetised body the effect of the magnetisation is to generate a field within the body that acts to demagnetise the body [2]. In a pole magnet the NS poles generate a field H around the magnet, while within the magnet the poles generate a demagnetising field H_d . The demagnetising field is dependent on the demagnetising factor N_d and the magnetisation of the domain, M ,

$$H_d = -N_d M . \quad (1-7)$$

The demagnetising factor N_d is dependent on the geometry of the domain. It is this demagnetising factor which determines the shape anisotropy of the domain. The shape anisotropy is calculated from the magnetostatic energy of the domain.

The magnetostatic energy of a domain is the energy of a magnetised body M in a magnetic field H . The magnetostatic energy is determined through the following volume integration [2]

$$E = -\frac{1}{2} \mu_0 \int_v H \cdot M dv . \quad (1-8)$$

Where no external field is present the only field within the sample is the demagnetising field H_d . Thus, the energy generated by a domain is determined by,

$$E = \frac{\mu_0}{2} N_d M^2 . \quad (1-9)$$

The anisotropy of a single domain prolate spheroid given in figure (1-1) results from the different demagnetising factors, N_C for the semi major axis C and N_A the semi minor axis A . The magnetisation of the domain is represented by M , its orientation with respect to the C axis is given by θ .

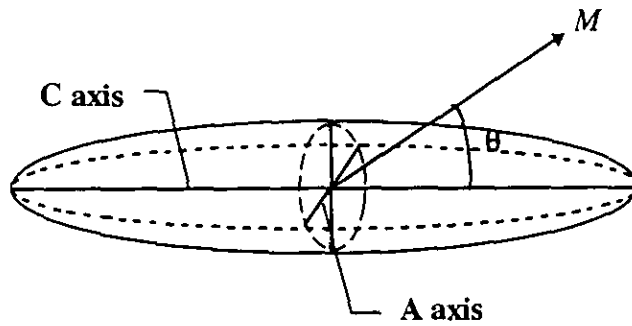


figure (1-1): A prolate spheroid.

The magnetostatic energy of a prolate spheroid having a single domain is determined from the magnetisation components along the different demagnetising axes.

$$E_{MS} = \frac{\mu_0}{2} [N_C (M \cos \theta)^2 + N_A (M \sin \theta)^2] \quad (1-10)$$

Rearranging the above equation and substituting the identity $\cos^2 \theta = 1 - \sin^2 \theta$ the magnetostatic energy of a prolate spheroid can be determined as

$$E_{MS} = \frac{\mu_0}{2} M^2 N_C + \frac{\mu_0}{2} (N_A - N_C) M^2 \sin^2 \theta . \quad (1-11)$$

This expression relates the magnetostatic energy of the spheroid to the orientation angle of its moment.

The shape anisotropy K_{SHAPE} of the spheroid is the coefficient of the magnetostatic energy and is defined by

$$K_{SHAPE} = \frac{1}{2} \mu_o (N_A - N_C) M^2. \quad (1-12)$$

1.4.2 Magnetocrystalline anisotropy

The energy associated with magnetising a ferromagnetic material is dependent on the direction of magnetisation with respect to the crystal lattice of the material. The origin of magnetocrystalline anisotropy is the direct and/or indirect spin-orbit coupling between lattice sites and conduction electrons [1]. The two most common types of magneto-crystalline anisotropy found in particles in recording media are uniaxial and cubic.

Uniaxial anisotropy results from a hexagonal or tetragonal structure. A hexagonal structure of cobalt is shown in figure (1-2). This crystal structure has a single easy axis represented by the c axis, all other axes are found to be hard. The easy and hard axis found in this crystal structure and in other crystal structures are a result of the spin orbit coupling of the electrons with the crystal lattice.

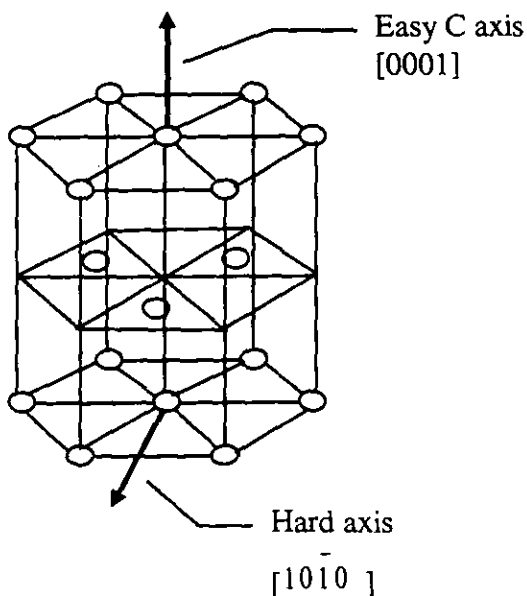


figure (1-2): The hexagonal close packed structure of cobalt.

The structure of cobalt has an energy E_K given by

$$E_K = K_0 + K_1 \sin^2 \theta + K_2 \sin^4 \theta + \dots, \quad (1-13)$$

where K_0, K_1 and K_2 are anisotropy constants for a particular crystal and θ is the angle between the moment direction and the easy axis. In the analysis of magnetic particles the higher terms K_2 and above are usually neglected as being small. In the analysis of reversal mechanisms K_0 is also neglected since it is independent of the magnetisation state within the domain.

Cubic anisotropy is expressed in terms of direction cosines α with respect to the easy axes directions $\langle 100 \rangle$ within the crystal lattice. Shown in figure (1-3) is the body centred cubic structure of iron.

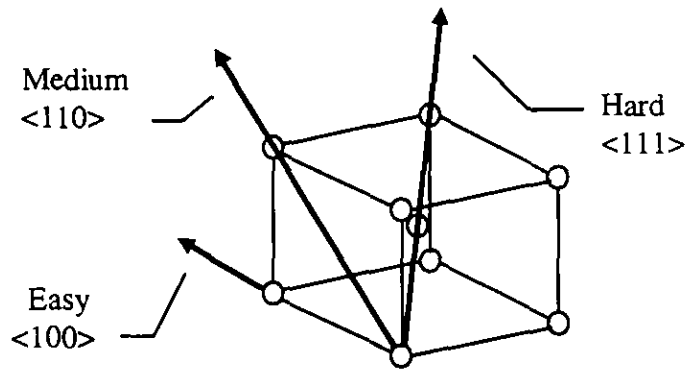


figure (1-3): The crystal structure of iron.

The direction cosines α corresponding to the easy axes directions are always related by $\alpha_1^2 + \alpha_2^2 + \alpha_3^2 = 1$. The anisotropy energy E_K for a cubic structure is given by

$$E_K = K_0 (\alpha_1^2 + \alpha_2^2 + \alpha_3^2) + K_1 (\alpha_1^2 \alpha_2^2 + \alpha_2^2 \alpha_3^2 + \alpha_3^2 \alpha_1^2) + K_2 (\alpha_1^2 \alpha_2^2 \alpha_3^2) + \dots, \quad (1-14)$$

where K_0, K_1 and K_2 are again the anisotropy constants for a particular crystal. As with uniaxial anisotropy, the higher order anisotropy constants are considered insignificant and are ignored. The first term in the equation is also ignored, since it is independent of the magnetisation orientation within the crystal.

1.4.3 Mixed anisotropy

The particles commonly found within particulate media have an anisotropy which results from both its shape and its crystalline structure. The resultant anisotropy energy for such a particle is the simple addition of the different anisotropy sources. For example, if the anisotropy energy of a particle is being calculated, all its anisotropy sources are considered separately to determine its overall anisotropy energy. An example of this technique can be found in the book by Cullity [7] who determines the properties of a cobalt particle that has two sources of anisotropy, its shape and its crystalline structure.

1.5 Domain wall

A domain wall is a junction between two domains of different magnetised states. At the junction there is a transition region where the atomic moments rotate from one magnetised state to the other. The energy associated with this change is the wall energy. Bloch [8] proposed a theoretical structure for a domain wall given in figure (1-4).

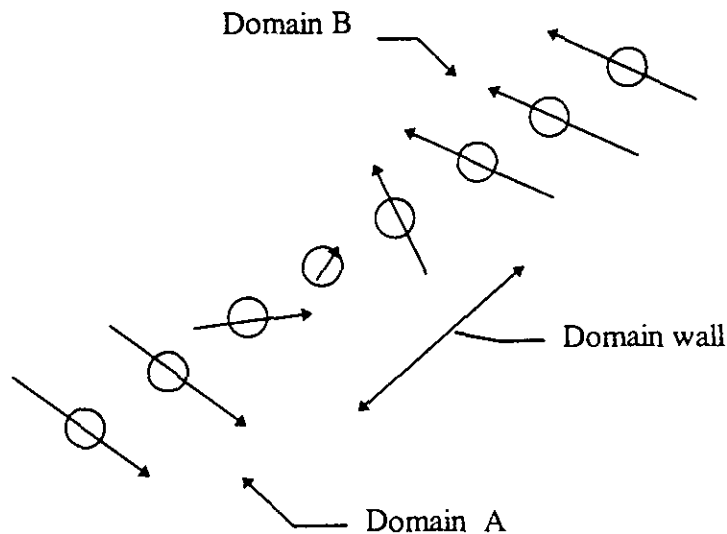


figure (1-4): A Bloch wall structure.

The Bloch domain wall structure is the simplest transition from one domain to another. Other forms of domain walls can be found, they are Neel and cross-tie [7]. The

Bloch wall thickness is determined by the magnetocrystalline anisotropy energy and the exchange energy associated with the transition of moments from one domain direction to another. The exchange energy within the wall will try to reduce the angle from adjacent moments. This will have the effect of increasing the wall thickness. The magnetocrystalline anisotropy energy will try to align the moments with the easy axes of the material. This will tend to lead to instantaneous transitions from one easy axis to the next. In an actual Bloch wall the thickness is determined by minimising the total energy of the system; thus the thickness of the wall is determined by the relative magnitudes of the magnetocrystalline anisotropy energy and the exchange energy.

The configuration and generation of domains within a magnetised body depend on the reduction of the total energy of the body. Changing the size of the domains and their arrangement within the body can reduce the total energy within the body. A typical arrangement, shown in figure (1-5) would be the generation of closure domains in a magnetised body containing two domains (sample A) to a body containing four (sample B). Closure domains minimise the formation of free poles and reduce the magnetostatic energy of the magnetised body.

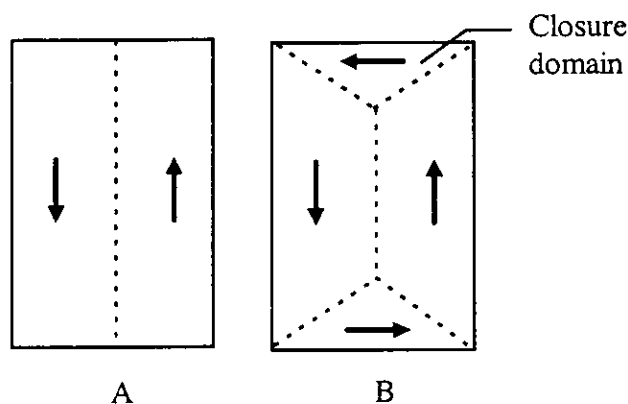


figure (1-5): Domain configurations.

The reversal mechanism within a multidomain magnetised body occurs through domain wall motion and the realignment of the domains into the applied field direction. The action of domain wall motion is to rotate moments from one domain to the next. The ease with which a domain wall traverses through a magnetised body is dependent on the imperfections within the body. These imperfections generate energy barriers that inhibit domain wall motion. Domains can also rotate as a whole into an externally

applied field direction. This reorientation into an external field is dependent on the magnitude of the external field and the anisotropy within the domain.

1.6 The single domain particle

A single domain particle occurs when it is energetically favourable to have one domain with its large associated magnetostatic energy rather than having a domain wall with its associated energy. Single domain particles become prevalent as the size of a magnetised body reduces and the relative contributions of the domain wall energy increases and the magnetostatic energy decreases. The geometry of a typical single domain particle found in commercial particulate recording media and studied in this investigation is of a prolate spheroid with an aspect ratio of 10:1 and a length of $0.3\mu\text{m}$.

The reversal mechanism within single domain particle's has been and still is an important area of research [9-11]. The reversal mechanism of a particle determines to a large extent its magnetic properties, its switching field, its remanence and the speed of reversal. A particle's switching field is the field required to reverse its moment. A particle's switching speed is becoming increasingly important in the strive for faster read/write times in recording media [12-14]. The two basic forms of moment reversal within a single domain particle are coherent and incoherent

1.6.1 Coherent reversal

Stoner and Wohlfarth (SW) [9] proposed to model the switching mechanism of a single domain particle by assuming that all the atomic spins of the atoms remain parallel to one another during the reversal process, indicated in figure (1-6). This form of reversal has subsequently been known as coherent rotation or Stoner-Wohlfarth (SW) mode of rotation.

Since the publication of Stoner-Wohlfarth model it has been found that the switching fields (field at which the moment of a particle reverses) of SW particles are consistently greater than the switching fields of the corresponding real particles [10]. The reason for the error was thought to be the assumption that the magnetisation remains uniform during reversal process and hence exchange interactions play no role in the reversal process. Consequently non-uniform reversal modes for the particle switching process have been suggested [15], e.g. fanning, curling and buckling.

1.6.2 Incoherent reversal

The fanning mode of reversal was suggested experimentally by the shape of electrodeposited iron particles observed with an electron microscope [16]. The shapes of the particles were similar to a long chain of peanuts. Jacobs and Bean proposed a model that represented a single domain particle by a chain of spheres [10]. Their model considered the applied field energy and the magnetostatic energy of the dipole dipole interactions between the spheres. They examined both symmetrical fanning and coherent rotation. In the fanning mode indicated in figure (1-6) they found that north and south poles are brought together, thus reducing the magnetostatic energy, while in the coherent mode like poles were aligned, thus increasing the magnetostatic energy. The effect of an increased magnetostatic energy contribution in the coherent mode was to make the fanning mode a more energetically favourable reversal mechanism.

Curling was investigated theoretically in micromagnetics by Frei *et al.* [11]. The curling mode is characterised by the existence of no free poles on the particles surface during the reversal process, thus no external magnetostatic fields are generated during the reversal process. The diagram in figure (1-6) indicates the classical description of curling, where all the moments lie parallel to the surface of the particle. A full description of the main aspects of curling and the other forms of reversal can be found in the book by Cullity [7].

Buckling is another form of reversal mechanism that has been investigated [7,11]. The mechanism gave theoretically lower switching field for particles with specific geometric conditions than coherent, fanning or curling reversal mechanisms. Buckling is characterised by moments reversing locally within the particle and these reversed moments acting as points of nucleation for further reversal.

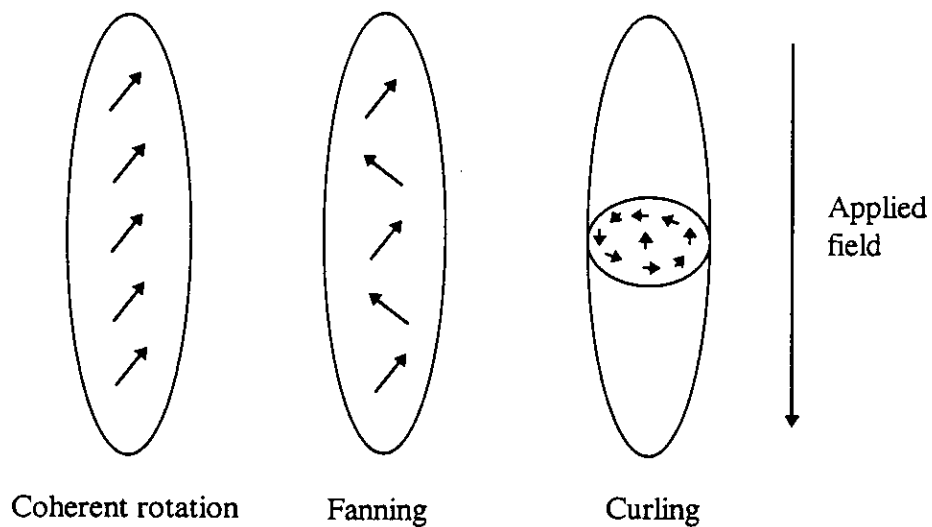


figure (1-6): Reversal mechanisms.

1.7 Magnetic interactions in particulate media

The properties of particulate media are determined by properties of the particles, the particle orientation distribution within the media and the interaction effects between particles. The interactions within particulate media are magnetostatic (long range) and tend to lead to the formation of flux closures.

An explanation of the interaction effects within a simple system of magnetically identical particles given in figure (1-7) is used as an example. In the system all the fields shown are the fields generated from particle A. It is clear that particle A will affect particles B and C differently due to their relative distance, orientation and position. Particle B experiences a magnetising field, while particle C experiences a demagnetising field from particle A. These interaction effects becomes apparent when external fields are applied to switch the particles. If an external field is applied in the negative z direction, then the field from particle A would aid switching of particle C and oppose the switching of particle B. This would result in particle C reversing its moment at a lower field value than that of particles A or B.

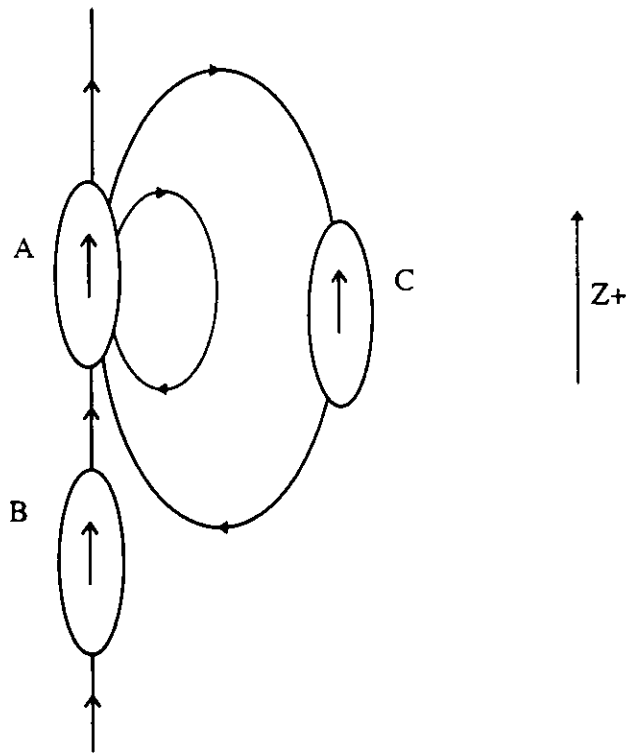


figure (1-7): Interaction effects between particles.

If now all interactions are considered during the switching process of the system, particle C would switch first, aided by the demagnetising interaction fields of particles A and B. The interaction field of a switched particle C would oppose demagnetisation of both particles. However, particle A will experience a greater magnetising field from switched particle C than particle B. The next particle to switch would be particle B, its interaction field would then try to demagnetise particle A and initiate its switching. This simple example has shown how difficult interaction effects are to understand. In fact the number of interactions considered in any system is the factorial of the number of particles within the system. In this case a system of three particles contains six interactions, a ten-particle system would contain over 3.6 million interaction fields. This indicates just how complex a real system would be to model or describe.

A mean field approximation has been proposed [6] to describe the effects of interactions within particulate media. The model represents the effect of inter-particle interactions by a mean field determined from the medium's mean magnetised state. If a particle is considered to lie in a magnetised body, as in

figure (1-8), the particle will experience the effect of the applied field H_{APP} , its own demagnetising field H_d and the field H_{HOLE} . The field H_{HOLE} is generated by the

mean magnetised state of the media, assuming there is a hole in instead of the particle. The effective field the particle experience is a result of all these fields and is given as

$$H_{EFF} = H_{APP} + H_d + H_{HOLE} \quad (1-15)$$

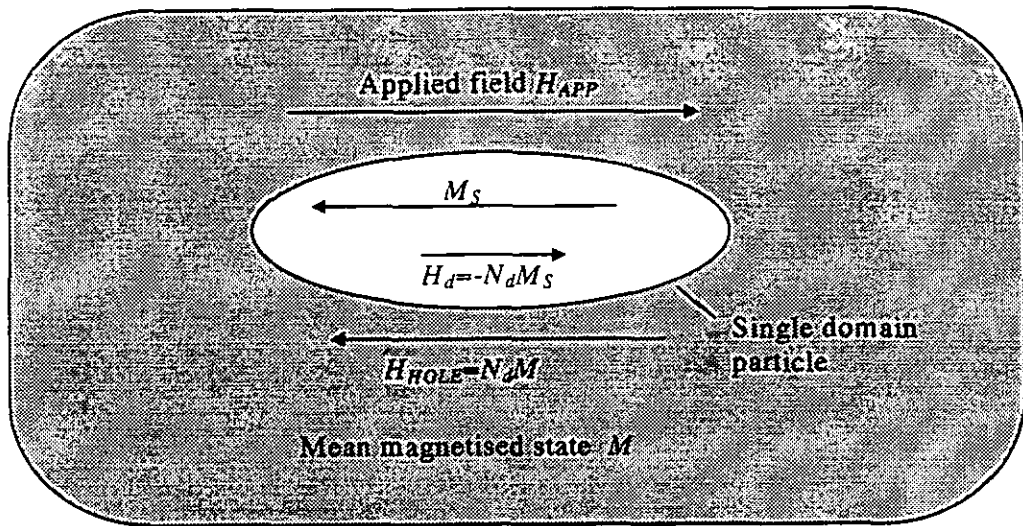


figure (1-8): Mean field approximation.

The effect of the field H_{HOLE} before half the medium had switched is to oppose the switching of particles, after half the medium has switched the effect of H_{HOLE} is to aid further switching of particles. The mean field approximation predicts that the switching field distribution of a medium will be at a lower mean field value and have a broader distribution.

The packing density of a medium influences the properties of the individual particles within the media. The properties of particles within the medium are determined by the properties of the particles and the interaction effects between the particles. As the packing density within the media increases, particles begin to touch and so lose some of their shape anisotropy. The loss of shape anisotropy reduces the particle's coercivity. Another consequence of an increased packing density is increased interaction field between the particles. This field can either magnetise or demagnetise the sample as a whole depending on the relative orientation of the particles within the medium.

The effect of packing density was first investigated by Neel [17] who proposed an empirical relationship between the packing density of the media, the coercivity of an isolated particle with shape anisotropy only and the coercivity of the media as a whole. Neel's empirical relationship given as

$$H_c(p) = H_c(0)(1 - p), \quad (1-16)$$

where $H_c(0)$ represents the coercivity of an individual isolated particle and p is the volumetric packing fraction. This empirical relationship indicates that as the packing density increases to unity the coercivity reduces to zero. This relationship was later used in the study by Knowles [18,19] who found a good agreement in $\gamma\text{-Fe}_2\text{O}_3$ samples between experiment and theory in a packing density range of 0 to 0.4.

1.8 Particulate recording media

Particulate recording media are still one of the most common forms of magnetic media used commercially today. The medium consists of a dispersion of magnetic particles coated onto a support material in an organic binder. Information is stored as a magnetic pattern by the application of a magnetising field. The recording head is an electromagnet, through which a current passes that represents the write signal. Information is written on to the media by a time varying current signal as the head moves at a constant velocity along the medium. The signal is represented by the spatial variation of the remanent magnetisation in the media. The motion of the read/write head across the media reads the information. The head picks up an induced voltage signal proportional to the remanent magnetisation and the velocity of the head across the medium. This read signal is not an exact facsimile of the original write signal but constitutes a reproduction of it. The raw signal is electronically processed to become a reproduction of the original write signal.

Particulate media must have specific properties to allow the successful recording and reading of magnetically coded information. The particles within the media must have an adequate remanent magnetisation to generate sufficient field for the read/write head to measure. The coercivity of the particles must be small enough to allow successful writing and large enough to resist signal degradation with storage time. The switching field distribution of the particles within the medium should be narrow to

allow sharp transitions from one magnetised state to the next, this facilitates the ability to record data at high densities. If the switching field distribution of a medium is broad a number of problems are encountered. A distribution that extends to excessively large coercivities will cause problems in the erasure and the overwriting of old data with new. This is particularly problematic for analogue data that requires a thorough erasure, digital data however can tolerate some residual overwritten signal. A distribution that extends too low coercivities can lead to problems of instability in the magnetised signal and the phenomena of print through. Print through occurs when a magnetised signal from one tape layer is transferred weakly to an adjacent layer in the reel [20]. Particles must also be stable chemically and physically under conditions they are liable to encounter in their use.

The transition density, essentially the information density within a medium is determined by the physical size of the particles. A recorded segment should contain a large number of particles to give a small signal to noise ratio. For a high density media with low noise the magnetic particles should be as small as possible. There is a requirement to minimise the separation between the media and the read/write head to allow an efficient read/write process. This process depends partly on the smoothness of the recording surface. These requirements have led to a trend to smaller magnetic particles. As the size of these particles reduce they become increasingly susceptible to magnetic fluctuations due to thermal energy. The moment of a particle can reverse by a thermally activated transition, this reversal phenomena is called time dependence [21]. The limit of magnetic stability occurs when the thermal energy becomes of the same order as the anisotropy energy, at this point the particles are said to be superparamagnetic, they act like individual spin moments of paramagnetic materials.

There is a constant trend to increase data densities within particulate media by the reduction of particle size and the increased perfection of particle morphology. Particle size determines the finite limit of recording density, since a bit of information can not change over the physical length of a particle. Particles with greater morphology perfection have a narrow switching field distribution, this allows sharper magnetic transitions. As consequence of increased recording densities there is a tendency for particles to have larger coercivities to counteract the effect of the internal demagnetising fields generated at magnetic transitions. Thus, in particulate media there is a general

trend to small morphologically perfect particles with high coercivities, but not so high as to prevent recording heads from writing data.

There exists a wide variety of commercial particulate recording media that have been developed for data storage. For example, gamma-ferric oxide, cobalt modified gamma-ferric oxide, chromium dioxide, metal and barium ferrite. All these particulates, except for barium ferrite are acicular in shape and have a strong shape anisotropy.

Gamma ferric oxide ($\gamma\text{-Fe}_2\text{O}_3$) particles are acicular in shape with a typical length of 0.3-0.4 μm and a diameter of 0.06-0.03 μm [22-24]. The particles have a cubic crystal structure with a magnetocrystalline anisotropy constant of $K_1 = -4.64 \times 10^3 \text{ J/m}^3$ [24]. Gamma ferric oxide saturation magnetisation is 336-340 kA/m. The particles anisotropy results predominantly from its shape giving coercivities of 20-28 kA/m. There is a discrepancy between the measured coercivity of a gamma ferric oxide particle and its theoretical coercivity from Stoner-Wohlfarth model. This is thought to arise from the morphology of gamma ferric oxide, since rather than having a clean surface the particles are dendritic. The effect of the dendrites results in the formation of a number of nucleation points which subsequently leads to a reduction in the coercivity [25,26]. Apart from the morphological problems associated with gamma ferric oxide, it remains a popular particulate due to its high chemical stability and low cost.

Cobalt modified gamma ferric oxide ($\text{Co-Fe}_2\text{O}_3$) particles were a technological advance in the coercivity of metal oxide particles. The particles can either be cobalt doped into the iron oxide structure [27] or cobalt absorbed onto the oxide surface. Cobalt doped iron oxide structures were the first attempt to increase the coercivity of iron oxide structures. The coercivity of these structures was increased by exchange interactions between the electronic structure of cobalt and the iron oxides. This led to a coupling of the high magnetocrystalline anisotropy of cobalt $K_1 = 4.3 \times 10^5 \text{ J/m}^3$ to the iron oxides, increasing its coercivity to 43-60kA/m. [28,29]. Cobalt doped iron oxides are not satisfactory for magnetic media, since the coercivity is temperature dependent and displays progressive loss of short-wavelength signal amplitude with repeated playback [23]. In an attempt to avoid these problems cobalt was surface doped onto the iron oxide particles [30,31]. Surface doping had the effect of improving the temperature dependence of the switching field of particles and increasing its coercivity. The surface doped cobalt iron oxide particles have similar size and shape to that of iron oxide

particles. Their saturation magnetisation is 350-355 kA/m and their magnetocrystalline anisotropy constant is $K = -5$ to $+100 \times 10^3 \text{ J/m}^3$ [24].

Chromium dioxide (CrO_2) was developed as a recording particle for its high coercivities typically 26-157kA/m. Chromium dioxide particles are acicular in shape with a length of 0.5-0.1 μm and an aspect ratio of 30-5:1 [32,33]. Chromium dioxide has a tetragonal rutile crystal structure. The easy direction of the magnetocrystalline anisotropy has been reported parallel to the c axis [34] or inclined by 40° to the c axis [35]. The anisotropy of chromium dioxide particles is dominated by their strong shape anisotropy. The reversal mechanism within chromium dioxide has been investigated theoretically and experimentally [11,36]. Results indicated a curling mechanism, which is only possible in highly smooth particles with few dendrites. Chromium dioxide particles have few imperfections (few dendrites) and are uniform in shape, this aids in efficient packing and good orientation of the particles within the medium.

Metal particles of pure iron were investigated as a particulate in magnetic recording media for their large saturation magnetisation typically 870-1110 kA/m, which is four times that of an iron oxide. The initial problems associated with the development of metal particles were associated with their tendency to oxidise. This problem with oxidation was solved by the development of a surface passivation layer, which inhibits oxidation of the bulk iron. The particles are acicular in shape with a length of 0.1-0.3 μm and an aspect ratio of 10-5:1, giving coercivities of 30-131 kA/m. The reversal mechanism within metal particles has been found to be dependent on its shape and crystal structure. Under certain physical conditions the fanning mode is appropriate [16], while under other conditions curling is more appropriate [11].

Barium ferrite was initially developed with an application to perpendicular recording in view. The benefit of perpendicular recording is a reduction in self-demagnetisation, this allows for the retention of sharp transitions within the media, and hence high recording densities are possible. Pure barium ferrite was found to have an excessive coercivity and size for high density recording. This problem was solved by the substitution of Fe with Co and Ti within the barium ferrite structure [37], this led to particles having typical diameters of 0.1 μm with a thicknesses of 0.017 μm [23,38] and coercivities of 160-238 kA/m [24]. Barium ferrite has a hexagonal lattice in a platelike structure. Its anisotropy is predominately uniaxial magnetocrystalline with the easy axis

perpendicular to its plane, while its shape anisotropy is in the plane of the platelike structure. The physical and chemical properties of barium ferrite are found to be stable.

Particulate recording media are produced by the well-established technique of coating a support material with a dispersion of discrete magnetic particles in an organic binder [39]. This creates a magnetisable layer on the surface of a nonmagnetic support layer, such as polyethylene terephthalate (P.E.T.). Particulate media basically consist of single domain particles held to a substrate by a binder. Magnetic layers can typically range in thickness from 0.25 μm for a rigid disk to 12 μm for an audio tape [23].

A dispersion is a careful blend of magnetic pigments, wetting agents, abrasive agents, organic resins, lubricants and one or more volatile solvents. The magnetic pigment used is specifically chosen to have the appropriate coercivity for the recording application in which the medium is to be used. The organic resins are used to separate the particles in the dispersion and to provide a binding for the particles in a tough, flexible tape coating. Wetting agents are added to reduce the formation of agglomerates within the dispersion. Lubricants are added to reduce the friction generated by the contact between the tape and the read/write head. A common lubricant is carbon black, which has the advantage of also being an anti-static agent. Abrasive agents such as alumina are imbedded into the tape to remove the accumulation of polymer molecules from the read/write head.

The preparation of the dispersion goes through many stages in its production process. These include premixing, milling, letdown and activation [39]. The completed dispersion can be spread onto the support film via a number of techniques, including knife coating and the use of a rotating drum [38,39]. During the coating process the particles on the tape can be given a orientation in the plane of the tape by the application of a magnetic field.

Chapter Two

Measurement of the properties of isolated magnetic particles: Experimental Theory

2.1 Introduction

A technique was proposed by J.E. Knowles [1] in 1978 to measure the magnetic properties of isolated acicular magnetic particles. The basic technique involved observing under a microscope the reaction of a particle to a weak aligning and a large pulsed magnetic field. The technique essentially measured the switching field of a particle, the applied field at which the moment of the particle reversed, identified by the rotation of the particle through 180° .

The technique required the preparation of a dilute viscous particle dispersion. This dispersion was sealed within a micro-slide tube, placed between two pulsed field coils and was observed under a microscope. Under observation, the particles were aligned in an orientation field ($\sim 1\text{mT}$) generated from weak permanent magnets and an opposing pulsed magnetic field generated from a field coil was applied, indicated by the schematic diagram in figure (2-1). After the pulsed field was applied, if the particle remained stationary, then its moment had not switched and another pulsed field of greater magnitude was applied. This technique was repeated until the particle was seen to rotate through 180° . This indicated the moment of the particle had switched in the applied pulsed field and was now realigning within the orientation field.

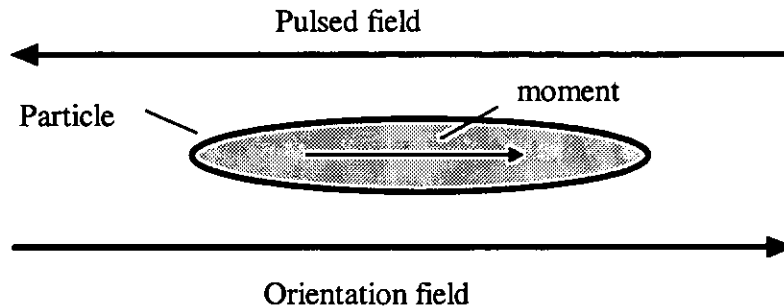


figure (2-1): Schematic diagram of the experimental technique for the measurement of an isolated magnetic particles switching field.

The technique was selective as only apparently single isolated particles were measured. Small agglomerations that appeared to be single isolated particles were identified by their reaction to pulsed magnetic fields. If after a pulsed magnetic field the suspect particle rotated, but not through 180° then it was assumed the particle had been demagnetised, indicating it was a multiple or a multidomain particle.

The basic apparatus for the measurement of the switching field of an isolated particle can be divided broadly into two areas, the optics and the magnetic field generation. The optics allows the visualisation of the particles under investigation, while the magnetic field generation allows the investigation of the particles magnetic properties.

2.2 Sample preparation

The particle dispersion used as samples for the measurement of the properties of isolated magnetic particles required specific characteristics. The particles within the dispersion were required to be isolated and to remain in the field of view during the time frame of the experiment. As a consequence the particles were dispersed in a viscous resin.

The dispersion was derived from particles originating from commercial and hand spread tapes. The particles within a sample were extracted by soaking the sample ($\sim 6\text{cm}^2$) in cyclohexane ($\sim 5.5\text{g}$). This solution was agitated in an ultrasonic bath until

the resin binding the particles to the tape had dissolved and a suspension of particles was created. The dispersion was produced by stirring ~0.2g of the suspension into ~5.0g of Vagh resin , which is a vinyl chloride using a Turrax™ high shear blender.

The viscosity of the dispersion for the experiment was controlled by further additions of solvents or resin. If the motion of particles within the dispersion during the experiment was problematic (the particles moving out of the optics field of view), then more resin was added. If the particle took an excessive amount of time to rotate, more than a minute, then more solvent was added.

2.3 Experimental techniques

The basic apparatus for the switching field measurement of a particle consisted of a platform that held a pulsed field coil and two permanent magnets that aligned the particles. A schematic overview of the platform is presented in figure (2-2).

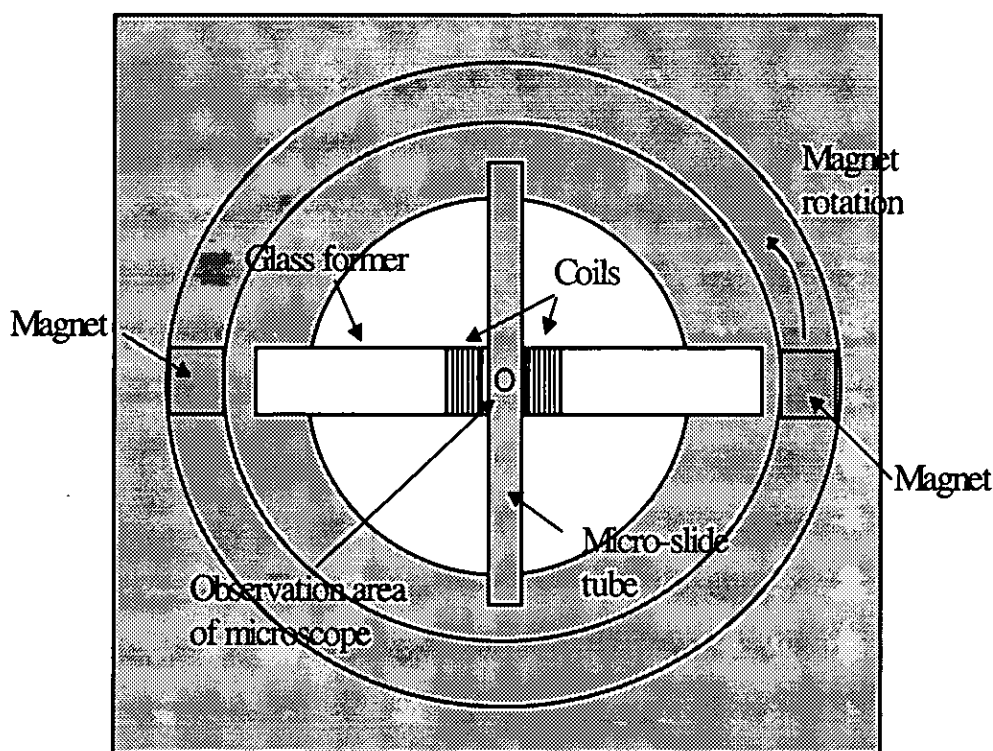


figure (2-2): Pulsed field coil platform.

A number of techniques were developed by Knowles [2,3] as extensions to the basic technique for the switching field measurement of a particle. The techniques allowed for the measurement of

1. The switching field as a function of the applied field angle with respect to the easy axis of a particle
2. The remanent magnetisation of a particle
3. The effect of A.C. demagnetisation upon an apparently single particle
4. The anisotropy field of a particle

Techniques 1 and 2 are described with their experimental results in chapter 3. The other two techniques were not utilised within this study and are not discussed.

2.4 Microscope

A schematic diagram of the microscope used for the measurement of isolated particles is found in figure (2-3). The schematic indicates all the main components of the microscope and its basic experimental set up.

The microscope had an oil immersion objective with an oil immersion condenser. The oil immersion system consisted of an oil film with a similar refractive index to crown glass in between the condenser and specimen and the specimen and objective [4]. The oil film filled the air gap found between the specimen and the objective, allowing more oblique light rays to pass through the objective. This had the effect of increasing the numerical aperture (N.A.) of the objective. A similar effect occurred for the oil immersion film between the specimen and the condenser.

The N.A. is a term commonly used to compare the resolution of various objectives regardless of their working medium and magnification. The N.A. is quoted as a number which has a linear relationship with the resolving power of the microscope and is defined as

$$NA = n \sin \alpha . \quad (2-1)$$

Here n is the refractive index of the medium between the object and the lens, and α is half the intake angle of the lens.

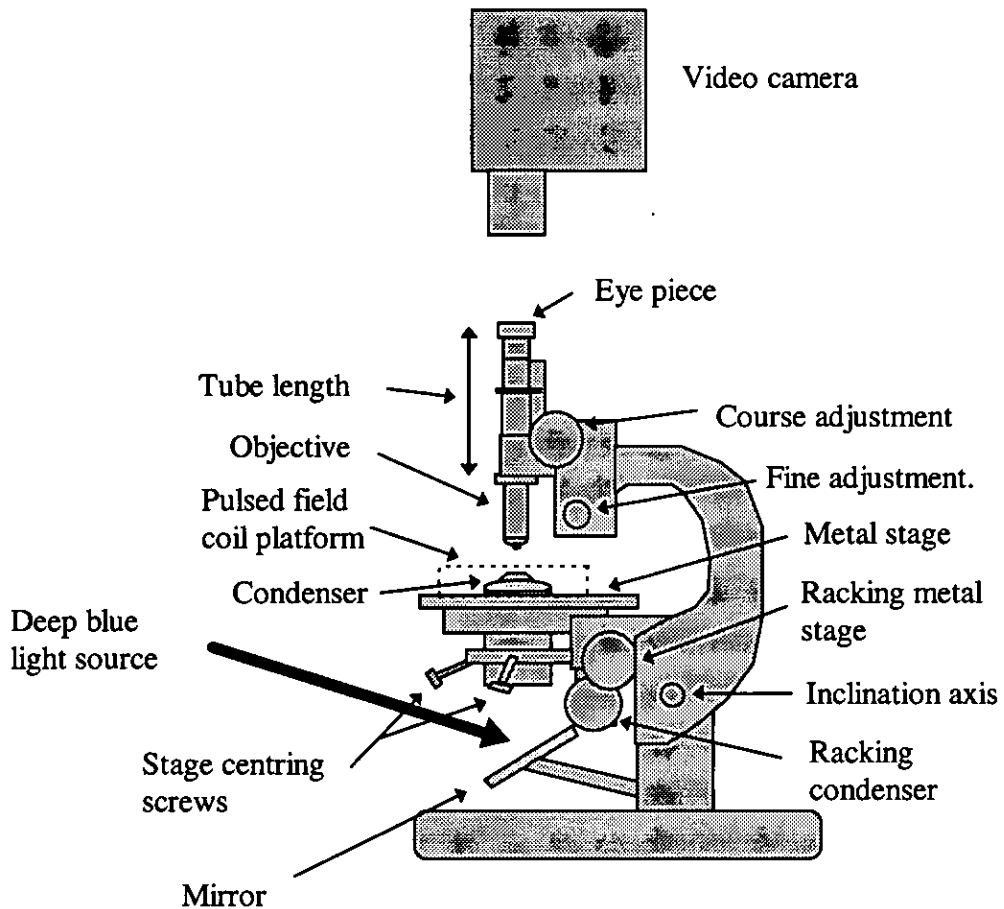


figure (2-3): Microscope.

The objective is a lens or a combination of lenses. Its main purpose is to collect the light passing through the specimen. There are many forms of objectives; including Achromatic, Semi-Apochromatic or fluorite and Apochromatic. These terms refer to the colour correction for the chromatic aberrations of white light within the lens. The objective found within the microscope for the single particle measurements was an oil immersion Semi-Apochromatic. This objective had a N.A. of 1.25 with a x63 gain. This type of objective has the same focal point for two wavelengths in the visible spectrum, in practice all other spectral colours are very near to the same focal point. In most circumstances a semi-apochromatic objective is indistinguishable from apochromatic objectives where three spectral components have the same focal length.

The objective tube length for the objective lens used in the single particle measurements was 160mm. This is the optical path length when the image from the objective has been fully corrected for spherical aberrations. The working distance of the objective is an important parameter when using high resolution microscopy. For objectives with large apertures that have a small working distance, problems can arise when the working distance of the objective is less than the outer thickness of a microslide tube or the thickness of a cover glass. Simply it is not possible to focus on the sample within the tube or below the cover glass.

The condenser is a lens or a system of lenses placed below the sample under investigation. The purpose of the condenser is to illuminate the sample at a controlled angle. Within the condenser there is an iris diaphragm that controls its aperture. For high resolution work the highly corrected objectives with large apertures requires the condenser's aperture to match that of the objective to give the maximum resolution. The condenser found within the microscope for single particle measurements has a N. A of 1.4. It also contains a patch stop near its iris diaphragm.

The patch stop is a disc made of glass with an opaque centre. The patch stop generates a hollow cone of light that reduces the direct light entering the objective. This increases the contrast when observing small opaque objects. This is because the more axial the light the more it will be affected by diffraction effects at the particle, blurring the projected image at the eyepiece [5].

The function of the microscope eyepiece was to act as a magnifier, enlarging the image resolved by the objective to a size suitable for the eye to perceive. The eyepiece within the microscope had a gain of x20. The eye piece projected the image onto a Philips black and white video camera, which was then displayed on a monitor. The overall magnification of the microscope and the video camera was ~10000, which could be increased to ~15000 by increasing the distance between the eyepiece and the video camera.

The light source of the microscope was deep blue having a wavelength of approximately 460 nm. The light source power was generated by a 100 watt bulb powered by a 12 volt power supply unit.

The resolution of the microscope depended on whether the objective had a sufficient aperture to accommodate the cone of light through the sample and the first order diffraction spectra generated by the aperture of the condenser. The diffraction effects within the microscope determine its finite resolution. The diffraction effects are determined by the N.A. of the microscope and the wavelength of light used. The experiments performed by Abbe [5] led to the conclusion that the resolving power R of a microscope was

$$R = \frac{\lambda}{2N.A.} \quad (2-2)$$

The resolution of the microscope calculated from equation (2-2) was $0.19\mu\text{m}$. This resolution limit determined the lowest particle size observable within the microscope.

2.5 Pulsed field generation

The technique to measure the switching field of an isolated particle required the particle to be aligned in an orientation field (~ 1.0 mT), while a large opposing pulsed magnetic field was applied, indicated earlier in figure (2-1). The generation of a large pulsed magnetic field required the construction of a pulsed field coil and a pulsed voltage source. For the measurement of commercial magnetic particles the pulsed field generated from the coil and driven by the voltage source was required to be in excess of 0.15 Tesla. The pulsed field should also ideally be uniform over its duration and the experimental observational area of the microscope to allow repeatable and consistent experimental results.

2.6 Pulsed Field Coil

In the previous work by Knowles the field coil former was constructed from optical quality glass which was in optical contact with the objective of the microscope and its condenser. This experimental set up for the microscope is essential for maximum resolution. If there is not an optical contact between the specimen tube and the optics the resolution of the microscope is reduced and as a consequence, it would be impossible to

resolve a single magnetic particle. For these reasons the pulsed field coil and the experimental set up developed by Knowles were adopted in this work.

The pulsed field coil design consisted of a field coil former constructed from optical quality glass slides with enamelled copper wire wound onto a former to create a Helmholtz pair. The sample tube in the final constructed pulsed field coil would lie in between the two coils of the Helmholtz pair.

The coil former was fashioned from three pieces of optical quality glass. The main piece approximately 3x35x0.8-1.0 mm was fractured from a glass slide with dimensions of 76x26x0.8-1.0 mm. The edges of this fractured piece were smoothed using emery paper and its physical dimensions measured. The other two pieces were fractured from a cover slip with dimensions of 22x22x0.17mm to match the width of the main glass slide. These three fractured glass pieces were glued together with commercial cyanoacrylate in the form given in figure (2-4).

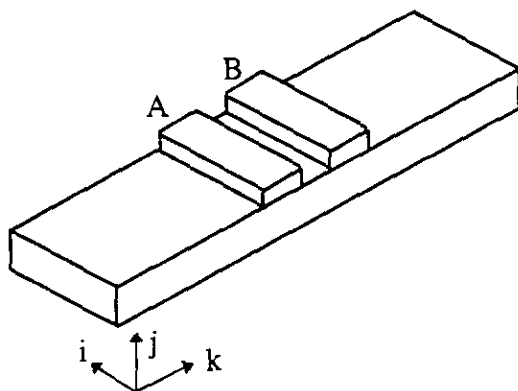


figure (2-4): Coil former.

The next stage of construction was the coils' winding. Coils were wound with 0.05mm enamelled copper wire under a strong magnifying glass at points A and B in figure (2-4). Particular care was taken at this stage to achieve good coil uniformity as this is essential for field uniformity. After the completion of each coil winding stage, the coils were glued to the glass former with commercial cyanoacrylate. The final construction stage was to solder the two coil ends together to create a Helmholtz pair. A diagram of the final constructed pulsed field coil is given in figure (2-5).

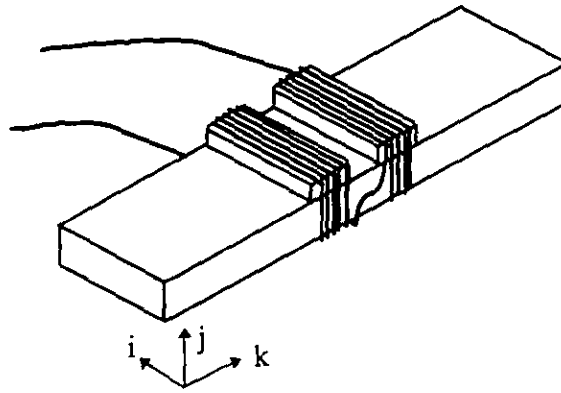


figure (2-5): Constructed pulsed field coil.

After the construction of the pulsed field coil its dimensions were measured and its field profile was calculated.

2.6.1 Field Calculation

Due to the nature of the pulsed field coil construction, it is practically impossible to construct coils with the same dimensions. For this reason it was necessary to calculate the field produced by a pulsed field coil. A numerical program was developed to calculate the field profile for a square Helmholtz coil found in the pulsed field coil. The program was written in GWBASIC and used the Biot-Savart law found in equation (2-3) to calculate the field components in i , j and k as a function of the distance z away from the pulsed field coil centre. Biot-Savart law expresses the vector field \mathbf{B} at some point P as the sum of the contributions to the field made by the elements, $d\mathbf{l}$, of a current carrying conductor

$$\mathbf{B} = \frac{\mu_0 I}{4\pi} \int \frac{d\mathbf{l} \times \hat{r}}{r^2} \quad (2-3)$$

The program considered a square coil as four individual straight wires. The calculation of the field was determined from the solution of Biot-Savart equation for straight wire and summed for all four wires of each coil in the Helmholtz pair.

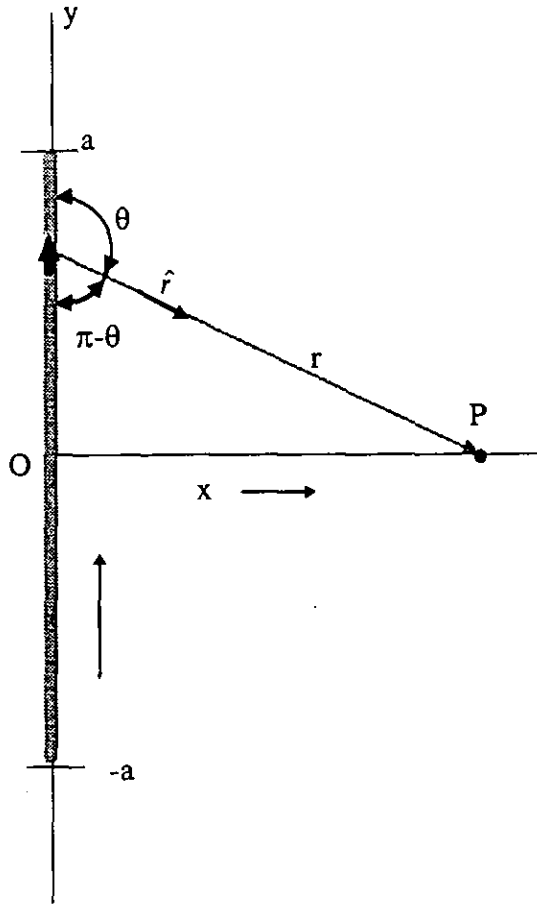


figure (2-6): Magnetic Field of a straight conductor.

The vector element dl of the conductor is dy , the distance $r = \sqrt{x^2 + y^2}$ and $\sin \theta = \sin(\pi - \theta) = x / \sqrt{x^2 + y^2}$. The direction of $d\mathbf{B}$ is perpendicular to the plane of the figure, into the plane, and in this example the direction of $d\mathbf{B}$'s from all the elements of the conductor are the same. Thus, the total field at point P is determined by the integration of all the elements of the conductor. Using equation (2-3) and substituting appropriately for this example, the magnitude of the total field at point P becomes

$$B = \frac{\mu_0 I}{4\pi} \int_{-a}^a \frac{xdy}{(x^2 + y^2)^{3/2}}. \quad (2-4)$$

which yields

$$B = \frac{\mu_0 I}{4\pi} \frac{2a}{x\sqrt{x^2 + a^2}}. \quad (2-5)$$

The field from the Helmholtz pair was calculated using the numerical program and physical characteristics of the coils. These included the inner coil separation, the number of turns in the coils, the wire diameter, the centre height of the sample with respect to the axis height of the coil, the depth of coil, the width of coil, the outer separation of the coils and the maximum current rating of the voltage pulsed driver. The position of each turn of the coil on the former was calculated assuming an average separation between each turn. The resistance of the pulsed field coil was calculated within the numerical program, the program used this value with the maximum pulsed voltage generated from the voltage pulsed driver to calculate the maximum pulsed field profile of the coil. An example of the results from this program is presented in figure (2-7) for coil OC11.

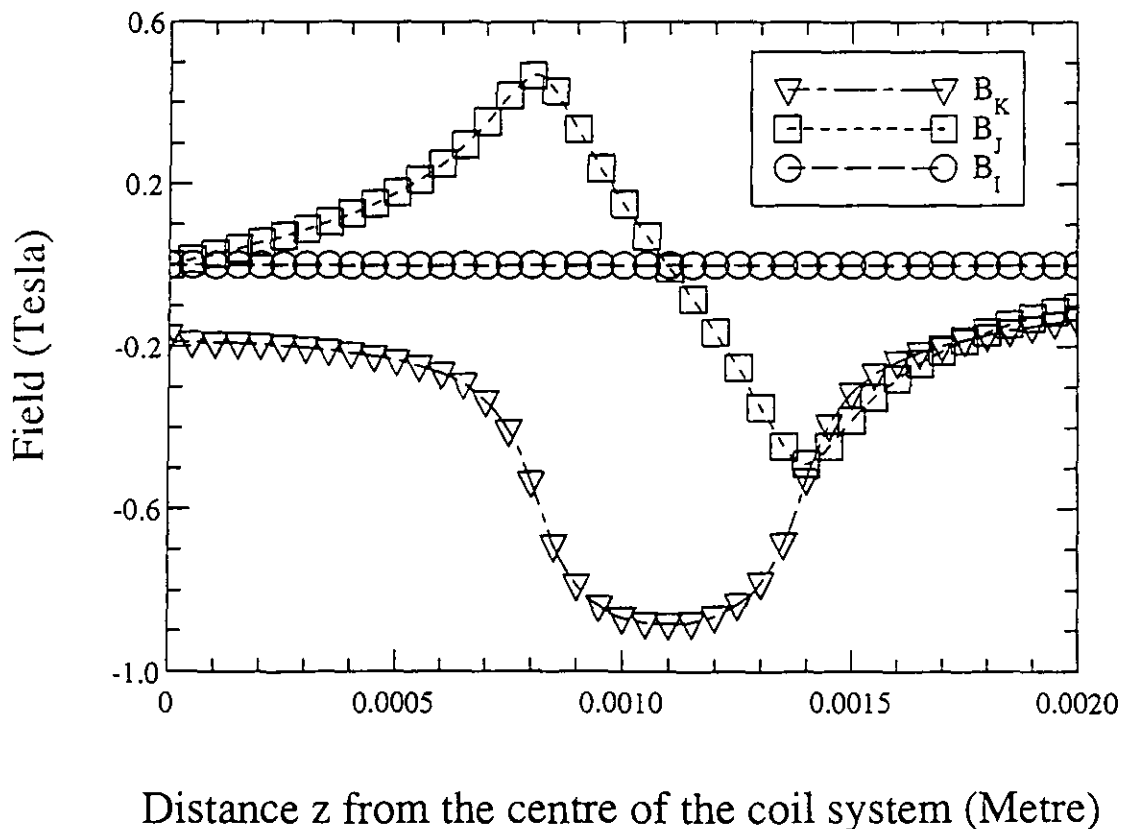


figure (2-7): Field Profile for coil OC11.

The program was also used as a design tool for the determination of the optimum number of turns for a specific pulsed field coil former. It was also important to consider the voltage driver in the determination of the optimum characteristics for the coil. The voltage driver had a maximum voltage of 127 volts and was current limited at 100 Amps. The maximum power transfer from the driver to the coil occurred when the current in the coil was defined by the resistance of the coil and not by the maximum current rating of the pulsed voltage driver.

General maxims for the coil former design were to construct a former with the field coils as close to the sample tube as possible and to reduce the width of the coil former. In reducing the width of the former the length of wire used to wind the coils was reduced, thus reducing the coils resistance and increasing the maximum current for the coil.

The number of turns within a coil was critically important for its maximum field and its field uniformity. It was found that coils with too few turns had a low resistance with a poor power transfer from the voltage driver. The field uniformity from these coils were also found to be poor due to the limited number of turns used to generate the field.

Coils with too many turns led to a problem where the outer turns of the coils did not contribute enough to the coils field to compensate for their resistance. The increased coils resistance reduces the current passing through the coil, thus reducing all the other turns contribution to the coils field. A point was reached where the extra turns on the coil did not increase the coil's field but actually decreased it by the reduction of the current through the coil. These coils had good field uniformity but they had a limited maximum field.

A compromise had to be taken between these two extremes of design. This compromise was achieved simply by running the program to calculate the field profile for a coil former with different number of turns. The results were compared for their maximum field generated and for their field uniformity.

2.6.2 Field Calculation Uncertainty

Analysis of the computed pulsed field coil profiles indicated that the field varied across the observational area of the microscope. For this reason it was decided to calculate the uncertainty in the calculated field profile for the positional uncertainty of a particle and the uncertainty in the measured parameters used to calculate the original field profile. The uncertainty in the field calculation was determined by calculating the fields for the combinations of all the errors. The errors taken for the calculations were the width and depth of the coil former ($\pm 0.1\text{cm}$), the inner and outer separation of the coils ($\pm 0.1\text{cm}$) and the positional uncertainty of the particle (ij plane $\pm 0.1\text{cm}$, j direction $\pm 0.01\text{cm}$). The results from these calculations for coil OC11 are presented in a histogram given in figure (2-8).

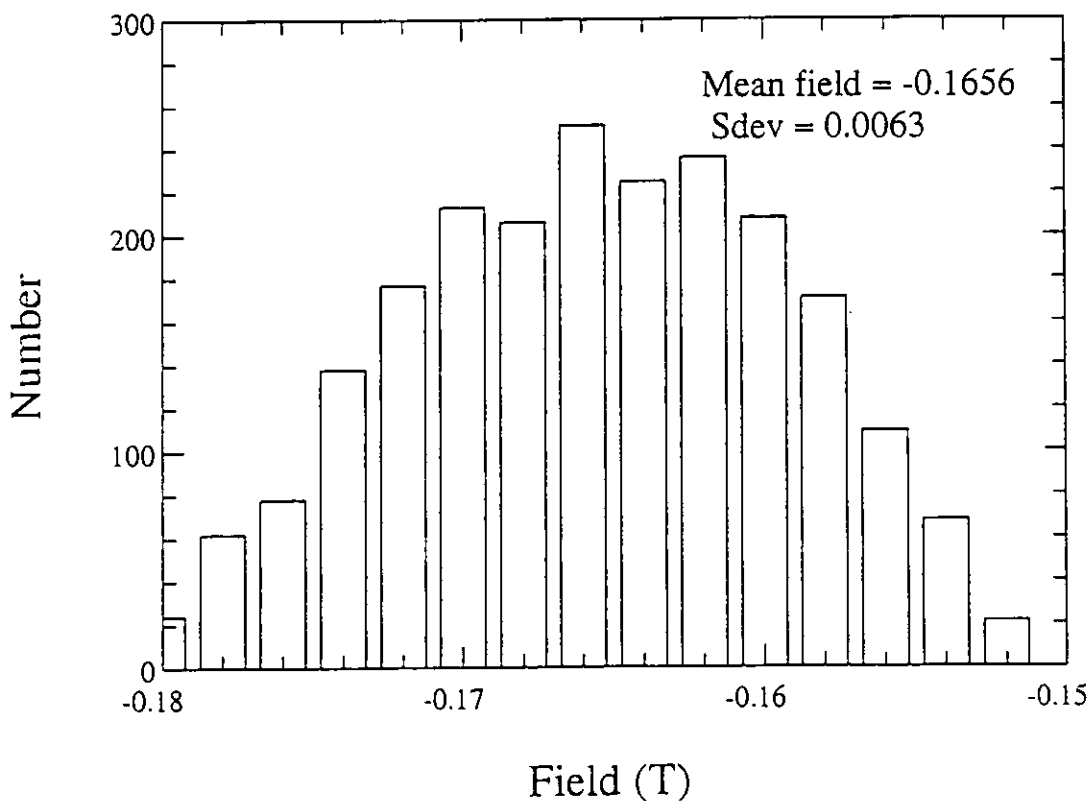


figure (2-8): Field calculation histogram for coil OC11.

The calculation presented in figure (2-8) indicates that the mean maximum field for coil OC11 was 0.1656 Tesla with a standard deviation of ± 0.007 Tesla. This calculated maximum field with its associated error was used in the presentation of all results determined using this coil.

2.7 Pulsed Voltage Source

The magnetic pulsed field is generated by a large pulsed voltage applied to the pulsed field coil. The original pulsed voltage source donated to the department by J. E Knowles had consistently broken down during experimental measurements. It was decided to construct a new pulsed voltage unit, incorporating its own signal generator in a modular unit.

The new pulsed voltage unit was designed in a modular form allowing improvements to the unit at later dates by simply replacing a board. There are four main boards within the unit, the signal generator, the discharge board, the capacitor bank board and the power supply board. A schematic diagram of the complete unit is presented in figure (2-9).

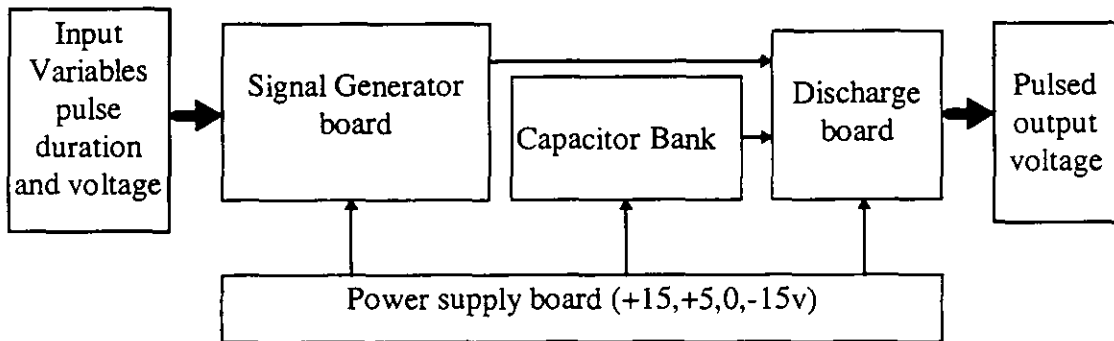


figure (2-9): Schematic diagram of the modular pulsed voltage generator.

The generator was designed to develop a voltage pulse of a fixed amplitude for a specified duration or a repetitive pulse of fixed amplitude, fixed duration and a fixed duty cycle. The pulse parameters are determined by control knobs at the front of the unit.

The power board (board 1) provides the power lines for the analogue and digital circuitry from a 127 volt power supply unit, capable of producing 100 mA. The board also charges the discharge capacitors to a preset level determined on the board by a potentiometer. A circuit diagram for the power board is given in figure (2-10).

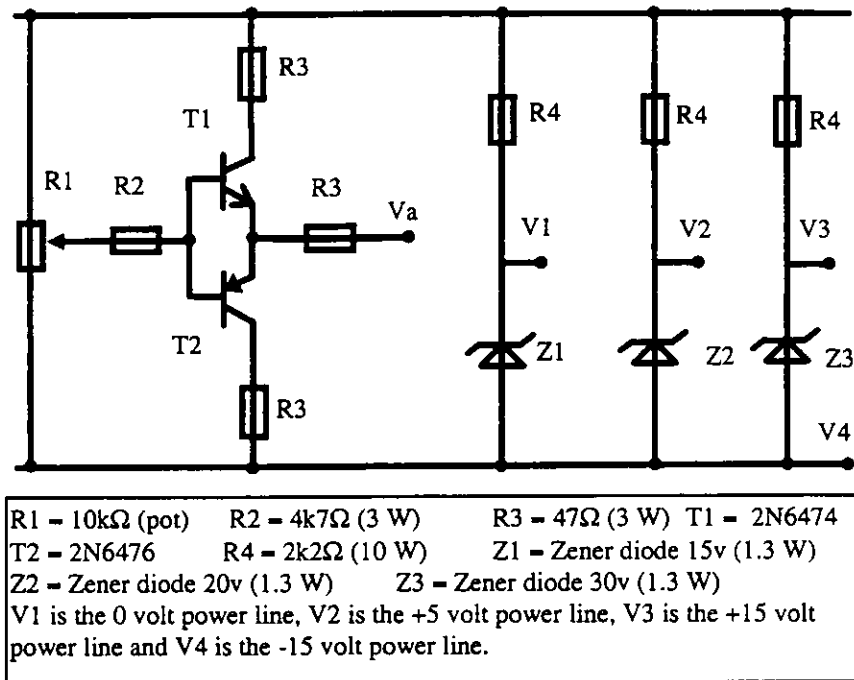


figure (2-10): Power supply circuitry.

The potentiometer R1 determines the voltage V_a to which the discharge capacitors are charged, the potentiometer is a multi-turn and is found on the control panel of the unit. All the power lines within the board are decoupled with a 6600 μ F capacitor on the capacitor bank board (board 4).

This signal generator board (board 2) is the most complex board within the unit. This board generates a single pulse at fixed duration or repetitive pulses at a fixed duty cycle and a fixed duration. The pulse duration and the duty cycle are controlled by potentiometers within the circuitry of the board. The board consists of two astable generators, one of the astable generators is used as a trigger source for the pulse duration monostable generator, while the other sets the duty cycle for the repetitive pulse mode. The two monostable generators determine the pulse duration and the time delay between consecutive pulses, this avoids multiple pulses generated in the single pulse mode. The

analogue switching circuitry allows the transition from single pulse mode to the repetitive pulse mode. A schematic design of the signal generator board is given in figure (2-11).

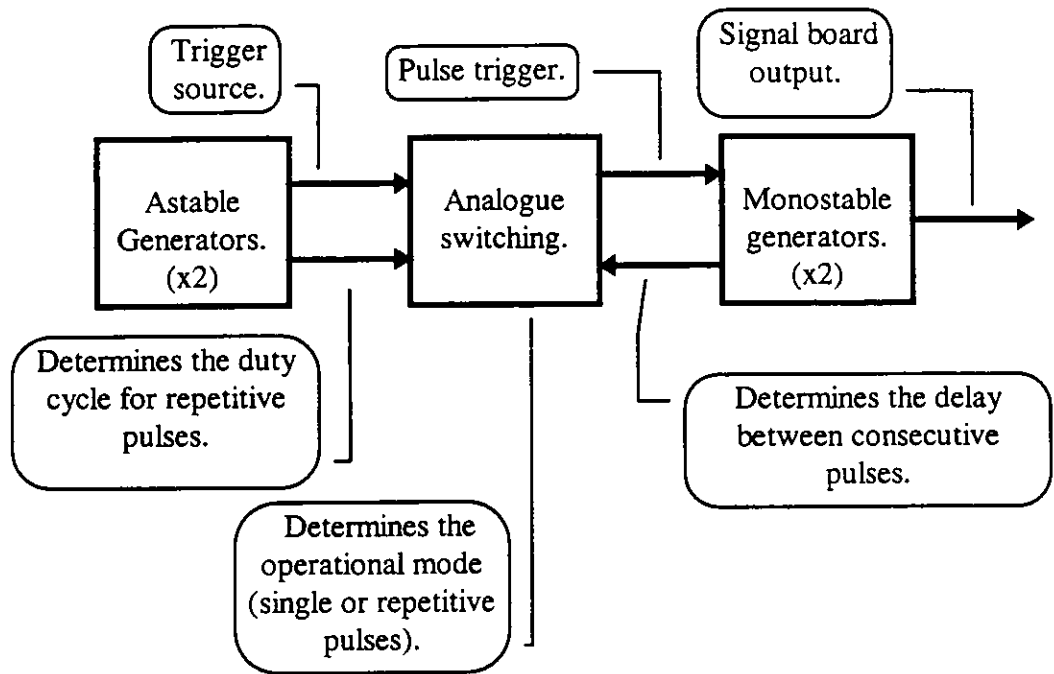


figure (2-11): Schematic diagram of the signal generator board.

The circuit diagram for the astable generators within the signal generator board is presented in figure (2-12). The potentiometer R2 is found on the pulsed voltage source control panel and it determines the duty cycle in the repetitive pulse mode.

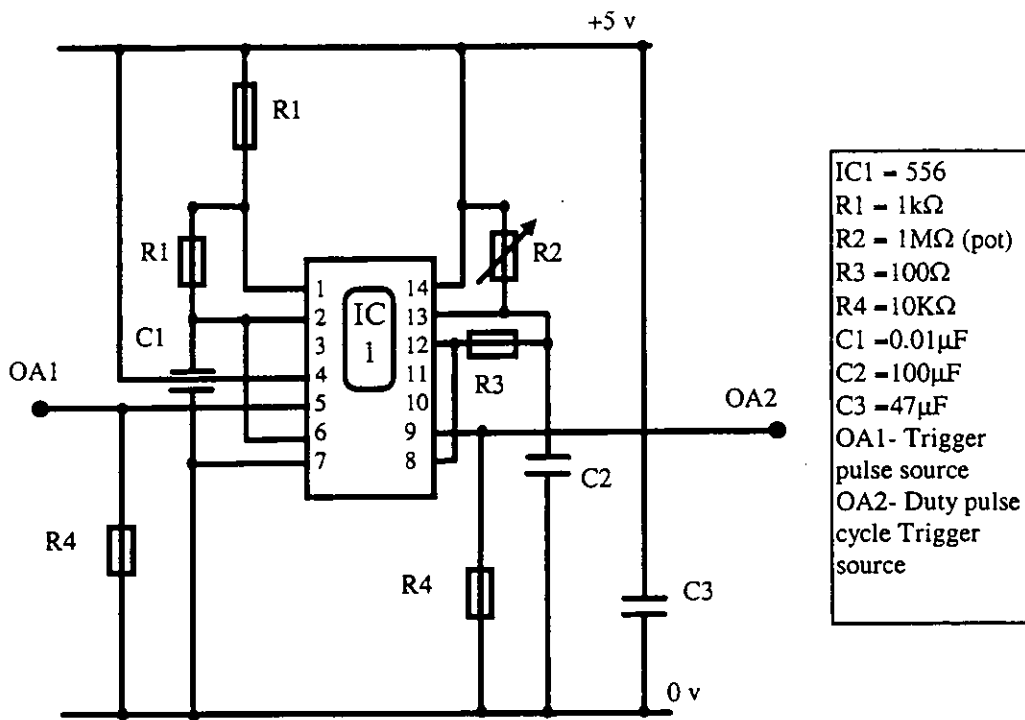


figure (2-12): Astable generators of the signal generator board.

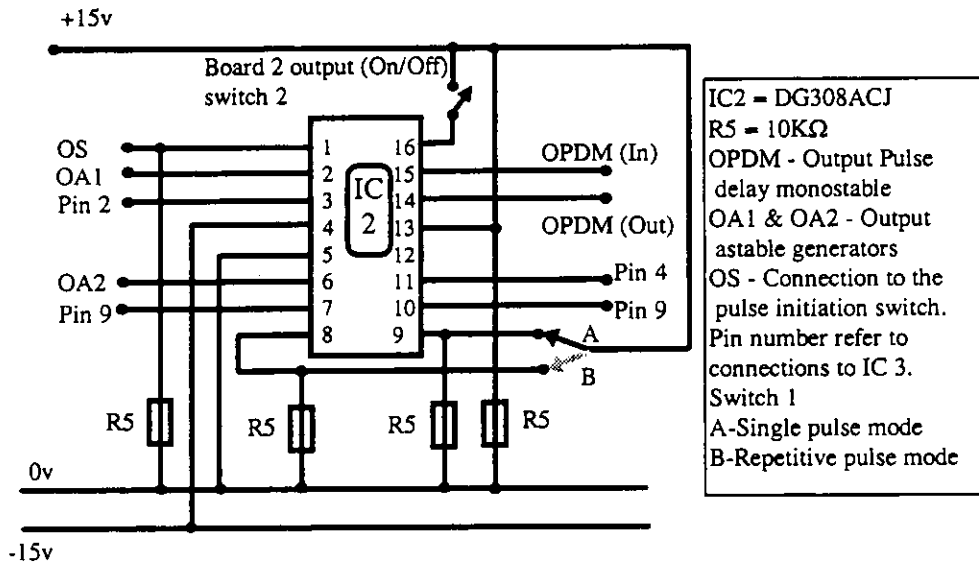


figure (2-13): Analogue switching circuitry of the signal generator board.

The analogue switching circuitry switches between repetitive pulse mode B and single pulse mode A by switch 1.

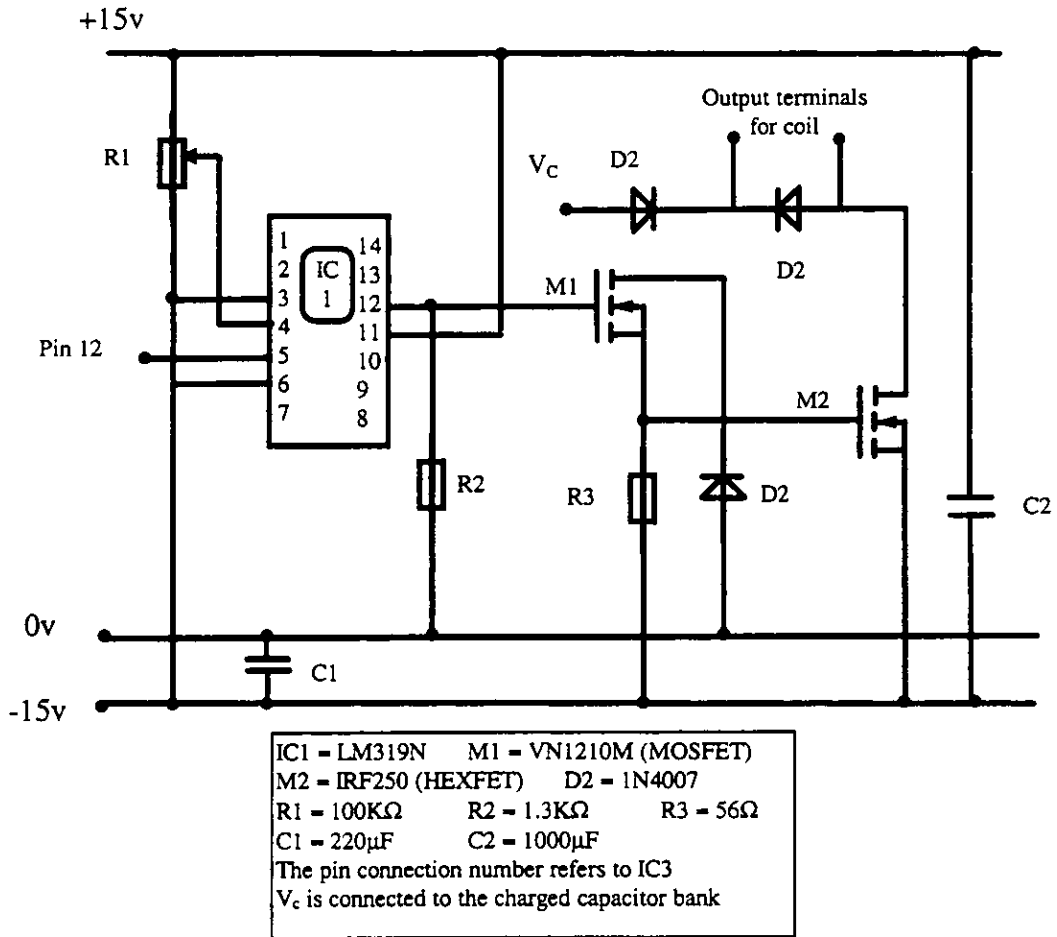


figure (2-15): Discharge board.

The discharge board presented in figure (2-15) allows the charge from the capacitor bank to be discharged through the output load for the duration of the signal pulse. The discharge board contains a comparator (IC1) that monitors the output from the signal board and controls a large electronic switch (a HEXFET) that dumps the energy from the capacitor bank through the output load.

After the construction of the pulsed voltage unit it was necessary to calibrate the multiturn potentiometer on the control panel that controls the pulse duration and the multiturn potentiometer that controls the magnitude of the pulse. The results from these calibrations are presented in figure (2-16) and figure (2-17).

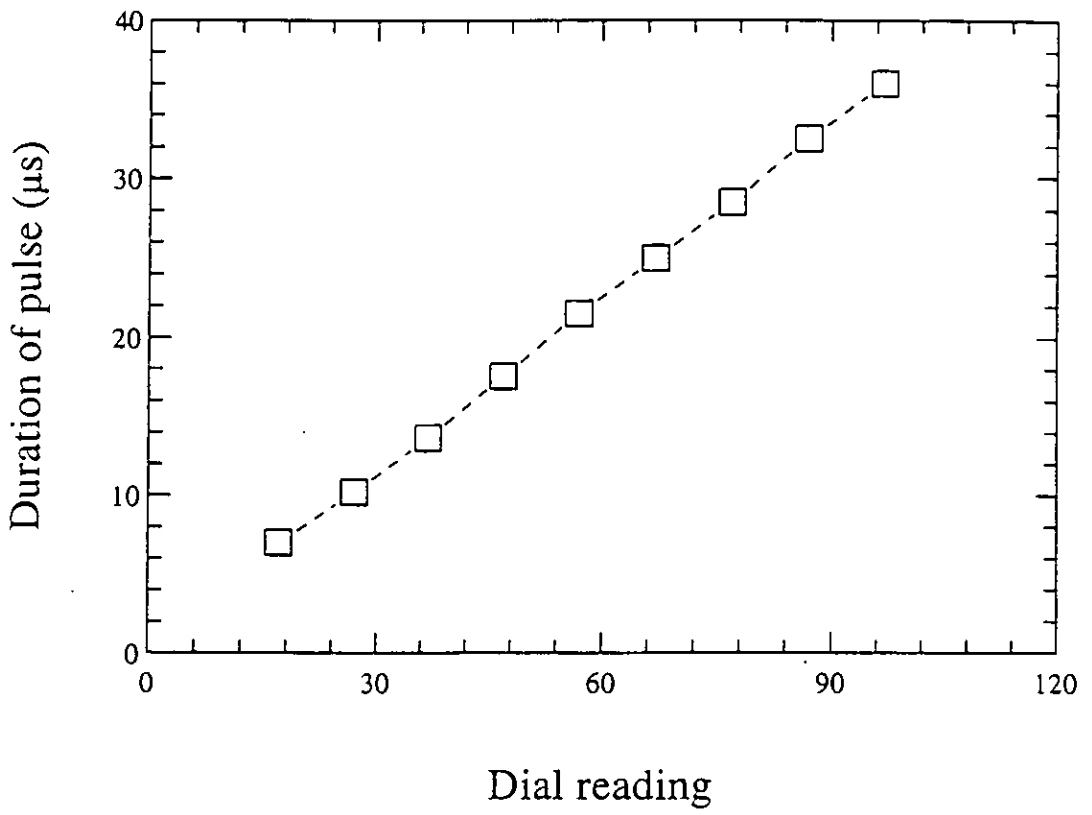


figure (2-16) Calibration of pulse duration.

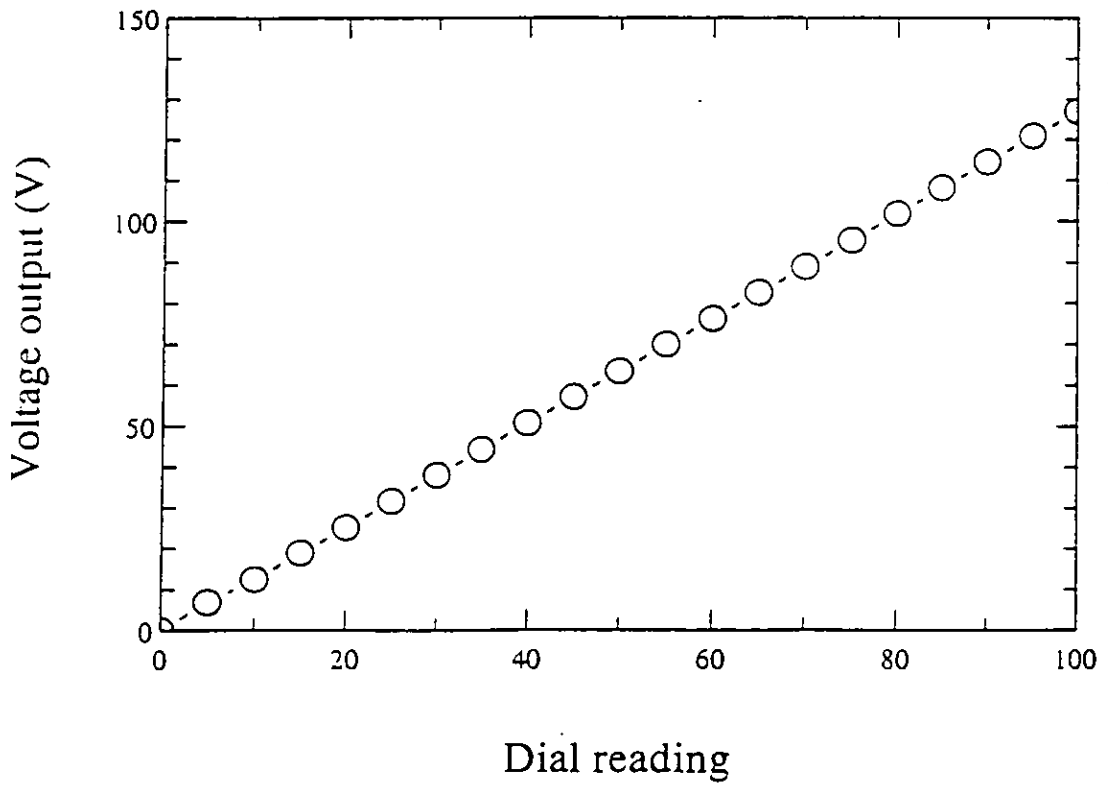


figure (2-17): Calibration of voltage pulse magnitude.

2.8 Calibration of the pulsed field coils

In the experimental study of the properties of isolated particles it was initially thought acceptable to only have a numerical calculation of the field generated from the pulsed field coils. This field calculation would have been adequate if the same pulsed field coil was used throughout all the measurements. During experiments, however, the field coils were found to be susceptible to damage, in particular the coil fusing and the coil former cracking. This led to the problem of obtaining comparable and repeatable results for different particle systems measured with the different field coils. As single particle measurement had only rarely been produced for some systems, that now can not be calibrated the accuracy of the numerical calculation of the field generated from the pulsed field coil had to be addressed.

To test the repeatability of the calculated fields generated from different coils, switching field distributions (SFDs) on a Chromium dioxide particle sample measured with three different field coils were compared. The graph given in figure (2-18) shows SFD histograms of the Chromium dioxide particles measured with pulsed field coils OC6, OC9 and OC11.

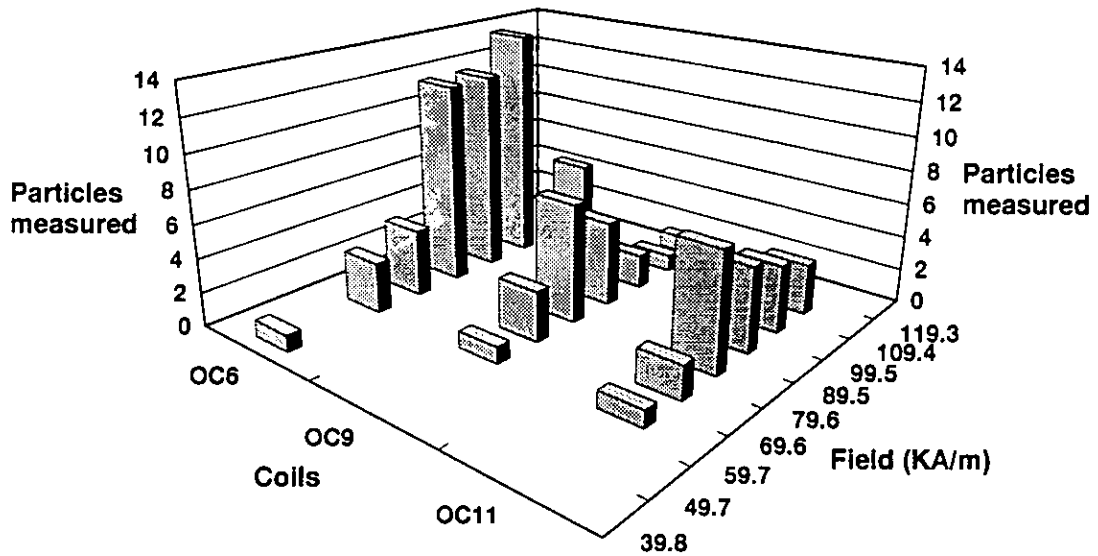


figure (2-18): Histograms of the switching field distributions of CrO_2 particles.

For a numerical comparison of the SFDs measured with the three different field coils, the histograms were curve fitted using a normal distribution to determine their

mean and standard deviation. The results of the curve fits are presented in table (2-1). The results for the different field coils indicated a discrepancy of less than 6KA/m between their mean SFD's. This gave some confidence in the calculated fields from the coils, but gave no confidence in the absolute field generated from the field coil.

Coil	Mean	Standard Deviation (1sd)	Particles measured
OC6	89 KA/m	13.4 KA/m	50
OC9	82.3 KA/m	10.8 KA/m	20
OC11	87.3 KA/m	14.1 KA/m	22

table (2-1): Results of the curve fitted normal distribution.

The table below indicates which coils were used for single particle measurements, which coils had their results compared for the same particle systems and which had been calibrated, described later in this chapter.

COILS	Calculated field profile	Compared results. switching field distributions of CrO ₂ particles	Experimentally Calibrated	Measured single particle results
OC6	X	X	-	X
OC9	X	X	-	X
OC11	X	X	X	X

table (2-2) : Results and analysis used for each coil.

2.8.1 Experimental calibration technique

To confirm that the field coils were producing the field calculated theoretically from the GWBASIC program, an experimental technique was devised. In principle the technique measured the switching field of a single particle using a known field and the field generated by the field coil. The problem was to generate a known field to measure the switching field of a particle.

The solution proposed to calibrate the pulsed field coil was to vary the orientation field aligning the particles within the pulsed field system. The technique measured the switching field of a particle at two known orientation fields. Equating the difference between the two measured switching fields for the particle and the known difference between the orientation fields an absolute measure of the field generated from the pulsed coil system can be obtained.

For an accurate calibration of the pulsed field coils by the technique described above, the design of the orientation coils was crucial. The characteristics of these coils determined the final accuracy of the pulsed field coil calibration. The calibration technique required an orientation field as large as possible to reduce the inaccuracies within the calibration. The field generated from the orientation coils must also be uniform on and off axis to allow it to be measured and calibrated successfully with a Hall probe.

2.8.2 Design, construction and characterisation of the orientation coils

It was initially necessary to determine the position and the size of the orientation coils that could be incorporated between the condenser and the objective of the microscope. To increase the available space for the orientation coils the pulsed field coil platform on the metal platform of the microscope was removed and lowered. This had the effect of increasing the available space for the orientation coils without altering the optics of the microscope.

As a consequence of this decision to remove the pulsed field coil platform it was necessary to make a new platform for the pulsed field coil, so that the coil could lie in the centre of the metal platform and between the final position of the orientation coils. The new platform was constructed from a printed circuit board (PCB) which had tracks connecting the coils' wire to the pulsed field generator cables. The PCB was held to the metal platform with wooden blocks, which were bolted to the metal platform and to PCB itself. The position of the orientation coils and their maximum size was determined

to be 39 mm apart with an inner coil diameter of 10mm, an outer coil diameter of 36mm and a coil length of 20mm.

To have an understanding of how the field profile of the orientation coils varied along its axis and to have a measure of the field produced by the orientation coils before construction a numerical program was written. The GWBASIC program used the Biot-Savart law to calculate the on axis field profile for the orientation coils. In figure (2-19) there is a representation of a current loop within the orientation coil.

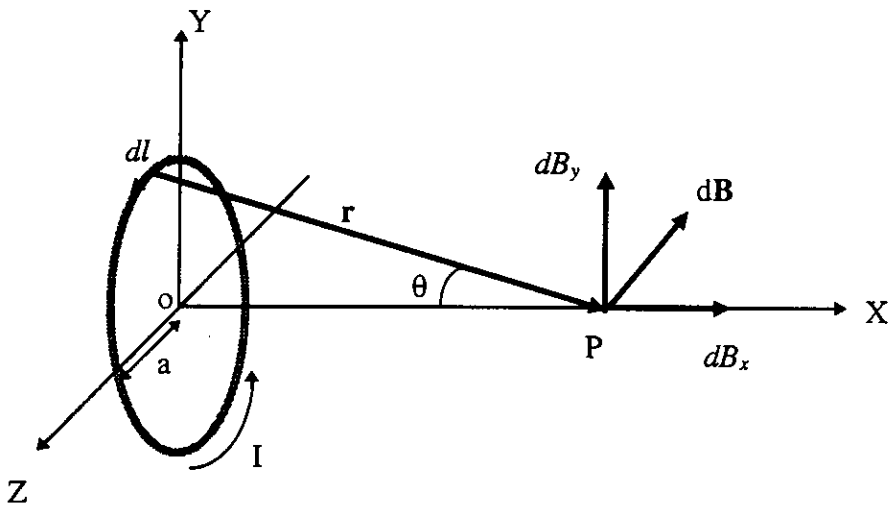


figure (2-19): On axis field calculation of a current loop

Here o represents the centre of the orientation coil, a is the radius of the current loop, I is the current passing through the loop, P is the position where the field $d\mathbf{B}$ from a current element $d\mathbf{l}$ is calculated. The on axis field calculation for the current loop requires the calculation of the B_x field component from Biot Savart law given in equation (2-3).

$$B_x = \frac{\mu_0 I}{4\pi} \int \frac{d\mathbf{l} \times \hat{r}}{r^2} \sin \theta \tag{2-6}$$

Expressing $\sin \theta$ as $a / \sqrt{a^2 + x^2}$ and r as $\sqrt{a^2 + x^2}$ into equation (2-6).

$$B_x = \frac{\mu_o I}{4\pi} \frac{a}{(a^2 + x^2)^{3/2}} \int_0^{2\pi} dl \quad (2-7)$$

The on axis field component from a current loop is determined by integrating equation (2-7).

$$B_x = \frac{\mu_o I}{2} \frac{a^2}{(a^2 + x^2)^{3/2}} \quad (2-8)$$

To calculate the field profile of a coil it is necessary to know the number of turns within the coil, their positions and the current passing through the coil. The GWBASIC program determined the orientation field from the diameter of the wire used, the diameter of the copper within the wire, the maximum current rating of the wire, the separation of the coils, the outer and inner diameter of the coils and their axial lengths. The program calculates for a 100% packing density, the number of turns within the coil and the electrical resistance of the coils. The electrical resistance is an important parameter that should be determined; there is no point constructing a coil if there was no power supply that can drive it. The power supply available for the orientation coils was a Farnell stabilised power supply type TSV70 Mk2, capable of producing 0-35v at 10A or 0-70 at 5A.

From the orientation coils physical characteristics the on axis field profile was calculated for enamelled copper wire of 0.27mm diameter. The program determined the resistance of 88 Ohms per coil. The electrical characteristics of the coil are compatible with being driven by the Farnell power supply unit. The on axis field profile for the orientation coils was calculated with an applied current of 0.33 amps, the rated current for the enamelled wire used in the coils windings. The on axis field calculated field profile for the orientation coils is presented in figure (2-20). The results indicate that the orientation coil had a field of $8.46 \pm 0.08 \text{mT}$ within 2mm of its axial centre.

In the previous calculation for the “on axis” field profile using the Biot-Savart law, the symmetry of the problem aided its solution. This is not the case for the “off axis” field profile, indicated in figure (2-21).

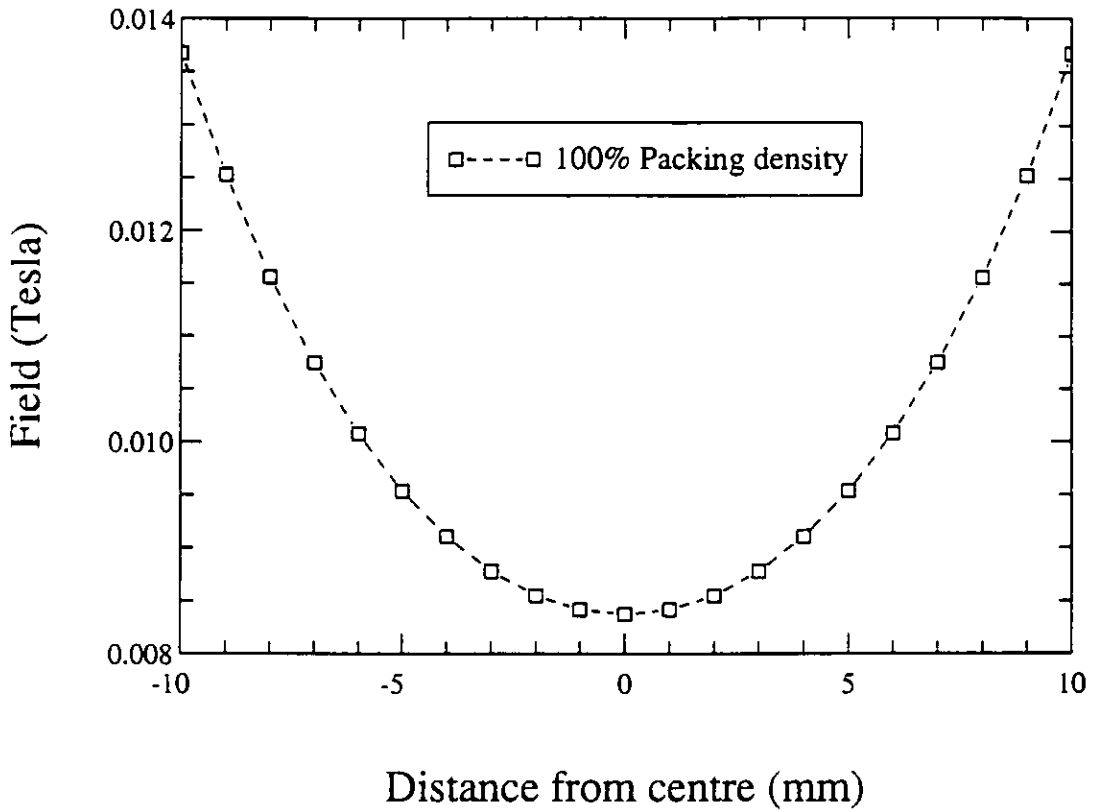


figure (2-20): Orientation coil on axis field profile.

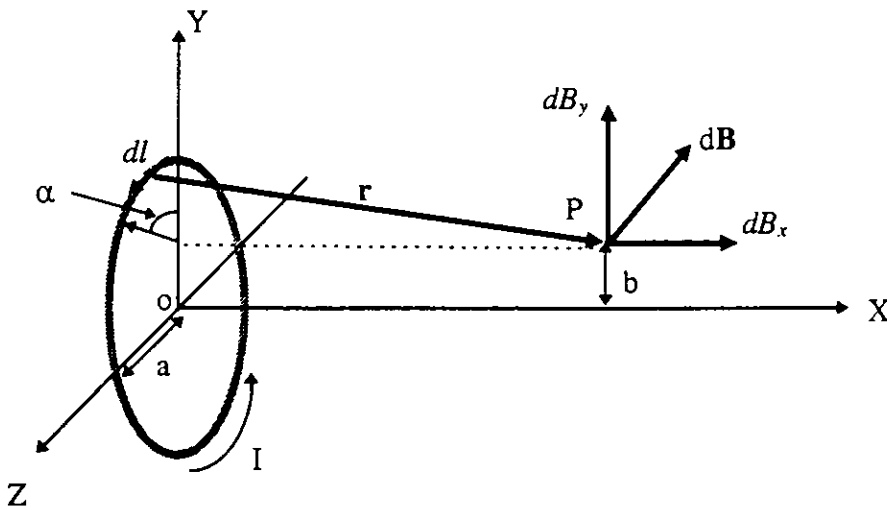


figure (2-21): Off axis field calculation for a current loop.

Here α represents the angle between the current element and the y axis and b represents the distance off axis from point P where the field component dB_x requires to be calculated. The off axis field calculation for the orientation coils required the field component B_x to be calculated from equation (2-6).

Again the equation was solved by the expressing $\sin\theta$ and r in terms of the parameters a b and α , where $r = ((a - b \cos\alpha)^2 + x^2)^{1/2}$.

$$B_x = \frac{\mu_0 I}{4\pi} \oint \frac{(a - b \cos\alpha)}{((a - b \cos\alpha)^2 + x^2)^{3/2}} dl \quad (2-9)$$

We can replace the element dl within equation (2-9) by $a d\alpha$, thus making the integral tractable.

$$B_x = \frac{\mu_0 I}{4\pi} \oint \frac{a(a - b \cos\alpha)}{((a - b \cos\alpha)^2 + x^2)^{3/2}} d\alpha \quad (2-10)$$

The calculation of the off axis field profile was essentially the same as for the on axis field profile. The exception was the off axis field program determined the field from the current loop by the numerical integration of the current elements within the loop using the trapezoidal rule. The on axis field calculated field profile for the orientation coils is presented in figure (2-22). The calculated off axis field profile for the orientation coils indicated a maximum field of $8.39 \pm 0.02\text{mT}$ (1s.d) within 1.5mm of its axial centre.

The results from the numerical investigation of the orientation coils suggested that the calibration of the pulsed field coils was possible using this coil design. The orientation coils were constructed to the physical parameters determined by the parameters of the microscope and the characteristics of these coils investigated.

The Hall probe used for the calibration of the orientation coils was calibrated in its forward and reverse direction by three calibration magnets 148.5mT, 495mT and 1.006T. The results from the calibration of the Hall probe are presented in figure (2-23).

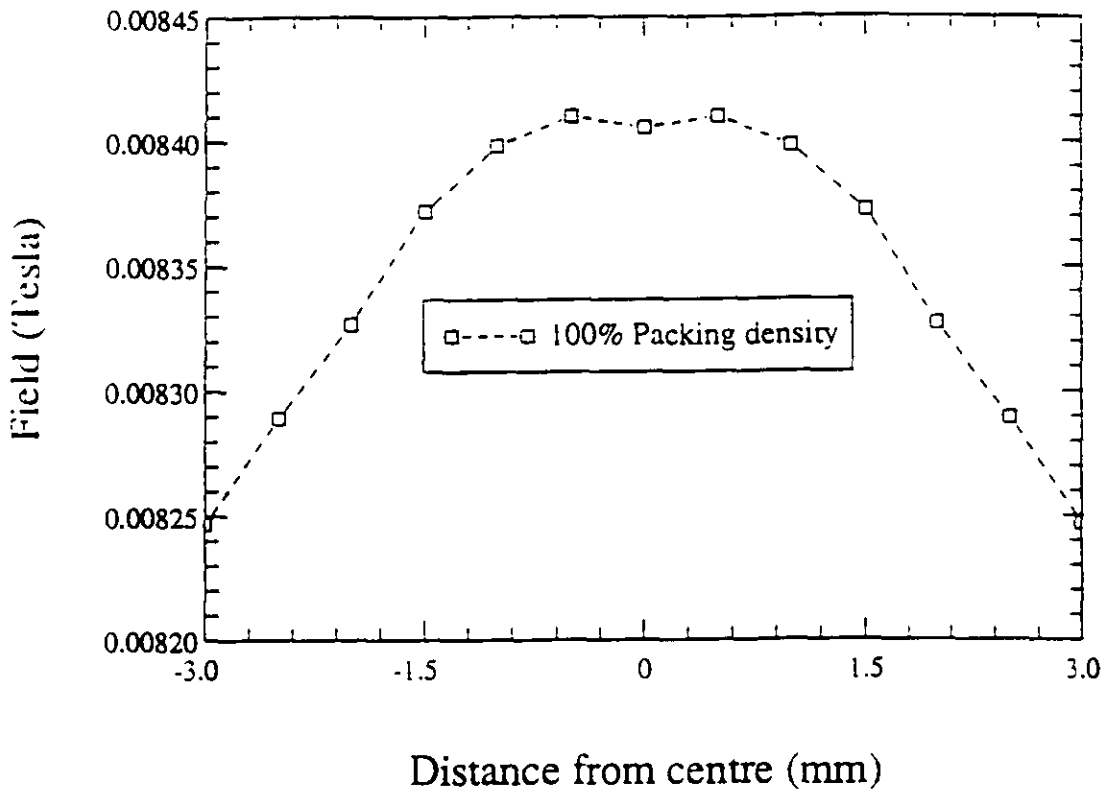


figure (2-22): Off axis field calculation of a current loop.

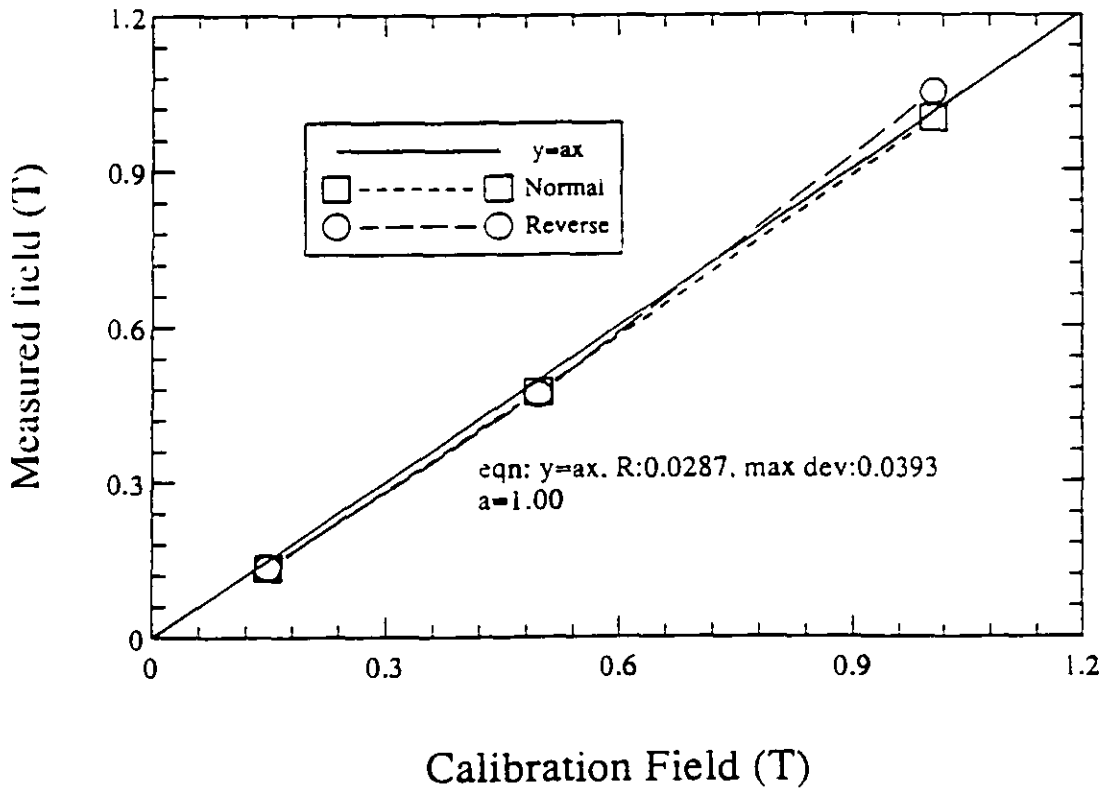


figure (2-23): Hall probe calibration

The field generated from the orientation coils was calibrated for the current passing through the coils by the calibrated Hall probe. The current calibration of the orientation coils is presented in figure (2-24).

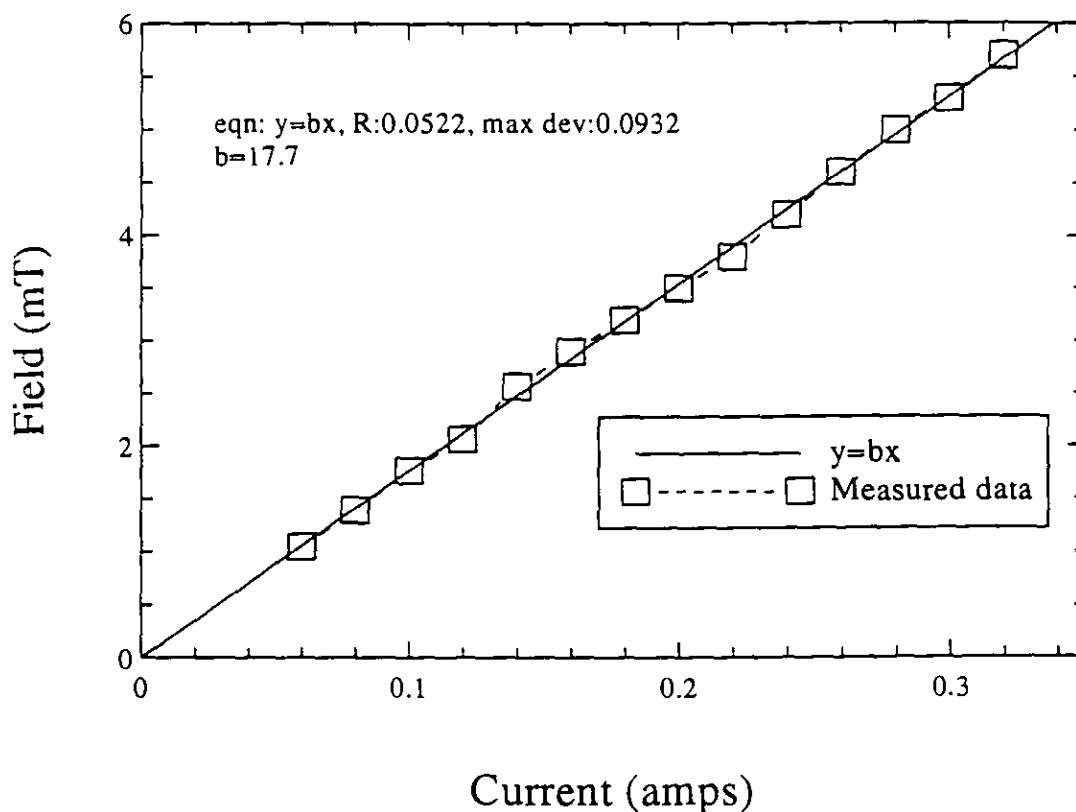


figure (2-24): Calibration of the orientation coil.

The measured field generated from the orientation coils represents 88% of the theoretical field calculated by GWBASIC programs. This reduced field is the product of a reduced packing density within the orientation coils. The reduction of the orientation coils' field has no effect on its field uniformity. The only effect is a reduction in the final accuracy of the pulsed field coils calibration. This reduction in the field generation within the orientation coils can be compensated somewhat by increasing past its maximum recommended limit the current through the coil for the time of the experiment.

2.8.3 Calibration of pulsed field coil OC11

The calibration of the pulsed field coil OC11 was performed using the basic technique described within the sections earlier. The switching field (V_{SF}) of the particle was measured by the voltage applied to the pulsed field coil from the pulsed voltage generator. The orientation field (I_O) was measured by the applied current through the orientation coil generated from the Farnell power supply unit. The pulsed field coils absolute field was determined by measuring the switching field of a particle at two different orientation fields. The difference between the two switching fields $\Delta V_{SF} = |V_{SF1} - V_{SF2}|$ was equated to the difference between the two orientation fields $\Delta I_O = |I_{O1} - I_{O2}|$. Since the orientation field I_O had been calibrated, indicated in figure (2-24) then an absolute measure of the ΔV_{SF} can be obtained and an absolute measure of the particles switching field can be deduced.

The calibration was performed on twenty Chromium dioxide particles taken from the sample used previously for the comparison of SFD's measured with different pulsed field coils. The difference in the two switching fields ΔV_{SF} (volts) for each particle was plotted against the difference in the two orientation fields $b\Delta I_O$ (mT), given in figure (2-24). The errors associated with the calibration results were calculated from the quantifiable errors, the error in the measured current ($\delta I_O \pm 0.01$ Amp) and the error within the applied pulsed voltage ($\delta V_{SF} \pm 0.1$ volt). The error within ΔV_{SF} and ΔI_O were calculated [6] by

$$\delta \Delta I_O = \sqrt{2} \delta I_O \quad (2-11)$$

and

$$\delta \Delta V_{SF} = \sqrt{2} \delta V_{SF} \quad (2-12)$$

The error calculations did not take into consideration the errors arising from the pulsed field profile, the motion of a particle during the calibration or the possibility that the object under observation was a multiple particle.

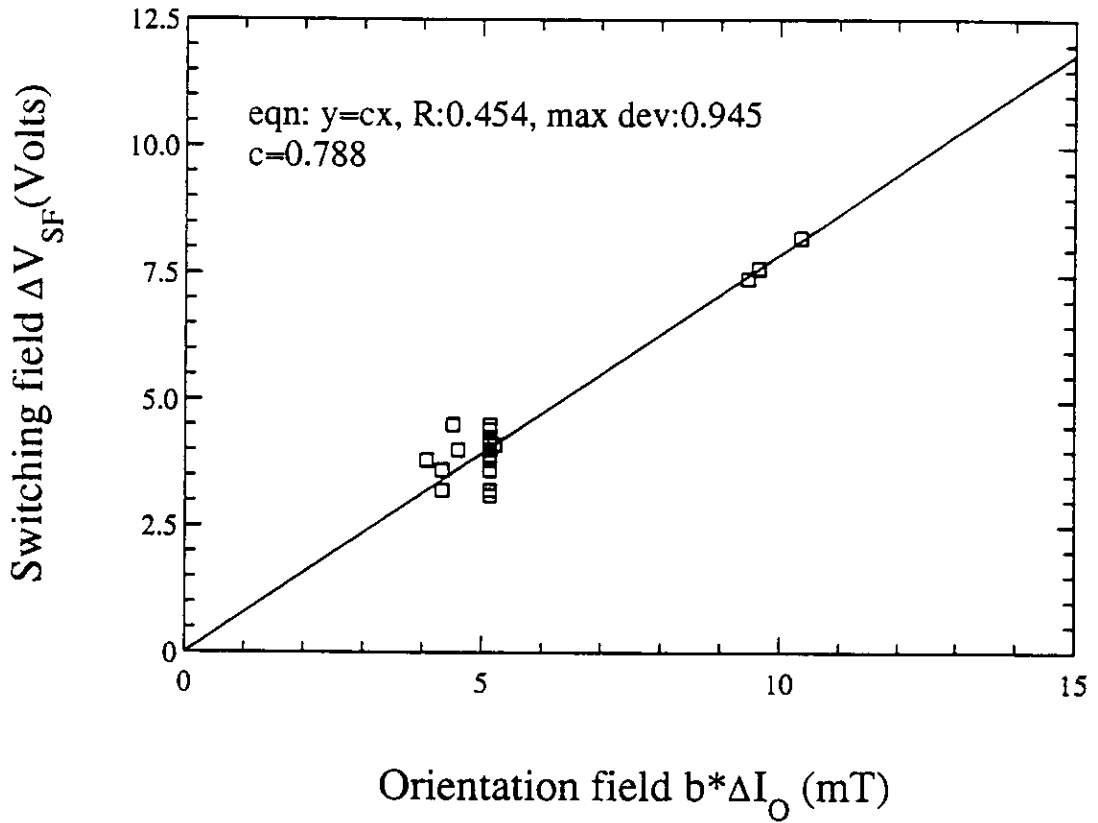


figure (2-25): Calibration of coil OC11.

Equating the gradient of the calibration curve of coil OC11 to the maximum pulsed voltage (127 volts) then the maximum field generated from coil OC11 was 0.1612T. This measured field was comparable with the theoretical calculation of its field $0.1656 \pm 0.007T$ (1.Sd). These results confirmed the theoretical calculations of the pulsed field coils field profile.

Chapter Three

Measurement of the intrinsic properties of the individual particles.

3.1 Introduction

To further the development of particulate recording media it is necessary to fully understand the properties of the media and their origins. The properties of particulate recording media originate from a number of sources. These include the magnetic and physical properties of the particles that constitute the media, the interaction effects between these particles and the physical distribution of the particles within the media.

In this chapter, experiments investigating the magnetic properties of particles using apparatus developed by Knowles [1] are reported. This apparatus allows the measurement of the properties of isolated magnetic particles. The techniques used were the measurement of particle switching field as a function of the applied field angle, the measurement of the switching field for an ensemble of isolated particles and the measurement of the remanent magnetisation of a particle. The physical properties of the particles were also of interest, particularly their aspect ratio and their length. These parameters measured by a Scanning Electron Microscope (SEM) were used in chapter six for the numerical modelling of the properties of individual magnetic particles.

In measuring the magnetic properties of single particles and in conjunction with the bulk measurements of the medium, particularly its particle easy axis distribution it is possible to simulate a theoretical medium without interactions. A comparison between the measured characteristics of a medium with its theoretical representation allows a direct measure of its interaction effects. As a consequence the results of the single particle measurements in this chapter were curve fitted for a numerical representation of their properties.

3.2 Samples

The magnetic particles investigated within this work were taken from commercial and hand spread media samples. The samples investigated were a series of three $\gamma\text{-Fe}_2\text{O}_3$, three CrO_2 and a metal particle sample. The microscope used within this investigation had a resolution limit of $0.2\mu\text{m}$. As there is a general trend towards commercial particles with smaller dimensions, lengths of less than $0.2\mu\text{m}$, there is a lack of recent commercial particles which are suitable for this experimental technique. The sample types investigated are presented in table (3-1).

Sample type	Sample No	Manufacture	Format
$\gamma\text{-Fe}_2\text{O}_3$ particulate media	1	Ampex	Audio
	2	Scotch	Audio
	3	TDK	Audio
CrO_2 particulate media	4	Hand spread	-
	5	Fuji	Audio (Double Coated)
	6	Philips	Audio
Metal particle media	7	Sony	Video

table (3-1): The format and manufacturers of the samples investigated.

3.3 Measurement of the switching field distribution of an ensemble of particles

Magnetic media manufacturers would prefer to use highly regular particles with well-defined magnetic and physical characteristics. These particles would allow the manufacture to produce a medium with a narrow Switching field distribution (SFD) determined by the particles physical size, the thickness of the media and the particles' easy axis distribution within the media. Commercial magnetic particles, however, are not perfectly uniform. They have variations in their magnetic and physical properties. The magnetic variations include bulk saturation magnetisation, crystalline anisotropy and bulk crystalline imperfections. The particle physical variations includes size, shape and the presence of surface irregularities, such as bumps and pits. These variations broaden the particles' switching field distribution (SFD) and hence broaden the SFD of the media. This is detrimental to recording performance as discussed in chapter 1.

The single particle apparatus as discussed in chapter 2 was configured so that the pulsed field coils were in the opposite direction to the aligning magnets ($\theta=0^\circ$), as indicated in figure (3-1).

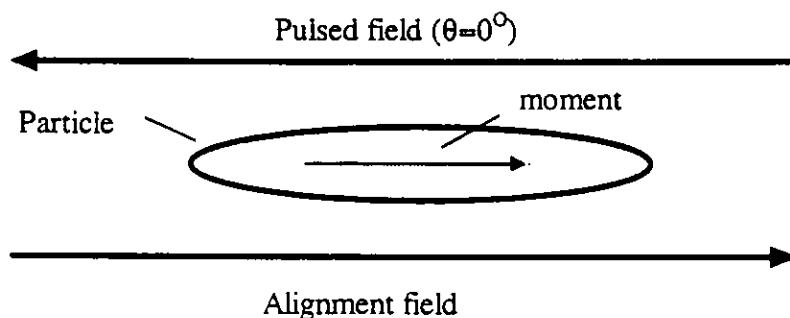


figure (3-1): Configuration of single particle apparatus for the switching field distribution investigation.

The switching fields were measured for an ensemble of 50 isolated particles taken from each sample. These results were plotted as histograms to generate a SFD for non-interacting ensembles of particles. As a sample of 50 particles was small, only a small number of histogram bins were chosen for each sample. It was found that ~10 bins gave a reasonable histogram for the measured samples. It was assumed a large data

sample could be represented by a Gaussian distribution. A numerical measure of the SFD data was obtained by curve fitting the histograms with a Gaussian distribution, given as

$$SFD(H) = \frac{d}{2\pi\sigma} \exp\left\{-\frac{1}{2}(H - H_{MEAN})^2 / \sigma^2\right\}. \quad (3-1)$$

Here $SFD(H)$ is the prominence of the distribution as a function of the applied field, σ is the standard deviation of the SFD, H_{MEAN} is the mean switching field of the SFD, H is the applied field and d represents a curve fitting parameter.

A normalised standard deviation $\sigma_M = \sigma/H_{MEAN}$ of the particles measured was evaluated. This allowed a direct comparison between experimental results and numerical model results to be performed later in chapter 6. The standard deviation can be used as a figure of merit for the particles quality. This figure of merit is only valid when comparing particle systems with similar mean switching fields. The lower the value of σ , the more regular the particles and conversely the higher its value the more irregular the particles. The measured switching field histograms of 50 particles with their Gaussian distribution curve fits are presented in figure (3-2) through to figure (3-8). The curve fit parameters and the normalised standard deviation are presented in table (3-2).

A visual interpretation of the Gaussian distribution curve fits indicated that they gave a reasonable representation of the measured SFD histograms. The standard deviation parameter of samples 2-7 were similar, below 14.6 kA/m, indicating these particles had a similar spread in their switching fields. However, Sample 1 had a much larger σ (17.0 kA/m) than the other samples investigated. This might be attributed to a greater variation of particle properties within sample 1, particularly a greater degree of particle imperfections. These results are unsurprising as sample 1 was produced in the 1960's, while the other samples were produced with the improved production techniques of the 1980's. It was also noted that the mean switching fields of samples 1-4 and 6-7 were similar (55.4-85.6kA/m), while sample 5 the audio double coated CrO₂ tape had a mean switching field of 108.0kA/m.

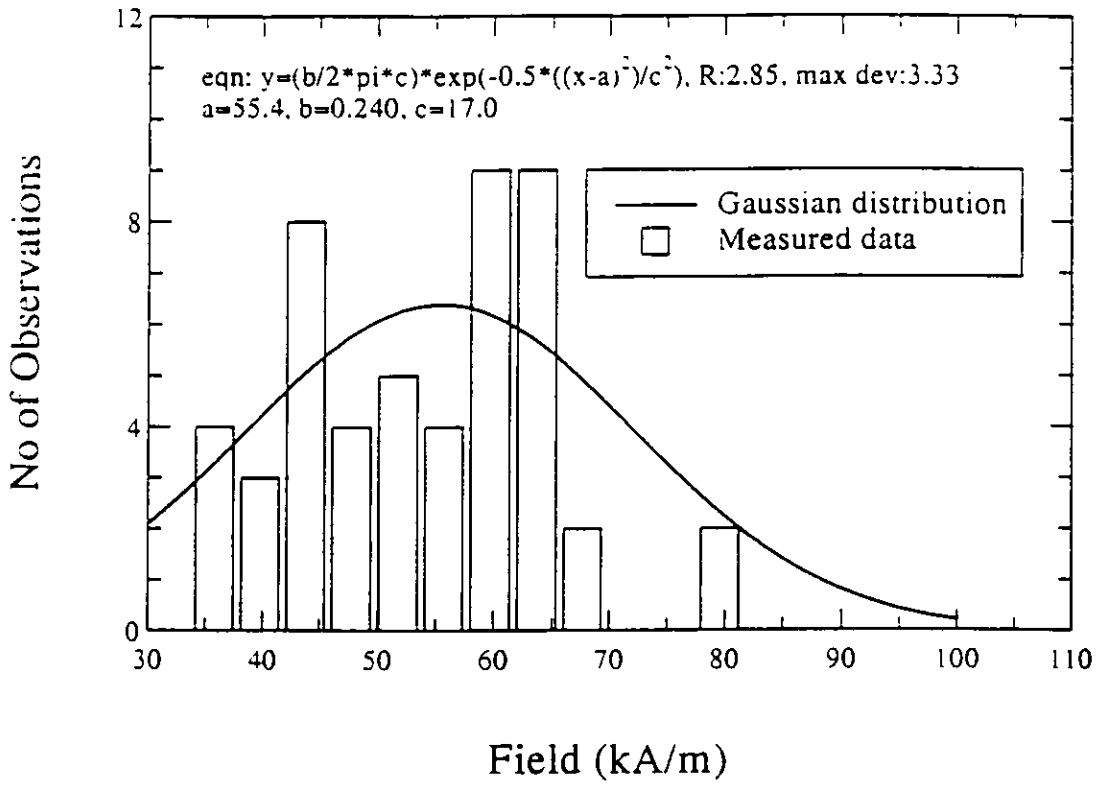


figure (3-2): Switching field distribution of sample 1.

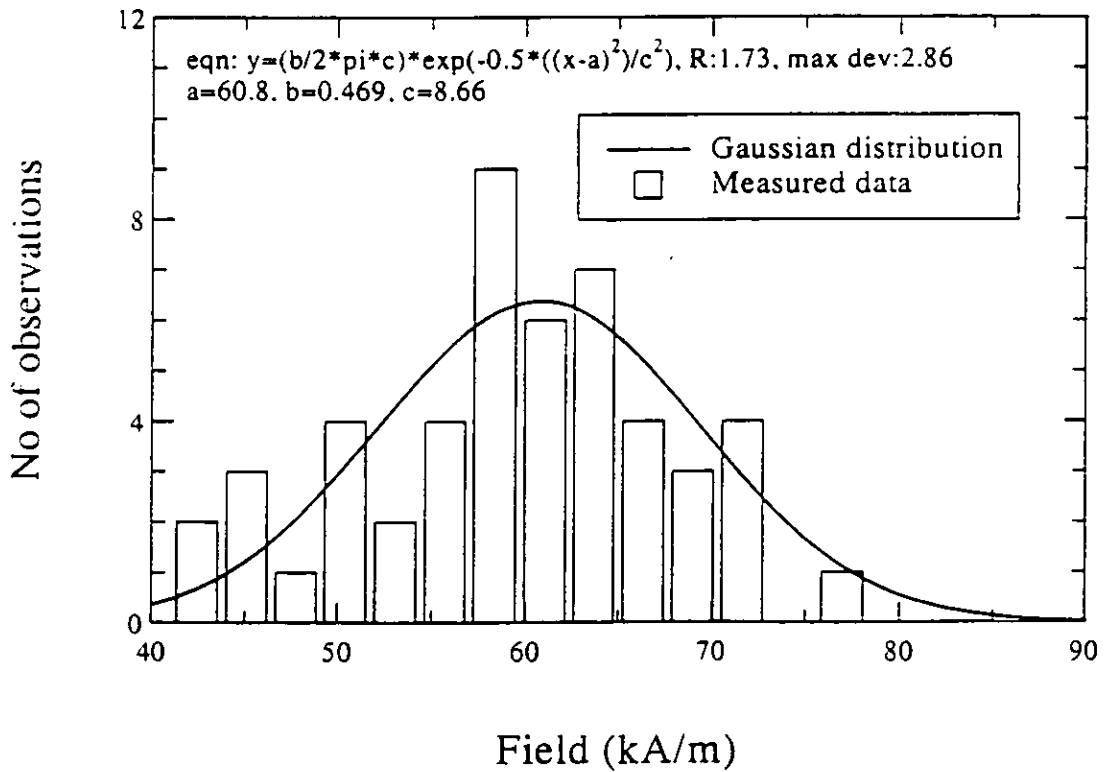


figure (3-3): Switching field distribution of sample 2.

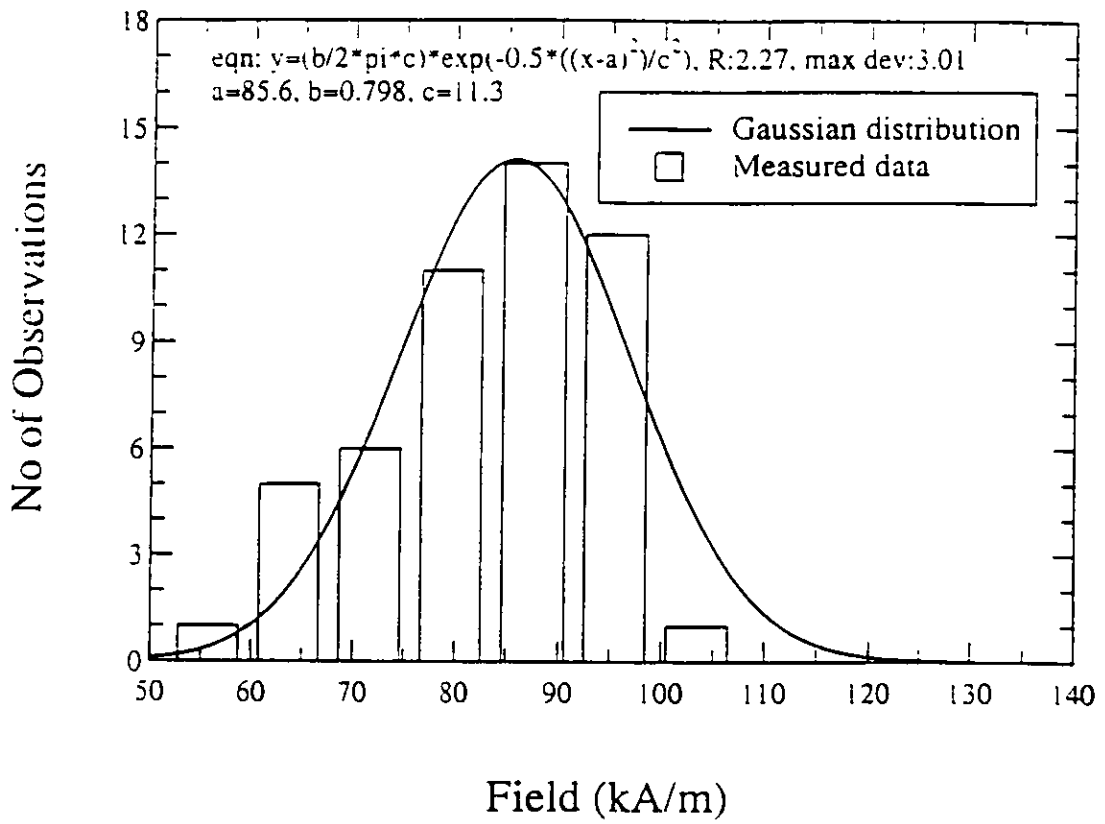


figure (3-4): Switching field distribution of sample 3

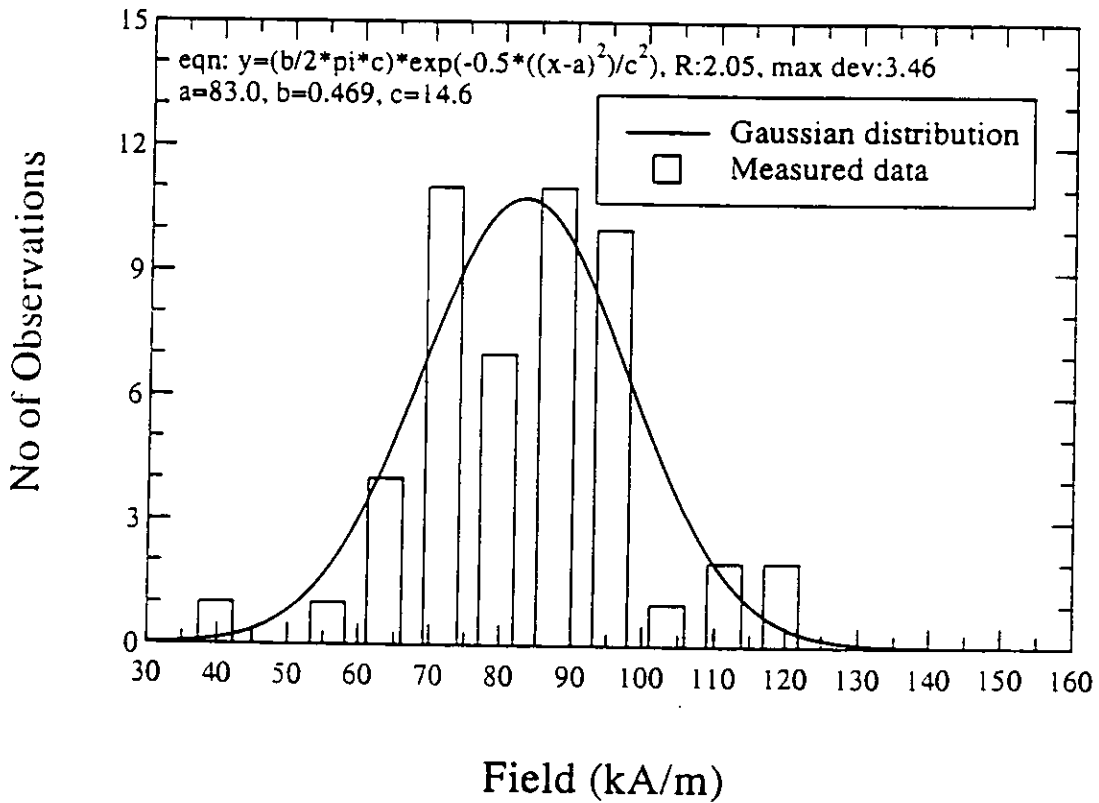


figure (3-5): Switching field distribution of sample 4

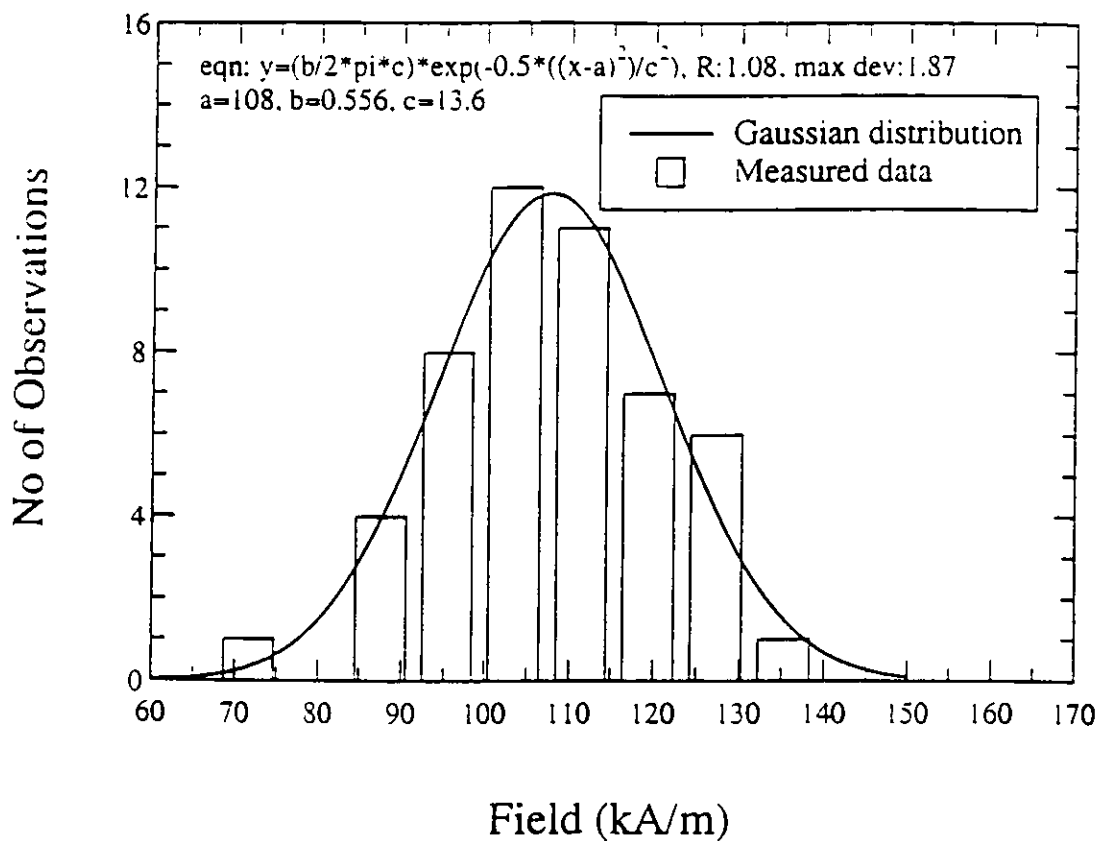


figure (3-6): Switching field distribution of sample 5

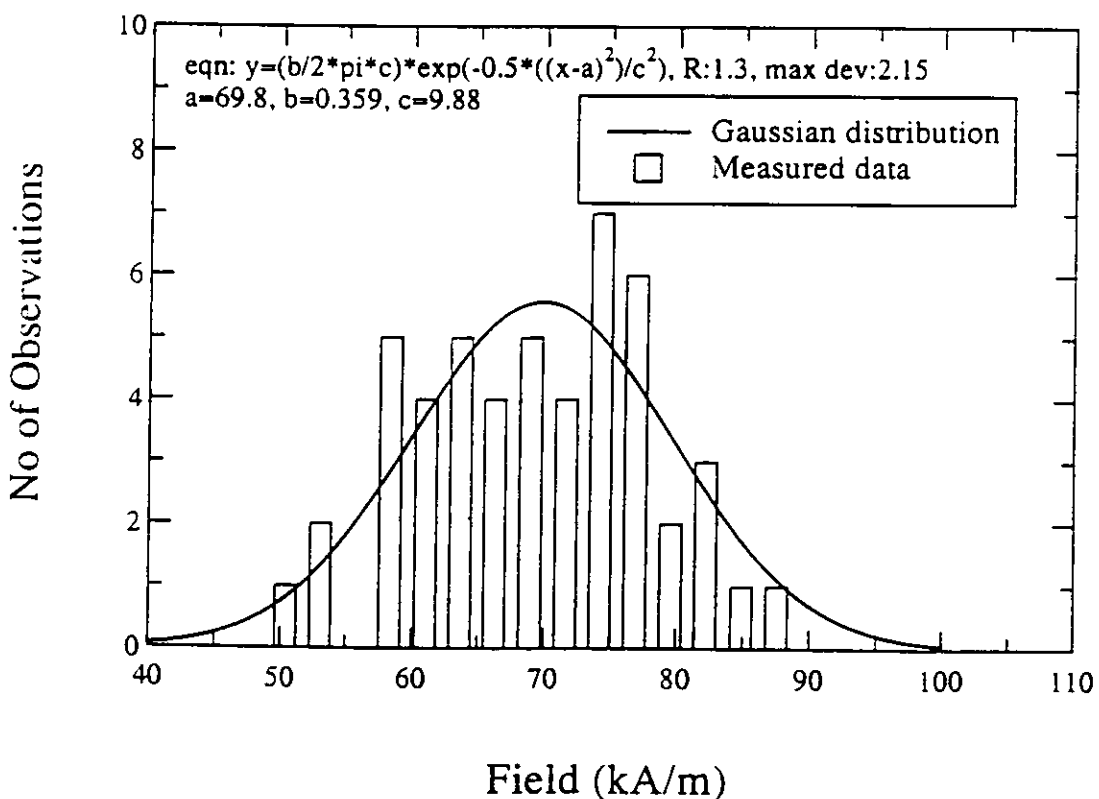


figure (3-7): Switching field distribution of sample 6

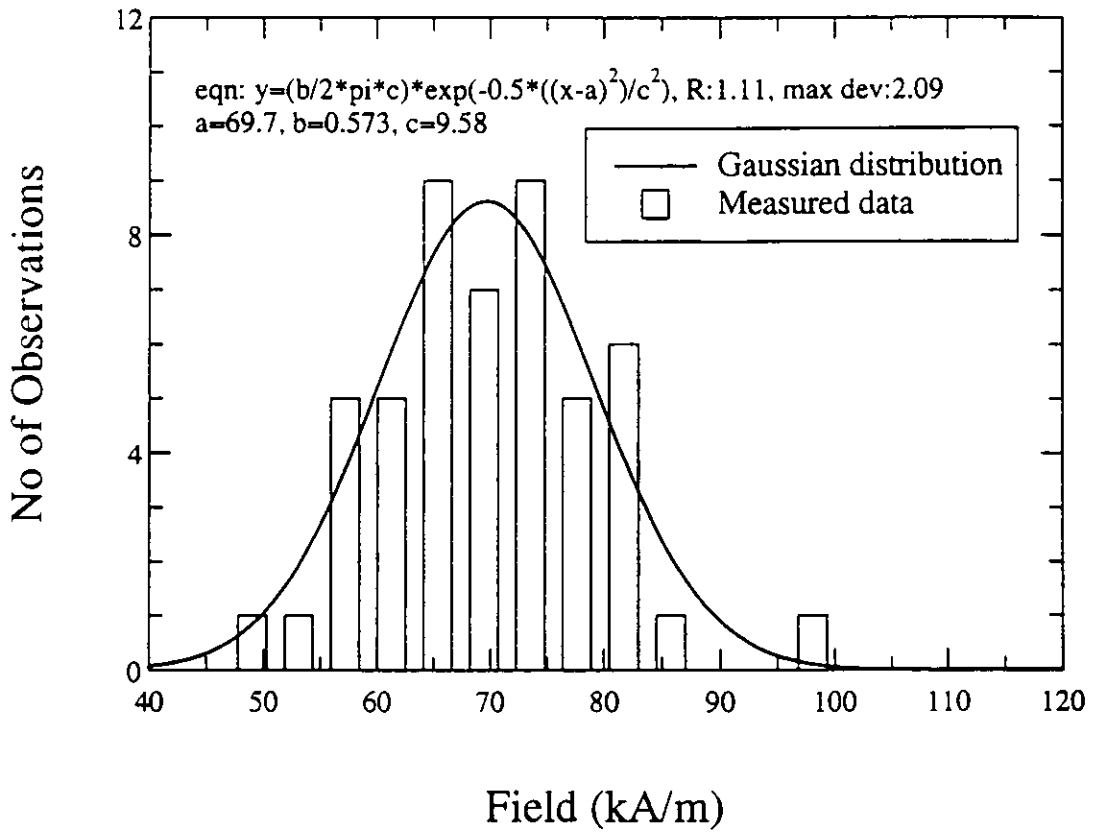


figure (3-8): Switching field distribution of sample 7

Sample type	Sample No	H_{MEAN} (kA/m)	σ (kA/m)	H_{MEAN}/σ
γ -Fe ₂ O ₃ particulate media	1	55.4	17.0	0.307
	2	60.8	8.7	0.143
	3	85.6	11.3	0.132
CrO ₂ particulate media	4	83.0	14.6	0.176
	5	108.0	13.6	0.126
	6	69.8	9.9	0.142
Metal particle media	7	69.7	9.6	0.138

table (3-2): Switching field distribution curve fitted parameters.

3.4 The switching field measurement of a particle as a function of the applied field angle

The switching field characteristics of a particle are dominated by its reversal mechanism, which is directly dependent on the direction of the applied field with respect to its easy axis direction. The switching field measurement of a particle as a function of the applied field angle allowed a direct comparison with theoretical data available within the literature on the angular dependence of reversal mechanisms [2-5].

The switching field of a particle was measured with the pulsed field direction directly opposed to the alignment field direction, an angular separation of 180° . The aligning magnets were rotated by 10° , rotating the easy axis of the particle and its switching field was measured again, indicated in figure (3-9).

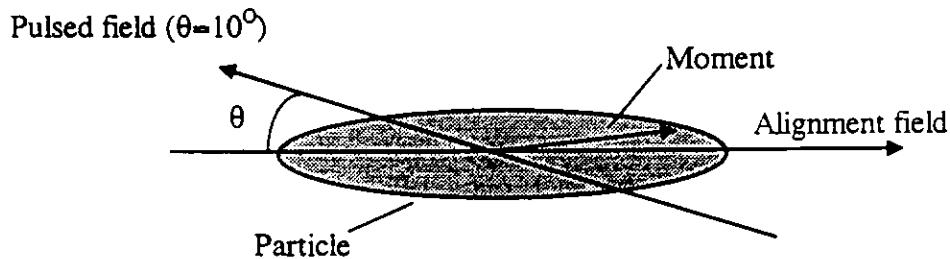


figure (3-9): Configuration of the single particle apparatus for the investigation of a particle's switching field as a function of the applied field angle.

This procedure of incremental increases in the pulsed field angle and the subsequent switching field measurement of the particle continued until the particle had drifted out of the field of view, the pulsed field angle had reached 90° or the maximum pulsed field available was not great enough to switch the moment of the particle. The experimental results for samples 1 to 7 are presented in figure (3-10) through to figure (3-16).

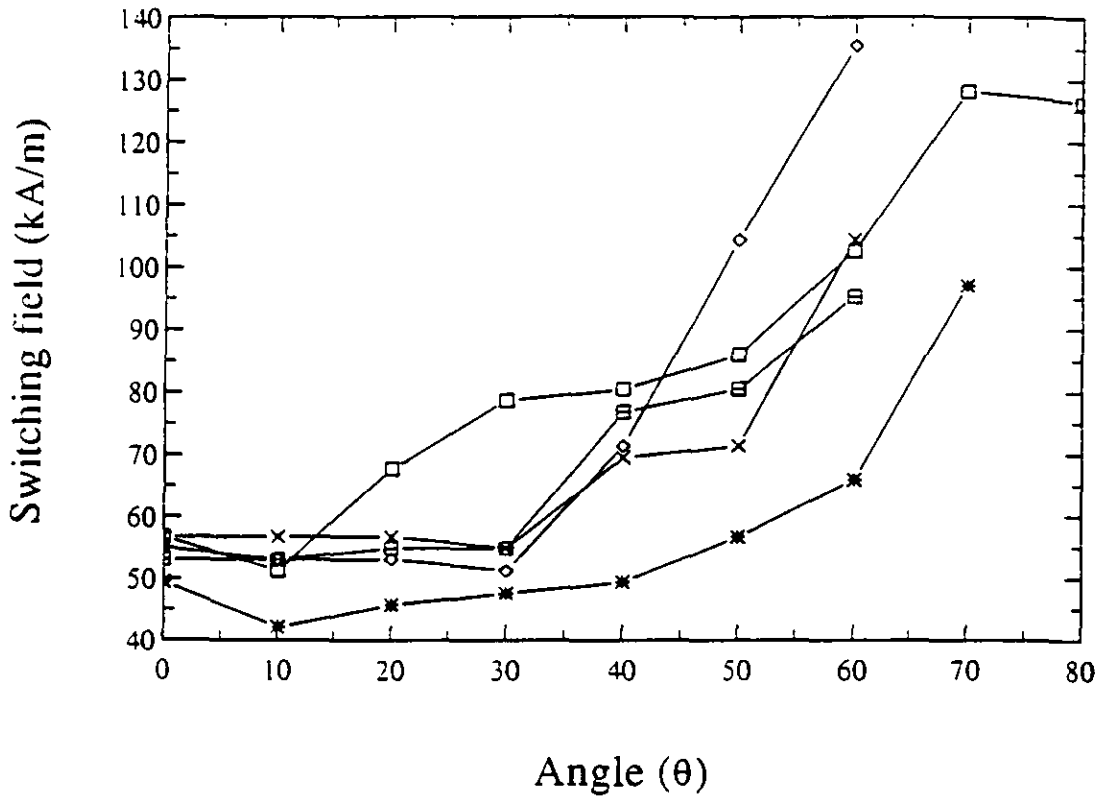


figure (3-10): Switching field as a function of angle for 5 particles of sample 1.

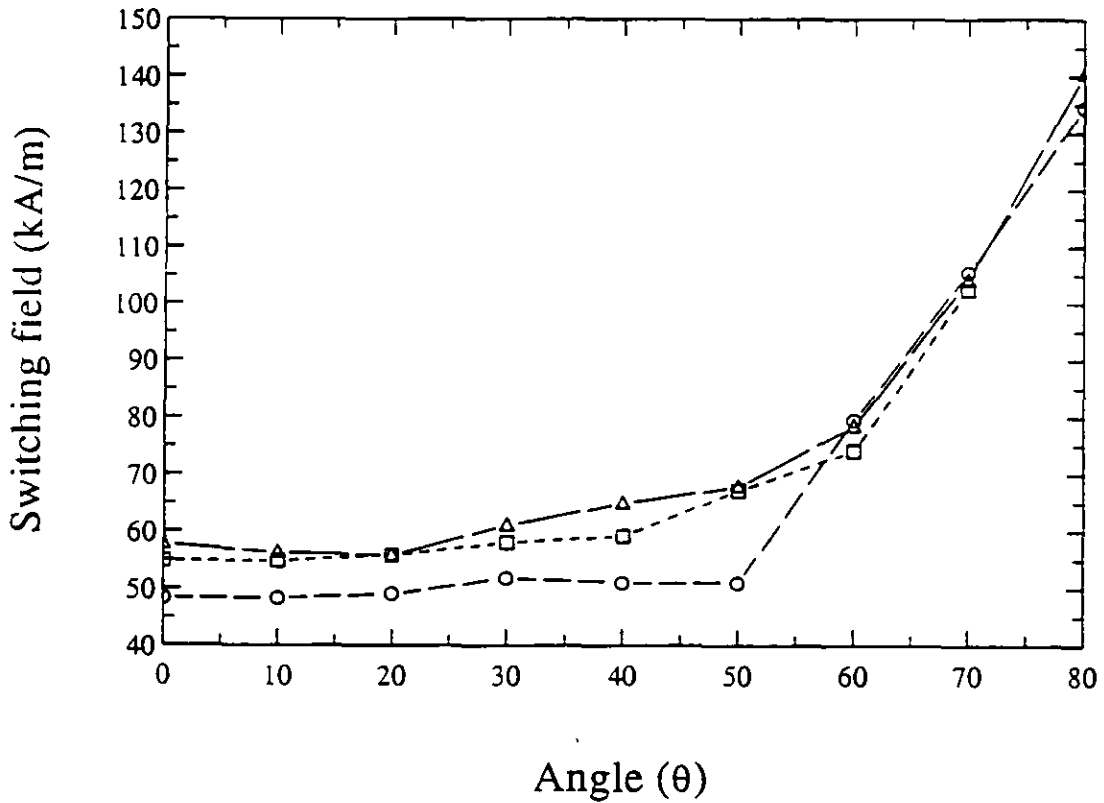


figure (3-11): Switching field as a function of angle for 3 particles of sample 2.

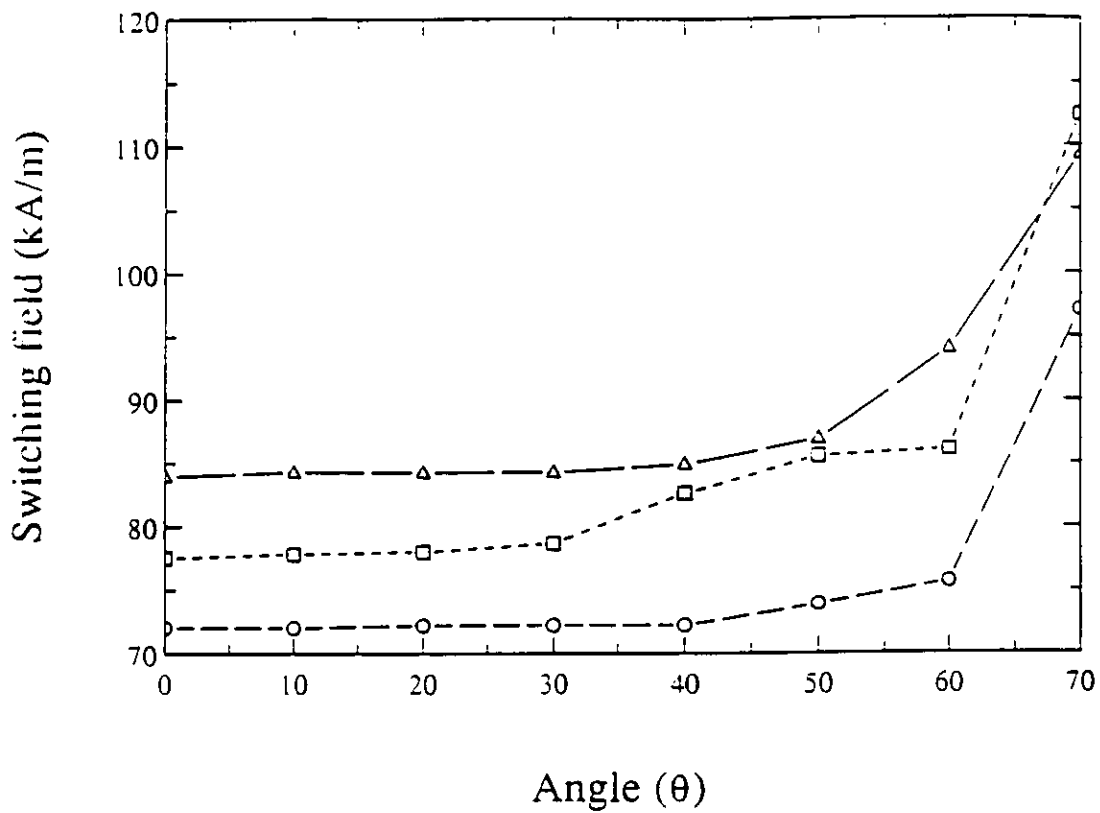


figure (3-12): Switching field as a function of angle for 3 particles of sample 3.

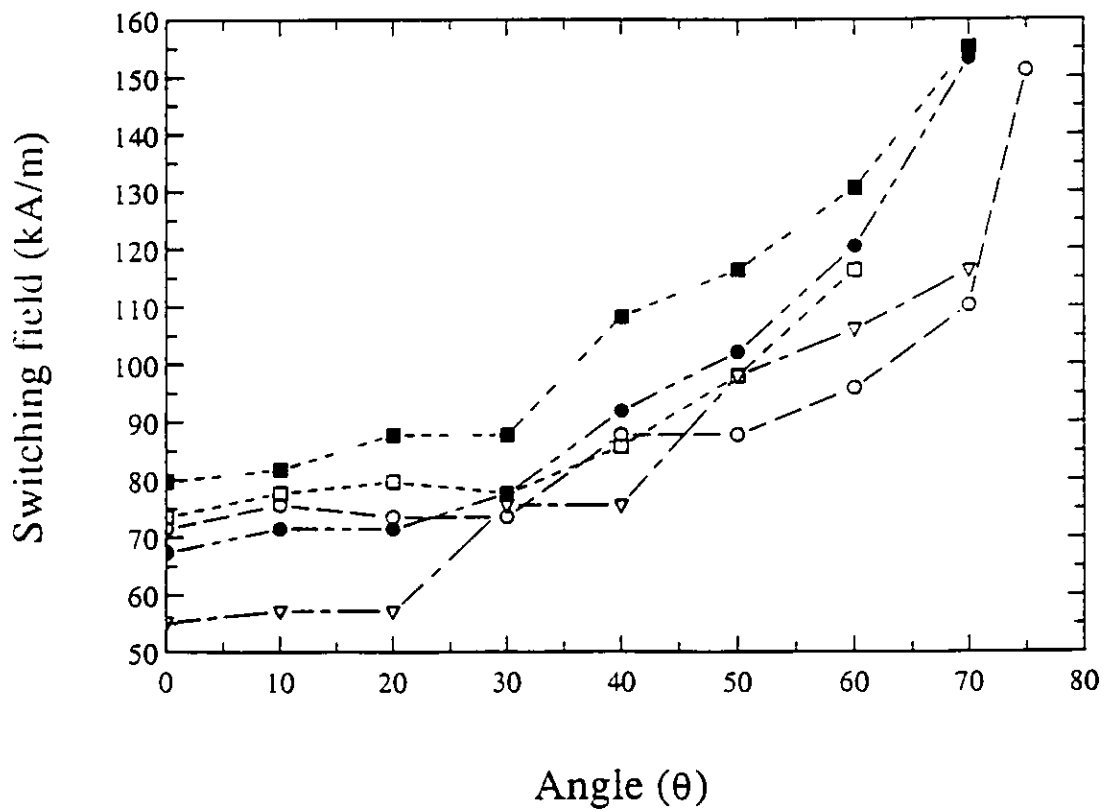


figure (3-13): Switching field as a function of angle for 5 particles of sample 4.

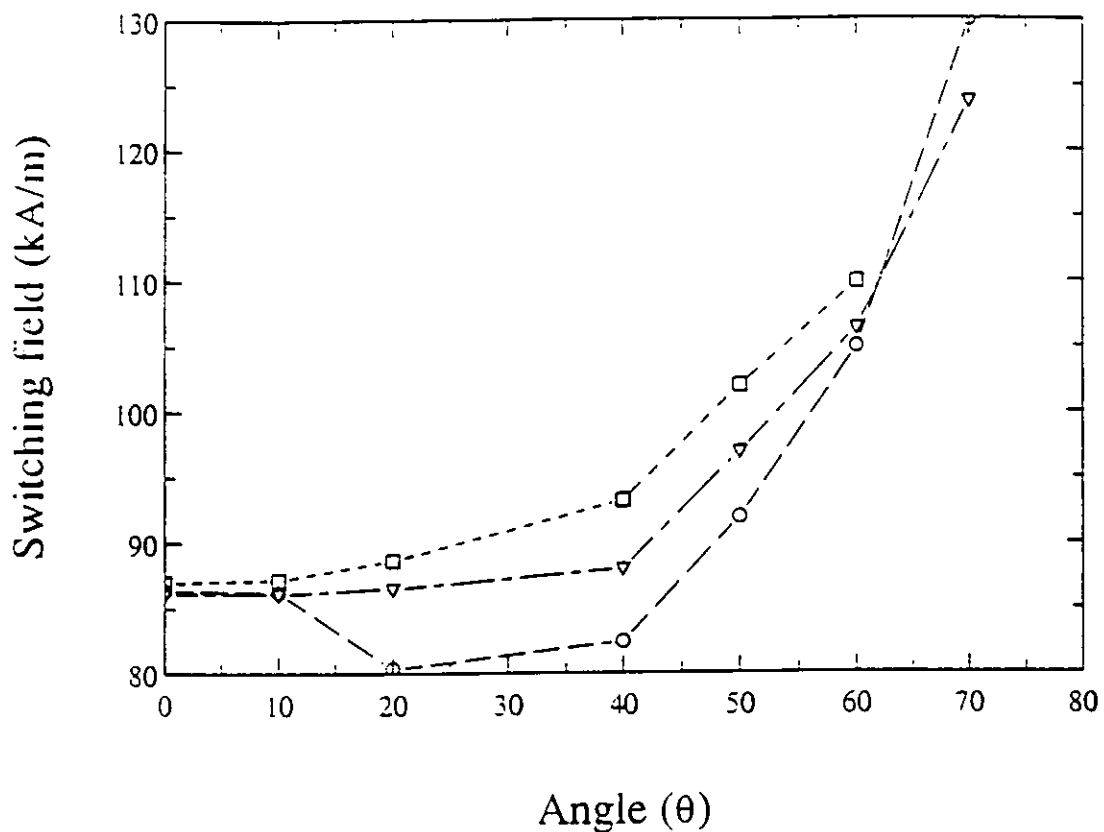


figure (3-14): Switching field as a function of angle for 3 particles of sample 5.

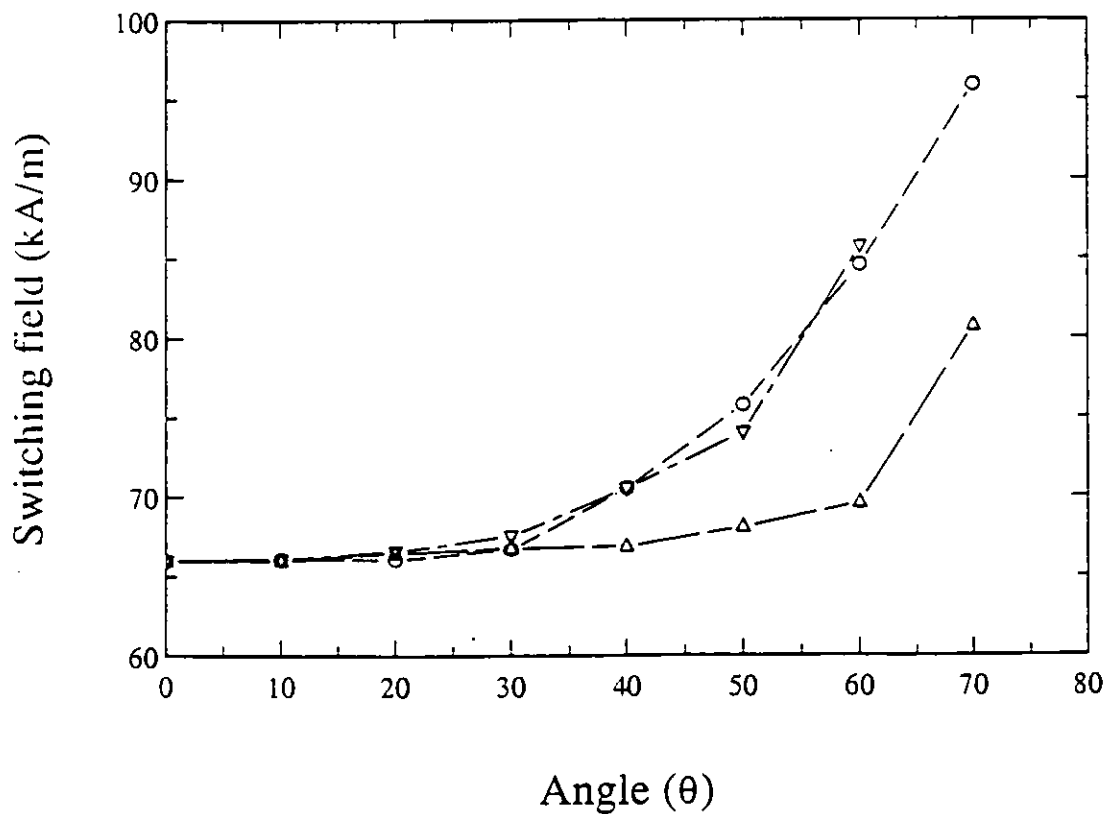


figure (3-15): Switching field as a function of angle for 3 particles of sample 6.

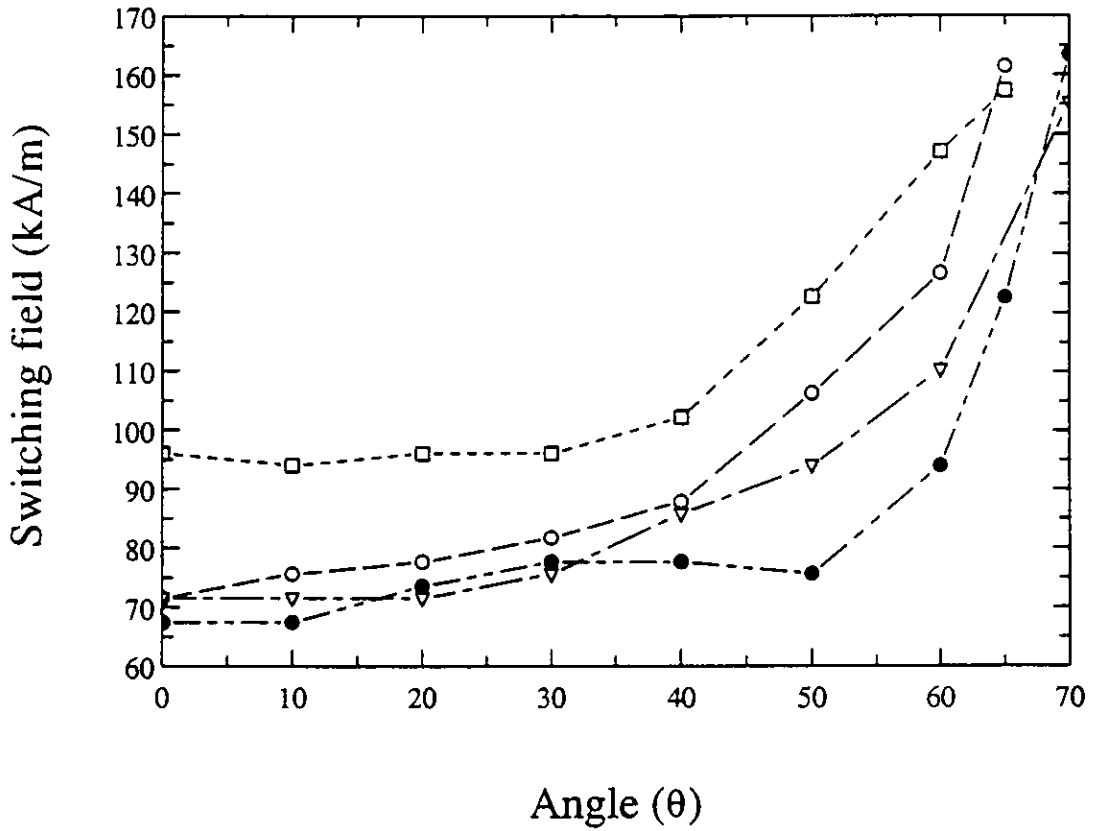


figure (3-16): Switching field as a function of angle for 4 particles of sample 7.

The measured switching field as a function of the applied field angle for the particles investigated in this study can be represented numerically by

$$H_{TOTAL} = H_{(\theta=0)} + e10^{f\theta}, \quad (3-2)$$

where e and f are curve fitting parameters, H_{TOTAL} and $H_{(\theta=0)}$ are the switching fields at angles θ and $\theta=0$ respectively. An example of the curve fit for a typical particle within sample 2 can be found in figure (3-17).

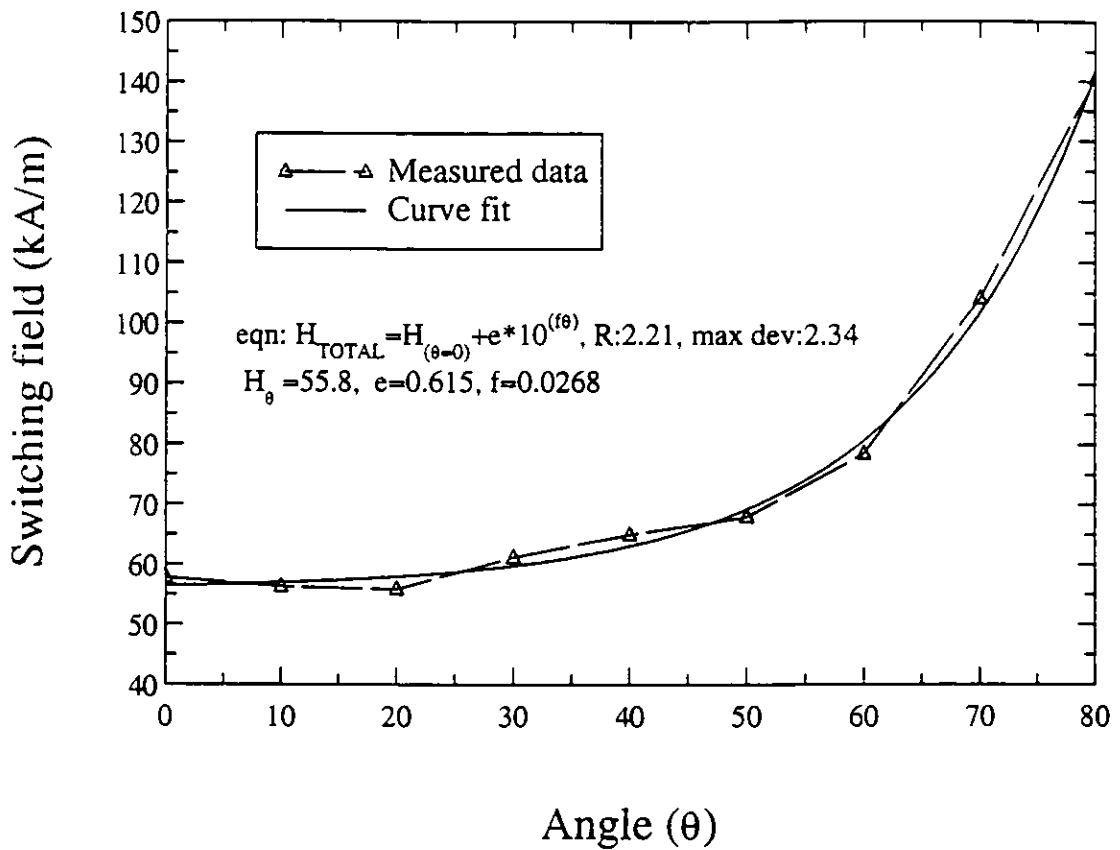


figure (3-17): A particle from sample 2 curve fitted numerically.

The switching field angular component of the particles taken from a sample were investigated. For a numerical measure of how the switching field of a sample varied, the switching field at $\theta=0$ for each particle was subtracted from its switching field at all applied field angles, the results for all the particles within a sample were then curve fitted with equation (3-3), modified to represent only the angular variation of the switching field.

$$H_{\theta} = e10^{f\theta}, \quad (3-3)$$

here e and f are curve fitting parameters representing the angular variation in the switching field of particles from a sample. An example of this analysis for sample 1 with the curve fit is presented in figure (3-18). The results for all the other samples investigated are presented in table (3-3). As there were only a very small number of particles investigated for the switching field as function of angle the results were not taken as absolute, but as a guide to the general trend.

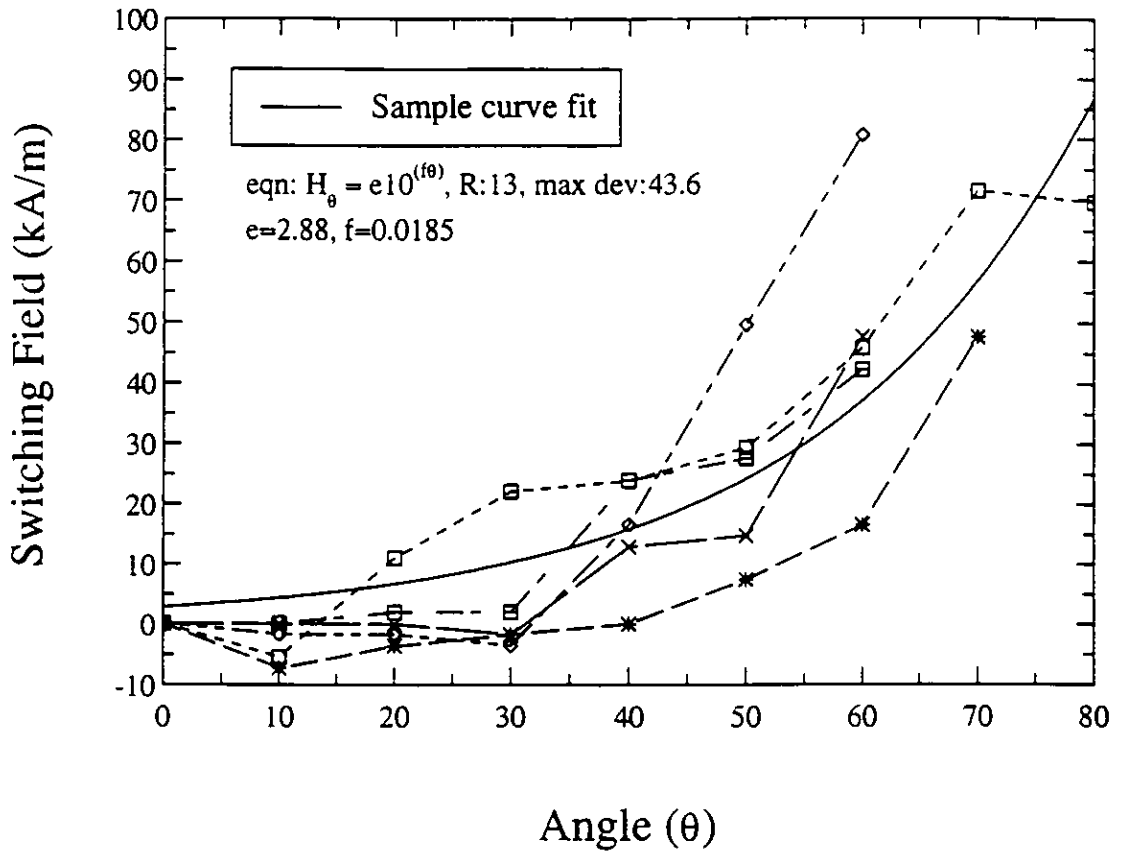


figure (3-18): Curve fit of the angular switching field component of sample 1.

Sample type	Sample No	Curve fit parameter e	Curve fit parameter f
γ -Fe ₂ O ₃ particulate media	1	2.880	0.0185
	2	0.639	0.0267
	3	0.0074	0.0512
CrO ₂ particulate media	4	3.111	0.0190
	5	0.578	0.0269
	6	0.310	0.0269
Metal particle media	7	0.741	0.0299

table (3-3): Numerical curve fits of the samples angular switching field component.

The relative variation in the switching field (H_R) as a function of the applied pulsed field angle for the particles taken from each sample was investigated. The curve fits of the switching field as a function of the applied field angle for each sample were normalised to its mean switching field (H_{MEAN}) of its switching field histogram.

$$H_R = \frac{H_{TOTAL}}{H_{MEAN}} = \frac{H_{(\theta=0)} + e^{10^{i\theta}}}{H_{MEAN}} \quad (3-4)$$

The relative variation in the switching field as a function of the applied field angle for all the samples is presented in figure (3-19).

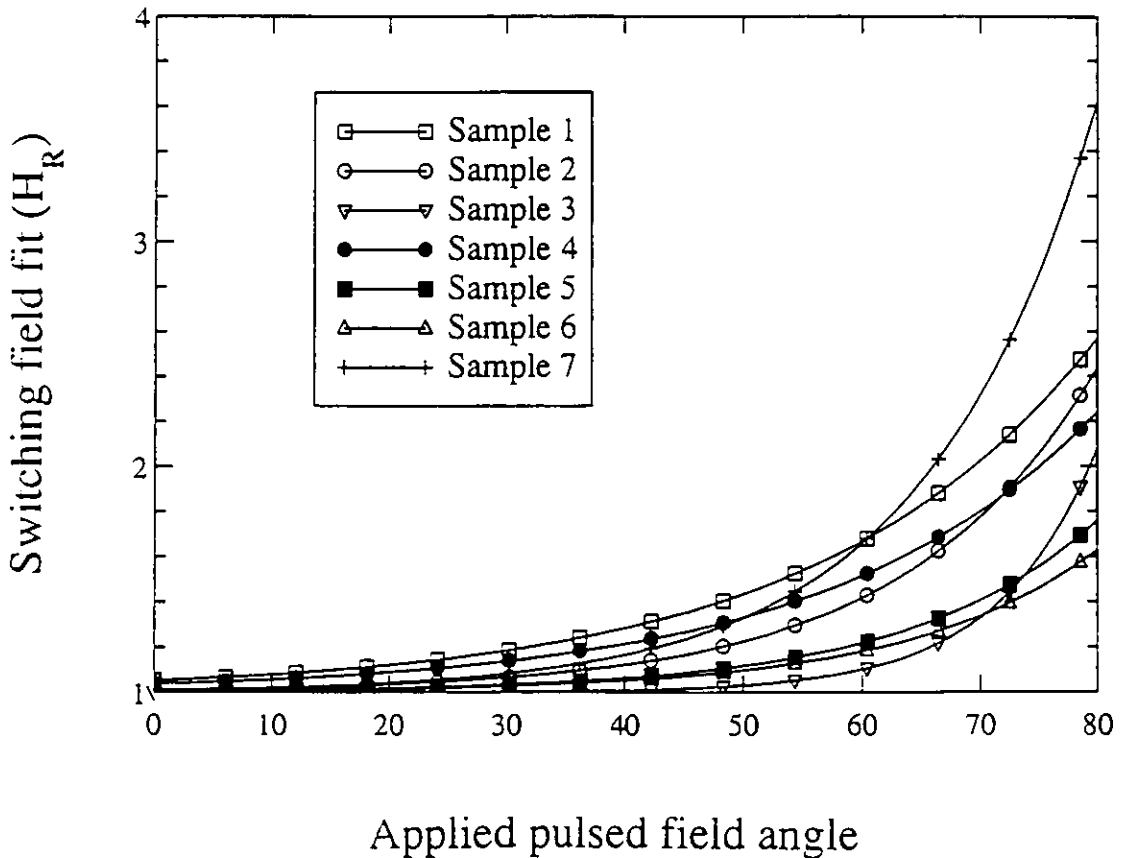


figure (3-19): The relative variation in the switching field (H_R) as a function of the applied pulsed field angle for the particles taken from each sample.

The results for the γ - Fe_2O_3 and CrO_2 samples indicated a similar switching field angular dependence. The results for the metal particle sample indicated it had a larger angular dependence in its switching field when compared to all the other samples investigated. One possibility for these observations could be the presence of similar

reversal mechanisms within the $\gamma\text{-Fe}_2\text{O}_3$ and CrO_2 particles, while a more angular dependent reversal mechanism was occurring in the metal particles. As $\gamma\text{-Fe}_2\text{O}_3$ and CrO_2 particles have similar bulk saturation magnetisation values and all the particles within this study have similar dimensions, the more angular dependent reversal mechanism found within the metal particles might be attributed to the effect of its significantly higher bulk saturation magnetisation.

The measured switching field as a function of the applied field angle for all the sample particles investigated indicated similar results. The observed switching field remained approximately constant below 30° , while above 30° the switching field increased markedly with the applied field angle. This is consistent with the incoherent reversal models, such as fanning, buckling and curling. These reversal modes can initiate reversal at lower switching fields than those achieved by coherent reversal at low applied field angles, the angle between the easy axis of the particle and the applied field direction. As the applied field angle increases these reversal models become more coherent, thus increasing the switching field of the particle [1,3,6]. These results are comparable with the studies by Knowles [1,7] and by Luo *et al.* [8]. Knowles measured the switching field as a function of angle for commercial $\gamma\text{-Fe}_2\text{O}_3$ and CrO_2 particles, while Luo *et al.* measured characteristics of individual commercial iron particles by Magnetic Force Microscopy (MFM).

The measurements of isolated magnetic particles performed in this study has extended the work by Knowles for recent commercial particles, commercial MP for example. The results from the single particle measurement have in later chapters been used to derive an absolute measure of interaction field within particulate media. These results have also been used as an comparison with modelled reversal properties of the particles measured in this chapter, and thus obtain a direct comparison with experimental and modelling results for isolated particles.

In the recent work by Sailing *et al.* [9] and Lederman *et al.* [6,10] the switching field characteristics of $\gamma\text{-Fe}_2\text{O}_3$ particles were investigated using Transmission Electron Microscopy (TEM) and MFM. Their results indicated the reversal mechanism to be coherent at large applied field but as the applied field angle θ approached zero, curling became the more probable reversal mechanism. An example of the results by Lederman

et al. is presented in figure (3-20). These measured results are significantly different to those here, and those obtained by Knowles and by Luo *et al.* This can be attributed to the particles used within Sailing *et al.* and Lederman *et al.* studies. These particles were especially fabricated to be very close to prolate ellipsoids and had very few surface imperfections [11]. Particles with these characteristics would generate a uniform demagnetisation field aiding coherent reversal and with few surface nucleation sites for the initiation of incoherent reversal.

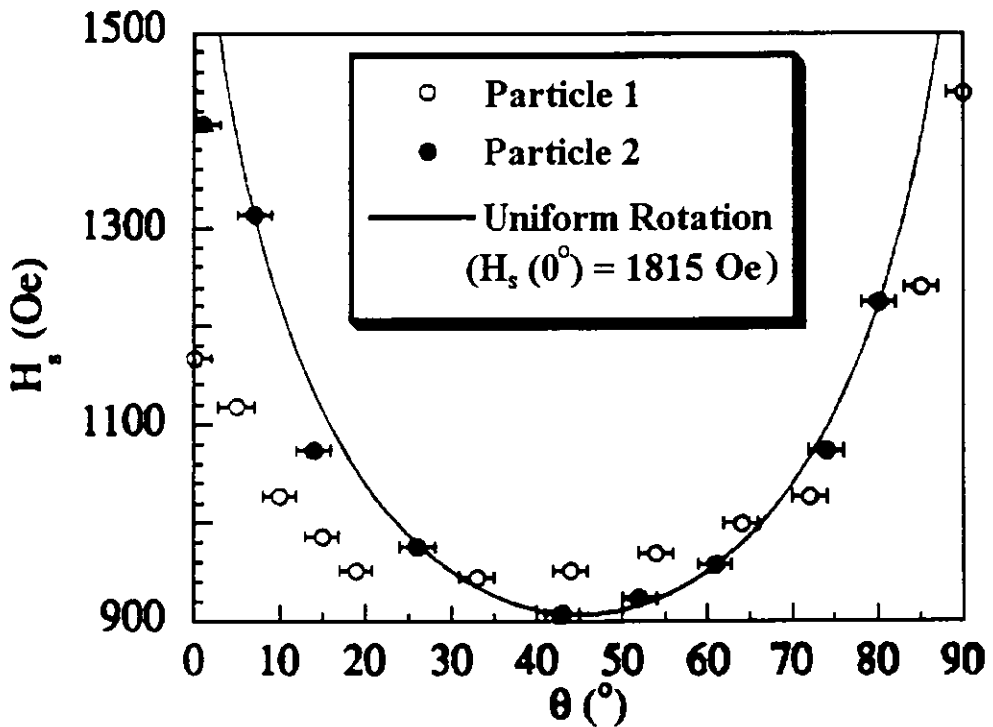


figure (3-20): Angular dependence of the switching field $H_s(\theta)$ of two isolated single domain $\gamma\text{-Fe}_2\text{O}_3$ particles. The solid curve represents $H_s(\theta)$ predicted by Stoner-Wohlfarth (uniform rotation) with a saturation magnetisation $M_s=350\text{emu/cm}^3$ and an aspect ratio of 4.6. (After Lederman *et al.* [10]).

3.5 The remanent curve measured from an individual particle

As the remanent magnetisation of a particle is strongly dependent on its physical structure, an examination of its remanent magnetisation can be instructive in the evaluation of its physical structure. A particle composed of a number of domains would exhibit demagnetisation effects through its remanence curve, identified by a reduction in its remanence approaching its switching field.

The remanent magnetisation of a particle was determined by measuring the time taken for a particle to rotate into an aligning field through a known angle [1]. The inverse of this time was taken as an arbitrary measure of its remanent magnetisation.

The technique assumed that the torque Γ_p acting on a particle by a weak alignment field as it rotates in a viscous resin was equivalent to the torque Γ_R generated from the resin as the particle rotates.

$$\Gamma_p \equiv \Gamma_R \quad (3-5)$$

The torque generated from the moment of the particle as it rotates in an alignment field is defined as

$$\Gamma_p = \mu_o H M \sin \theta , \quad (3-6)$$

where M is the moment of the particle, H is the weak alignment field and θ is the angle between the particle moment and the alignment field, indicated in figure (3-21).

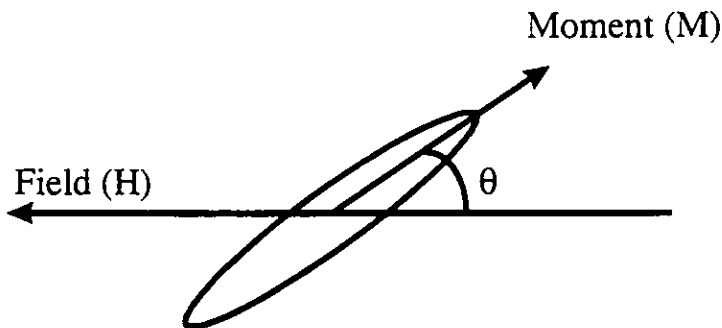


figure (3-21): Particle configuration for the measurement of its remanence.

The torque Γ_R generated by the viscous resin as the particle rotates is proportional to its angular velocity ω .

$$\Gamma_R \propto \omega \quad (3-7)$$

Equating this proportionality to the torque generated on the particles moment by the alignment field,

$$\frac{d\theta}{dt} = \omega \propto M \sin \theta. \quad (3-8)$$

Hence

$$t = \int dt \propto \frac{1}{M} \int_0^\pi \frac{d\theta}{\sin \theta} = \frac{1}{M} \left[\ln \left(\tan \left(\frac{\theta}{2} \right) \right) \right]_0^\pi \quad (3-9)$$

The time t taken for a particle to rotate through a known angle is thus inversely proportional to its moment. Equation (3-9) does not have a finite solution for the limits 0 to π as there is no torque mathematically at these points and so the particle cannot rotate. In a real situation the moment of a particle would move from the unstable equilibrium position through field misalignment or thermal agitation of its moment.

The experimental procedure adopted to measure the remanence curve of an individual particle is as follows. The particle under investigation was initially saturated with the maximum pulsed field available. The alignment magnets generating the alignment field were then rotated by 90° and the time taken for the particle to realign within the alignment field was measured. This was repeated twice more to obtain a mean for the particle realignment time. The reciprocal of this mean was taken as an arbitrary measure of its saturation moment [1]. A small reversed pulsed field was then applied, and it was noted whether the particle rotated by 180° , indicating its moment had been switched and was rotating within the alignment field direction. The remanence of the particle was measured with the described technique. This procedure was repeated for incremental increases in the applied pulsed field until the particle had been switched and saturated in the reverse field direction, indicated through the rotation of the moment towards the alignment field.

The results for the samples 1,4 and 7 are presented in figure (3-22), figure (3-23) and figure (3-24). Samples 1 and 7 exhibit a step function in their remanence curves indicating no demagnetisation effects. The particle of sample 4 however indicated demagnetising effects within its remanence curve, identified by a reduction in its

remanence approaching its switching field. These demagnetising effects could be attributed to this particle being multidomain or a multiple particle. These experimental results indicating a step function and demagnetising effects are similar to those by Knowles [7]. Since the experimental technique was very time consuming, the motion and subsequent loss of the particles in the field of view was extremely problematic. As a consequence and the insignificance of the quantitative data, this investigation was not extended to further samples.

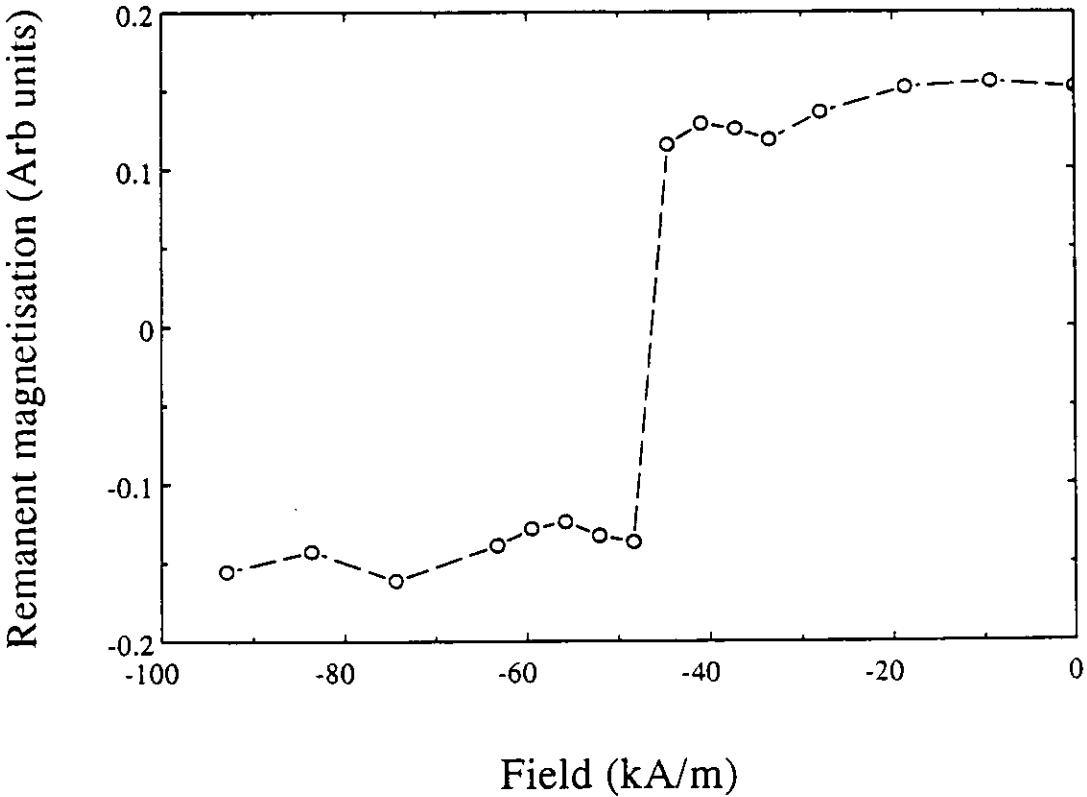


figure (3-22): Remanence curve for an individual particle of sample 1.

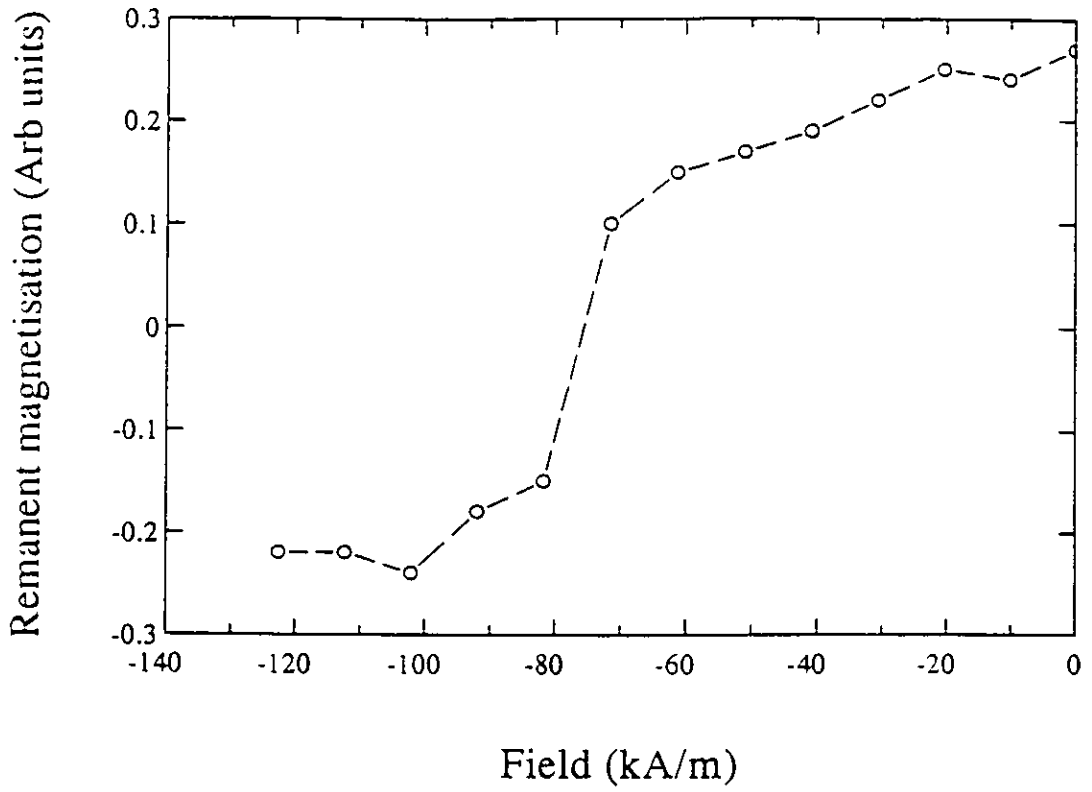


figure (3-23): Remanence curve for an individual particle of sample 4.

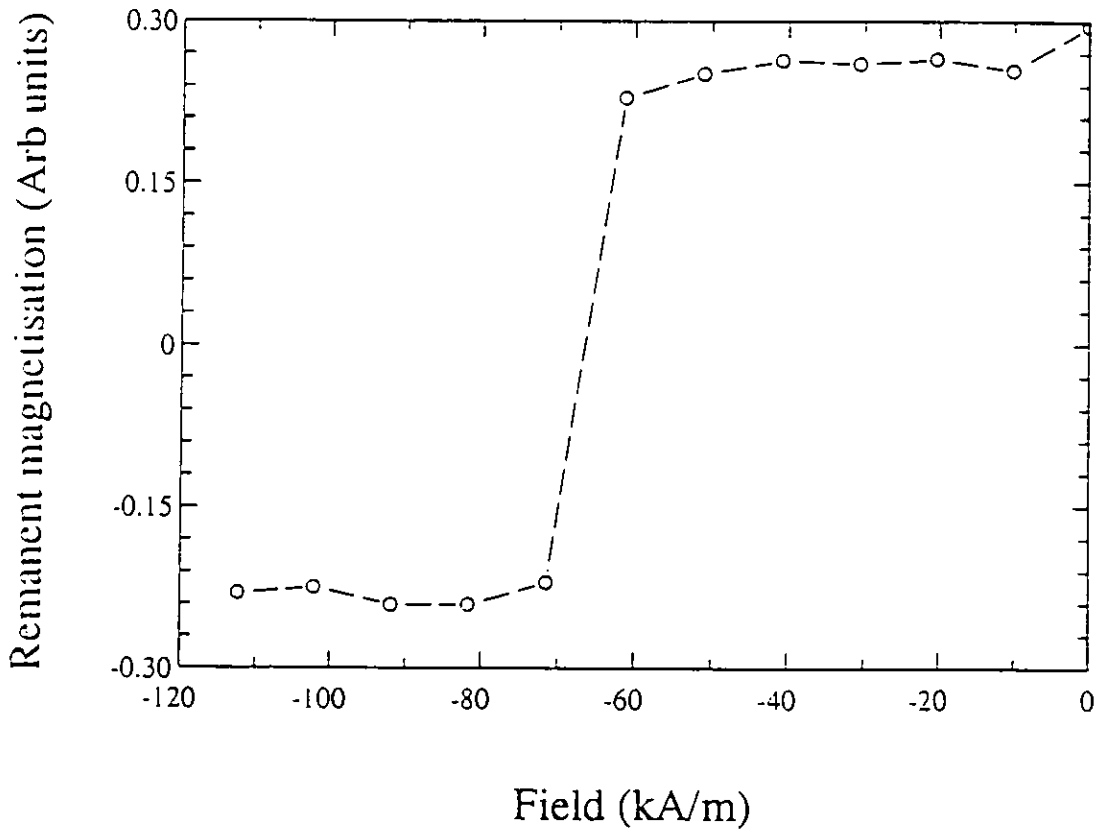


figure (3-24): Remanence curve for an individual particle of sample 7.

3.6 Measurement of the physical dimensions of the particles

For a full evaluation of the particles investigated it would be necessary to have an understanding of their size and physical structure. The measurement of the particle size was not possible with the optical microscope used within this study as diffraction effects dominate its image, effectively blurring its shape. Thus, a Scanning Electron Microscope (SEM) was utilised to determine the physical dimensions of a particle, while its structure was assumed from the available literature [12-21]. The SEM used throughout this work was a JEOL JSMT300 at Manchester Metropolitan University and this work was performed in association with Mr G Heydon.

A schematic diagram of a SEM with its basic components is presented in figure (3-25). The SEM generates a narrow beam of electrons from an electron gun. This electron beam passes down through the evacuated column of the SEM ($\sim 10^{-6}$ τ) towards the sample. As the beam passes through the electromagnetic condenser lenses it is demagnified, becoming narrower. The beam then passes through the scanning coils that scan the beam on to the surface of the sample. Before the beam intersects the sample it passes through the objective lens of the SEM that focuses the beam on to the surface. As the electrons strike the sample, secondary electrons are produced which are attracted towards the potential of the collector. The production of these secondary electrons is dependent on the energy and direction of the primary electron, the density of the sample and its surface structure. A full discussion of the many aspects of scanning electron microscopy can be found in the books by Hayat, Oatley, Kay *et al.* and Thornton [22-25].

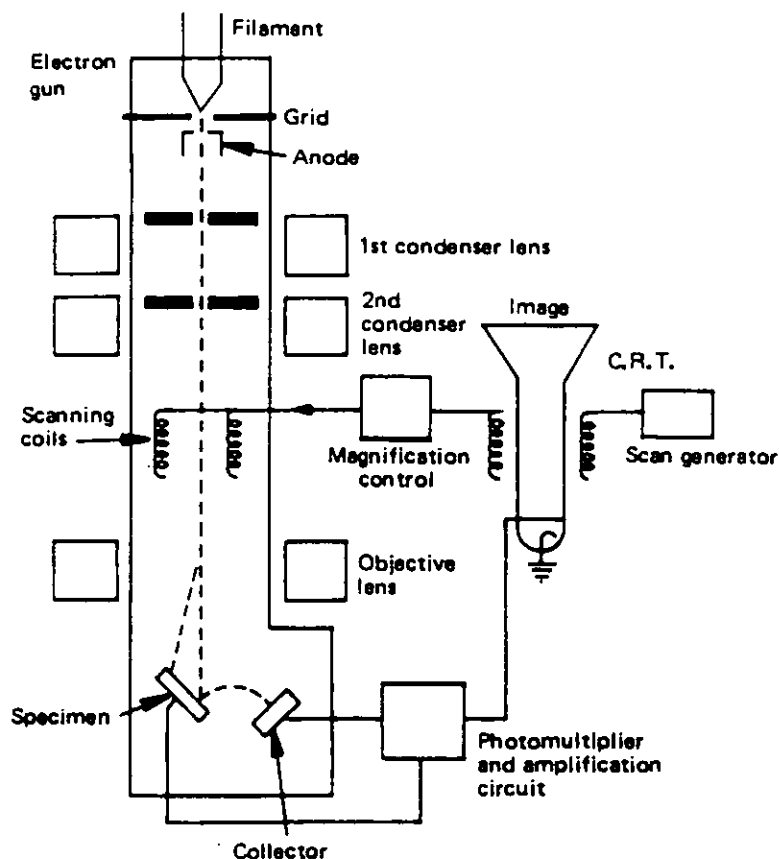


figure (3-25): Schematic diagram of a scanning electron microscope, after Hayat [22].

The preparation of the SEM sample required the extraction of the particles from their media. The particles were extracted from their media by the action of a solvent, Methylenechloride in an ultrasonic bath. The solvent dissolved the resin of the media, while the ultrasonic bath lifted the particles away from the backing film. A drop of the particle suspension was deposited on a SEM sample block and allowed to evaporate, leaving the particles behind.

The SEM sample blocks were observed within the SEM. The images obtained from the SEM were in the form of Polaroid photographs. It was found that they all gave similar images indicating the formation of agglomerations on the sample block. A number of attempts to eliminate the formation of these agglomerations at Preston and at Manchester Metropolitan University were all unsuccessful. These included the application of AC and DC alignment fields during the evaporation of the solvent. This had no discernible effect on the formation of the agglomerations on the sample blocks

surface. An example of a typical SEM image obtained with a gain of 30K for sample 1 is presented in figure (3-26).

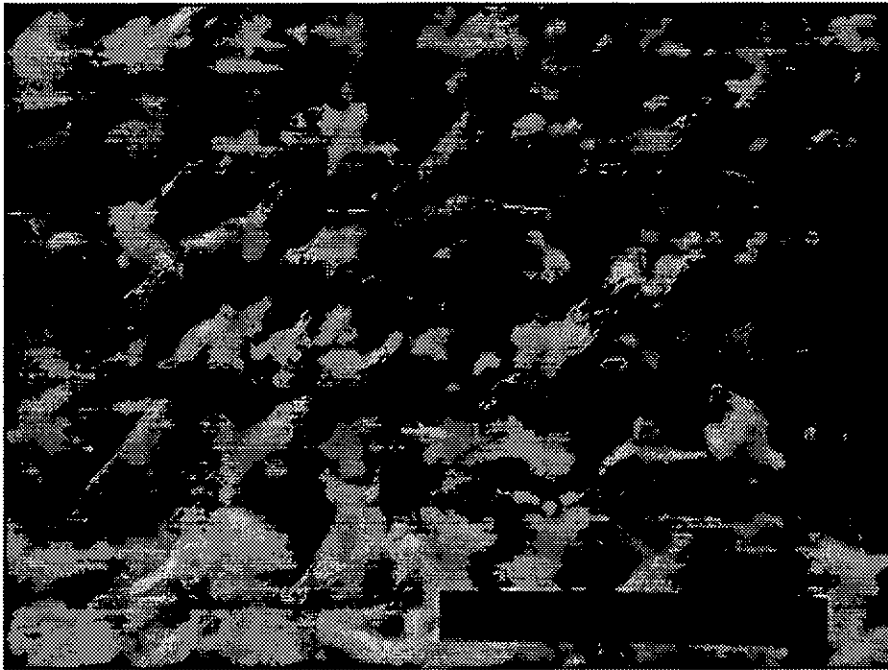


figure (3-26): SEM polaroid image of sample 1.

The dimensions of the particles were measured from the SEM images. As the images tended to have particles within agglomerations it was difficult to identify particles and so only a small number of particles could be measured. These measurements were also susceptible to errors associated with the projection of the particle with respect to the plane of the image. The histograms of the particle length and its aspect ratio for all the samples investigated are presented in figure (3-27) through to figure (3-33).

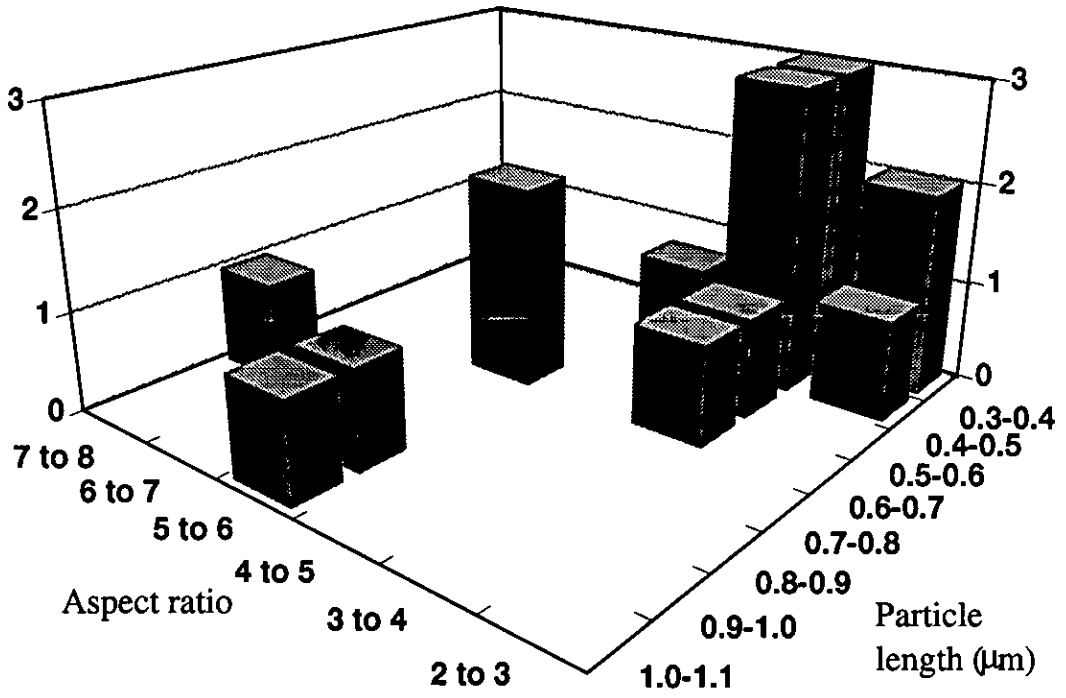


figure (3-27): Particle length and aspect ratio histogram for 17 particles of sample 1.

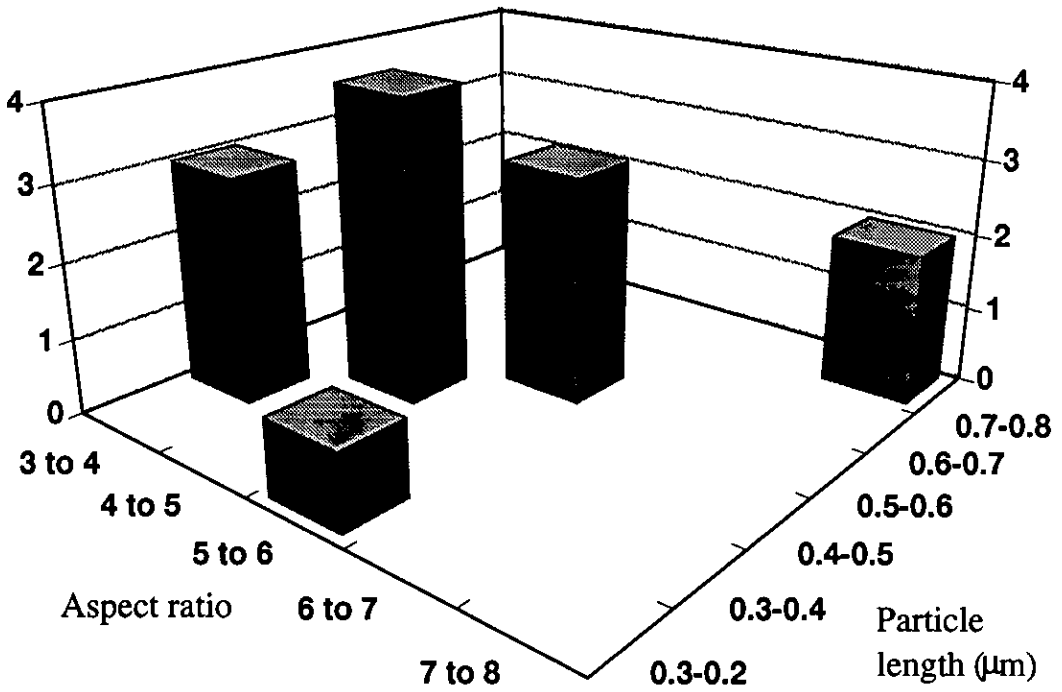


figure (3-28): Particle length and aspect ratio histogram for 13 particles of sample 2.

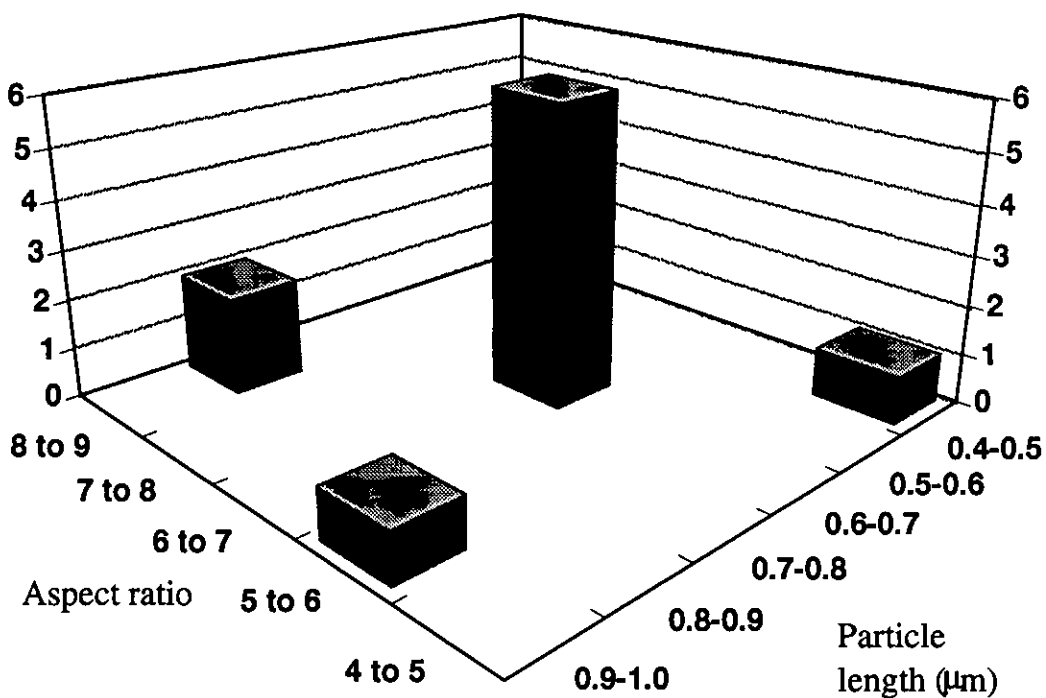


figure (3-29): Particle length and aspect ratio histogram for 10 particles of sample 3.

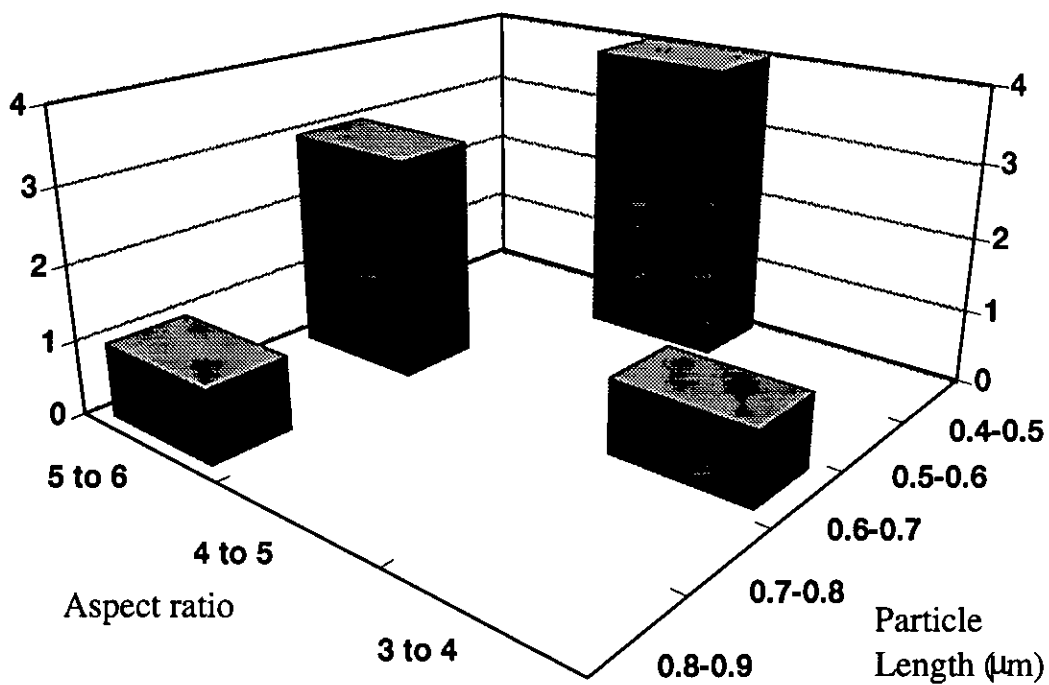


figure (3-30): Particle length and aspect ratio histogram for 9 particles of sample 4.

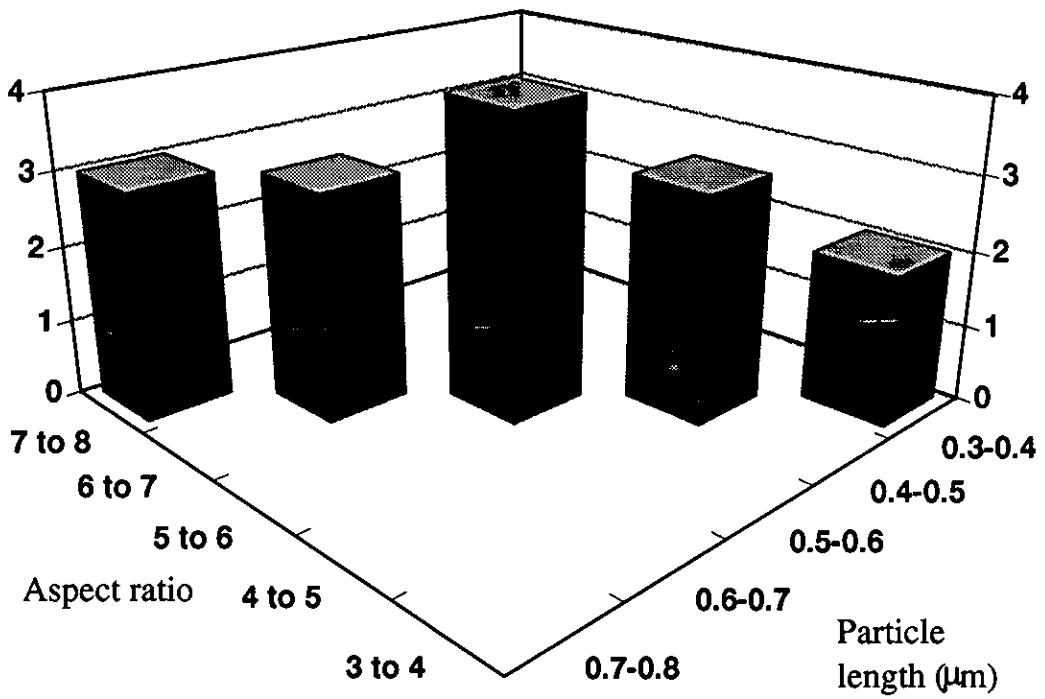


figure (3-31): Particle length and aspect ratio histogram for 15 particles of sample 5.

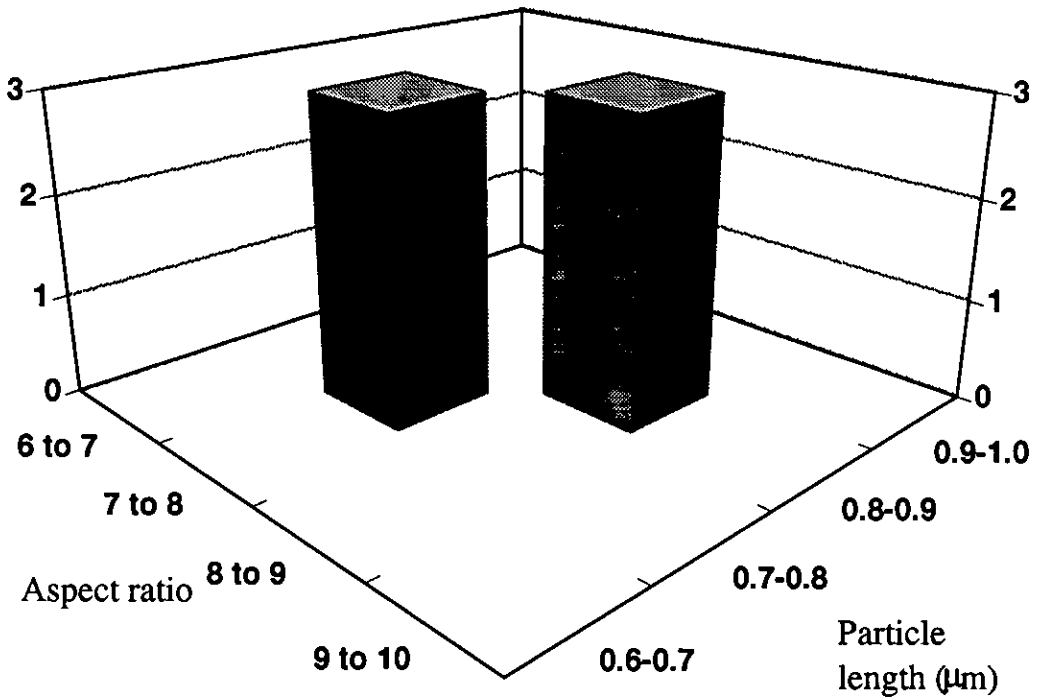


figure (3-32): Particle length and aspect ratio histogram for 6 particles of sample 6.

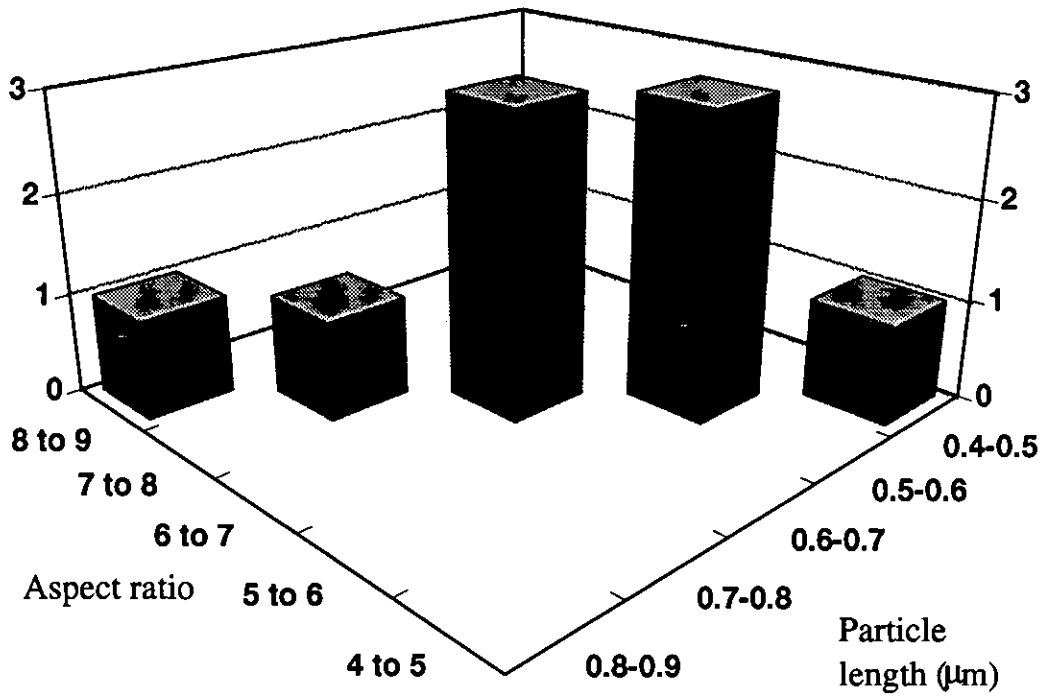


figure (3-33): Particle length and aspect ratio histogram for 9 particles of sample 7.

The results from the SEM images have indicated that the particles taken from the samples under investigation were observable using the available optical microscopy. Typically the particles had an aspect ratio ranging from 3:1 to 9:1 with a particle length ranging from 0.3µm to 1.0µm.

Chapter Four

Bulk measurements and analysis of particulate media

4.1 Introduction

In this chapter the bulk measurement techniques are introduced and the properties of the measured samples are presented. The bulk properties measured were hysteresis, remanence and the orientation of particles within the media. These measurements in association with the study of particle properties in chapter 3 are considered further in chapter 5, to derive an absolute measure of interaction effects within the samples.

A Vibrating Sample Magnetometer (VSM) [1] has been used to measure hysteresis loops and remanence curves. These measurements in association with analysis techniques, particularly Henkel plots [2] and orientation ratios have given an insight into the interaction effects and particle orientations.

Transverse susceptibility measurements [3] have been made to investigate the anisotropy field of a sample and its out-of-plane demagnetising field [4]. Analysis of these results, in conjunction with measurements performed on the VSM, has allowed the absolute magnetisation and the thickness of the sample to be derived. With these results an orientation ratio out-of-plane has been calculated and functions representing the orientation of particles out-of-plane for the samples have been proposed.

The orientation of particle's in-plane within a sample, known as its in-plane Easy Axis Distribution (EAD) has been investigated. The technique utilised a Bi-axial VSM [5] that enabled the moment of the sample to be measured in the field direction and orthogonal to it. The measured EAD in-plane for the samples were compared with their

orientation ratios in-plane. The results indicated the orientation ratio to be a reasonable measure of particle orientation.

4.2 Hysteresis measurements

Hysteresis describes the ability of a magnetic material to retain its magnetisation after the removal of its magnetising field. It should be noted that the magnetisation is not a unique function of the applied field, but is dependent on the direction and magnitude of previous applied fields. A hysteresis loop represents the magnetisation of a sample through the cyclic rotation of an applied field. An example of a major hysteresis loop where the magnetisation of the sample is saturated in both applied field directions is given in figure (4-1).

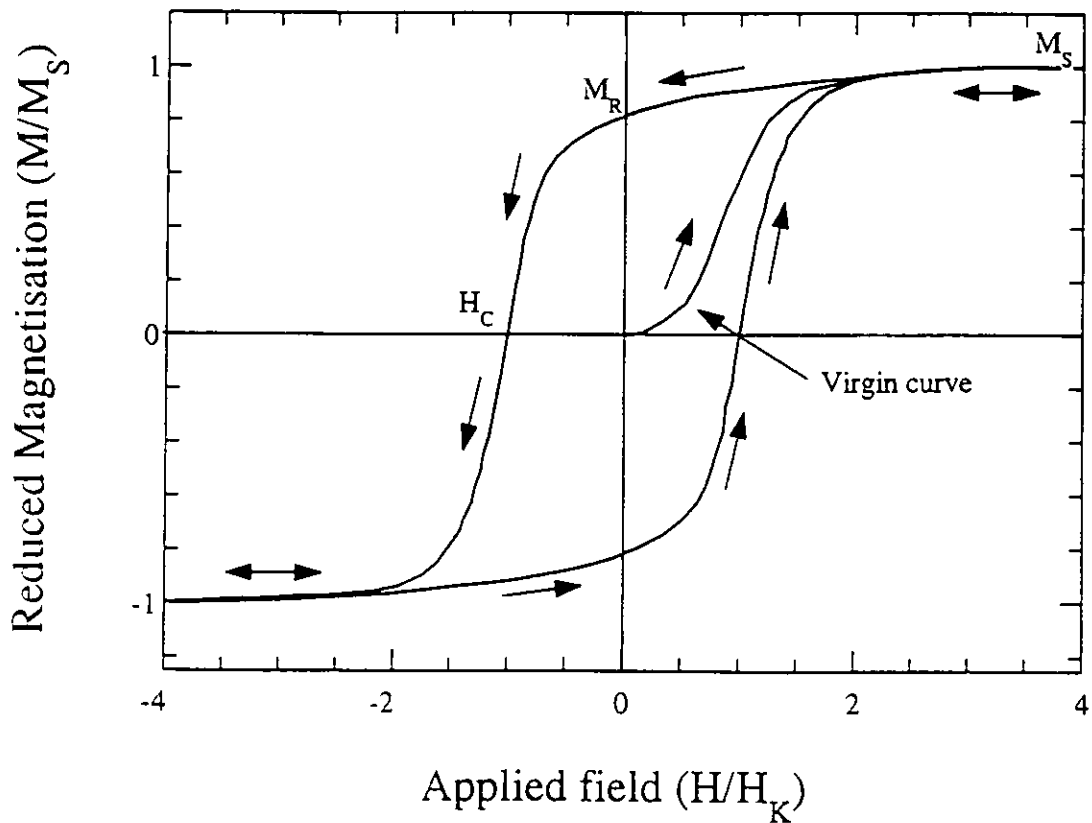


figure (4-1): A typical hysteresis loop for a particulate medium, indicating typical measurement parameters.

The direction of the arrows in figure (4-1) represent the magnetising field direction. Initially the sample is demagnetised and a positive field applied. This field magnetised the sample by the rotation and the switching of the moments into the applied field direction. This part of the hysteresis plot is referred to as the virgin curve, it can

also be referred to as the initial curve. As the positive applied field increased a point was reached where the magnetisation of the sample remained constant, this point identified its saturation magnetisation (M_S). The field was now reduced to zero allowing the magnetisation to relax. The magnetisation at this point, referred to as its remanent magnetisation (M_R) does not return to zero, since there is an energy barrier originating from the anisotropy of the sample.

At this stage a negative applied field was applied. The effect of this field was to demagnetise the positively magnetised sample. As the negative applied field increased a point was reached where the field was great enough to reduce the magnetisation to zero. This field identified as the coercivity (H_C) of the sample represents an important parameter within magnetic recording media. It determines the field required to magnetise/demagnetise a signal.

As the negative applied field decreased the sign of the magnetisation became negative, as this field decreased further the magnetisation became negatively saturated. This represented half the major hysteresis loop from positive saturation to negative saturation. The loop was completed in a similar process of sweeping the applied field from negative to positive field saturation.

Apart from the Major hysteresis loop described above there exist an infinite number of minor loops. These loops exist within the major loop and can be both symmetrical and unsymmetrical depending on the application of the applied field [4,6], but were not investigated.

Apart from the hysteresis loop parameters already discussed there exist three other parameters utilised in this study. They are its squareness ratio, its orientation ratio and its Switching Field Distribution (SFD) defined from the differential of the major hysteresis loop.

The loops squareness ratio (Sq) is defined as

$$Sq = M_R / M_S . \quad (4-1)$$

The squareness ratio is an important parameter in the characterisation of magnetic media by manufacturers, since it is proportional to the magnitude of the read signal from a magnetic transition within the media. The squareness ratio also indicates the degree of particle orientation within the media and is a measure of the reversible component in the

sample's saturation magnetisation. For a random assembly of uniaxial single domain particles it has been shown theoretically [7] to be 0.5, while for a perfectly aligned sample the squareness ratio is 1.0. In manufactured aligned particulate media the typical squareness ratio is within the range 0.7-0.9 [8-10].

The orientation ratio in-plane $Or(I)$ is a measure of the particle alignment within a system, its Easy Axis Distribution (EAD). It is defined by the squareness ratio $Sq(I)$ measured in-plane within the EAD direction and squareness $Sq(T)$ measured in-plane and transverse to the EAD direction,

$$Or(I) = Sq(I) / Sq(T). \quad (4-2)$$

The squareness in-plane and transverse to the EAD direction for sample 2 was 0.83 ± 0.01 and 0.32 ± 0.01 respectively. This gave an in-plane orientation ratio of 2.59 ± 0.09 . An orientation ratio of 1.0 would indicate no alignment, while an orientation ratio greater than 1.0 would represent particle alignment within the sample, indicating a EAD direction.

The SFD of a media is dependent upon the consistency of its particles, their orientation and the interaction effects between them. As a consequence of the SFD sensitivity to these characteristics and its importance to media manufacturers a number of techniques have been developed for its determination, discussed by Wohlfarth [11] and Koster [12]. The SFD can be obtained from a hysteresis loop by differentiating the loop in the region from negative to positive saturation (dM/dH), indicated in figure (4-2). It should be noted that this SFD examines both the irreversible and reversible magnetisation processes within the hysteresis loop. The width of the SFD can be measured by its half pulse width, ΔH_C [13]. However, the most common measure of the SFD is the quantify $1-S^*$, where S^* is the length of the line joining the magnetisation axis at saturation magnetisation on to a tangent to the curve at $H=H_C$.

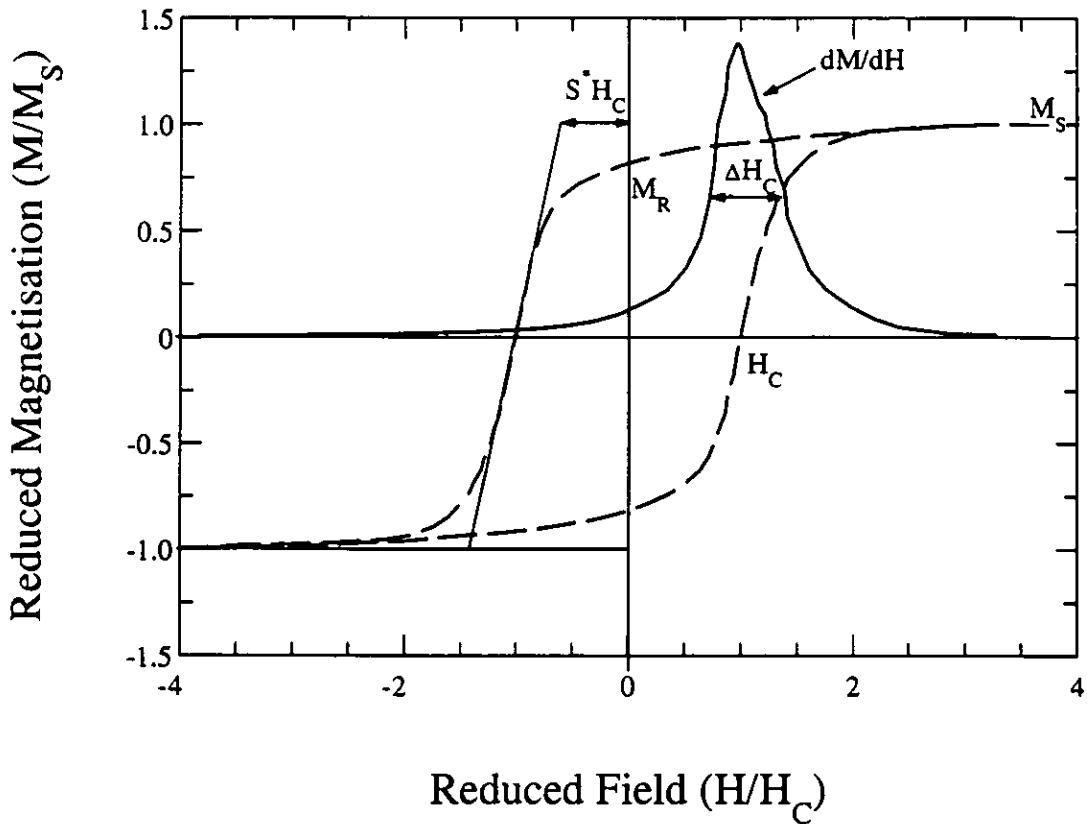


figure (4-2): Hysteresis loop showing basic parameters for the derivation of its switching field distribution.

The VSM used throughout this work had a field resolution of 800 A/m, while the measured moment had a resolution of $0.01 \cdot 10^{-3} \text{ Am}^2$. The VSM was calibrated with a Nickel sample (0.232g) which generated a moment of $12.618 \cdot 10^3 \text{ Am}^2$. The nickel sample shape (5 * 10mm) was important as the response of the VSM is dependent on the sample position within its pickup coils. For this reason the shape of the sample was cut to match the calibration sample. A further reduction in the measured accuracy could be inadvertently created by the poor alignment of either the calibration or the measurement sample.

The hysteresis plots for the samples investigated were performed and the basic parameters obtainable are presented within table (4-1). The results indicate a low squareness value for sample 1 ($Sq=0.69$), a 1960's $\gamma\text{-Fe}_2\text{O}_3$ Ampex tape and sample 4 ($Sq=0.74$), a hand spread CrO_2 tape. These results would seem to suggest poorer particle alignment within samples 1 and 4 compared to the other samples investigated. The results from the orientation ratio in-plane support these findings, especially for sample 1 where its in-plane orientation ratio is significantly smaller than all the other samples

where its in-plane orientation ratio is significantly smaller than all the other samples investigated. The results also show sample 1 to have a broader SFD compared to the other samples investigated. This broad SFD may be the result of a broad particle SFD within the media or poor particle alignment in the media. It should also be noted that the coercivities for samples 1-6 were similar (23.08-57.85kA/m), while the metal particle sample was significantly larger 117.94kA/m.

Sample type	Sample No	Coercivity kA/m (± 0.13)	Squareness S_q (± 0.01)	Orientation ratio (in-plane)	1-S* (± 0.01)
γ -Fe ₂ O ₃ particulate media	1	23.08	0.69	1.64 \pm 0.05	0.41
	2	26.58	0.83	2.59 \pm 0.08	0.24
	3	32.31	0.86	2.50 \pm 0.08	0.24
CrO ₂ particulate media	4	39.31	0.74	2.24 \pm 0.07	0.37
	5	57.85	0.87	2.49 \pm 0.08	0.33
	6	38.28	0.78	2.33 \pm 0.08	0.34
metal particle media	7	117.94	0.82	2.41 \pm 0.10	0.33

table (4-1): Hysteresis loop characterisation results.

4.3 Remanence curves

Remanence curves provide a technique for the investigation of the irreversible magnetisation process in magnetic recording media [13,14]. They measure the sample moment in zero applied field, hence no reversible magnetisation component. The two types of remanence curves are Isothermal Remanent Magnetisation (IRM) and DC Demagnetisation (DCD).

Experimentally the IRM curve was obtained by initially demagnetising the sample in an AC field. A small magnetic field H was applied, the field was reduced to

zero and the samples remanent magnetisation was measured $M_{IRM}(H)$. This process of incremental increases in the applied field and then the subsequent measurement of the samples remanent magnetisation was repeated until the sample was saturated $M_{IRM}(\infty)$.

The DCD curve was obtained in a similar fashion as the IRM curve. The only difference is that the sample was initially saturated in a positive field and not demagnetised. A small negative magnetic field was applied to the sample, removed and the remanent magnetisation of the sample was measured $M_{DCD}(H)$. This process was repeated until the sample had been saturated in the applied field direction $M_{DCD}(\infty)$.

An example of both types of remanence curves for sample 2 with their remanent coercivities H_{RC} and H'_{RC} identified is presented in figure (1-3). The DCD curve remanent coercivity H_{RC} is defined at zero remanent magnetisation, while the IRM curve remanent coercivity H'_{RC} is defined at half the saturation remanent magnetisation. Both remanence curves are normally plotted in their reduced units, where $I_{DCD}(H) = M_{DCD}(H) / M_{DCD}(\infty)$ and $I_{IRM}(H) = M_{IRM}(H) / M_{IRM}(\infty)$.

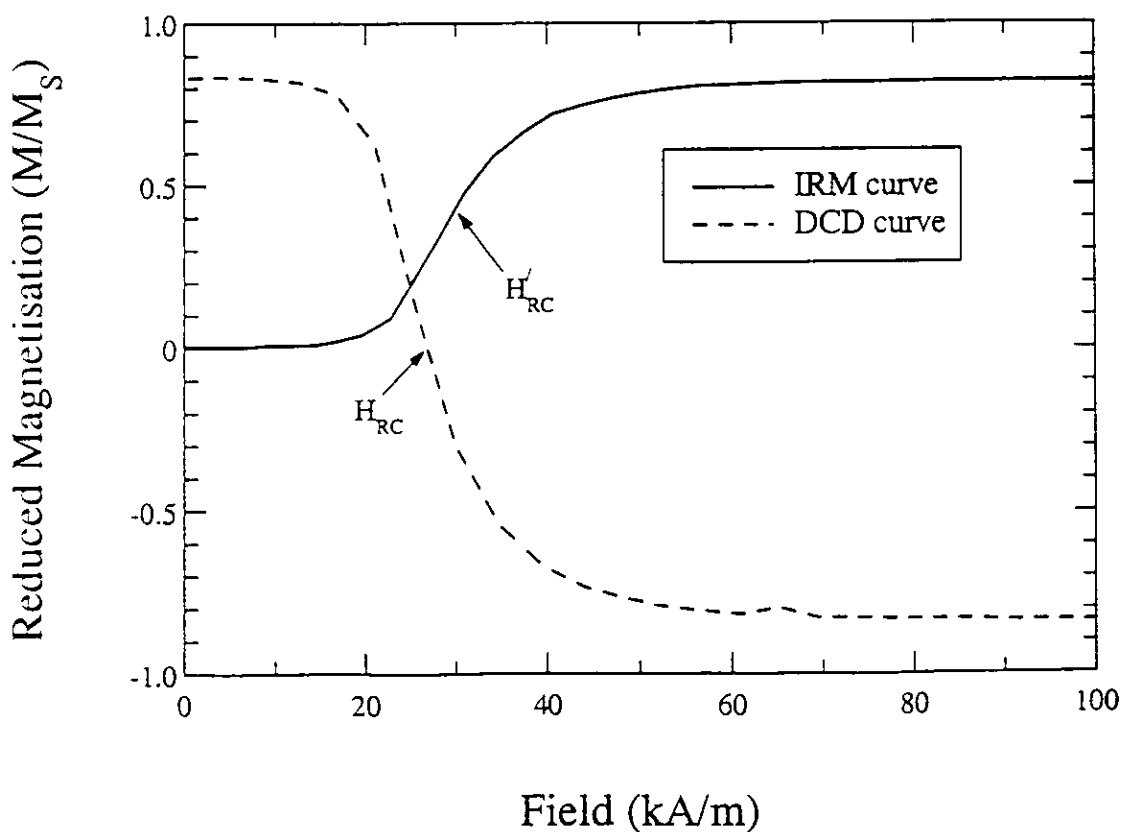


figure (4-3): IRM and DCD remanence curves for sample 2

The SFD for both remanence curves can be obtained through the differentiation of their curves. In the case of the IRM, where the sample state was initially random the SFD is given by,

$$SFD_{IRM} = \frac{dI_{IRM}}{dH} . \quad (4-3)$$

In the case of the DCD curve, where the sample was initially saturated the SFD is given by

$$SFD_{DCD} = -\frac{1}{2} \frac{dI_{DCD}}{dH} . \quad (4-4)$$

In the absence of interactions the SFD from both remanence curves should be identical [13]. An example of SFD derived from both the IRM and DCD curves of sample 2 is presented in figure (4-4). These results are typical for the particulate media investigated and for particulate media as a whole. The interaction field within the DCD remanence curve demagnetises the sample shifting its switching field distribution peak to a lower field.

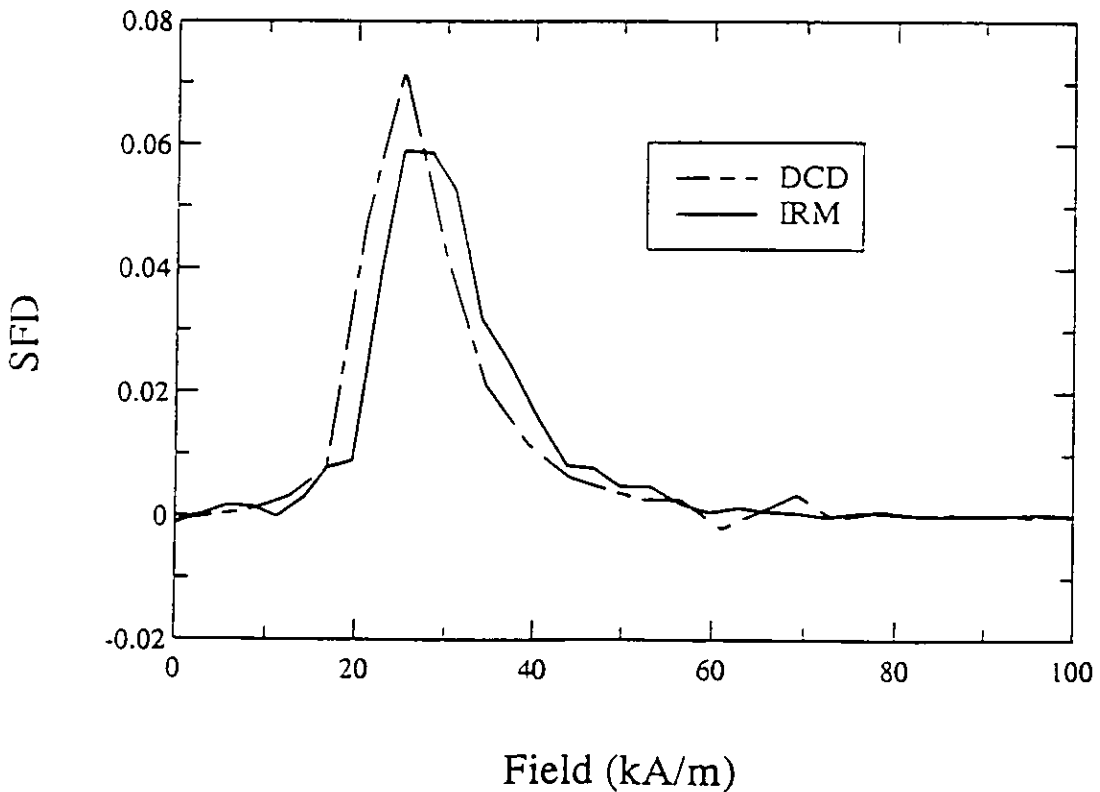


figure (4-4): Typical SFD's for IRM and DCD curves

4.4 Henkel plots

In 1958 Wohlfarth [15] showed that the DCD and IRM remanence curves for a system of non interacting single domain particles were linked. A proof of this relationship is given in appendix A. This link has become known as the Wohlfarth relationship,

$$I_{DCD}(H) = 1 - 2I_{IRM}(H). \quad (4-5)$$

Here $I_{DCD}(H)$ and $I_{IRM}(H)$ are the DCD and IRM curves normalised to the appropriate saturated remanent magnetisation of the sample.

In 1964 Henkel [2] proposed a technique utilising the Wohlfarth relationship to investigate interaction effects within hard magnetic materials. Henkel plotted $I_{DCD}(H)$ vs $I_{IRM}(H)$ and According to equation (4-5) in the absence of interaction effects the relationship should be linear. Any deviation away from this straight line would indicate interaction effects within the system. Deviations above the straight line would indicate positive interactions, the system opposing demagnetisation, while deviations below this line would indicate negative interactions, demagnetising the system.

In 1988 Spratt *et al.* [16] extended the technique developed by Henkel to investigate interaction effects within particulate recording media. They investigated interaction effects within CrO_2 particulate media Their study indicated negative interactions within this system. In particulate media it has been found that most systems exhibit negative interactions [17,18], only in high locally aligned systems can these interactions be positive [19,20].

In 1989 Kelly *et al.* [21] proposed an extension to equation (4-5) for examination of the deviation away from the Wohlfarth relation as a function of the applied field,

$$I_{DCD}(H) = 1 - 2I_{IRM}(H) + \Delta I(H). \quad (4-6)$$

Here $\Delta I(H)$ represents the deviation away from the Wohlfarth relationship normalised to the saturation magnetisation of the sample. The value of $\Delta I(H)$ is normally plotted against the applied field H to indicate the effect of interactions with the applied field and to allow a direct comparison with the hysteresis loop of the sample. For small

deviations away from the Wohlfarth relationship the ΔI plot is a clearer representation of the effect of interactions than the Henkel plot.

A technique was proposed by Bottoni *et al.* [22] to investigate the magnitude of interactions within particulate systems. It was based on the magnitude of the ΔI deviation away from the Wohlfarth relationship. They plotted ΔI vs. $I_{DCD}(H)/I_{DCD}(\infty)$ and assumed the magnitude interactions could be expressed as the integral of the ΔI deviation,

$$\Delta \text{ (plot area)} = \int_{-1}^1 \Delta I dx, \quad (4-7)$$

where $x = I_{DCD}(H)/I_{DCD}(\infty)$ and Δ (plot area) quantifies the total deviation away from the Wohlfarth relationship. A positive value of Δ (plot area) would indicate a tendency for the sample to oppose demagnetisation, while a negative value would indicate a tendency for the sample to demagnetise [21,23].

Bottoni *et al.* [24] has investigated the influence of the volumetric packing density P on the coercivity of iron powders. Their investigation suggested that using packing density has a measure of interaction strength could be misleading due to agglomerations within the sample effectively increasing its packing density locally. As a consequence the Δ (plot area) was thought to be a more appropriate measure of the interaction strength within their particle systems. In their investigation the Δ (plot area) also appeared to be sensitive to particle configurations within the samples. In particular at a packing density of $5 \cdot 10^{-3}$ the Δ (plot area) was positive, suggesting axial interactions through the formation of chains. As the packing density increased the Δ (plot area) reduced, indicating lateral interactions through the formation of particle bundles. Further increases in packing density reduced the Δ (plot area) until its sign reversed, suggesting predominately negative interactions caused by lateral interactions within the particle bundles.

The ΔI plot as proposed by Bottoni *et al.* Was produced for each of the samples investigated. The results are presented here in figure (4-5), figure (4-6) and figure (4-7) for the $\gamma\text{-Fe}_2\text{O}_3$, CrO_2 and metal particle samples. The Δ (plot area) for all the samples investigated are presented in table (4-2). The results of the ΔI plots indicated negative interactions for all the samples investigated. The magnitude of these interactions given

by the Δ (plot area) for the $\gamma\text{-Fe}_2\text{O}_3$ and CrO_2 samples were similar. In the metal particle sample the magnitude of interactions was significantly smaller than all the other samples investigated. This was surprising as the saturation magnetisation of metal particles is approximately a factor of 3 greater than $\gamma\text{-Fe}_2\text{O}_3$ and CrO_2 . Thus, assuming a similar EAD and a similar packing densities for the samples, the magnitude of interactions within the metal particle sample should be greater not smaller than the other samples investigated. These results might indicate the presence of positive axial interactions within localised chains of particles within the sample. The modelling study of Lyberatos *et al.*[25] discussed in chapter 5 confirms this possibility.

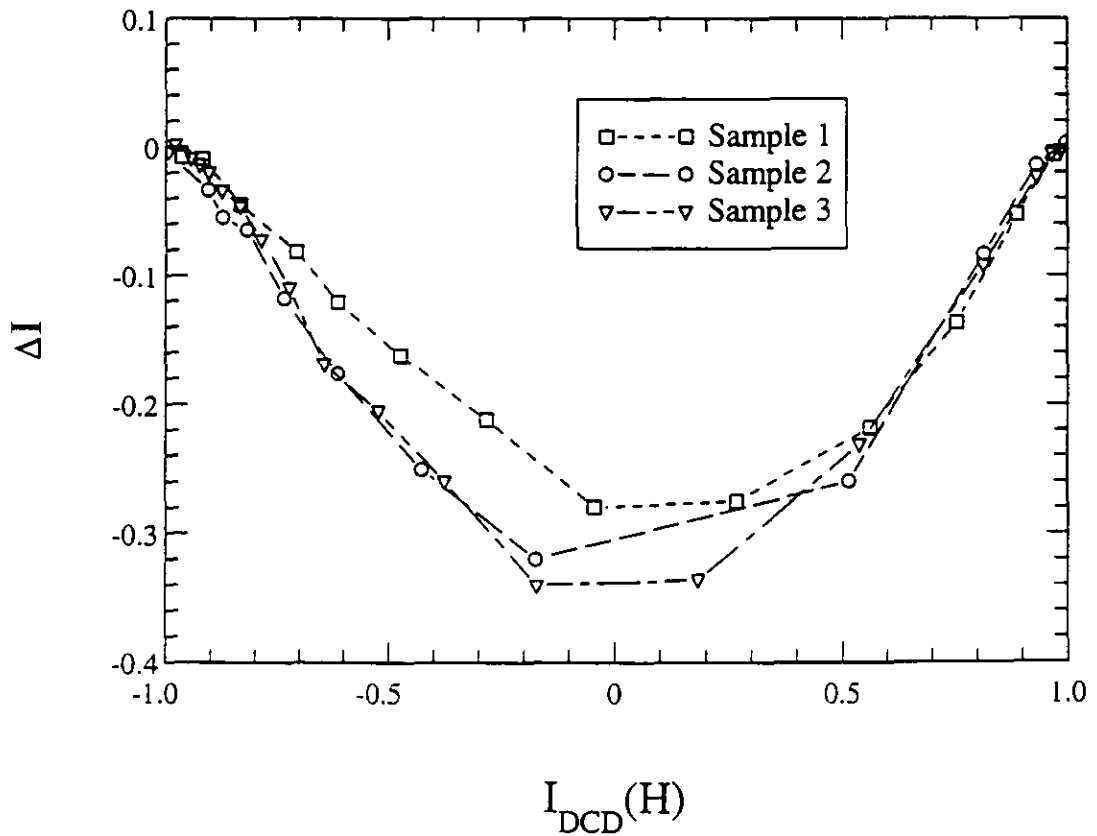


figure (4-5): ΔI deviation for the $\gamma\text{-Fe}_2\text{O}_3$ samples as a function of the normalised DCD remanence.

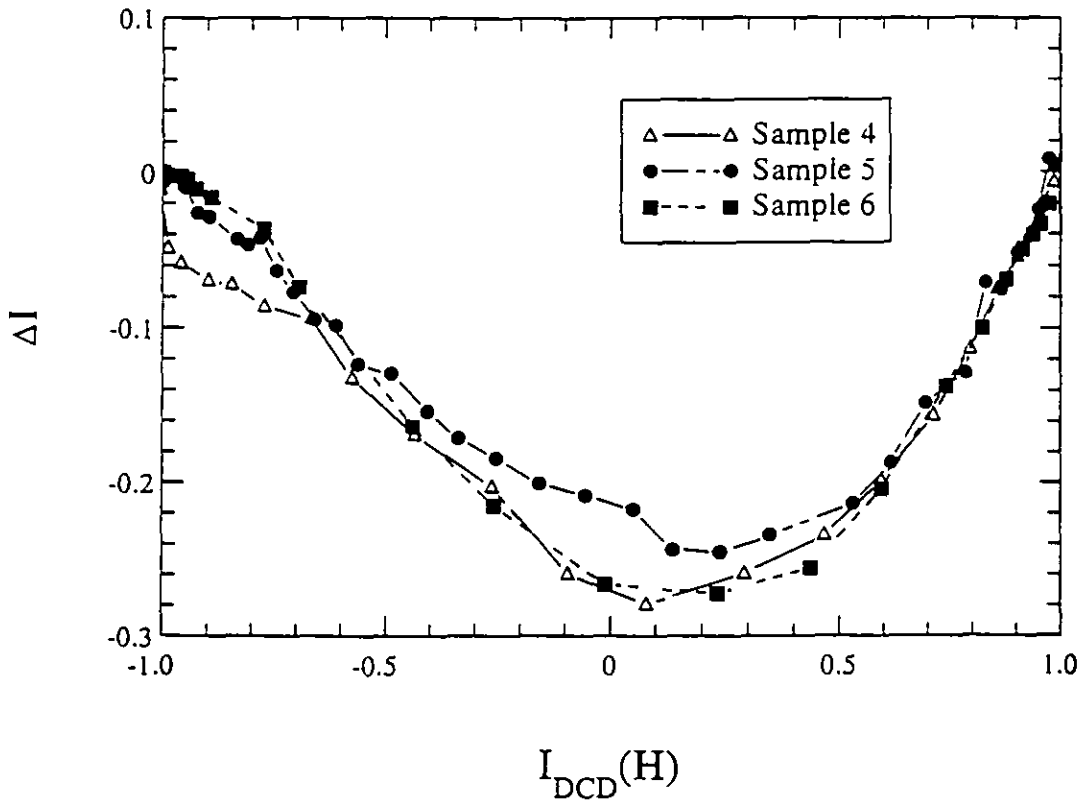


figure (4-6): ΔI deviation for the CrO_2 samples as a function of the normalised DCD remanence.

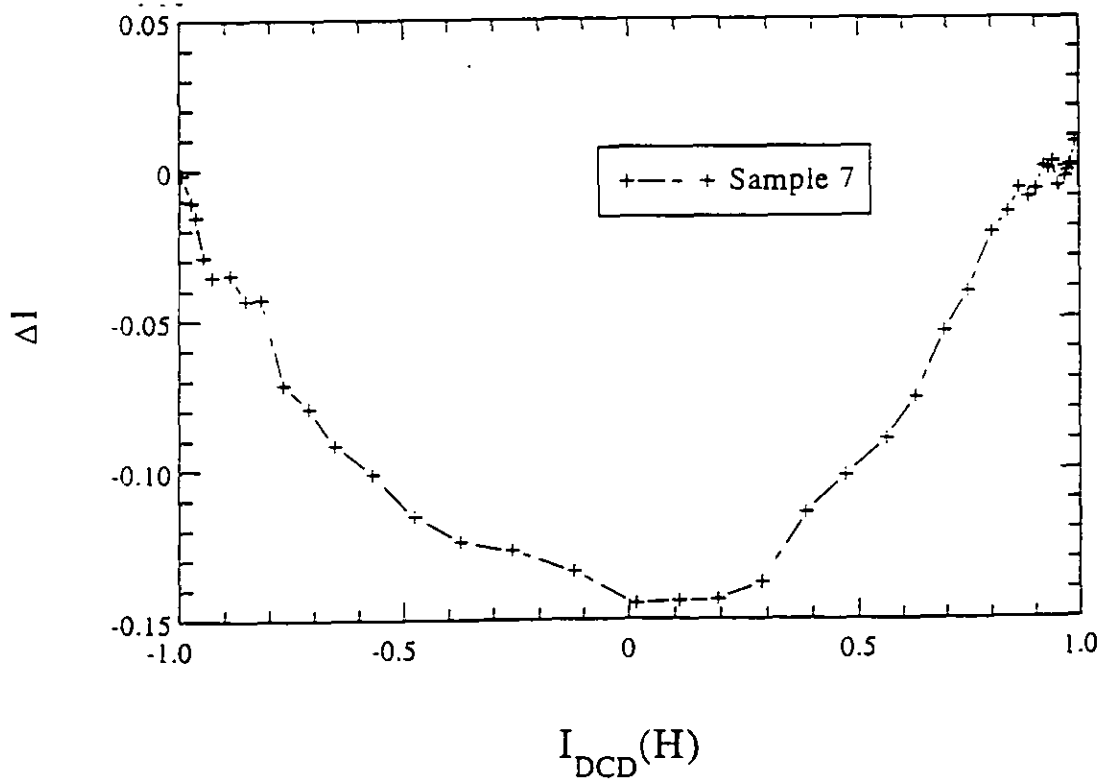


figure (4-7): ΔI deviation for the metal particle sample as a function of the normalised DCD remanence

Corradi and Wohlfarth [26] proposed an analytical technique for the measurement of the interaction field strength in a region around coercivity. This measure defined as the Interaction Field Factor (IFF) was determined from the coercivity H_C of the media, its DCD remanent coercivity H_R and its IRM remanent coercivity H_R' . The IFF was defined analytically as

$$IFF = \frac{(H_R - H_R')}{H_C} * 100 \%. \quad (4-8)$$

The IFF can indicate both negative and positive interactions. Negative interactions are represented by a positive IFF, while positive interactions are represented by negative IFF. Since IFF is a measure of the interactions around coercivity it can be a useful numerical parameter for the comparison of particulate media. The IFF results for the samples investigated are presented together with the calculated Δ (plot area) in table (4.2).

Sample type	Sample No	IFF %	Δ (plot area)
γ -Fe ₂ O ₃ particulate media	1	11.0±4.9	-0.343
	2	10.4±4.2	-0.400
	3	10.3±3.5	-0.413
CrO ₂ particulate media	4	8.7±2.9	-0.346
	5	7.2±1.9	-0.300
	6	7.5±2.9	-0.331
Sony metal particle tape	7	4.4±1.0	-0.182

table (4-2): Δ (plot area) of samples investigated.

A direct comparison between the Δ (plot area) and IFF values was performed in figure (4-8). The results showed that IFF value and the Δ (plot area) gave similar indications of the interaction effects within the media. The results also indicate a linear relationship between the Δ (plot area) and the IFF value. These results are in agreement with the work by Bottoni *et al.* [24] who measured coercivity as a function of

Δ (plot area) and found similar characteristics to Corradi *et al.* [26] who measured coercivity as a function of IFF.

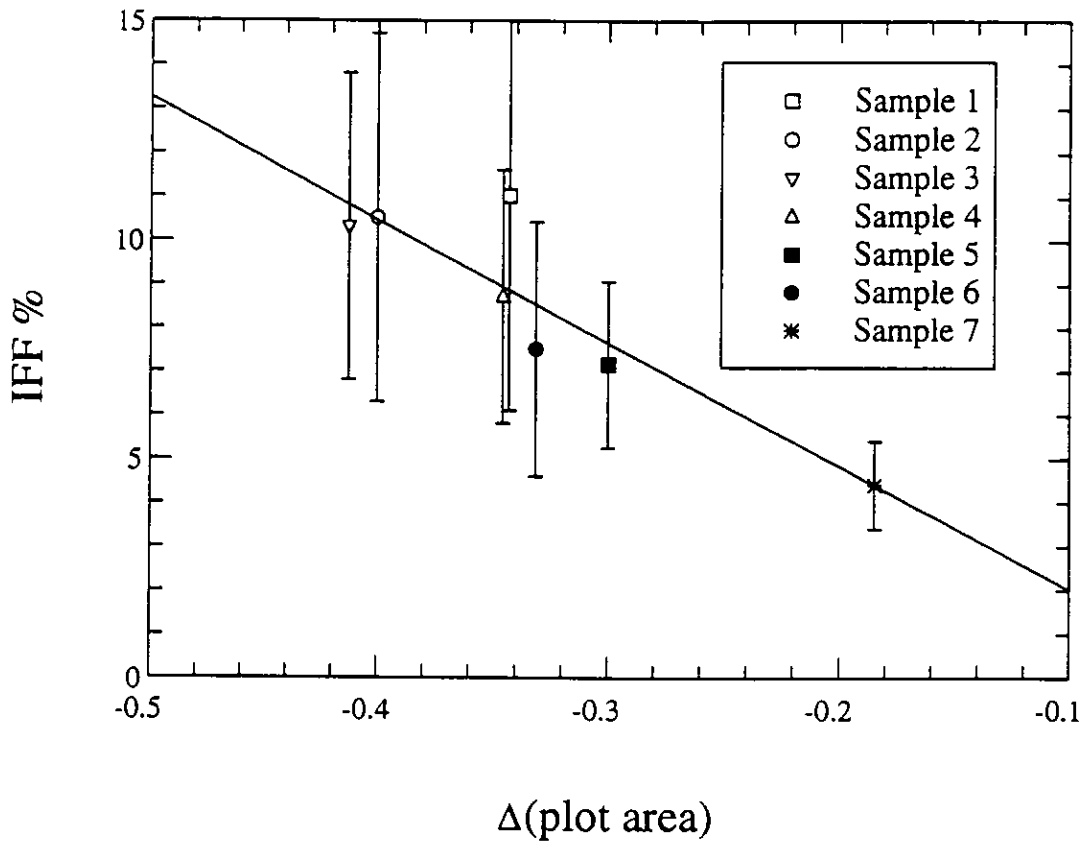


figure (4-8): IFF as a function of the Δ (plot area).

4.5 In-plane, Easy Axis Distribution Measurements of the Media

The orientation of particles within a media is referred to as its Easy Axis Distribution (EAD). The EAD in and out of the plane of the sample are important parameters in its characterisation, as they affect its squareness and its SFD. A medium with randomly orientated particles has a squareness approaching 0.5 with a broad SFD. A media with these characteristics would have poor recording properties, characterised by a wide transition width reducing data densities and a small replay signal.

The EAD within the plane of a media was determined by a technique developed by Flanders *et al.* [27]. The measurement technique implemented by Schmidlin *et al.* [5] utilises a bi-axial VSM that allows the measurement of the moment from a sample to be made both in the field direction and orthogonal to it. The VSM also has the ability to

rotate the sample. The calibration sample for this VSM was a disc lying in the measurement plane. This avoided any angular variation in the calibration as a sample rotated with respect to the pick up coils within the VSM. The samples used throughout all measurements were also circular discs lying in the measurement plane.

Initially, the easy axis centre of the sample, its EAD direction was determined. The sample was saturated in a large magnetic field, the field was removed and the remanent magnetisation in the field direction was measured. This step was repeated at different sample orientations until a maximum remanent magnetisation in the applied field direction was achieved, this identified the EAD centre ($\alpha=0.0$) of the sample.

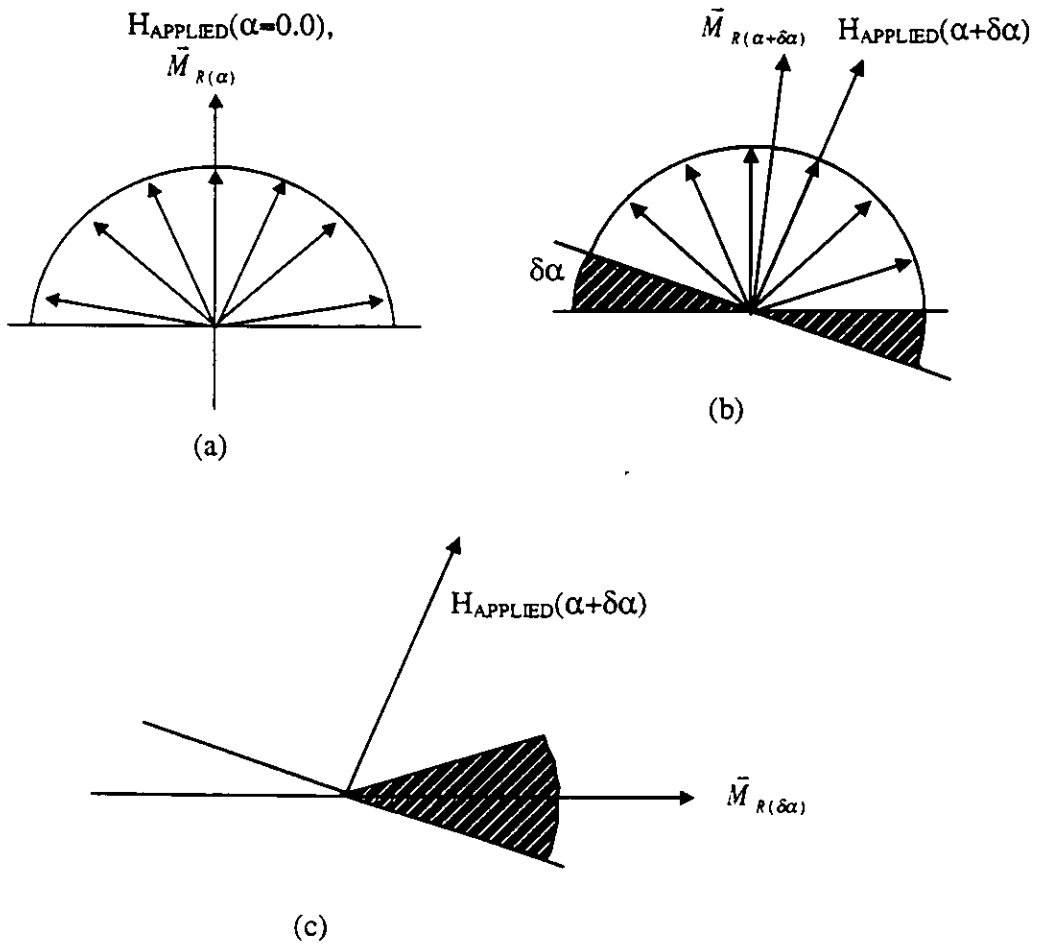


figure (4-9): Schematic representation of particles orientated within a media (a) after the application of a saturation field in the easy axis centre $\alpha=0.0$, (b) after the application of a saturation field at an angle $\alpha+\delta\alpha$, (c) the switched remanent magnetisation of the moment between applied saturating field directions of α and $\alpha+\delta\alpha$.

Once the centre of the EAD had been identified the experimental procedure to determine the EAD of the sample was implemented. The sample was saturated with a large magnetic field in its easy axis centre, so all the particles are switched into the field direction, diagram (a) in figure (4-9). The vector remanent magnetisation of the sample was measured $\vec{M}_{R(\alpha)}$. The sample was rotated in its plane by an angle $\delta\alpha = 2.0^\circ$ and again saturated with a large magnetising field. When the field was removed all the particle moments within the sample occupied the easy axes directions closest to the saturating field direction, indicated as diagram (b) in figure (4-9). The shaded area within this diagram represented the switched moments from consecutive saturating applied field directions α to $\alpha + \delta\alpha$. The remanent magnetisation as a function of the sample orientation was measured until a maximum was achieved, this identified the samples vector remanent magnetisation. The vector remanent magnetisation $\vec{M}_{R(\delta\alpha)}$ of the moments switched from consecutive saturating applied fields, indicated as diagram (c) in figure (4-9) was determined by the subtraction of the remanent magnetisation vectors $\vec{M}_{R(\alpha)}$ and $\vec{M}_{R(\alpha + \delta\alpha)}$.

$$\vec{M}_{R(\delta\alpha)} = \vec{M}_{R(\alpha + \delta\alpha)} - \vec{M}_{R(\alpha)}. \quad (4-9)$$

The magnitude of $\vec{M}_{R(\delta\alpha)}$ between angles α and $\delta\alpha$ represented a measure of the particles that lay with their easy axes within those angles. By subsequently repeating the measurement process for an incremental increase in α from 0° to 180° , the EAD for the sample could be obtained in that measurement plane.

Typical results are presented in figure (4-10) for sample 2, a $\gamma\text{-Fe}_2\text{O}_3$ sample. The measured results have been fitted by a Lorentzian distribution to obtain a numerical measure of the distribution width,

$$f(\alpha) = \frac{g\gamma^2}{(\alpha^2 + \gamma^2)}. \quad (4-10)$$

Here $f(\alpha)$ represents the magnitude of the EAD, α represents the angle in-plane with respect to the samples easy axis direction, γ gives the width of the distribution and g is a curve fitting parameter. The decision to use this particular function was that it

followed work by Templeton *et al.* [28] and Schmidlin *et al.* [5]. Their work indicated that the function gave a good fit to the in-plane EAD of particulate recording media.

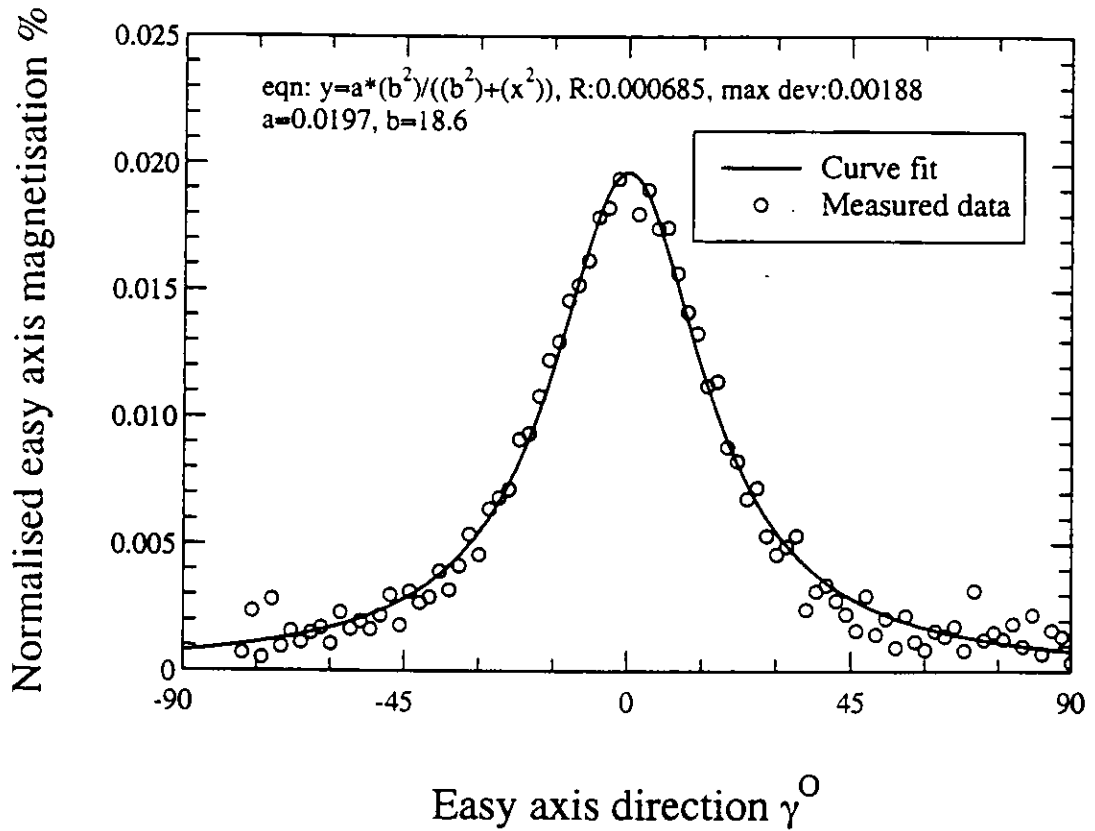


figure (4-10): Measured and curve fitted in-plane easy axis distribution for sample 2.

The measured EAD of sample 2 indicated that as the examined particles easy axis direction extended past the sample's distribution width parameter the measured signal became increasingly noisy; this was of a direct consequence of the measurement technique. At angles increasing further away from the EAD direction the amount of particles switched from consecutive saturating applied field directions becomes increasingly small and the background noise within the system starts to dominate.

Results from the in-plane EAD Lorentzian curve fits for the samples investigated are presented in table (4-3).

Sample type	Sample No	Distribution width γ (degrees)
γ -Fe ₂ O ₃ particulate media	1	32.1
	2	18.3
	3	20.0
CrO ₂ particulate media	4	19.4
	5	16.5
	6	15.7
Metal particle media	7	21.0

table (4-3): Lorentzian distribution widths of investigated samples.

These EAD results indicated similar distribution width parameters γ for all the samples investigated, apart from sample 1. This indicated that sample 1 has a poor particle alignment when compared with the other samples investigated. This confirms the low value of the in plane orientation ratio calculated for sample 1 in section 4.2.

In theory it should be possible to measure the out-of-plane EAD for a sample using this technique if the demagnetising field can be calculated during the experiment and compensated for. However, this has been difficult to achieve since if there is any miscalculation of the demagnetising field at any angle, the accuracy of the measured vector magnetisation at that angle will be incorrect. This inaccuracy will compound and invalidate the measurements of the vector remanent magnetisation at all subsequent measurement angles. As it was not possible to measure the out-of-plane EAD the orientation ratio has been investigated as a measure of the EAD within the samples.

The in-plane EAD width (γ) of a media can be linked to its orientation ratio in-plane $OR(I) = Sq(I)/Sq(T)$ by its EAD function $f(\alpha)$. The squareness at an angle in plane (ϑ) away from its EAD centre can be calculated using the distribution $f(\alpha)$ through the summation of its moments contribution to the samples remanence [5].

$$Sq(\vartheta) = \int_{\vartheta-90}^{90} f(\alpha) \cos(\alpha - \vartheta) d\alpha + \int_{90}^{90+\vartheta} f(\vartheta + 180^\circ) \cos(\alpha + \vartheta) d\alpha. \quad (4-11)$$

A calculated orientation ratio as a function of the Lorentzian EAD width parameter γ can be determined using equation (4-11). The angle 180° in the function $f(\alpha + 180^\circ)$ is a consequence of the numerical calculation of the orientation ratio. The calculated and the samples measured in-plane orientation ratio were plotted as a function of the Lorentzian EAD width parameter γ , given in figure (4-11).

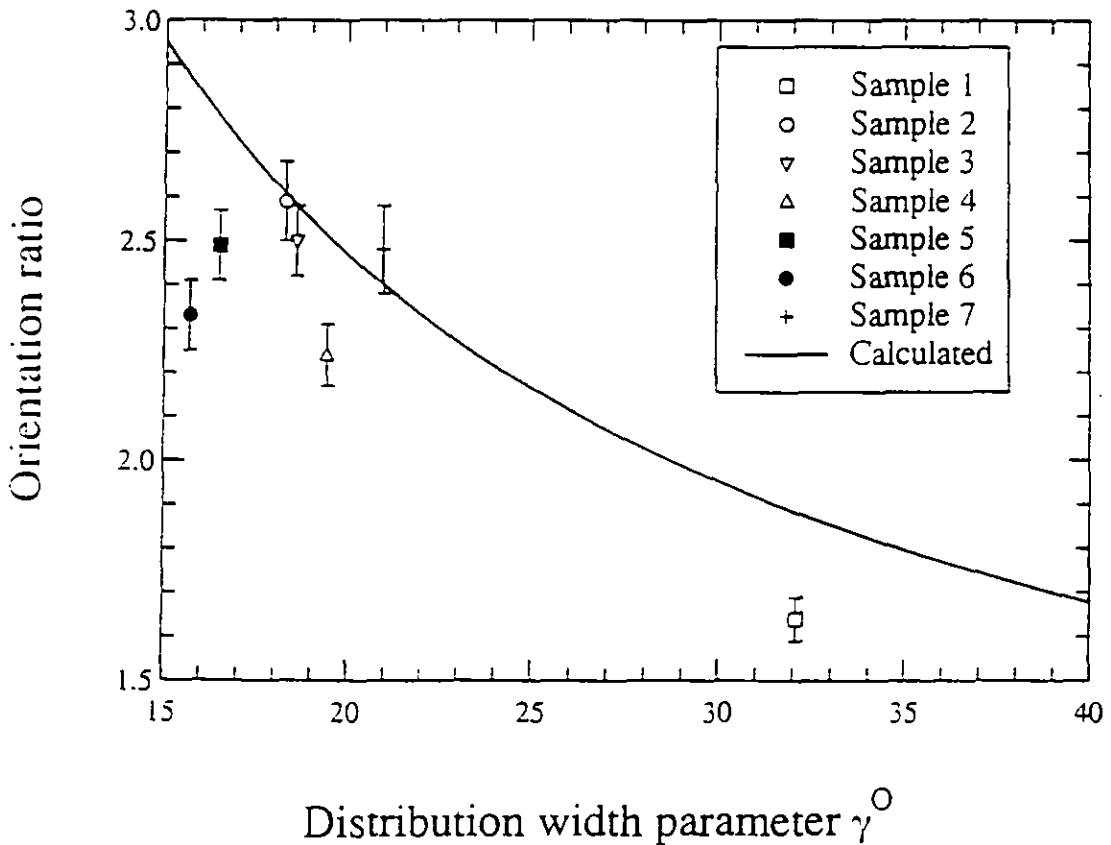


figure (4-11): Comparison between the measured and the calculated in-plane orientation ratio.

The measured in-plane orientation ratio as a function of the distribution width parameter indicates reasonable agreement with the calculated orientation ratio. Although there is some discrepancy between the measured and calculated data this could be attributed in some cases to the errors associated with the Lorentzian distribution curve fit. The calculated orientation ratio also indicates that as EAD of a media becomes increasingly narrow, the orientation ratio as a measure of the EAD improves. This would seem to suggest that for highly orientated systems the orientation ratio would be a good measure of its EAD.

The out-of-plane orientation ratio for a medium can be evaluated and used to derive an out-of-plane EAD if the demagnetising field out-of-plane can be calculated. The demagnetising field is dependent on the thickness of the medium and its absolute magnetisation, as described in chapter 1,

$$H_d = N_d M . \quad (4-12)$$

With the evaluation of the sample's orientation ratio out-of-plane a Lorentzian distribution width parameter could be calculated and a EAD could be proposed. The absolute magnetisation of the sample was thus investigated using a technique derived from transverse susceptibility measurements.

4.6 Transverse Susceptibility theory and measurements

Transverse susceptibility (χ_t) essentially measures the AC susceptibility of a material as a function of the applied DC field perpendicular to the AC field direction. χ_t has been found experimentally [3] and theoretically [29,30] to give sharp peaks at the anisotropy field and at its coercivity. The experimental technique to measure the anisotropy field of a sample is indicated in figure (4-12). It consists of a static applied DC field perpendicular to the EAD of the sample with a small probing AC field in the EAD axis direction.

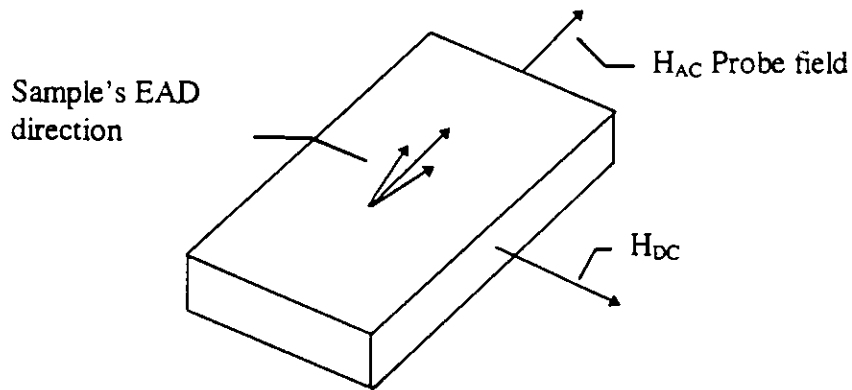


figure (4-12): Transverse susceptibility experimental configuration.

The AC susceptibility of a sample is measured as a function of the static DC field within the AC field direction. The AC probe field (~ 1600 A/m) examines the energy profile within the sample by inducing oscillations in its moment which are measured by search coils. As the DC field approaches the anisotropy field, a broad energy minimum is created that allows the moment of the sample to have large oscillatory displacements within the AC field direction. These displacements become a maximum at the anisotropy field. If the DC field is increased further the broad energy minimum reduces dissipating the moments displacement within the AC field. The χ_t response was measured for each sample by sweeping the applied DC field to positive saturation, then negative saturation and then back to positive saturation. An example of the results for a CrO_2 tape, sample 4 is given in figure (4-13). This figure indicates the anisotropy field of the sample, the parameters $\chi_T(\text{max})$ and $\chi_T(H=0)$, which have been used in a ratio as a measure of the anisotropy peaks prominence [31].

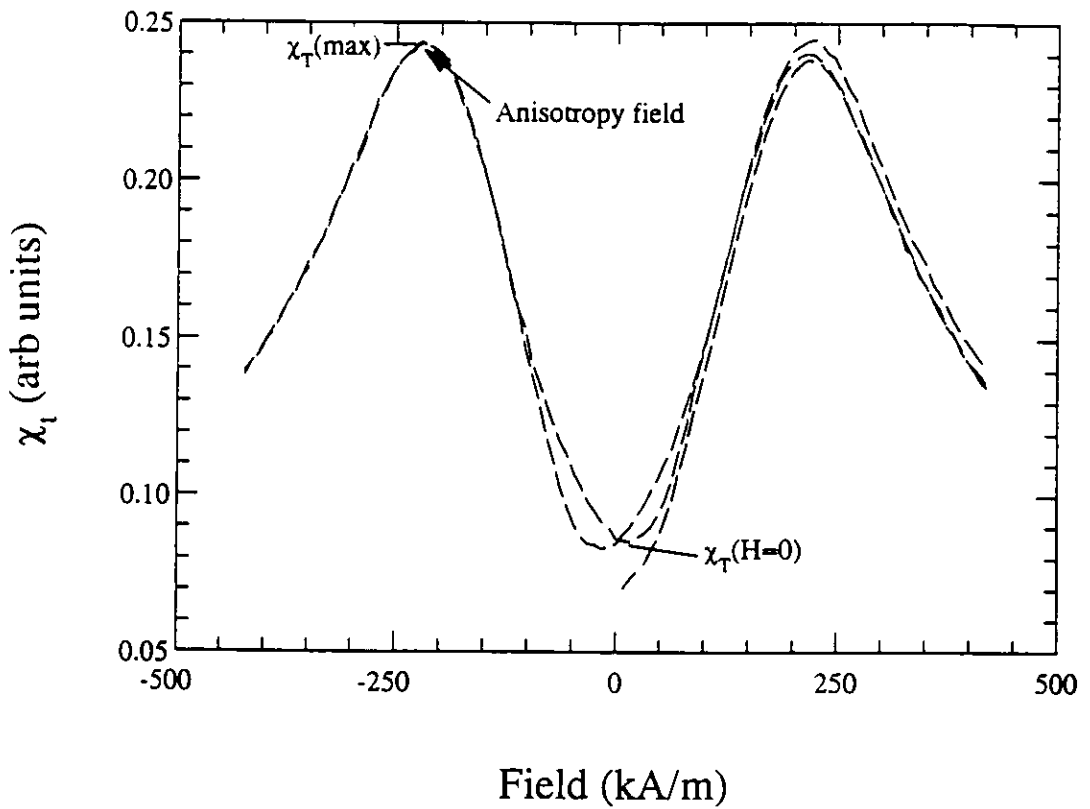


figure (4-13): χ_T measurement of a CrO_2 tape, sample 4.

4.6.1 The absolute magnetisation measurement of the samples

Measurement of the absolute magnetisation of a sample requires measurement of its moment and its volume. The moment and its surface area are easily determined; however, the sample thickness is not. As a consequence of this difficulty, Sollis and Bissell in 1991 [32] proposed a technique based on χ_t measurements in association with VSM measurements to determine the sample thickness and its absolute magnetisation.

As stated earlier, χ_T measures the AC susceptibility of the sample as a function of DC field perpendicular to the AC probe field direction. The determination of the demagnetising field within the sample was achieved by measurement of the χ_T in different DC field configurations. In configuration A the χ_T response was measured with the DC field in-plane and perpendicular to the EAD of the sample with the AC field in-plane and in the EAD direction of the sample, indicated in figure (4-14). In configuration B the χ_T response was measured in a similar configuration to A, but in this case the DC field was out-of-plane and perpendicular to the EAD direction of the

sample, indicated also in figure (4-14). These configurations respectively investigated the anisotropy field, and the anisotropy field in conjunction with the out-of-plane demagnetising field.

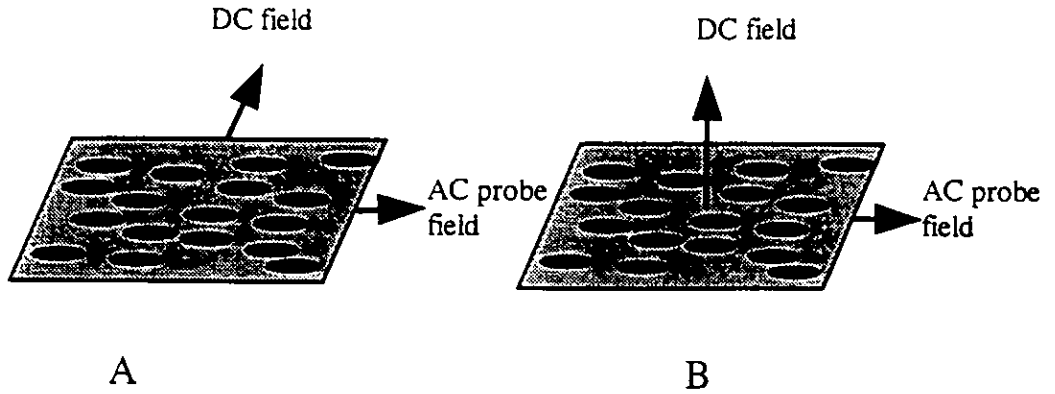


figure (4-14): Transverse susceptibility configurations.

The χ_T responses from both configurations were investigated as a function of the applied DC field from positive saturation to zero applied field. This region of the χ_T response avoids coercivity effects, it only examines the relaxation of moments to their easy axes directions. The graph in figure (4-15) represents this part of the curve in both DC field configurations for sample 2.

It was observed that the effect of the DC field out-of-plane was to shift the χ_T peak at H_1 , configuration A, to the higher field value H_2 , configuration B. Since the AC field is in the same orientation for both configurations, the peak shift must be mainly attributed to the demagnetising field, H_d , perpendicular to the plane of the sample. The demagnetising field in this case can be written as

$$H_2 - H_1 = H_d = N_d M_2 = M_2, \quad (4-13)$$

where N_d is the demagnetising factor perpendicular to the sample plane and is equal to 1, the value for a sheet, M_2 is the magnetisation of the sample at field H_2 applied perpendicular to the sample plane.

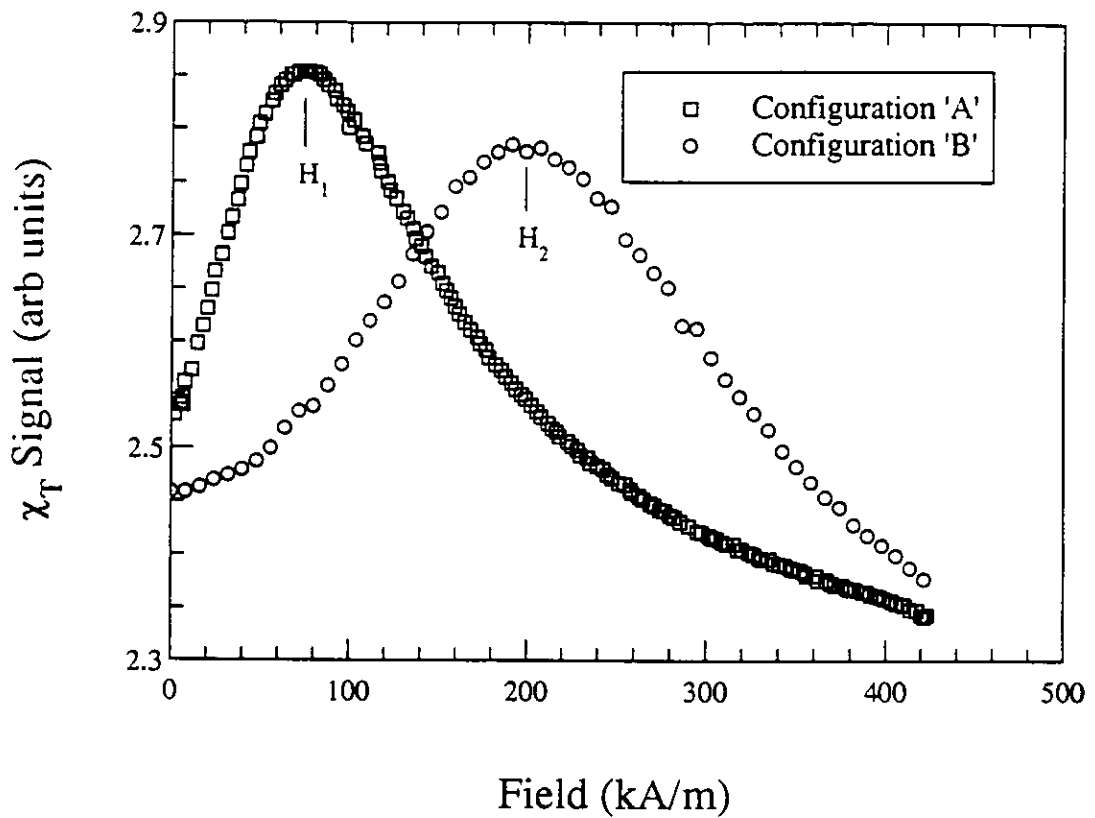


figure (4-15): χ_T response for sample 2 as function of an applied DC field from saturation to zero applied field in configurations A and B.

For $\gamma\text{-Fe}_2\text{O}_3$ sample 2 the value of the peak positions H_1 and H_2 were $73.6 \pm 2.8 \text{ kA/m}$ and $191.4 \pm 7.4 \text{ kA/m}$ respectively. The anisotropy peak position was measured from both positive and negative saturation to zero applied DC field. The mean of these two values was determined and the maximum discrepancy between the calculated mean and the measured value was taken as the error in the measured anisotropy peak position. The calculated value of the demagnetising field was $117.8 \pm 6.4 \text{ kA/m}$, where the value of the demagnetising factor was assumed to be error free.

To determine the absolute magnetisation of a sample the VSM had to be calibrated for the sample geometry, with the sample plane perpendicular to its applied field direction. The magnetisation of the sample was determined by measuring its magnetisation at the applied field H_2 with the sample orientated, so that its plane was perpendicular to the applied field direction.

The absolute saturation magnetisation of the sample $M_S(sample)$ was derived by

$$M_S(sample) = \frac{M_2}{\left(\frac{M}{M_S}\right)_{H_2}} \quad (4-14)$$

The determined value of $M_S(sample)$ was $140.2 \pm 7.8 \text{ kA/m}$, where M_2 was $117.8 \pm 6.4 \text{ kA/m}$ and $\left(\frac{M}{M_S}\right)_{H_2}$ was 0.84 ± 0.01 .

The derived absolute saturation magnetisation of the sample M_S , its moment $\mu_s = 0.670 \pm 0.013 \times 10^{-3} \text{ Am}^2$ and its area, $A = 12 \text{ cm}^2$ were used to determine its thickness,

$$t = \frac{V}{A} = \frac{\mu_s}{M_S(sample) A} = 4.0 \pm 0.2 \mu\text{m}$$

The accuracy of this technique was addressed in the work by Sollis and Bissell [32]. They determined that the assumption of 1 for the demagnetising factor was a good approximation for a particulate recording media, where film thickness is small, of the order $\sim 5 \mu\text{m}$ and has good thickness uniformity. The assumption, that the peak was only affected by the demagnetising field was more problematic. If it is assumed that the EAD within the sample had cylindrical symmetry, then the only effective difference between the χ_T response of both configurations was the effect of the demagnetising field. In particulate media, however, there is a likelihood that there is a difference between the EAD in and out-of-plane.

In the recent work by Sollis *et al.* [33] the effect of EAD on the anisotropy peak had been addressed. Their work concerned the dependence of EAD and interaction fields on the anisotropy peak in CrO_2 and $\text{Co-}\gamma\text{-Fe}_2\text{O}_3$ particle samples. The magnetic properties were investigated for a range of samples; these included a pseudo random hand spread (PRHS), a powder (P), a dried dispersion (DD) and an aligned hand spread (AHS). The pseudo random hand spread was prepared by stacking 40 discs in groups of 5 cut from the aligned hand spread with their alignment directions 22.5° apart, thus resulting in 8 easy axis directions within the sample. A selection of the results from their investigation are presented here in table (4-4).

Sample	Sq	IFF (%)	H _K (kOe)	$\chi_{T(H_{max})}$ / $\chi_{T(H=0)}$
CrO ₂ (P)	0.46	18.2	2.59	1.12
CrO ₂ (DD)	0.49	19.7	2.59	1.16
CrO ₂ (PRHS)	0.57	9.2	2.53	1.21
CrO ₂ (AHS)	0.82	13.5	2.81	3.58

table (4-4): Magnetic properties of the samples investigated by Sollis *et al.* [33].

For the CrO₂ AHS sample they found its anisotropy peak position and its $\chi_{T(H_{max})}/\chi_{T(H=0)}$ values were ~11% and ~308% greater than for the unaligned samples. It was reported that the packing densities were similar in all the samples, suggesting similar interaction fields. The measured IFF values indicated negative interactions with no observable correlation between the samples anisotropy field. As the only other major difference between the aligned and unaligned samples was their EAD, it was proposed that EAD within the sample does affect the anisotropy peak, its position and prominence.

In particulate media it is unlikely there would be an out-of-plane random particle distribution. It is more likely that there would be cylindrical symmetry within the media or even a narrower distribution out-of-plane through the action of the coating process. As a consequence, the difference between the in-plane anisotropy peak position and the out-of-plane anisotropy peak position corrected for the demagnetising field could be considered negligible. This assumption has been verified experimentally by Sollis [34], who compared the derived media thickness using χ_t measurements with the physical measurement of the thickness using a talysurf. The results showed reasonable agreement between both techniques for the determination of the media thickness.

In determining the absolute saturation magnetisation of a sample $M_S(\text{Sample})$ it is possible to determine the packing density P within the media if the bulk saturation magnetisation $M_S(\text{particle})$ of the particles are known,

$$P = \frac{M_S(\text{tape})}{M_S(\text{particle})} \quad (4-15)$$

For an approximate measure of the packing density within the samples investigated bulk saturation magnetisation value were taken from the literature, 338kA/m for $\gamma\text{-Fe}_2\text{O}_3$, 365kA/m for CrO_2 and 985 kA/m for metal (iron) [35-37].

The results for all the samples investigated, their saturation magnetisation, their magnetic media thickness and their packing density are presented in table (4-5).

Sample type	Sample No	Saturation magnetisation $M_s(\text{sample})$ kA/m	Tape thickness t μm	Packing density P
$\gamma\text{-Fe}_2\text{O}_3$ particulate media	1	105.0±5.5	11.8±1.1	0.30±0.02
	2	140.2±7.8	4.0±0.2	0.42±0.02
	3	135.6±14.0	4.2±0.4	0.40±0.04
CrO_2 particulate media	4	121.1±2.7	3.4±0.2	0.34±0.01
	5	174.6±4.7	4.2±0.2	0.47±0.01
	6	106.4±4.8-	4.8±0.8	0.29±0.01
Metal particulate media	7	369.7±11.1	1.3±0.1	0.37±0.01

table (4-5): Sample parameters derived from the samples saturation magnetisations.

4.7 Evaluation of the overall Easy Axis Distributions for the samples

Through the investigation of the orientation ratio in-plane and the measured EAD for the samples, it was shown that the orientation ratio of a sample gave a reasonable numerical measure of its EAD. A similar orientation ratio out-of-plane can be evaluated to investigate the out-of-plane EAD. However, this orientation ratio $Or(O)$ is more difficult to determine, since the demagnetising field must be compensated in the out-of-plane hysteresis loop, before the its squareness can be measured.

The orientation ratio out-of-plane is defined as

$$Or(O) = Sq(I) / Sq(O), \quad (4-16)$$

where $Sq(O)$ is the out-of-plane squareness corrected for the demagnetising field. The correction of the demagnetising field for the out-of-plane hysteresis loop was achieved by the transformation of its hysteresis loop by

$$H_{EFF} = H_{APPLIED} - N_d \left(\frac{M}{M_S} \right) M_S, \quad (4-17)$$

where H_{EFF} represents the field the sample experiences corrected for the demagnetising field, $H_{APPLIED}$ is the applied field exerted by the VSM, (M/M_S) is the normalised hysteresis loop magnetisation, M_S is the saturation magnetisation of the sample and N_d is the demagnetising factor of a magnetised sheet. The errors associated with this transformation are the measured accuracy of the sample's saturation magnetisation, the measured moment, the applied field, the sample alignment within the VSM and the assumption of the samples demagnetising factor.

An example of the measured out-of-plane hysteresis loop and the demagnetising field corrected loop for sample 2 can be found in figure (4-16). The effect of the correction is twofold, the squareness of the loop increased and the effective maximum field exerted on the sample was reduced. As an attempt to quantify the error in the corrected out-of-plane squareness the transformation was performed with the maximum errors associated with the transform parameters to give the largest variation in the determined out-of-plane squareness. The determined squareness out-of-plane and transverse to the EAD direction for sample 2 was 0.83 ± 0.01 and 0.32 ± 0.04 respectively. This gave an out-of-plane orientation ratio of 2.67 ± 0.35 .

The calculated orientation ratio in and out-of-plane for all the samples investigated are presented in figure (4-17). These results are near the reflection $y=x$ indicating the EAD of the media has cylindrical symmetry, this is in agreement with other research [38] on particulate recording media.

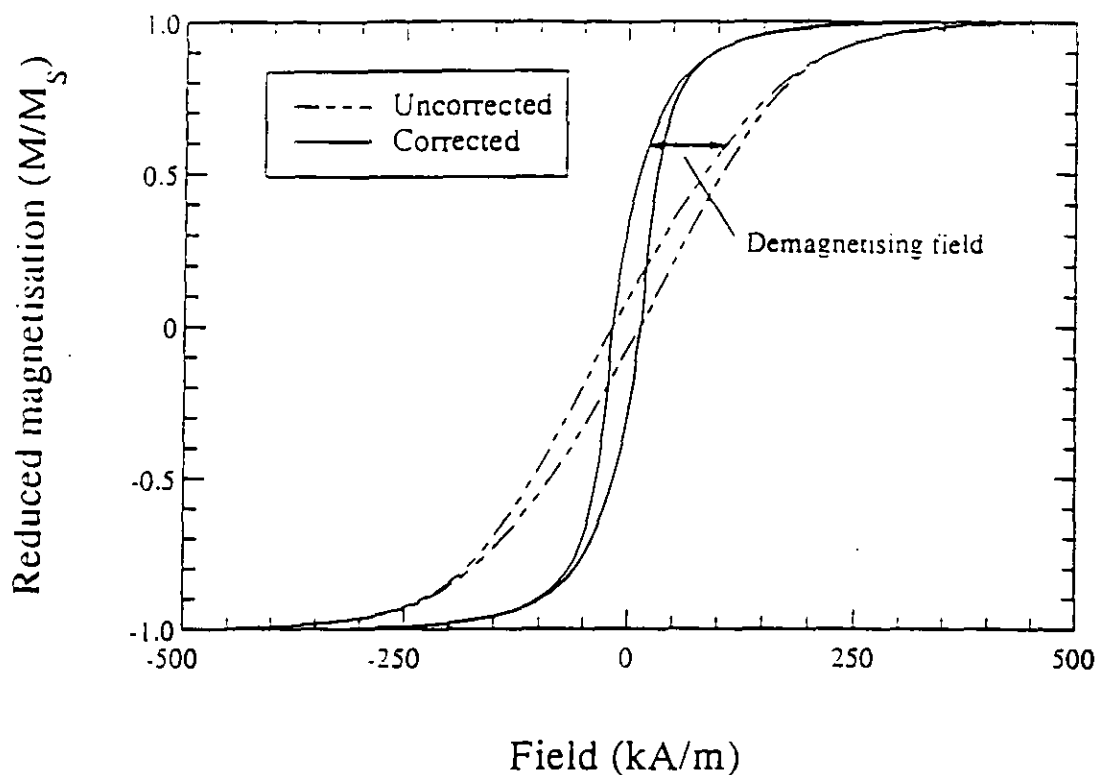


figure (4-16): Out-of-plane hysteresis loop of sample 2 corrected and uncorrected for the demagnetising field.

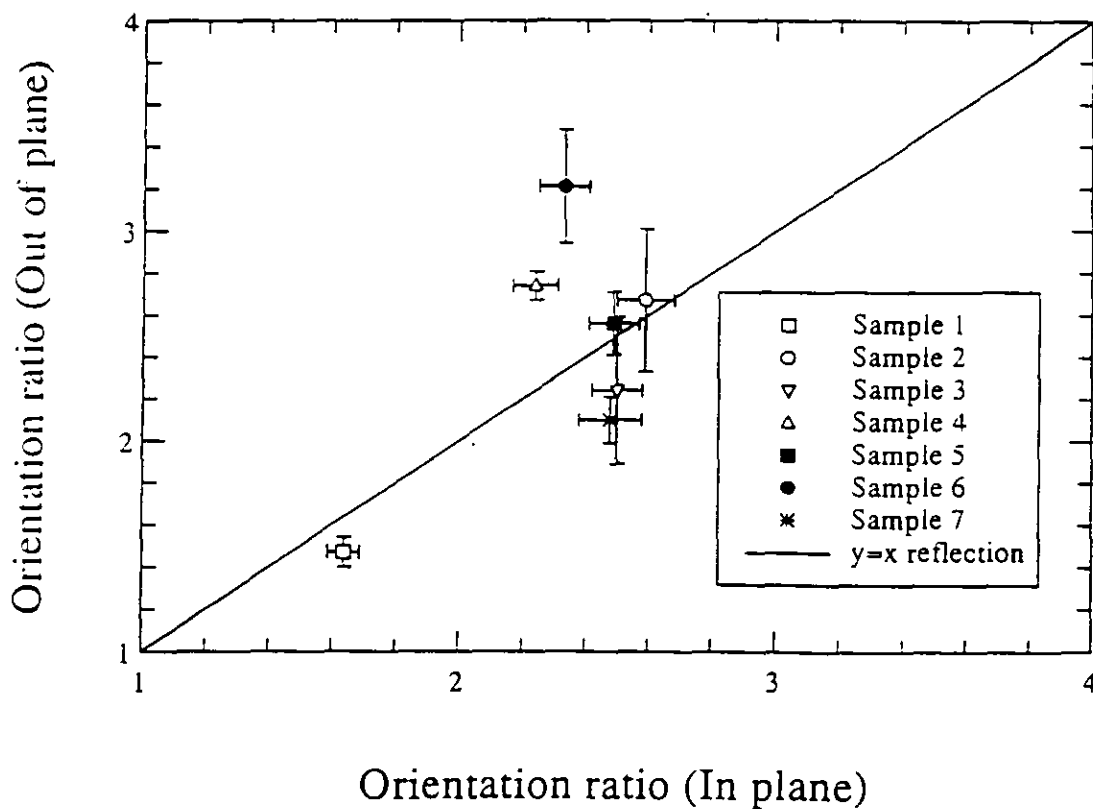


figure (4-17): Measured orientation ratio in and out-of-plane.

The orientation ratio out-of-plane was compared directly with the calculated orientation ratio assuming a Lorentzian distribution given in figure (4-11). This allowed the determination of a theoretical out-of-plane distribution width. With this distribution width, a Lorentzian distribution representing the out-of-plane EAD of the sample was proposed. The out-of-plane distribution width parameters (η) for most of the samples investigated were similar ~20 degrees. The distribution width parameters for all the samples are presented in table (4-6).

Assuming the EAD for the sample in and out-of-plane are not correlated, then a 3D representation of the EAD can be obtained. This was achieved by multiplication of the Lorentzian distribution functions that represented the measured EAD in-plane and the derived out-of-plane EAD.

With sample 2 as an example, its in-plane distribution can be written as

$$f(\alpha) = \frac{(18.3)^2}{(\alpha^2 + (18.3)^2)}, \quad (4-18)$$

and its out-of-plane distribution can be written as

$$g(\beta) = \frac{(18.7)^2}{(\beta^2 + (18.7)^2)}. \quad (4-19)$$

Here $f(\alpha)$ represents the EAD in-plane, $g(\beta)$ the EAD out-of-plane, α represents the angle in-plane with respect to the EAD direction and β represents the angle out-of-plane with respect to the EAD direction. The values 18.3 and 18.7 degrees refer to the measured and the derived Lorentzian distribution widths for the sample. The 3D distribution of the particle easy axes within the media was determined by

$$y(\theta, \phi) = f(\alpha)g(\beta), \quad (4-20)$$

where the function $y(\alpha, \beta)$ describes the 3D easy axes distribution within the sample. This function for sample 2 is presented in figure (4-18). The parameters for this sample and the others investigated are presented in table (4-6) and were used throughout the next chapter to derive the interaction effects within the samples.

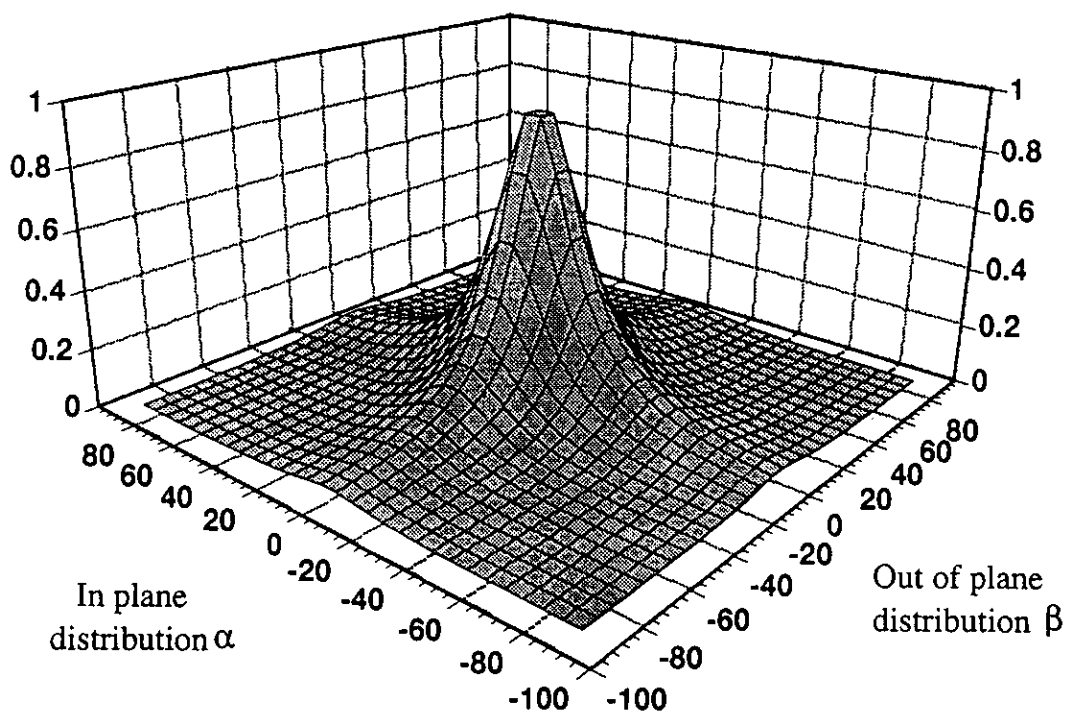


figure (4-18): Easy Axes Distribution for sample 2

Sample type	Sample No	Measured in-plane distribution parameter γ°	Derived Out-of-plane distribution parameter η°
γ -Fe ₂ O ₃ particulate media	1	32.1	53.0±0.7
	2	18.3	18.7±4.8
	3	18.6	25.2±6.8
CrO ₂ particulate media	4	19.4	17.1±2.0
	5	16.5	19.2±1.6
	6	15.7	13.3±1.7
Metal particulate media	7	21.0	26.4±2.6

table (4-6): Measured and derived in and out-of-plane distribution width parameters.

Chapter Five

Derivation and Analysis of Interaction Effects

5.1 Introduction

The magnetic properties of a media are dominated by the characteristics of the particles that compose the media and the interaction effects between these particles. These interaction effects are the result of the action of the magnetostatic field from each particle on the other particles in the media. This field can either demagnetise a particle or aid its saturation depending on the relative positions of all the particles. In particulate media a particle has many near neighbours which can generate a large local interaction field. In the media as a whole, these fields can significantly affect its characteristics, either magnetising or demagnetising the media.

There has been a number of analytical techniques developed from bulk measurements [1-3] for the examination of the interaction effects within particulate media. These techniques such as Henkel and ΔI plots only provide an indication of the sign and magnitude of the interactions, they do not give an absolute measure. An absolute measure of the interaction effects was derived from the individual particle properties, their orientation within the media and the properties of the media. With these parameters the characteristics of the media can be simulated with the interactions effectively “switched off”. A direct comparison between the characteristics of the simulated media with no interactions and the measured media with interactions allowed a direct and absolute measure of the interactions.

5.2 Mathematical simulation of a medium without interactions

The technique combines numerically the measured properties of particles with their angular distribution within the media, i.e. the Easy Axis Distribution (EAD). In combining these data, the characteristics of a medium with the interactions “switched off” can be simulated.

The measured particle characteristics, curve fitted with mathematical functions were reported in chapter 3. The switching field distribution $SFD(\theta=0^\circ)$ of an ensemble of 50 particles was measured and curve fitted with a Gaussian distribution, denoted as equation (3-1) in chapter 3.

$$SFD(\theta = 0^\circ) = \frac{d}{2\pi\sigma} \exp\left\{-\frac{1}{2}(H - H_{MEAN})^2 / \sigma^2\right\} \quad (5-1)$$

Here d represents a curve fitted parameter, σ represents the standard deviation of the switching field distribution and H_{MEAN} the mean of the distribution.

The angular variation H_θ of the particles' switching field within a sample has been measured and curve fitted by equation (3-3) in chapter 3, given as

$$H_\theta = e10^{f\theta}. \quad (5-2)$$

Here e & f represent curve fitting parameters and θ the angle between the easy axis of the particle and the applied field direction.

The Easy axis distribution of particles $y(\alpha,\beta)$ with respect to the EAD direction for a sample was derived in chapter four. The EAD in and out of plane were curve fitted with Lorentzian distributions $f(\alpha)$ and $g(\beta)$,

$$y(\alpha, \beta) = f(\alpha)g(\beta), \quad (5-3)$$

where α represents the angular displacement in plane to the EAD direction and β represents the angular displacement out of plane to the EAD direction.

These three mathematical functions were combined numerically with a number of assumptions to simulate a medium with no interactions. The simulation assumed the angular dependence for all the particles within the sample were the same. The angular

The number of particles that have been switched into the remanent state $\Delta R_{H_2-H_1}$ between the fields H_2 and H_1 was calculated in the quadrant $0^\circ < \alpha, \beta < 90^\circ$ by,

$$\Delta R_{H_2-H_1} = \int_{H_1}^{H_2} \int_0^{\beta=90} \int_0^{\alpha=90} y(\alpha, \beta) SFD(\theta) \cos(\theta) d\alpha d\beta dH, \quad (5-6)$$

$$\text{where } \theta = \tan^{-1}(\sqrt{(\tan \alpha)^2 + (\tan \beta)^2}) \leq 90^\circ.$$

Here α represents the angular displacement in plane to the EAD direction, β represents the angular displacement out of plane to the EAD direction and θ represents the angle between the EAD direction and the angular displacement of the particles. The algorithm that simulates the switching field distribution for a medium with no interactions is indicated in the flow chart in figure (5-1). Before the simulation was performed the mathematical functions representing the particle characteristics and the media characteristics were determined and entered in the program. In the simulation the field H_2 was set and the switched remanence by this field was calculated. The field H_2 was increased, H_1 was set to the previous H_2 , the switched remanence between the fields H_2 and H_1 was calculated and saved. This procedure of incremental increases in the applied field and the subsequent calculation of the switched remanence continued until all the particles had switched.

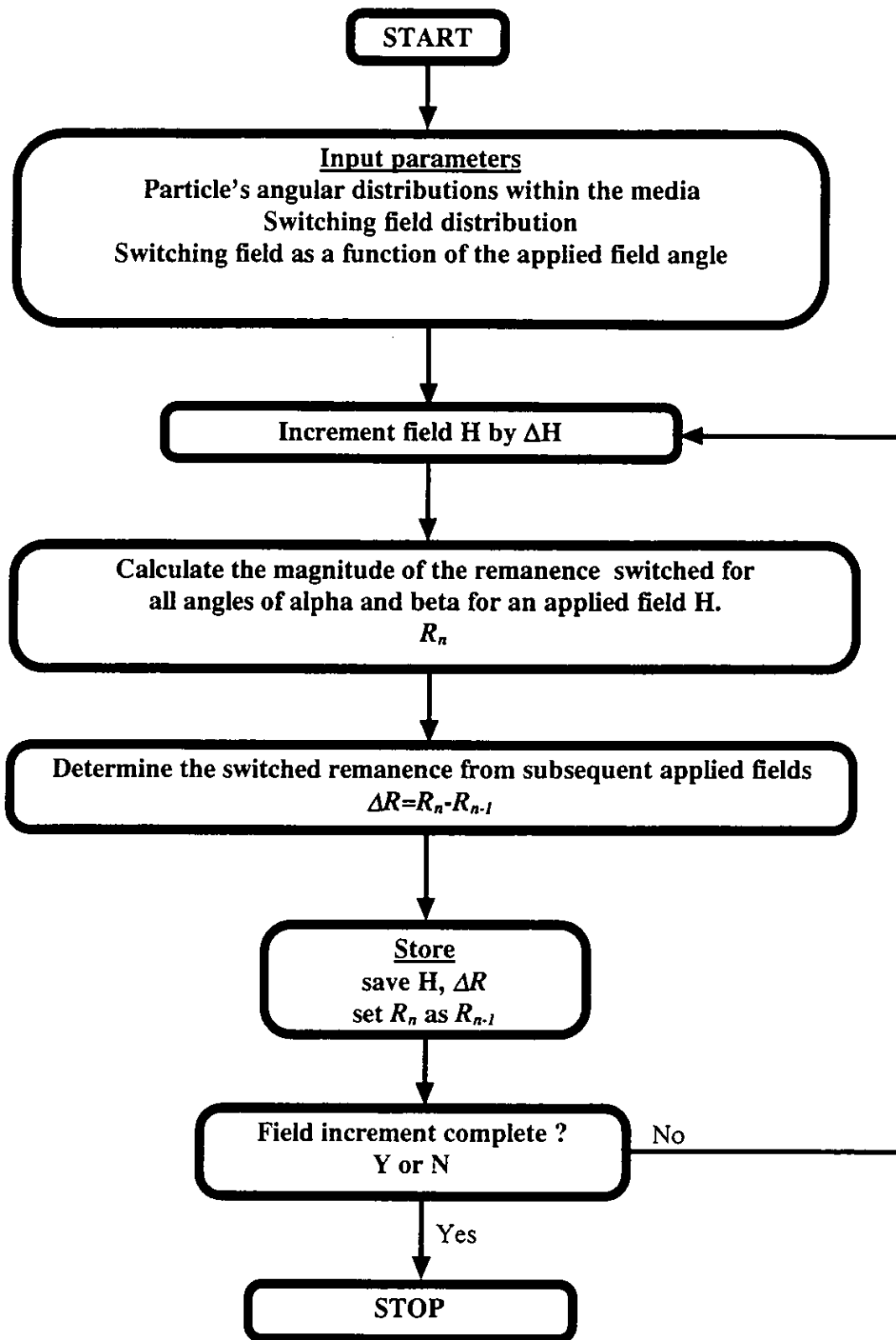


figure (5-1): Flow chart of algorithm to generate the switching field distribution on a non interacting system of particles.

dependence for each sample was reported in table (3-3). Thus, knowing the switching field of a particle at $\theta=0^\circ$ and the angular dependence of particles within a sample it was possible to determine the switching field of a particle at any angle (θ). This was represented mathematically in chapter 3 as equation (3-2), given by

$$H_{TOTAL} = H_{MEAN} + H_{\theta}, \quad (5-4)$$

where H_{MEAN} is the mean switching field of a sample at $\theta=0$, H_{θ} is the switching field angular component of a particle and H_{TOTAL} is the switching field of a particle, definable at any angle θ . The angular component for each sample was reported in table (3-3).

The simulation also assumed the measured switching field distribution $SFD(\theta=0^\circ)$ could be extended to represent a $SFD(\theta)$ at an angle θ . This was achieved by allowing the mean switching field of the distributions to be the switching field of the particle at that angle $\theta=0^\circ$, with the distribution width σ at $\theta=0^\circ$ being set directly proportional to the mean of the distribution. This was represented mathematically as

$$SFD(\theta) = \frac{dH_{MEAN}}{2\pi\sigma H_{TOTAL}} \exp\left\{-\frac{1}{2}(H - H_{TOTAL})^2 / (\sigma H_{TOTAL} / H_{MEAN})^2\right\}. \quad (5-5)$$

With mathematical functions representing the switching field distribution of particles at an angle θ , $SFD(\theta)$, the orientation of particles within the media, $y(\alpha,\beta)$ and the switching field of particles as a function of the applied field angle, H_{TOTAL} , a media with the interactions “turned off” can be simulated.

As the switching field distribution obtained from a media was derived from its IRM curve the mathematical functions $SFD(\theta)$, $y(\alpha,\beta)$ and H_{TOTAL} were used in conjunction with a $\cos(\theta)$ term to simulate the remanence of the media without interactions. By determining the switched remanence for incremental increases in the applied field a switching field distribution for the media can be simulated without interactions.

5.3 Numerical Results and Analysis

The numerical model simulated the sample's switching field distribution SFD_{NUM} without interactions. This SFD was compared directly with the derived SFD from the samples IRM remanence curve, SFD_{EX} . The difference between both SFD's can be directly attributed to the interaction effects within the sample. The results for all the samples investigated were normalised and presented in figure (5-2) through to figure (5-8).

The mean of the numerical SFD, \overline{SFD}_{NUM} and the mean of the experimental SFD, \overline{SFD}_{EX} were determined for all the samples. The difference between the mean of both SFD's within a sample was attributed to an interaction field $\overline{\Delta SFD}_{INT}$. A numerical measure of the strength of the interaction effects was obtained by evaluating the packing density P from the numerical SFD mean and the experimentally determined SFD mean,

$$P = 1 - \frac{\overline{SFD}_{EX}}{\overline{SFD}_{NUM}}. \quad (5-7)$$

For particulate media as the packing density increases the effect of the shape anisotropy is reduced. Thus, there is a reduction in the coercivity of the particles within the media and hence the media itself. The results from equation (5-7) represent the effect of the loss of shape anisotropy and inter-particle interactions within the media. These interactions can either be predominately negative demagnetising the sample, reducing its measured SFD mean or the interactions could be positive, magnetising the sample, increasing its measured SFD mean.

The measured SFD mean of the media, the derived SFD mean of the media, the interaction field and the evaluated packing density for all the samples investigated are presented in table (5-1).

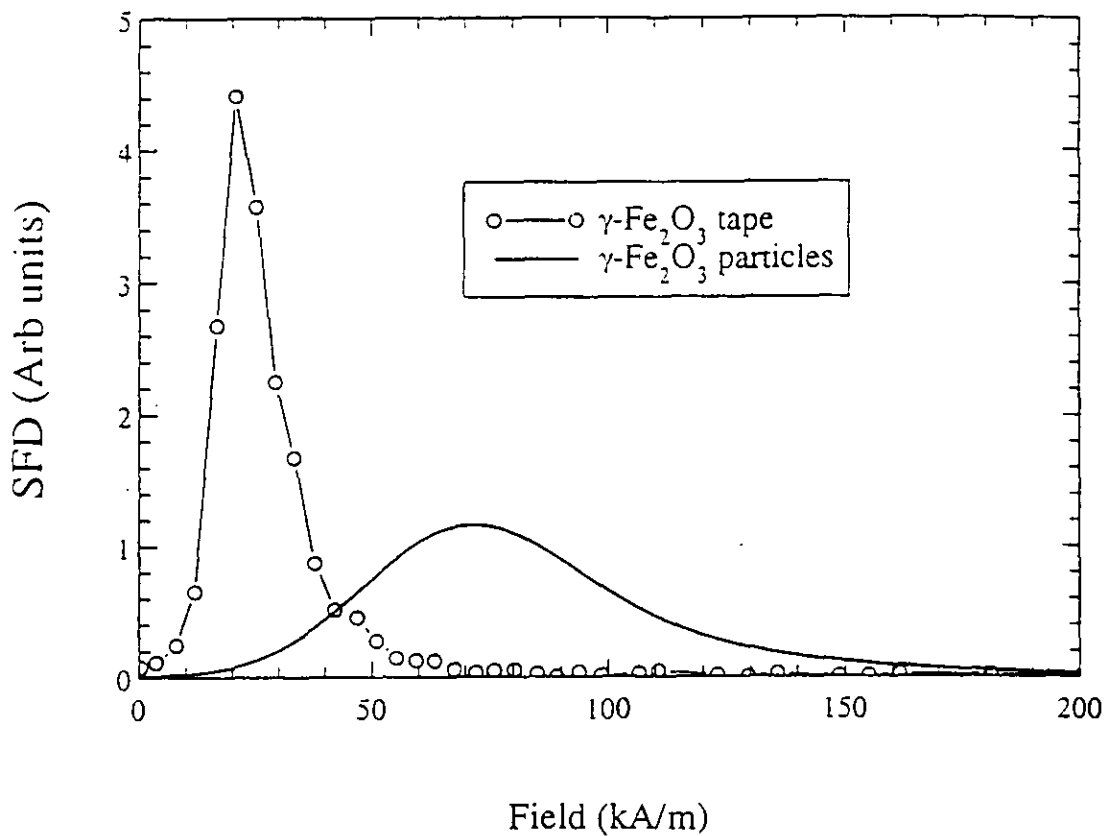


figure (5-2): Switching field distributions with and without interactions for sample 1.

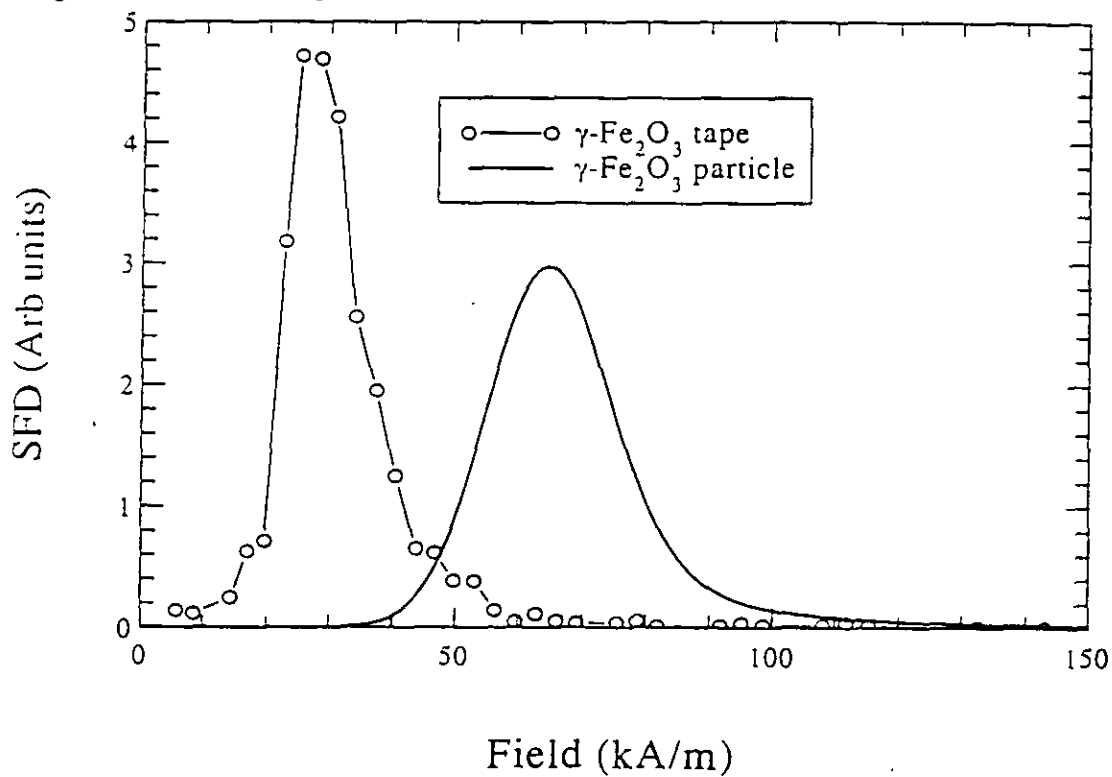


figure (5-3): Switching field distributions with and without interactions for sample 2.

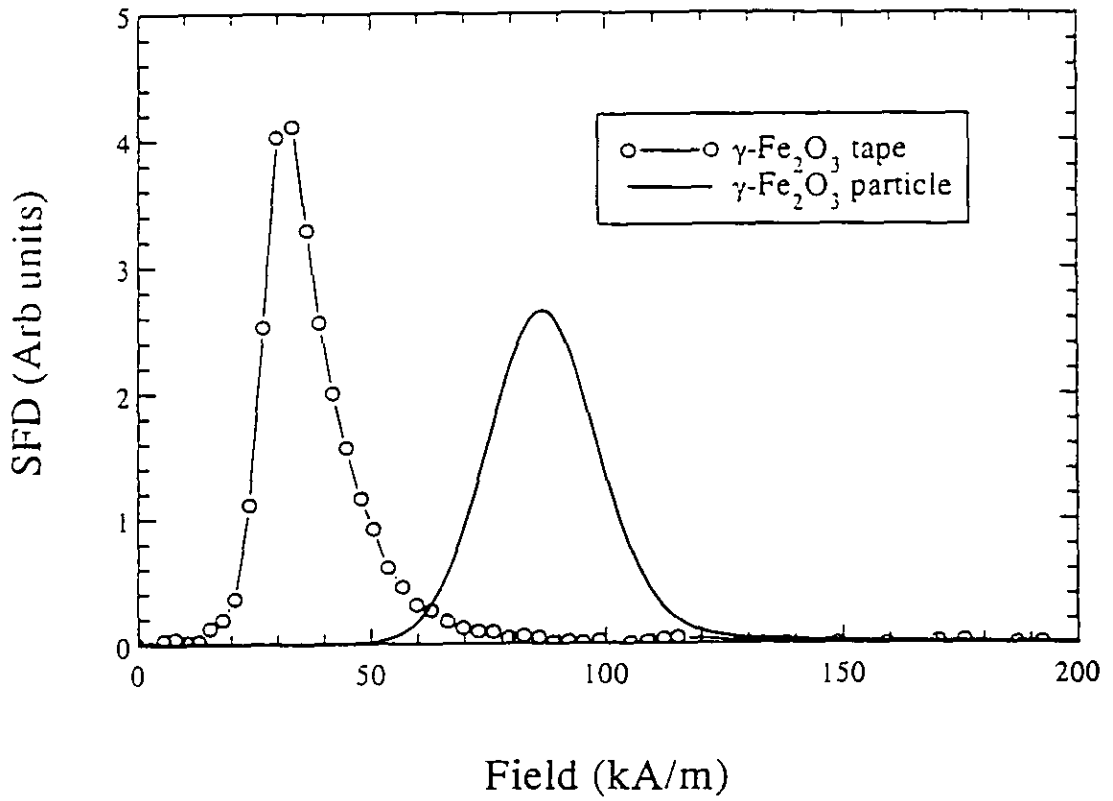


figure (5-4): Switching field distributions with and without interactions for sample 3.

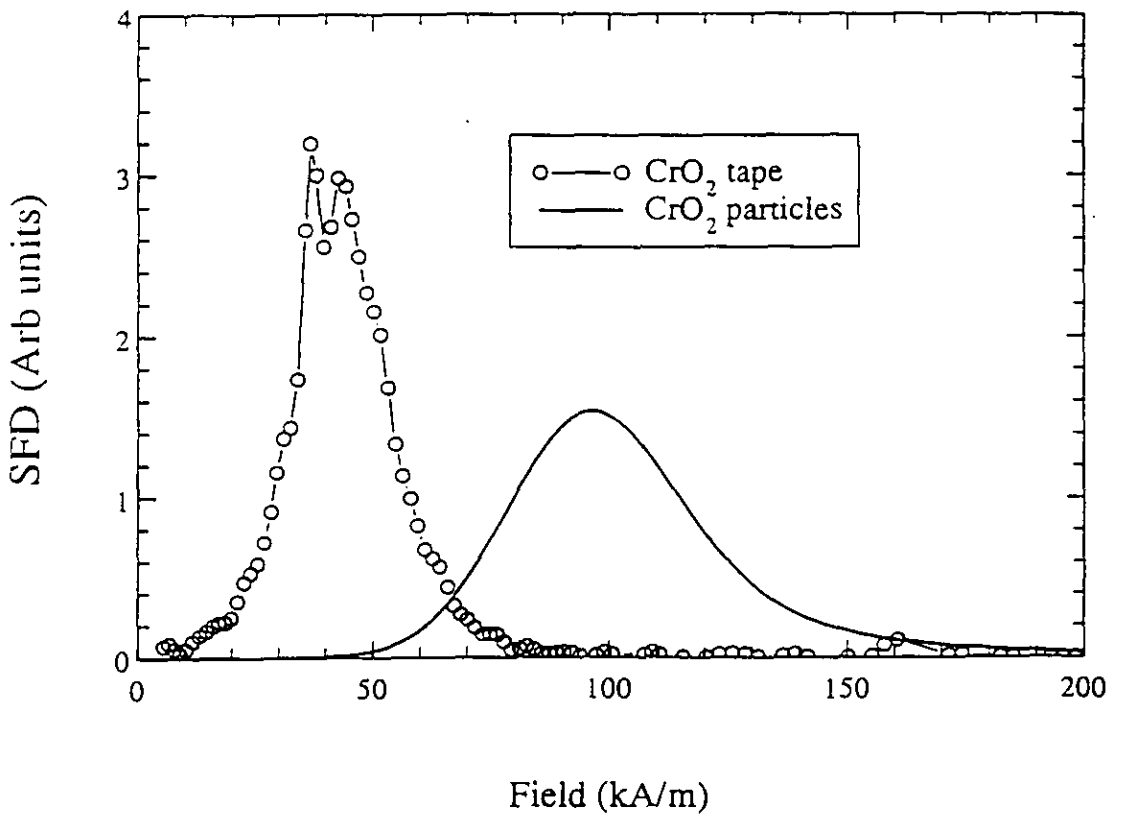


figure (5-5): Switching field distributions with and without interactions for sample 4.

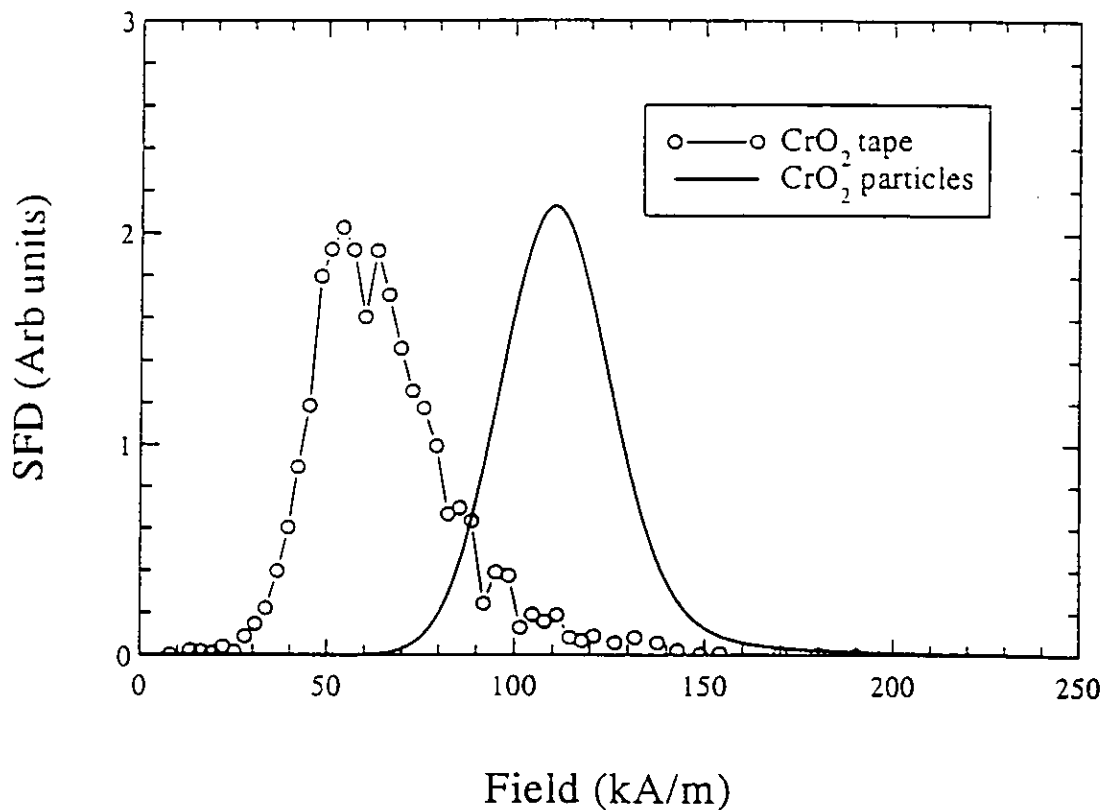


figure (5-6): Switching field distributions with and without interactions for sample 5.

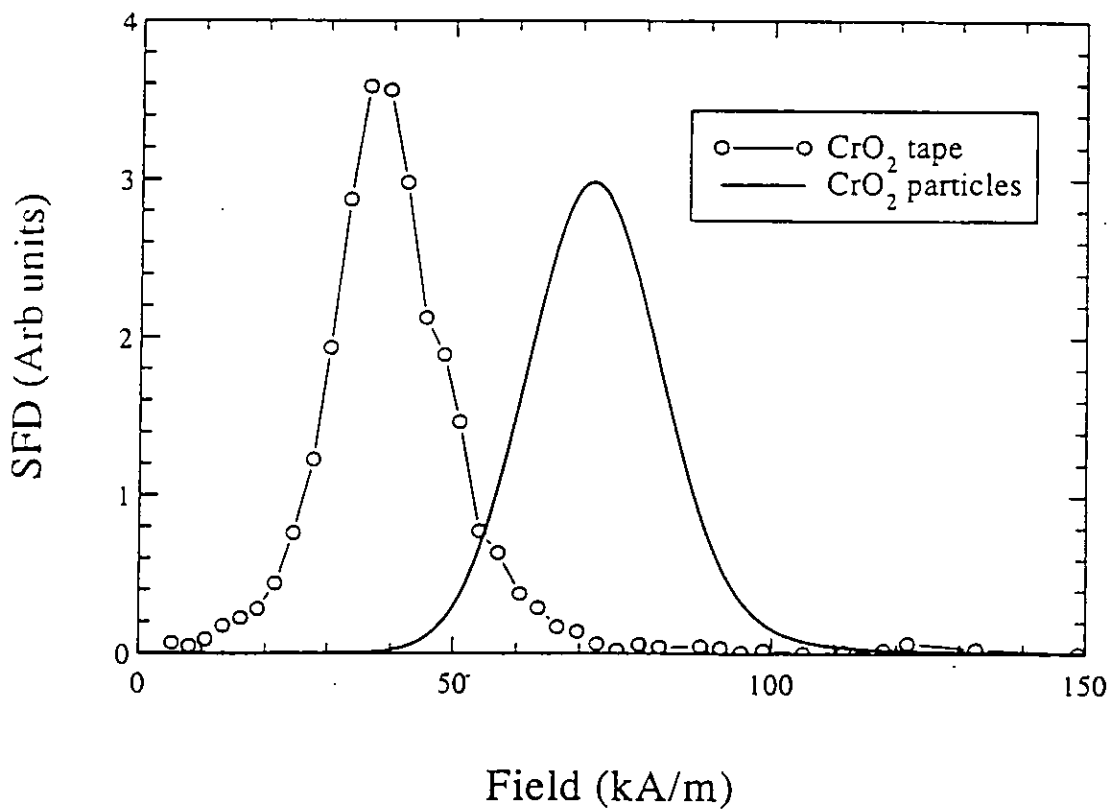


figure (5-7): Switching field distributions with and without interactions for sample 6.

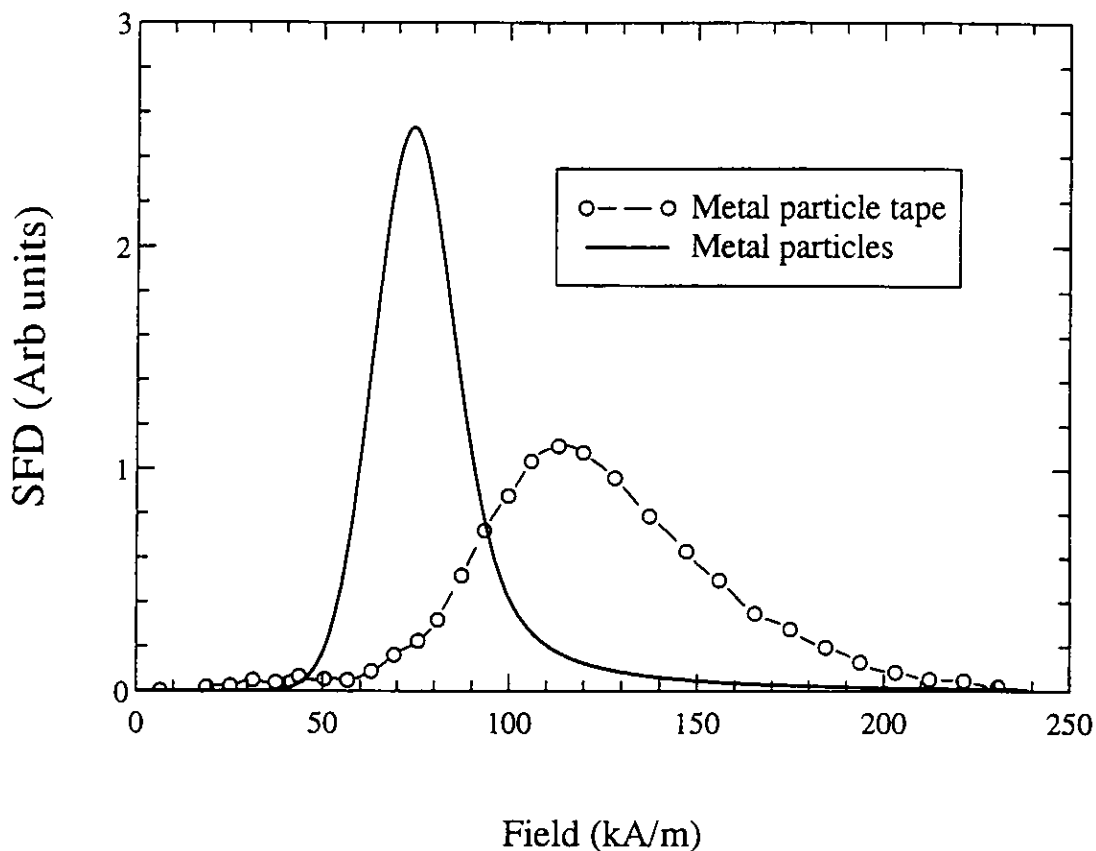


figure (5-8): Switching field distributions with and without interactions for sample 7.

The effect of interactions within the $\gamma\text{-Fe}_2\text{O}_3$ and the CrO_2 was in line with the findings of Knowles [4] and was consistent with the modified Henkel plots which indicated demagnetising or negative interactions. These measurements and the analysis can be described by a mean field approximation which shifts the sample's coercivity and hence its SFD to lower fields.

Sample type	Sample No	SFD numerical mean field \overline{SFD}_{NUM} kA/m	SFD measured mean field \overline{SFD}_{EX} kA/m	Interaction field $\overline{\Delta SFD}_{INT}$ kA/m	Packing density $P = 1 - \frac{\overline{SFD}_{EX}}{\overline{SFD}_{NUM}}$
γ -Fe ₂ O ₃ particulate media	1	71.9	21.3	50.6	0.70
	2	63.5	24.8	38.7	0.61
	3	86.2	33.6	52.6	0.61
CrO ₂ particulate media	4	94.7	31.9	62.8	0.66
	5	110.7	54.1	56.6	0.51
	6	71.1	37.7	33.4	0.47
Metal particle media	7	73.5	114.1	-40.7	-0.55

table (5-1): Comparison between the measured and derived SFD mean fields.

The calculated packing densities for the γ -Fe₂O₃ and CrO₂ samples, given in table (5-1) were approximately 0.65 and 0.55 respectively. These calculated values are high for commercial particulate media, where the volumetric packing density is of the order of 0.4 [5,6]. This discrepancy might be attributed to the localised formation of agglomerations within the sample, effectively increasing the media's packing density and increasing the localised interaction field within an agglomeration. Theoretical work by Coverdale *et al.* [7] and Saroh *et al.* [8] on fluid dispersions and on the microstructure of dried coatings supports these conclusions. Their investigations have indicated the presence of particle bundles and the formation of voids within the dried media. This would effectively increase the packing density of the media, increasing the localised interactions and thus reducing coercivity.

The results for the metal particle system, sample 7, were contrary to the mean field approximation, since the effect of interactions was to shift the SFD to higher field values giving a negative packing density of -0.51. This indicates interactions that oppose demagnetisation (positive interactions), a result which was contrary to the

modified Henkel plot for this sample and the findings of other workers [9] for metal particle media. Thus, at a microscopic level local inter-particle interactions appear to enhance the switching field and dominate the behaviour of individual particles. However, at a macroscopic level, behaviour is still predominantly that of a system in which interactions are demagnetising. These findings appear to be contradictory.

A possible explanation for this contradiction was that the measured single particles were not representative of the distribution in the tape or were damaged during removal and subsequent dispersion. The latter was unlikely since particles were removed by dissolving the binder system and dispersed using an ultrasonic bath. However, the experiment was 'selective' since many agglomerates were observed but ignored in the measurements. There is a possibility, albeit unlikely, that particles that formed agglomerates are different from those which remained isolated. Any multi-domain particles were also ignored in the measurements.

An alternative suggestion for this contradiction may be found in the modelling study of Lyberatos and Wohlfarth [10]. Chains of particles were introduced into a particulate system. This had the effect of increasing the system's coercivity. However, Henkel plots showed that interactions between adjacent chains dominated and exhibited an overall demagnetising behaviour. Only in very dilute systems did the interactions between particles in the chains start to dominate and produce positive interactions. It was therefore suggested that in the metal particle system studied there may be very strong local alignment of particles which has the effect of increasing the system coercivity whilst not affecting its bulk negative interactions. This suggestion has been supported by the experimental study of Bottoni *et al.* [11]. Their study proposed particle chaining as a mechanism for producing positive interactions, while negative interactions were produced by particle bundles. Examples of transmission electron microscopy images of metal particles in chains and bundles can be found in figure (5-9) through to figure (5-11).



figure (5-9): TEM micrograph image of iron particles appearing to form chains consisting of several short particles, after Bottoni *et al.* [11].

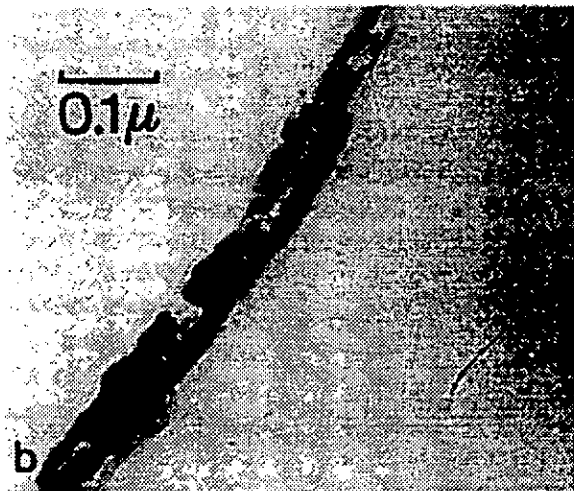


figure (5-10): TEM micrograph image of iron particles appearing to form two long chains flanking each other, after Bottoni *et al.* [11].



figure (5-11): TEM micrograph image of iron particles appearing to form bundles with chains of particles, after Bottoni *et al.* [11].

If, as suggested, the positive interactions measured within the metal particle system are the result of chaining, then why does this phenomenon not occur within the similar $\gamma\text{-Fe}_2\text{O}_3$ and CrO_2 particulate systems investigated. These particulate systems have particles of similar dimensions and have similar media characteristics, as measured in chapter 4. The only major difference between these samples and the metal particle sample is the bulk saturation magnetisation of the metal particles. Metal particles have a bulk saturation magnetisation of approximately three times that of $\gamma\text{-Fe}_2\text{O}_3$ or CrO_2 ; the effect of this increased saturation magnetisation is an increased magnetostatic interaction field within the media. This large magnetostatic field may promote particle chaining, increasing the positive interactions between the particles within the chain and effectively increasing their coercivity.

Chapter Six

Numerical investigation of particles

6.1 Introduction

A number of theoretical models have been developed over the years to simulate the reversal properties of single domain magnetic particles. Early theoretical models, such as the Stoner-Wohlfarth [1] and the chain of spheres [2] are simplistic and can only represent two forms of reversal, coherent and fanning. In recent years numerical micromagnetic models have been developed by Schabes *et al.* [3,4] and Della Torre *et al.* [5] to simulate more complicated reversal modes. These models can represent both the simplistic reversal modes and the more complicated modes such as curling and buckling.

In this chapter the Stoner-Wohlfarth and the chain of spheres models are introduced. Their switching fields have been modelled and compared with experimental results for isolated magnetic particles. A numerical model similar to that of Schabes *et al.* and Della Torre *et al.* has also been developed. This model utilised the measured physical parameters of a particle with bulk properties taken from the literature. These parameters and properties were used to simulate the magnetic characteristics of the particles measured experimentally. From the results of this model, a direct comparison with the experimentally measured characteristics of a particle was performed. The effect of model parameters on the simulation has also been investigated, particularly how they affect its switching field.

In comparing the experimentally measured properties of particles with their simulated characteristics, particularly their switching fields, it was anticipated that the effect of different particle parameters on the reversal mechanism within particles could be determined. This investigation was separated into two distinct areas, the simulation

of particles measured experimentally and the effect of the simulation parameters on the reversal mechanism within the model.

In the first area, an exact correlation between the simulation results and the experimental results was not expected, since any simulation cannot be an exact representation of the particle being modelled. Although an exact correlation was not expected, the results from the simulation were expected to indicate the properties of the particles being modelled. This would indicate that the model developed had some validity.

The second area of research was primarily involved in observing the effect of model parameters on the reversal mechanism. In particular, the aim was to observe how the reversal mechanism changed with the shape of the model and how this affected its properties, particularly its switching field and its remanence. This work was performed so that the model could be used to indicate how the properties of a particle would change with different physical characteristics. For example, the effect of aspect ratio on the properties of the particle, its reversal mechanism, its switching field and its remanence was investigated.

6.2 Stoner Wohlfarth model

In 1947, Stoner and Wohlfarth [1] proposed a model to describe the behaviour of a single domain particle. Their model assumed that the magnetisation of the particle remains uniform during reversal. This type of reversal in the literature is often referred to as coherent.

Their model described the magnetic properties of an isolated magnetised particle through the minimisation of its magnetic energy. The model considered uniaxial anisotropy energy and the energy associated with the moment of the particle interacting with an external applied field. The uniaxial anisotropy energy of a particle can be due to its shape or its crystalline structure, as described in chapter one. The uniaxial anisotropy energy was represented by

$$E_{ANI} = K_1 V \sin^2 \varphi , \quad (6-1)$$

where K_1 is the uniaxial anisotropy constant, V is the volume of the particle and φ is the angle between the moment direction and the easy axis direction.

The energy E_{APP} associated with interaction of an applied external field H_{APP} on a moment (M) was defined as

$$E_{APP} = -\mu_0 M H_{APP} \cos \phi. \quad (6-2)$$

where μ_0 is the permeability of empty space and ϕ is the angle between the moment direction and the applied field direction. The total energy E_{TOTAL} of the Stoner Wohlfarth model was

$$E_{TOTAL} = K_1 V \sin^2 \phi - \mu_0 M H_{APP} \cos \phi. \quad (6-3)$$

The definitions of the angles within the Stoner Wohlfarth particle are indicated in figure (6-1).

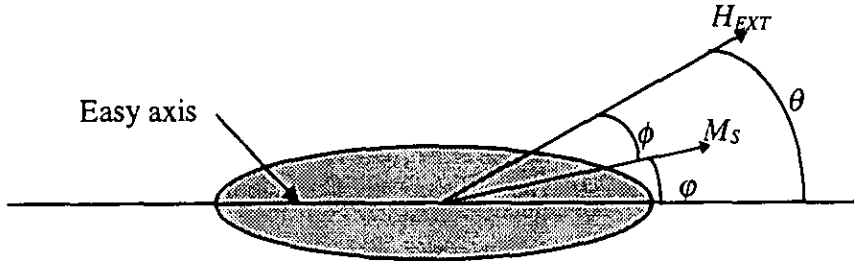


figure (6-1): Stoner Wohlfarth model.

The Stoner Wohlfarth simulation reduced the energy of the model towards a stable energy minima solution. This occurred when the torque generated from the applied field was equal and opposite to the torque generated from the uniaxial anisotropy.

The torque generated from the orientation of a moment away from its easy axis is given by

$$|\Gamma_{ANI}| = \left| \frac{dE_{ANI}}{d\phi} \right| = |2K_1 V \sin \phi \cos \phi|. \quad (6-4)$$

The torque Γ_{APP} generated by the action of the applied field on a moment is given by

$$|\Gamma_{APP}| = |\mu_0 H_{APP} M_S V \sin \phi|, \quad (6-5)$$

where the moment $M = M_S V$ is defined by the material saturation magnetisation and the volume of the material.

The moment tends towards the energy minimisation condition, where torque generated by the applied field is equivalent and opposite to the torque generated from the anisotropy, thus

$$|\Gamma_{APP}| = |\Gamma_{ANI}|, \quad (6-6)$$

$$|\mu_0 H_{APP} M_S V \sin(\theta - \phi)| = |2K_1 \sin \phi \cos \phi| \quad (6-7)$$

The field required to rotate the moment by 90 degrees away from its easy axis is defined as its anisotropy field, H_K . It is evaluated by allowing $\theta = 90^\circ$ and through the manipulation of equation (6-7) the anisotropy field of the particle is defined as

$$H_K = \frac{2K_1}{\mu_0 M_S}. \quad (6-8)$$

Stoner and Wohlfarth determined the orientation of the moment by an energy minimisation technique. Hysteresis loops for a Stoner-Wohlfarth particle with applied field angles between the easy axis and the applied field direction are presented in figure (6-2). The applied field, on the horizontal axis is given in reduced units $h = H_{EXT} / H_K$. The hysteresis loop for the applied field angle $\theta = 0^\circ$ indicates reversal through a purely irreversible process. An irreversible process occurs when a moment switches between two stable energy minima in a single irreversible process. As the applied field angle θ increases, the reversal process becomes increasingly reversible. At $\theta = 90^\circ$ the reversal process becomes totally reversible with no irreversible component. At the angles $\theta = 0^\circ$ and $\theta = 90^\circ$ there is a discontinuity at $h = 1.0$, this represents the saturation of the moment in the applied field direction, the anisotropy field of the particle.

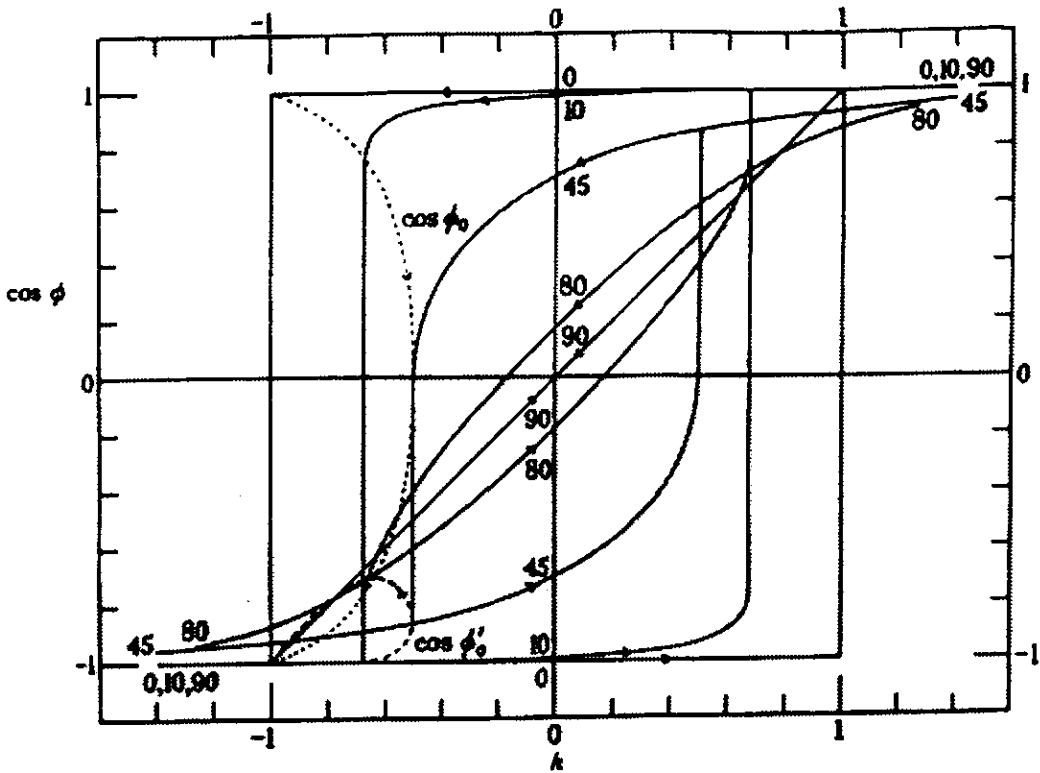


figure (6-2): Hysteresis loops generated from the Stoner-Wohlfarth model [1]

The switching field of a particle is identified from the external field required to reverse its moment. On a hysteresis loop, this is the point where the loop closes. The switching field of particle can be identified on its hysteresis loop at the point where its loop closes. The switching field for the Stoner-Wohlfarth model as a function of the applied field angle is presented in figure (6-3). These results are similar to experimental results on $\gamma\text{-Fe}_2\text{O}_3$ particles by Ledereman *et al.* [6]. The particles in their study closely resembled prolate spheroids with few surface imperfections. These particles would exhibit a uniform demagnetising field. Thus, when a uniform magnetising field is applied, the magnetisation of the particle remains uniform as it rotates, aiding coherent reversal [7].

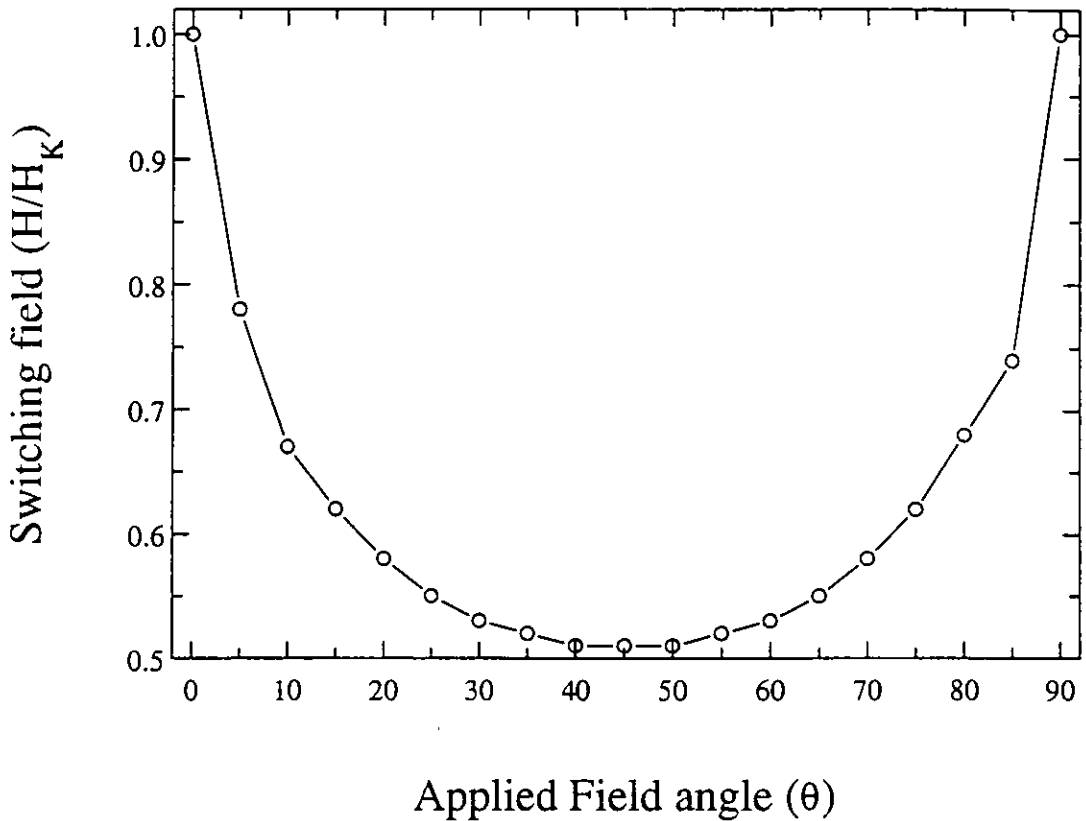


figure (6-3): Switching field as a function of the applied field angle for the Stoner-Wohlfarth model.

6.3 The chain of spheres model

A chain of spheres model was developed, similar to the model developed by Jacobs and Bean [2]. It represented a single magnetic particle as a chain of uniform isotropic single domain spheres with only point contact or even slightly separated, so as to be magnetically isolated. The moment M_i of each sphere (i) is free to adopt any angle (θ_i) in a two dimensional plane with respect to the vector joining the spheres. The total energy of a six sphere system consists of fifteen dipole-dipole terms and six applied field terms. The magnetostatic energy between two moments M_i and M_j , with angles θ_i and θ_j , separated by a distance r_{ij} is given by

$$E_{ij}^{mag} = (\mu_0 M_i M_j / 4\pi r_{ij}^3) * (\cos(\theta_i - \theta_j) - 3 \cos\theta_i \cos\theta_j). \quad (6-9)$$

The applied field energy E_i^{field} of a moment i is given by

$$E_i^{field} = -\mu_0 M_i H_{APP} \cos(\theta_i - \alpha). \quad (6-10)$$

Here $(\theta_i - \alpha)$ is the angle between the moment direction and the applied field direction. The applied field direction with respect to the long axis of the chain of spheres is given by α .

To obtain a stable solution the total energy of the system was minimised. The energy was minimised using the gradient descent technique used by Dean [8]. The energy gradient of each particle was calculated using

$$\frac{\partial E}{\partial \theta_i} = \mu_0 M_i H_{APP} \sin(\theta_i - \alpha) - \sum_{j=1, j \neq i}^6 (\mu_0 M_i M_j / 4\pi r_{ij}^3) (\sin(\theta_i - \theta_j) - 3 \sin \theta_i \cos \theta_j) \quad (6-11)$$

In order to have a dimensionless equation for the energy gradient of the i^{th} moment, equation (6-11) was divided throughout by the energy $2K_I V$, where K_I is the anisotropy constant and V is the volume of the particle. The following identities were used here.

$$\text{Internal field strength} \quad H_{int} = M_i V / d^3 \quad (6-12)$$

$$\text{Reduced field} \quad \bar{h}_{APP} = \bar{H}_{APP} / H_K \quad (6-13)$$

$$\text{Reduced magnetostatic interactions} \quad h_{int} = H_{int} / H_K \quad (6-14)$$

The separation between spheres was given as

$$r_{ij} = r_{ij}' d. \quad (6-15)$$

where normalised distance was r_{ij}' , the actual distance was r_{ij} and the separation between adjacent spheres was d .

The reduced energy gradient of the i^{th} moment is given as

$$\frac{dE}{d\theta_i} = h_{APP} \sin(\theta_i - \alpha) - \sum_{j=1, j \neq i}^6 (h_{\text{int}} / 4\pi r_{ij}^3) (\sin(\theta_i - \theta_j) - 3 \sin \theta_i \cos \theta_j). \quad (6-16)$$

The moment of each sphere was pushed down its associated energy gradient using

$$\theta_i^{n+1} = \theta_i - \lambda * \frac{\partial E}{\partial \theta_i}. \quad (6-17)$$

Here λ is a constant, θ_i is the angle of the moment before relaxation and θ_i^{n+1} is its angle after relaxation. A value of 0.1 for λ was found to be satisfactory by Dean [8] by trial and error. The energy gradient technique is based on the reduction of a moments energy. It calculates the individual energy gradient for each moment then pushes the angle of the moment towards its associated energy minimum state. A minimum energy state was defined when none of the moments rotated more than the minimisation criteria for a single iteration. The minimisation criteria was 0.01° , this was found to be satisfactory through trial and error. It should be noted that the energy minima found by the gradient descent technique is not a global energy minima for the system but individual minima for each moment.

The algorithm used within this model to generate a hysteresis loop for a chain of six spheres is as follows:-

- Initialisation routine
 1. All the moments within the system are aligned as in saturation.
 2. The applied field is set and the minimisation routine is initiated.
 - Minimisation routine
 3. The moments within the system are visited simultaneously and their energy gradients are calculated.
 4. The moments are relaxed simultaneously down their energy gradient.
- Stage 3 and 4 are repeated until a satisfactory energy minimum state has been achieved for every moment within the system. At this point the hysteresis routine is initiated.

- Hysteresis routine
5. The applied field value is changed by ΔH and the minimisation routine is initiated.
 7. After completion of half a hysteresis loop the program terminates.

Hysteresis loops generated from this model with $h_{int}=0.1$ for different applied field angles are given in figure (6-4). The results indicate that for low applied field angles the hysteresis loop exhibits a high remanence with a low switching field. As the applied field angle increases the remanence reduces and the switching field is seen to increase.

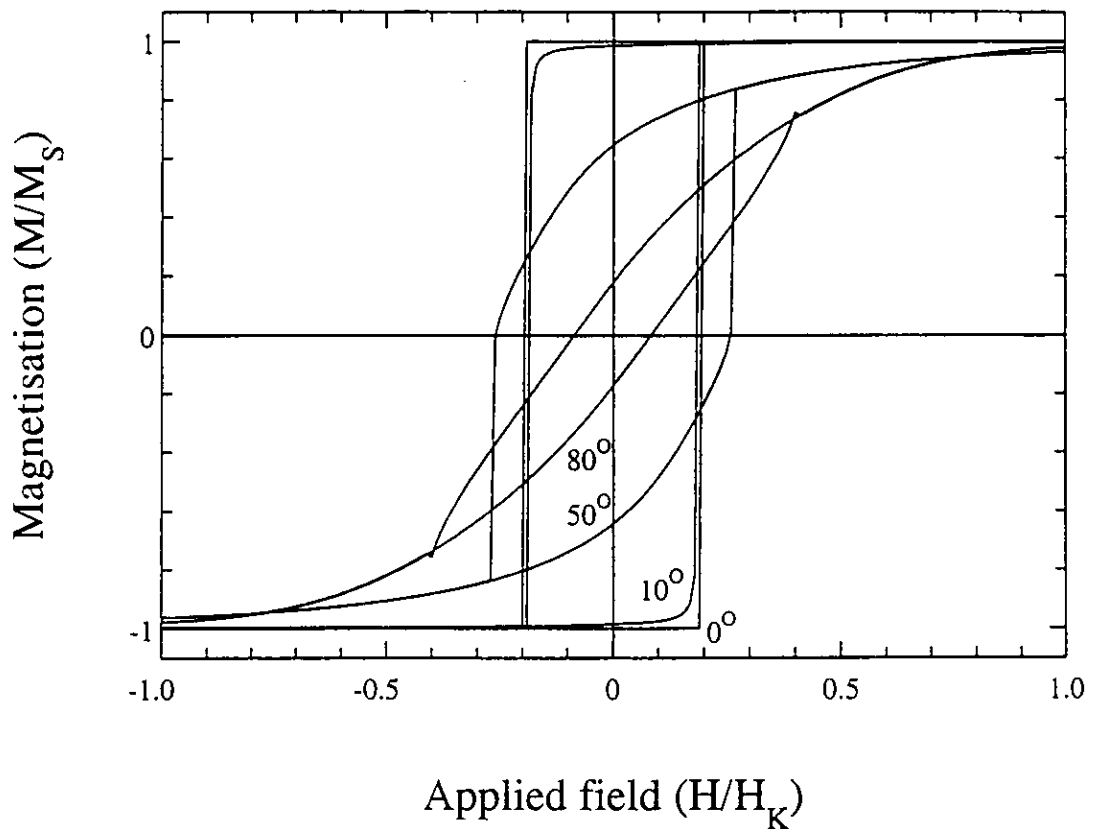


figure (6-4): Magnetisation curves for a chain of spheres model.

The switching field as a function of the angle obtained from the chain of spheres model is presented in figure (6-5). The switching field of the model remains flat up to -20° and then steadily increases with the applied field angle. These characteristics are similar to the switching field characteristics of the commercial particles measured within this study and in other studies [9-11]. Although the results are similar they do not

give an adequate interpretation of reversal mechanisms within commercial magnetic particles. In particular for CrO_2 particles the reversal mechanism has been reported to occur through curling [12,13] which can not be represented by the chain of spheres model. As a result of these limitations a more complex micromagnetic model was developed to represent the particles measured in this study.

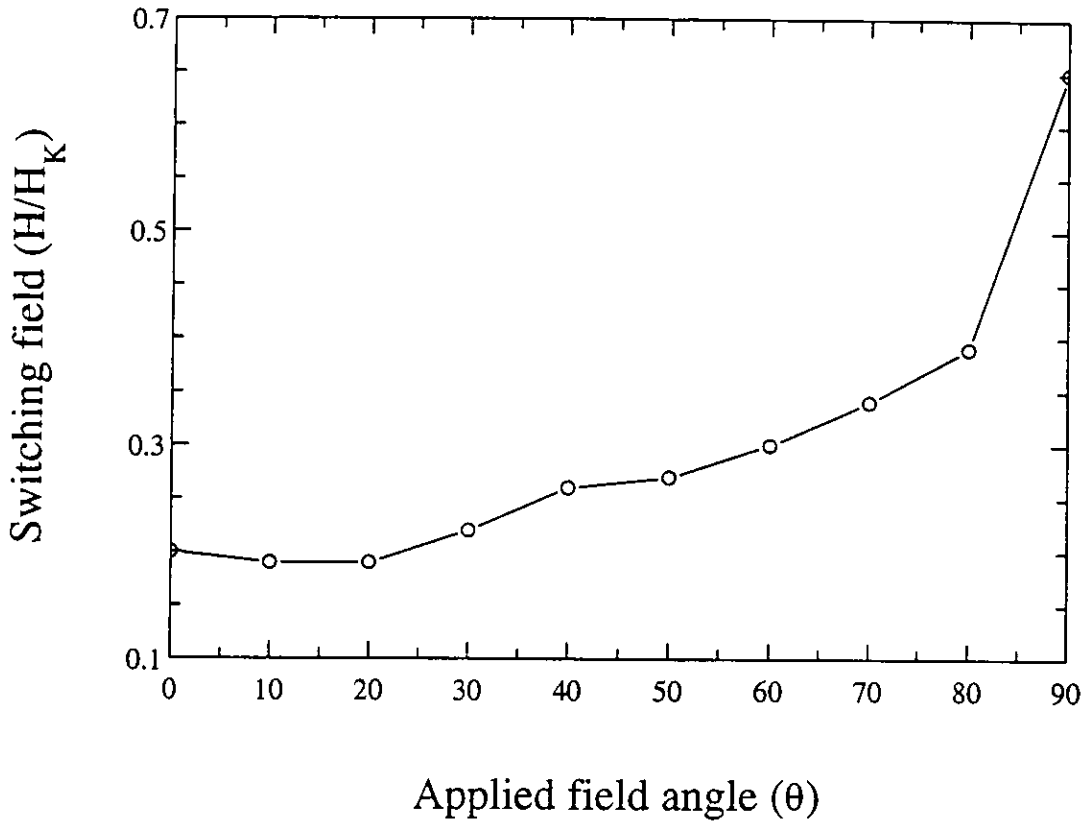


figure (6-5): Switching field as a function of the applied field angle for the chain of spheres model.

6.4 Micromagnetic model

A micromagnetic model was developed to simulate the reversal mechanisms within the commercial magnetic particles measured in chapter 3. The model represented the shape of the particle by an array of cubes in a lattice structure. At the centre of each cube, there was a dipole moment that was free to rotate in any direction. The model determined the effective field at the centre of each cube, it then rotated the moment dynamically towards its energy minimum. The calculation of the effective field and the

subsequent relaxation of the moments was repeated until all the moments within the model had achieved an energy minimum state, defined by the minimisation criteria.

The micromagnetic model utilised experimentally measured parameters, the size and shape of a particle with bulk properties taken from the literature. The model was used to simulate the hysteresis loops of particles measured experimentally in this study, $\gamma\text{-Fe}_2\text{O}_3$ particles from sample 2 and CrO_2 particles from sample 4. From this loop, the switching field was obtained and compared directly with the experimentally measured switching fields for particles with similar physical dimensions. The effect of changes in model parameters on the results of the simulation was also investigated, particularly how shape affected the switching field.

6.4.1 Co-ordinate system

The position of the cubes and dipoles was determined using a right-handed co-ordinate system. The distance between cubes i and j was normalised with respect to the distance between adjacent cubes and was defined as

$$\vec{r}_{ij}' = x_{ij}'\mathbf{i} + y_{ij}'\mathbf{j} + z_{ij}'\mathbf{k} , \quad (6-18)$$

where x_{ij}' , y_{ij}' , z_{ij}' represent the normalised unit dimensions between cubes i and j , while \vec{r}_{ij}' represents the normalised displacement vector between cubes i and j .

The direction of dipoles at the centre of each cube was identified within the model by spherical polar co-ordinates, indicated in figure (6-6).

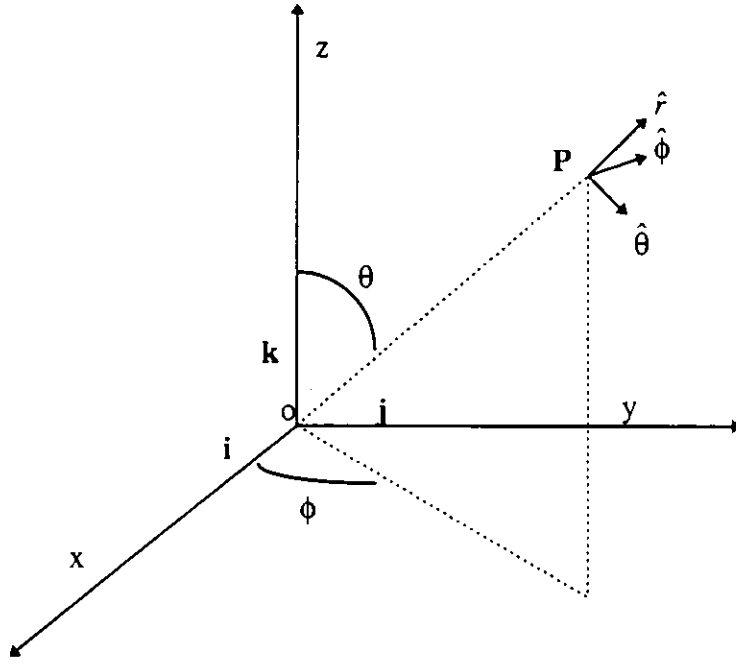


figure (6-6): Spherical polar co-ordinate system

The position of point P in space can be identified in terms of three co-ordinates (r, θ, ϕ) , The directions $\hat{r}, \hat{\theta}, \hat{\phi}$ in figure (6-6) are given by

$$\hat{r} = \hat{i} \sin \theta \cos \phi + \hat{j} \sin \theta \sin \phi + \hat{k} \cos \theta , \quad (6-19)$$

$$\hat{\theta} = \hat{i} \cos \theta \cos \phi + \hat{j} \cos \theta \sin \phi - \hat{k} \sin \theta , \quad (6-20)$$

and

$$\hat{\phi} = -\hat{i} \sin \phi + \hat{j} \cos \phi . \quad (6-21)$$

The unit moment magnetisation for cube i and j in spherical polar co-ordinates are defined as

$$\hat{m}_i = \hat{i} \sin \theta_i \cos \phi_i + \hat{j} \sin \theta_i \sin \phi_i + \hat{k} \cos \theta_i , \quad (6-22)$$

and

$$\hat{m}_j = \hat{i} \sin \theta_j \cos \phi_j + \hat{j} \sin \theta_j \sin \phi_j + \hat{k} \cos \theta_j , \quad (6-23)$$

6.4.2 Micromagnetic structure

A magnetic particle was represented by a three dimensional array of cubes, similar to that of other workers [4,5,14,15]. These cubic elements were assumed to be sufficiently small so that the magnetisation within a cube remained uniform across its dimensions. The magnetisation within each cube was the saturation magnetisation of the material and was free to rotate in any direction.

The number of cubes used to represent a particle determined the overall resolution of the model. This was limited by the practical number of micromagnetic calculations possible. If the cube's dimensions approached the atomic scale, a quantum mechanical treatment would have to be employed [16]. This limits their finite size in phenomenological models. As the number cubes N within a system increases, the number of magnetostatic interactions increases by $N(N-1)$. This limited N to typically less than 250 to be computed by a Pentium personal computer within one week.

An example of a simple model representing a particle with an aspect ratio of 6:1 is given in figure (6-7). This model has 25 cubes in the xy plane and 30 cubes in the z direction. An odd number of cubes was chosen within the xy plane to avoid any symmetry effects during reversal through this plane.

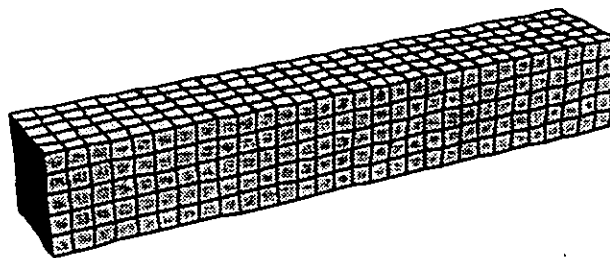


figure (6-7): Cubic lattice representing an isolated micromagnetic particle.

Yan and Della Torre [5] in their computational study of $\gamma\text{-Fe}_2\text{O}_3$ particles have proposed an extension to this basic cubic structure. Their extension involved removing cubes at the eight corner of the lattice, this produced a structure that is more

representative of a commercial particle. An example of this structure, referred to as a parallelepiped with pyramid ends is given in figure (6-8).

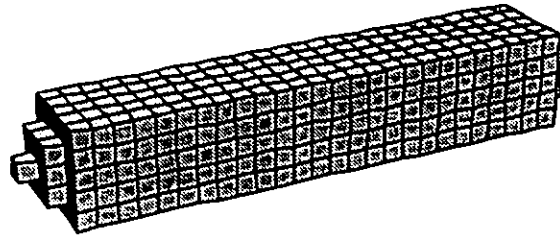


figure (6-8): Cubic lattice with pyramid ends.

The simulated $\gamma\text{-Fe}_2\text{O}_3$ particle of Yan and Della Torre had an aspect ratio of 6:1 discretised into $5 \times 5 \times 30$ cubes. They investigated how the reversal mechanism was affected by having a pyramid structure at the ends of their model. They found that for a model with no pyramid structures (flat ends), a large non uniform demagnetising field was induced at its ends. This field reduced the remanence of the model and aided its reversal. With the inclusion of the pyramid structures, they found the demagnetising field was more uniform. This increased the remanence of the model and aided coherent reversal, increasing its coercivity.

The results of the simulations in this study, by Yan and Della Torre and by other workers with similar models [4,15,17] have indicated symmetry effects. These occur when the structure of a model is symmetrical. This creates symmetrical patterns in magnetic microstructure and as a result unrealistic reversal mechanisms are initiated. As a consequence of this phenomenon, a cubic structure with surface irregularities was developed. This was achieved by allowing the surface cubes to be expanded or contracted by an amount chosen in a random number generator that followed a normal distribution. The magnitude and variation of the surface irregularity was described by the standard deviation of the distribution and the seed value for the random number generator. An example of this structure with a standard deviation of 10% of the cube's original width is given in figure (6-9).

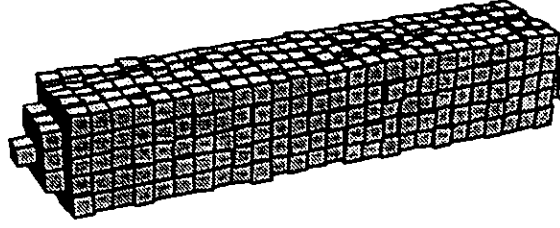


figure (6-9): Cubic lattice with pyramid ends and an irregular structure.

6.4.3 Field terms

The effective field \vec{H}_{EFF} that the dipole moment experiences at the centre of each cube was determined by summing the individual contributions, the magnetostatic \vec{H}_{MAG} , the exchange \vec{H}_{EXC} , the anisotropy \vec{H}_{ANI} and the applied field \vec{H}_{APP} .

$$\vec{H}_{EFF} = \vec{H}_{MAG} + \vec{H}_{EXC} + \vec{H}_{ANI} + \vec{H}_{APP}. \quad (6-24)$$

The magnetostatic field \vec{H}_{MAG} at the centre of a given cube i was calculated assuming a dipole approximation [18]

$$\vec{H}_{MAG} = \sum_j \frac{V_j}{4\pi|\vec{r}_{ij}|^3} (3\vec{M}_j \cdot \hat{r}_{ij}\hat{r}_{ij} - \vec{M}_j), \quad (6-25)$$

where V_j is the volume of cube j , \vec{M}_j is its magnetisation and \vec{r}_{ij} is the position vector from cube i to j .

The magnetostatic field is long rang in nature, thus all the cubes moment's will interact with one another. This creates a large number of magnetostatic fields that are required to be calculated for an accurate determination of the magnetostatic field at one point. In fact the number of magnetostatic field calculation required for a system of moments is the factorial of the number of moments within the system. A system of 10 moments would require 3.6 million calculations.

As a consequence of this difficulty, range truncation [19] was examined. This simple technique limits the range over which magnetostatic interactions are considered,

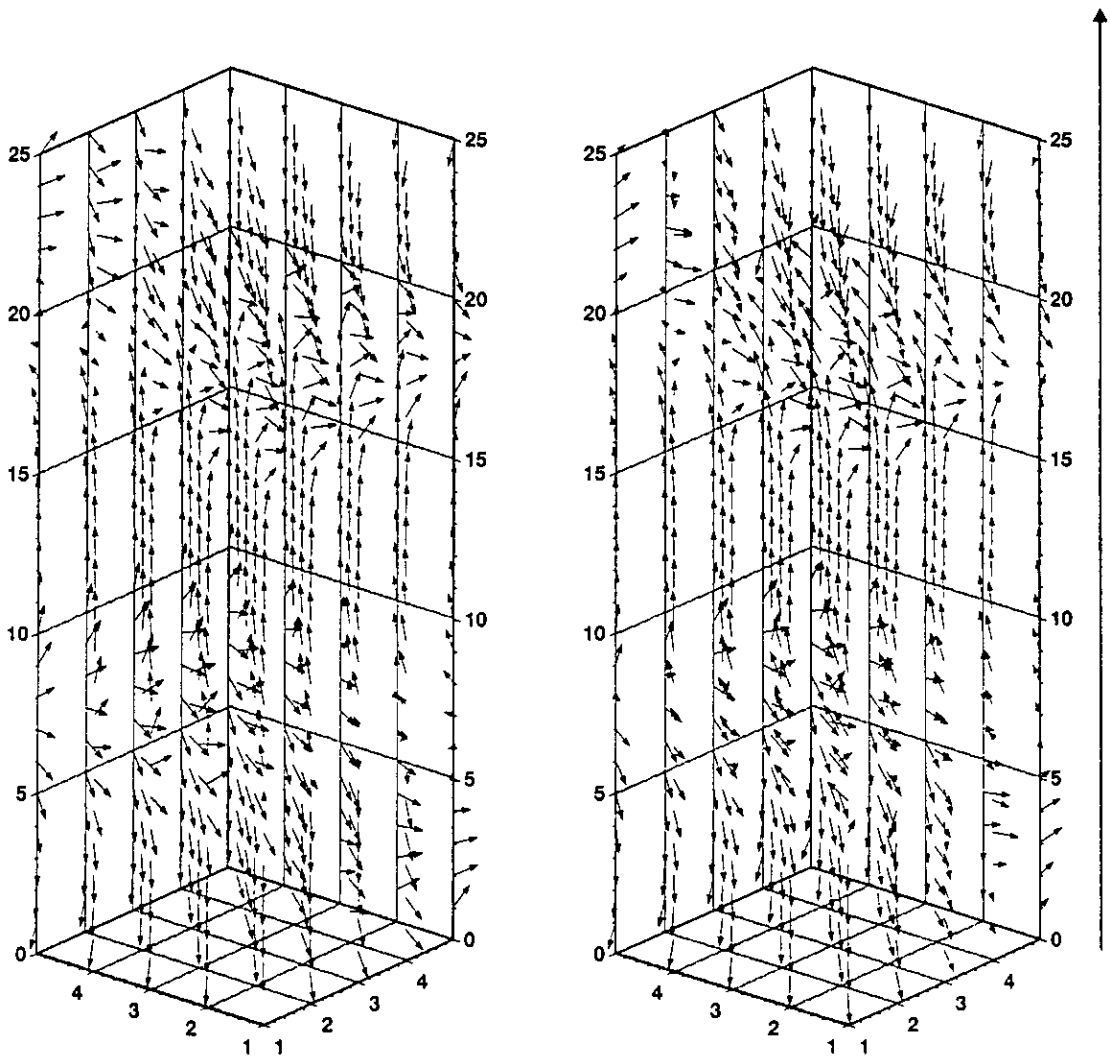
reducing computational time. Since the magnetostatic field decreases as $1/r^3$ it might appear to be a sufficiently accurate and computationally efficient technique for most micromagnetic simulations. In this case, however, the volume of material considered within the interaction is proportional to r^3 , so the effect of the magnetostatic field cannot be neglected at large r . Thus, this technique would seem insufficient for a large 3D micromagnetic simulation. In this particle model the volume of material contributing to the magnetostatic calculation at large r , greater than the particle width is approximately proportional to r , so the magnetostatic contribution falls off as $1/r^2$. Thus at large r , where the total moment excluded is small the effect of the magnetostatic contributions could be neglected [19].

An exact calculation of the magnetostatic field was not possible due to computational time constraints. As a consequence a compromise was taken between the accuracy of the magnetostatic calculation and the computational time available. Simulations were performed with different truncation lengths and the effects were observed. It was found that for a simulation with typical micromagnetic parameters a truncation length of 6 cube widths gave a satisfactorily accurate magnetostatic calculation with a considerable reduction in the computational time for a hysteresis loop, approximately 65%.

The effect of truncation on the parameters of the simulation was investigated. Truncation had no observable effect on the remanence of the simulation, while its switching field was reduced. Typically the reduction of the switching field was less than 10% for a simulation with an aspect ratio of 6:1, represented by an array 5x5x30. It should be noted that this discrepancy was likely to increase with an increase in the aspect ratio of a simulation. For simulations with large applied field angles with respect to the long axis of the simulation the discrepancy was likely to reduce. This is because the micromagnetic moments within the simulation are not aligned in the long axis of the model, they are aligned out of its long axis. Thus, as the applied field angle increases with respect to the long axis of the simulation the inaccuracy in magnetostatic calculation reduces, reducing the switching field discrepancy.

The effect of the truncation on the micromagnetic transient state at coercivity was also investigated. It was found that the effect of truncation was to allow the onset of

reversal to occur earlier than for a simulation with the exact magnetostatic calculation. The effect of truncation is similar to that of reducing the aspect ratio, thus increasing the demagnetising field aiding reversal. Presented in figure (6-10) are the transient states at coercivity for simulations using the exact and the truncated magnetostatic calculation. Examining these states it can be seen that there are some minor differences between the micromagnetic moments; however, the major features within the reversal are very similar. This is characterised by the formation of two reversal layers, the position of these layers and their structure.



Exact Magnetostatic calculation.

Truncated Magnetostatic calculation.

figure (6-10): Comparison between the transient states for a simulation with an exact magnetostatic calculation and a truncated magnetostatic calculation.

The exchange field \vec{H}_{EXC} arises from the coupling between adjacent moments; it is analogous to spin exchange coupling in quantum mechanics [20]. The field is short range in nature and tends to align adjacent moments, aiding coherent reversal. The exchange field was determined by

$$\vec{H}_{EXC} = \frac{C^* H_K}{M_S} \sum_j^{n.n} \vec{M}_j, \quad (6-26)$$

where n.n is the number of nearest neighbours of cube i , M_S is the saturation magnetisation, K_1 is the anisotropy constant and $H_K = \frac{2K_1}{\mu_0 M_S}$ is the anisotropy field. The parameter C^* is the inter-cube exchange constant [21] and is defined by

$$C^* = \frac{A^*}{K_1 a^2}, \quad (6-27)$$

where A^* is the effective energy exchange constant and a is inter-cube separation. In the models the inter-cube separation a varies with the position and size of the interacting cubes. As a result the inter-cube exchange constant C^* is calculated for each interaction field \vec{H}_{EXC} . The value of A^* determines the direct magnitude of the interaction between adjacent moments. It has been reported to be in the range 1.0-10.0pJ/m [3,5].

The crystalline anisotropy within a material refers to the preference of the material's moment to lie along a particular crystalline axis. This can be described by a field originating from the crystalline easy axis. The general formula [18] for the crystalline anisotropy field is

$$\vec{H}_{ANI} = \frac{2(\vec{K} \cdot \vec{M}_i)\vec{K}}{\mu_0 |K| |M_i|^2}, \quad (6-28)$$

where \vec{M}_i is the vector magnetisation of cube i , $\vec{K} = K_1 \hat{k}$, \hat{k} is the unit vector determining the easy axes directions, and K_1 is the magnitude of the anisotropy constant.

The reduced effective field at cube i is determined by normalising the effective field by the anisotropy field. It is further reduced through utilising the micromagnetic identities given in equations (6-12) (6-13) & (6-14)

$$\bar{h}_{EFF} = \frac{\bar{H}_{EFF}}{H_K} = (\hat{k} \cdot \hat{m})\hat{k} + h_{int} \sum_j \frac{v_j}{4\pi|\bar{r}'_{ij}|} (3\hat{m}_j \cdot \hat{r}_{ij}\hat{r}_{ij} - \hat{m}_j) + C * \sum_j \hat{m}_j + \bar{h}_{app}. \quad (6-29)$$

6.4.4 Dynamic calculations

With the evaluation of the effective field at the centre of each cube, the magnetisation of each cube can be determined. The magnetisation of each cube can be relaxed into the effective field direction by either the Gauss-Seidel or the Jacobi techniques [7], each technique having its own characteristics.

The Gauss-Seidel technique solves magnetisation direction for each cube sequentially, by relaxing, in turn, the magnetisation of each cube until a stable energy minima has been obtained. The sequential solution of the cube's magnetisation can introduce ordering effects, where a particular relaxation order sequence will obtain a different magnetic microstructure to another sequence. To avoid this effect the Jacobi technique was utilised within the model to solve simultaneously the magnetisation for all cubes. This technique is less efficient than the Gauss-Seidel technique as it calculates the magnetisation direction for each cube using the cube's magnetisation from the previous iteration.

The relaxation of the magnetisation towards its energy minima for each cube was simulated dynamically by the Landau-Lifshitz equation [19,21,22],

$$\frac{d\vec{M}}{dt} = \gamma_0 \vec{M} \times \bar{H}_{EFF} - \frac{\lambda}{M_s} \vec{M} \times (\vec{M} \times \bar{H}_{EFF}), \quad i=1,2,\dots,N. \quad (6-30)$$

where γ_0 is the gyromagnetic ratio and λ is the damping constant. The first term in the Landau-Lifshitz equation represents the torque exerted on the magnetisation by the effective field, commonly referred to as the precession term. The second term refers to phenomenological damping. This term allows the magnetisation vector to relax dynamically towards a localised energy minimum for each magnetised cube.

For simplicity the Landau-Lifshitz equation can be written in a reduced form by introducing a reduced time $\tau = t\gamma H_K$ and a reduced damping constant $\alpha = \lambda/\gamma$, which is the ratio of energy damping to the rate of gyromagnetic rotation.

$$\frac{d\hat{m}_i}{d\tau} = (\hat{m}_i \times \bar{h}_{EFF}) - \alpha \hat{m}_i \times (\hat{m}_i \times \bar{h}_{EFF}) \quad i=1,2,\dots,N. \quad (6-31)$$

Since the magnetisation direction was determined by polar co-ordinates, the reduced Landau-Lifshitz equation for a cube was derived in terms of θ and ϕ as two coupled differential equations.

$$\frac{\partial \phi_i}{\partial \tau} = \frac{1}{\sin \theta_i} (\cos \theta_i \cos \phi_i - \alpha \sin \phi_i) h_{ix} + \frac{1}{\sin \theta_i} (\cos \theta_i \sin \phi_i + \alpha \cos \theta_i) h_{iy} - h_{iz}. \quad (6-32)$$

$$\frac{\partial \theta_i}{\partial \tau} = (\alpha \sin \phi_i - \sin \phi_i \cos \theta_i) h_{ix} + (-\cos \phi_i + \alpha \sin \phi_i \cos \theta_i) h_{iy} - \alpha \sin \theta_i h_{iz}. \quad (6-33)$$

Here h_{ix}, h_{iy} and h_{iz} refer to the components of the reduced effective field \vec{h}_{EFF} .

The rate at which the magnetisation relaxes towards an energy minimum is dependent on the magnitude of α , the greater its value the more efficient the relaxation algorithm. Studies by Victoria [23] and by Zhu *et al.* [22] have found that micromagnetic simulations were insensitive to the value of reduced damping constant α in hysteresis loops, where the external field changed slowly. The reduced damping constant used throughout this investigation was $\alpha=1.0$. This is comparable to previous studies by other workers [14,24].

The reduced form of the Landau-Lifshitz equation was integrated using a 4th order Runge-Kutta routine [25] commonly utilised throughout micromagnetics [26]. A Runge-Kutta routine can approximate the solution for a system of first order differential equations. Let the differential equations be given by

$$\frac{d\vec{y}}{dx} = f(\vec{y}, x), \quad (6-34)$$

with $\vec{y}(0) = \vec{y}_0$. The Runge-Kutta method derivatives $\vec{k}_{1,2,3,4}$ are evaluated as follows

$$\vec{k}_1 = \vec{f}(\vec{y}_i, x_i), \quad (6-35)$$

$$\vec{k}_2 = \vec{f}\left(\vec{y}_i + \frac{h\vec{k}_1}{2}, x_i + \frac{h}{2}\right), \quad (6-36)$$

$$\vec{k}_3 = \vec{f}\left(\vec{y}_i + \frac{h\vec{k}_2}{2}, x_i + \frac{h}{2}\right), \quad (6-37)$$

$$\vec{k}_4 = \vec{f}(\vec{y}_i + h\vec{k}_3, x_i + h). \quad (6-38)$$

Here h represents the step size in the Runge Kutta routine and $\vec{k}_{1,2,3,4}$ represents the evaluated derivatives; once at the initial point, twice at the mid points and once at a trial

endpoint. Within the simulation, the components of $\bar{k}_{1,2,3,4}$ are the calculated derivatives $\frac{d\theta_i}{d\tau}$ and $\frac{d\phi_i}{d\tau}$ at the points, x_i refers to the reduced time τ , the components of \bar{y}_i are previous iterations angles, ϕ_i and θ_i , and the components of \bar{y}_{i+1} are the new calculated angles, ϕ_{i+1} and θ_{i+1} .

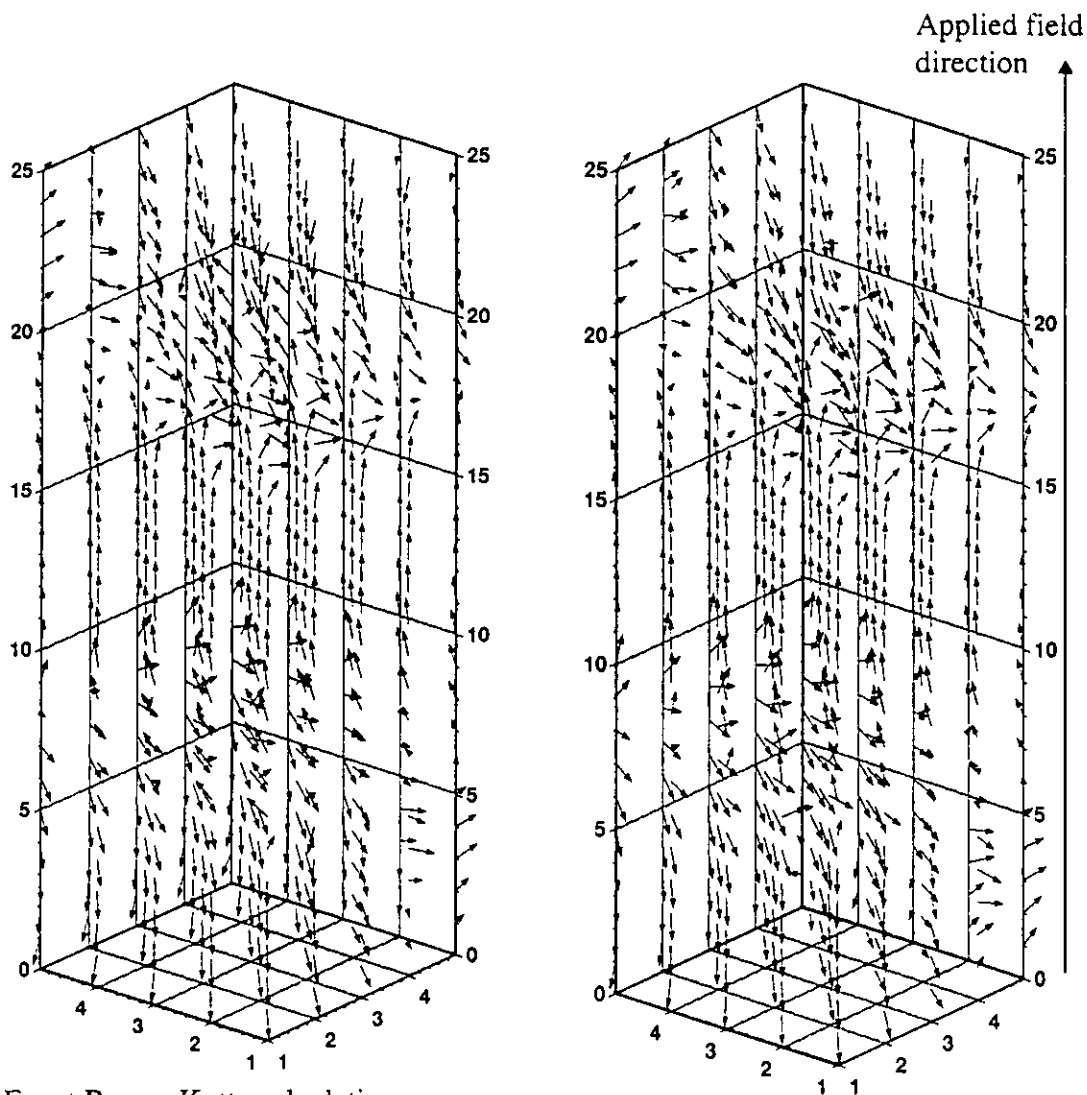
The solution for the Runge-Kutta method is obtained by generating a sequence of the evaluated derivatives

$$\bar{y}_{i+1} = \bar{y}_i + \frac{h}{6}[\bar{k}_1 + 2\bar{k}_2 + 2\bar{k}_3 + \bar{k}_4], \quad (6-39)$$

$$x_{i+1} = (i+1)h, \quad i=0,1,2,\dots \quad (6-40)$$

The Runge-kutta method iterates x_{i+1} until convergence of the series occurs, defined by θ_i and ϕ_i not changing by more than the convergence criteria for the model.

As the direction of each cubes magnetisation changes within the Runge-Kutta routine, the field calculation requires to be updated at each Runge-Kutta step. As the step size was small within all the simulations ($h=0.01$), θ_i and ϕ_i changed slowly for each Runge-Kutta step. Thus, the effective field at each cube remained approximately constant during the Runge-Kutta routine. This allowed a reduction in the processing time by a factor of ~ 4 through not updating the effective field at each Runge-Kutta step. This approximation was verified by running simulations with the field updated at each step and only updating the field calculation at the beginning of each Runge-Kutta step. The micromagnetic transient states at coercivity for both methods were compared, shown in figure (6-11). The transient states showed no significant difference between both algorithms for a fourfold improvement in the computational time. The switching field and the remanence of a simulation also showed no discrepancy between both algorithms. As a consequence all the simulations were performed with this approximation in the Runge-Kutta routine. With the inclusion of the truncation length and the Runge-Kutta step approximation the computational time for a hysteresis loop of a typical model corresponding to an array of 650 cubes took approximately a week.



Exact Runge-Kutta calculation.

Approximated Runge-Kutta calculation.

figure (6-11): Comparison between the transient states for a simulation with an exact and an approximated Runge-Kutta calculation.

The magnetisation of each cube was relaxed by the Landau-Lifshitz equation, integrated using the Runge-Kutta routine. The dynamic relaxation for all the cubes magnetisation continued until a stable dynamic minimum was achieved. This was identified by the magnetisation rotation for each cube in an iteration being less than a minimisation criteria, typically 0.01° . The minimisation criteria was determined for a particular set of micromagnetic parameters by running simulations with different criteria until an accurate and computationally fast criteria was found.

6.5 Simulation algorithm

The micromagnetic parameters for the particle being modelled were determined from the shape of the particle, its absolute size and the material of the particle.

The structure of the model was determined from the aspect ratio of the particle being modelled. For example, a particle with an aspect ratio of 3:1 was represented by an array of 5x5x15 cubes. The defined micromagnetic parameters for the particle were the type and magnitude of the crystalline anisotropy and the applied field direction within the jk plane. The calculated micromagnetic parameters were the magnetostatic and the exchange interaction constants h_{int} and C^* . These were calculated from the parameters of the material, its saturation magnetisation, its anisotropy constant, the value of the A^* parameter and the absolute distance between the magnetised cubes within the model.

A flow chart indicating the main features of the algorithm is presented in figure (6-12). For the determination of the simulation's hysteresis loop an external applied field loop was generated. Within this loop, the effective fields for all the cubes were simultaneously calculated, using the Jacobi technique. The magnetisation for each cube was then relaxed dynamically by the Landau-Lifshitz equation and integrated using the Runge-Kutta routine. After relaxation, the convergence criteria for all the cubes was tested. If all cubes passed, the simulation magnetisation in the applied field direction was saved and the external applied field updated. If any cubes failed, the simulation jumped back to the effective field calculation. The external applied field loop continued until the hysteresis loop of the model was completed.

As a further analytical tool in determining the reversal mechanism within a simulation, micromagnetic transient states were saved at the test for convergence within the hysteresis loop. These states were saved during simulation's reversal at magnetisations of 0.95, $\sum_{n=1}^{19} (1.0 - 0.1n)$ and -0.95.

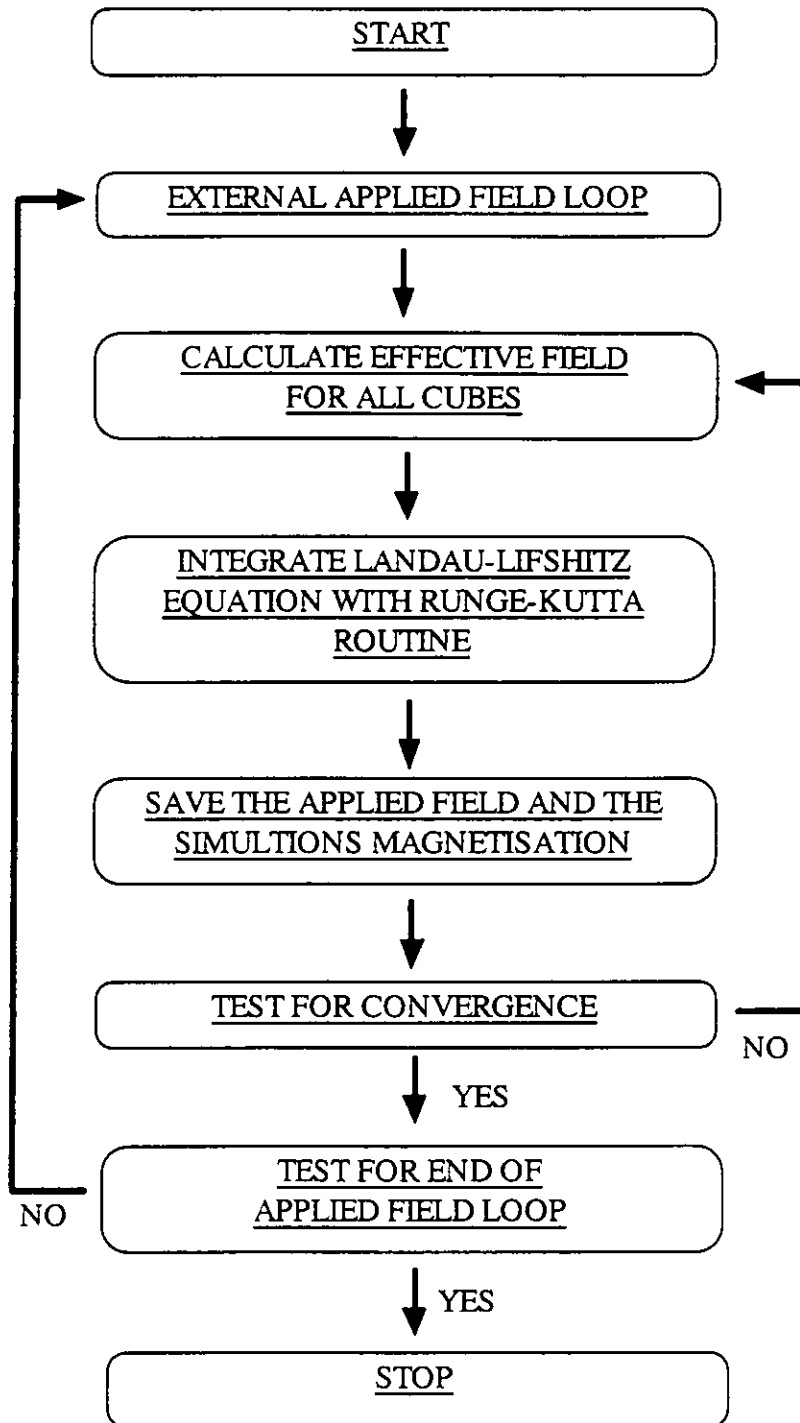


figure (6-12): Flow chart of simulations algorithm

6.6 Micromagnetic results and discussion

The developed model has been utilised in the investigation of commercial magnetic particles, $\gamma\text{-Fe}_2\text{O}_3$ and CrO_2 . Two aspects have been investigated; the simulation of particles measured experimentally in chapter 3 and the effect of model parameters on the simulation.

The simulation of the particles measured experimentally incorporated the physical parameters of particles measured in chapter 3 with the bulk parameters for the materials taken from the literature. The physical parameters were obtained from the results of the Scanning Electron Microscopy (SEM), where the length and diameter of the particles were measured. From these results, a *typical* particle was chosen. The structure of the simulation was then matched to the *typical* particle. For example, a *typical* particle with an aspect ratio of 6:1 was represented by an array of cubes $5 \times 5 \times 30$. As the SEM images were of insufficient clarity to identify surface irregularities, the magnitude of irregularities was approximated by a normal distribution. The magnitude of the distribution width was based on the type of material being simulated, a $\gamma\text{-Fe}_2\text{O}_3$ particle was taken as having a large number of crystal and surface imperfections [27-30], whereas a CrO_2 particle was taken as having few surface imperfection with a high degree of crystalline perfection [31-33]. The micromagnetic parameters for the simulations, h_{int} and C^* were calculated from the inter-cube separation and the bulk properties of the material. The inter-cube separation was derived from the actual physical dimensions of the *typical* particle and number of cubes used within the simulation.

The simulations assumed that the particle was composed of a single crystal with no bulk crystalline imperfections. This is in line with other workers [3-5], However, this is probably unrealistic for the majority of real $\gamma\text{-Fe}_2\text{O}_3$ particles [29]. The presence of bulk crystalline imperfections is likely to affect the reversal mechanism within a real particle. They may act as pinning sites or points of nucleation for reversal and could be reversal mode dependent.

Simulations on the *typical* particle were performed at different applied field angles with respect to the long axis of the model, its z axis. From the results of the

simulations, the switching field as a function of the applied field angle was measured and compared directly with the experimentally measured results for real particles, presented in chapter 3.

As there are many parameters within the developed model it was thought instructive to investigate the effect these parameters have on the simulation. These included, aspect ratio, particle size and the magnitude and type of surface irregularities. Due to limited computational time only the $\gamma\text{-Fe}_2\text{O}_3$ model was investigated in this way.

6.6.1 Simulations of a *typical* $\gamma\text{-Fe}_2\text{O}_3$ particle

The simulation parameters were derived to model the particles of Sample 2. This sample was chosen instead of sample 3 as more of its particles were measured using the SEM and so a more representative sample was obtained. Sample 1 was not chosen even though more particles were measured, since it appeared from the SEM images that these particles had poorly defined shapes compared to samples 2 and 3. This was unsurprising as sample 1 originated from the 1960's where as the other samples were produced in the 1980's.

The *typical* particle identified in sample 2 had an aspect ratio of 6:1 with a length of $0.6\mu\text{m}$. This was represented by a $5\times 5\times 30$ micromagnetic structure with pyramid ends and an irregular surface, presented in figure (6-9). The surface irregularity was represented by a normal distribution with a standard deviation of 10% of the cubes original width. $\gamma\text{-Fe}_2\text{O}_3$ parameters were taken from the literature as: the saturation magnetisation $M_s=340\text{kA/m}$ [34,35], the cubic crystalline anisotropy constant $K_1=-4.6\times 10^3\text{ J/m}^3$ [35] and the effective energy exchange constant $A^*=5.0\text{pJ/m}$ [3,5]. The cubic crystalline direction of $\gamma\text{-Fe}_2\text{O}_3$ particles are predominately in the $\langle 110 \rangle$ direction with respect to a long axis [27,30]. Similar models by other workers have used the $\langle 100 \rangle$ cubic crystalline direction or even uniaxial anisotropy [3,5]. For a direct comparison of the effect of different anisotropy directions, simulations have been performed with both cubic crystalline directions. The simulation parameters for the $\gamma\text{-Fe}_2\text{O}_3$ particles within this study are consistent with the numerical simulations of Schabes [3] and Yan *et al.* [5].

Simulations were performed at 5 different applied field angles 1° , 20° , 40° , 60° and 80° for both cubic crystalline directions. Simulations were not performed at 0° as this would create a purely symmetrical system for a model with no irregularities. Under these conditions reversal would be more difficult, as an unstable equilibrium condition occurs. An example of a simulated hysteresis loop indicating the critical parameters used in their evaluation can be found in figure (6-13).

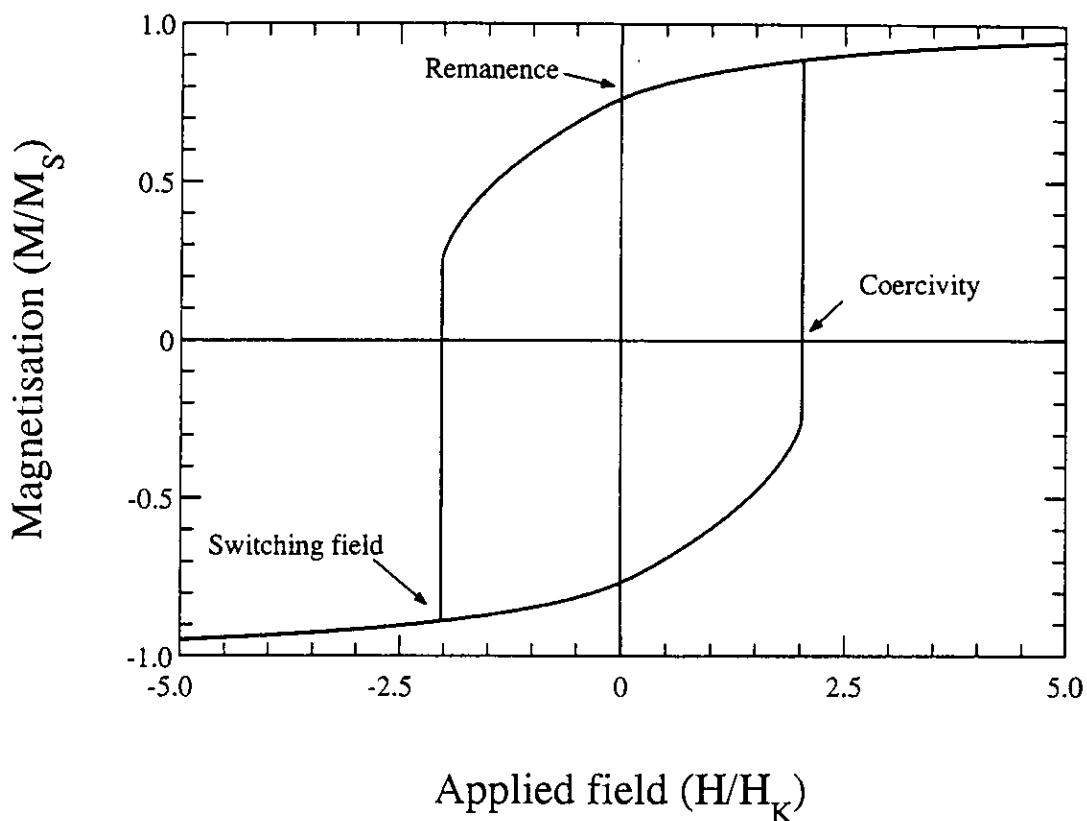


figure (6-13): Hysteresis loop for a simulated $\gamma\text{-Fe}_2\text{O}_3$ particle with a $\langle 100 \rangle$ cubic crystalline direction and an applied field direction of 40° .

From the simulated hysteresis loops, the switching field as a function of the applied field angle was generated and compared directly with two measured particles from sample 2, presented in figure (6-14). The measured switching field as a function of the applied angle was marginally more consistent for the simulation where the cubic crystalline axis was in the $\langle 100 \rangle$ direction rather than in the $\langle 110 \rangle$ direction. This is inconsistent with real $\gamma\text{-Fe}_2\text{O}_3$ particles which are likely to have predominately $\langle 110 \rangle$ cubic crystalline axis with respect to their long axis [27]. For the applied field angle $\theta=1^\circ$, the results for both cubic crystalline axes directions $\langle 100 \rangle$ and $\langle 110 \rangle$ were

consistent with the experimentally measured switching field. As the applied field angle increased, the discrepancy between the simulation results and the measured switching field became increasingly large. This could be attributed to assumptions and simplifications within the model, particularly the single crystal structure of the modelled particle, an over simplified model shape and the absence of any appropriate bulk crystalline imperfections.

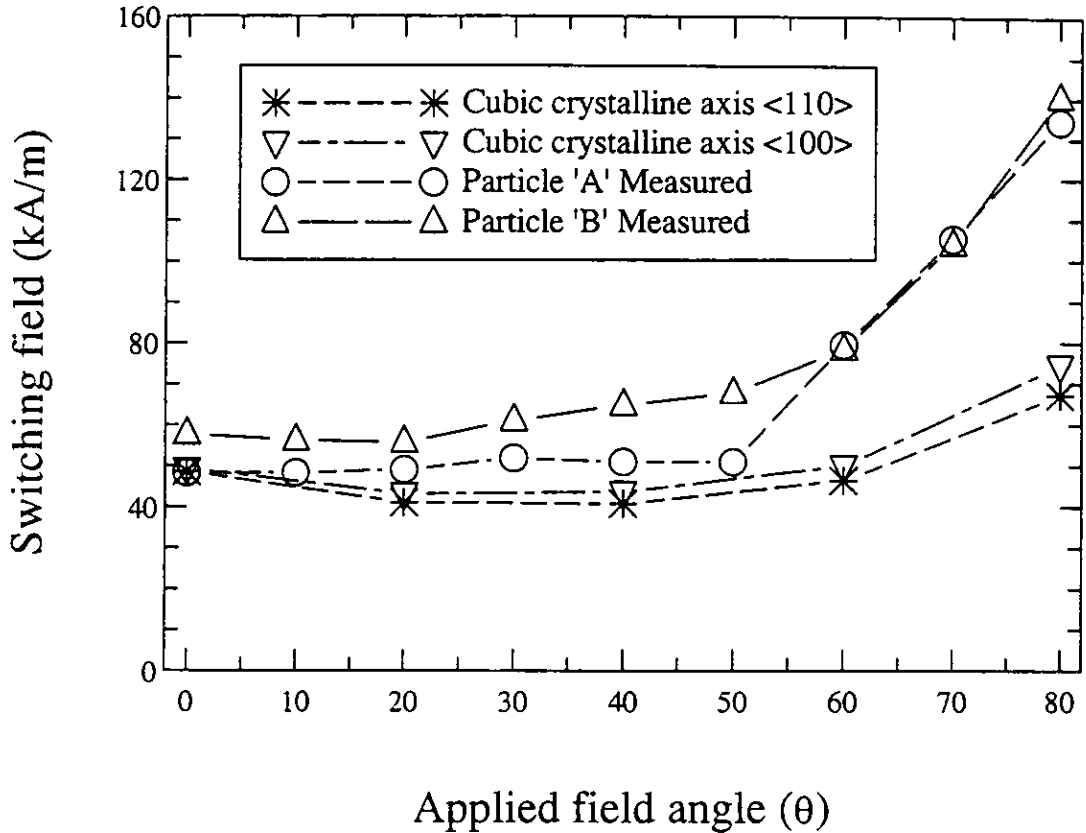


figure (6-14): Switching field as a function of the applied field angle.

The reversal mechanism for the simulations was investigated as a function of the applied field angle. This was achieved by examining transient states of the reversal mode. At low applied field angles less than and equal to 20° for both $\langle 110 \rangle$ and $\langle 100 \rangle$ cubic crystalline directions, the reversal mechanism is characterised by a vortex state, as described by Schabes *et al.* [24]. This state was initiated through the transformation of a flower state, as described by Schabes *et al.* [24] at remanence. It then propagated through the particle from one end to the other reversing the micromagnetic moments. An example of a typical vortex mechanism is shown in figure (6-15).

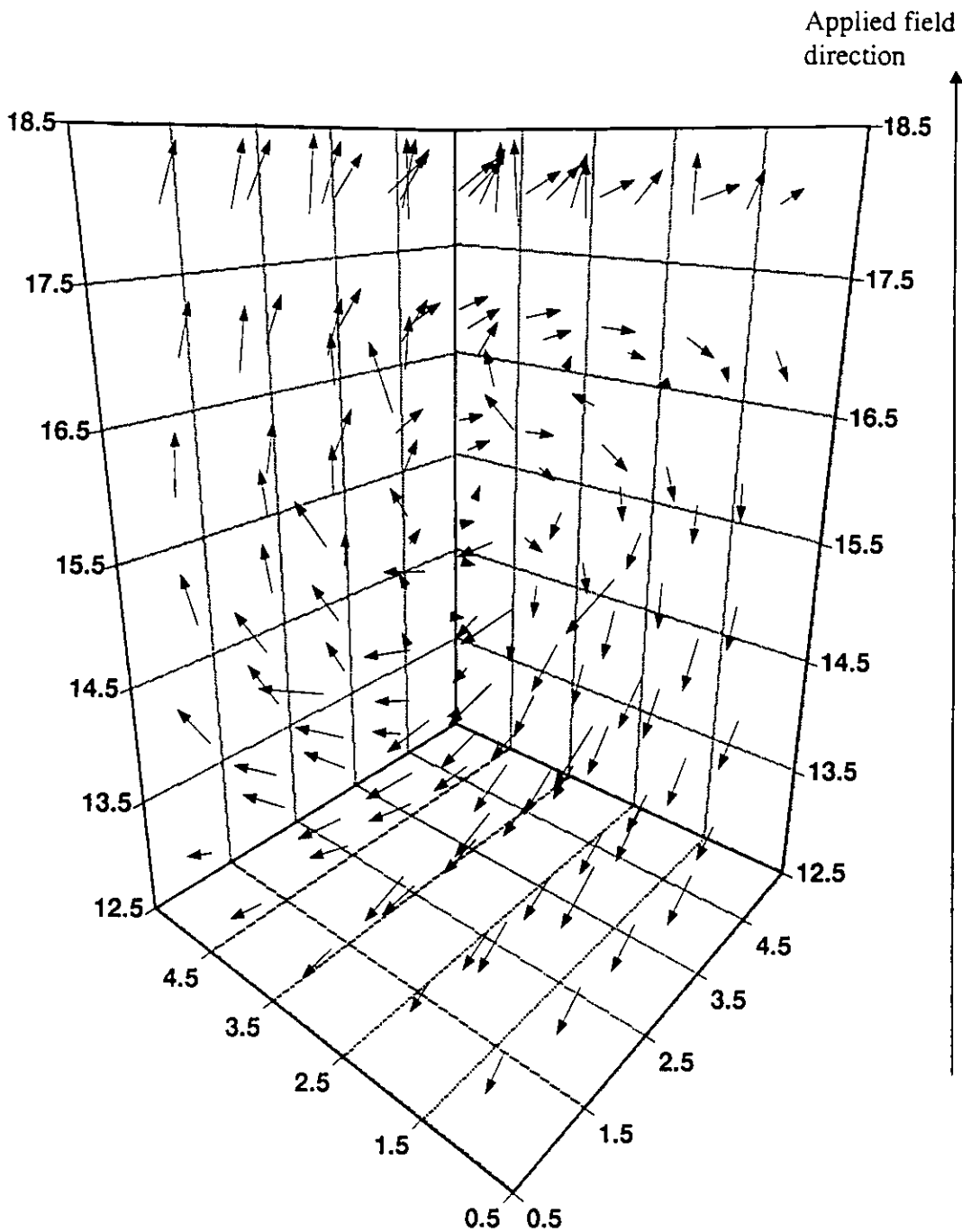


figure (6-15): Transient vortex configuration within the reversal mechanism of a modelled particle at coercivity.

As the applied field direction increased past 20° for both $\langle 110 \rangle$ and $\langle 100 \rangle$ cubic crystalline directions, the reversal mechanism became increasingly coherent. The crossover from an incoherent to a coherent reversal mode occurred through the transformation of the vortex state. As the applied field angle increased the vortex

enlarged until a point was reached where the vortex state could no longer be energetically supported and a more coherent reversal mode was initiated. Examples of the transient coercive state for the model with the cubic crystalline direction of $\langle 100 \rangle$ and the applied field directions of 1° and 40° are presented in figure (6-16) and figure (6-17).

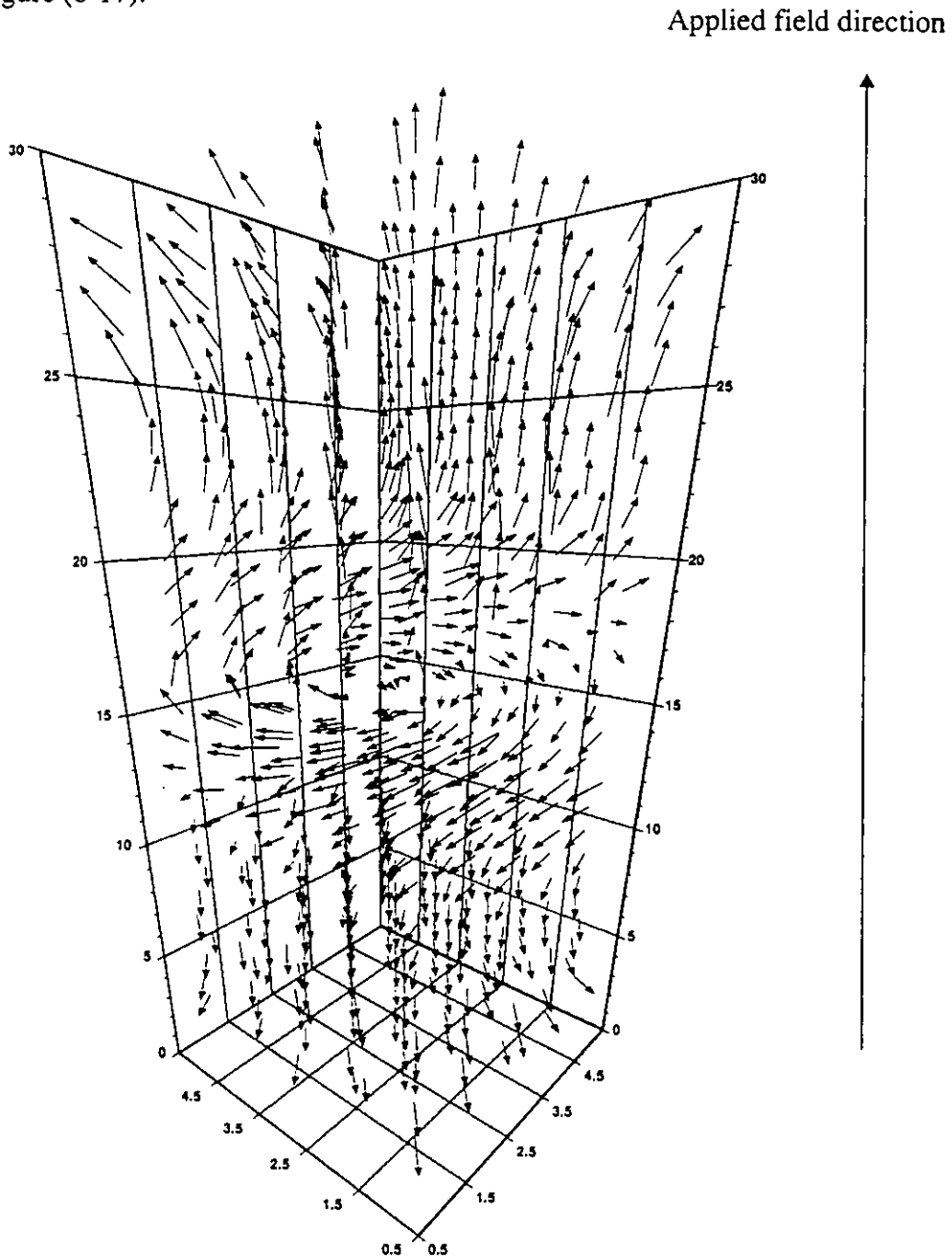


figure (6-16): Coercive state for an applied field direction of 1° with $\langle 100 \rangle$ cubic crystalline anisotropy, indicating a vortex reversal mechanism.

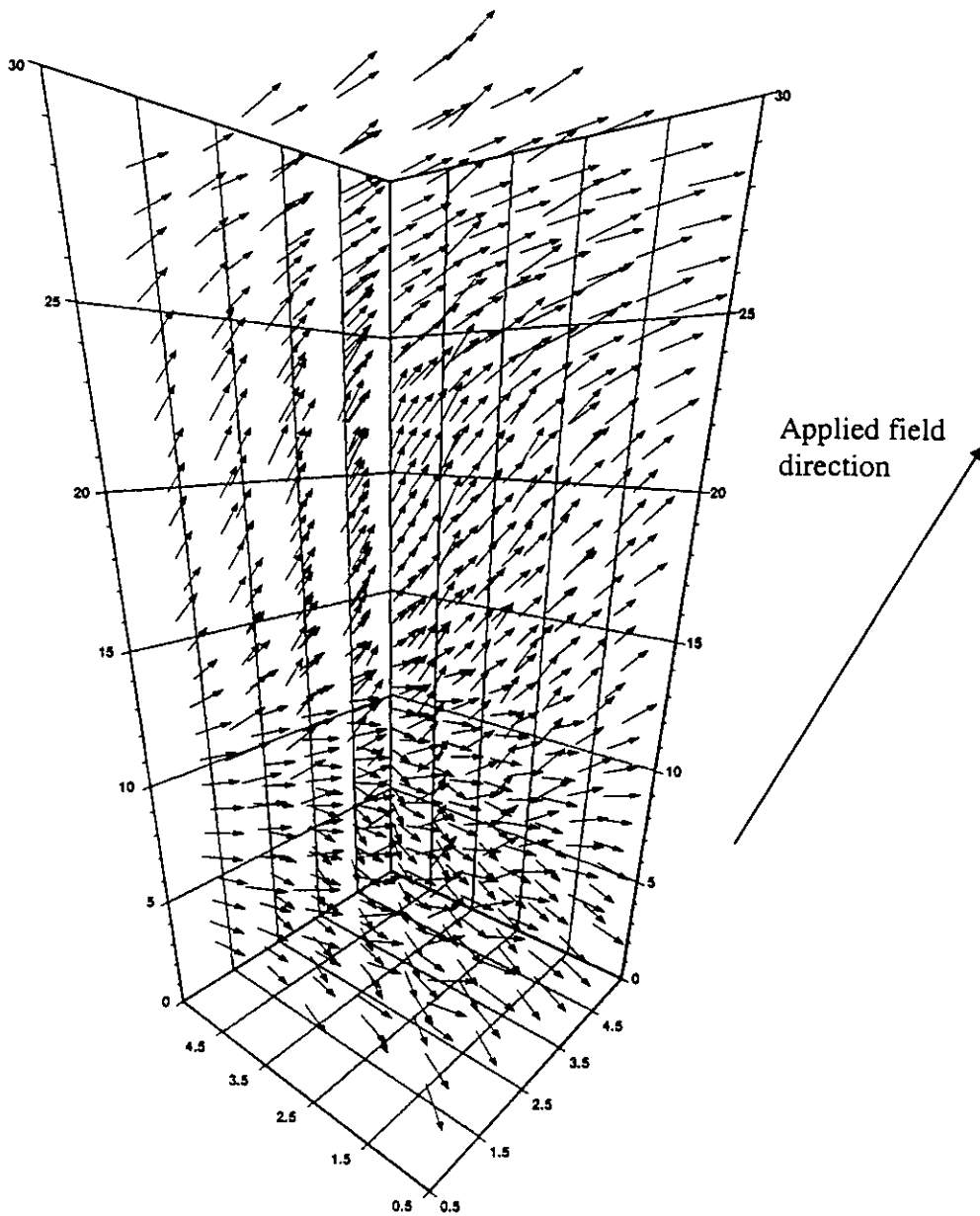


figure (6-17): Coercive state for an applied field direction of 40° with $\langle 100 \rangle$ cubic crystalline anisotropy, indicating a more coherent mode of reversal.

One possibility for the increased discrepancy between the measured switching field and the switching field of the simulation at large applied field angles could be the presence of bulk crystalline imperfections within the particles measured experimentally. These imperfections may have had a significant effect on different reversal mechanisms within the measured particles, either acting as nucleation sites or pinning sites during reversal. At low applied field angles the particle simulation indicated an incoherent reversal mechanism, characterised by a vortex configuration. This type of reversal might

easily accommodate the hard axes of bulk crystalline imperfection by deforming its micromagnetic microstructure, it may even act as a nucleation site, reducing the switching field of a particle. At larger applied field angles, the simulations indicated a more coherent reversal mode, which corresponded to the greatest discrepancy between the experimental results and those for the simulated particle. In coherent reversal the moments would have to propagate directly through a number of bulk crystalline hard axes, which would effectively oppose reversal and enhance the switching field of the particle. Thus, it could be proposed that bulk crystalline imperfections may act as weak nucleation or pinning sites for incoherent reversal, while these imperfections may act as pinning sites for coherent reversal.

6.6.2 The effect of model parameters on the $\gamma\text{-Fe}_2\text{O}_3$ particle simulation.

Since the micromagnetic model was so complex with a number of parameters, the effect of changes in these parameters, particularly on the switching field and the remanence, were investigated. These model parameters included aspect ratio, magnitude of A^* and surface irregularity.

The magnitude and type of surface irregularities can have a dominant effect on the properties of a magnetic particle. These surface irregularities can generate local variations within the demagnetising field which can either act as a nucleation site for reversal or a pinning site in opposing reversal. The two basic surface structures are a pit and a bump, illustrated in diagram A and diagram B of figure (6-18). A pit generates surface poles at its sides; these poles create a demagnetising field that opposes demagnetisation by the applied field. The bump also generates surface poles, but these poles create a demagnetising field that aids the external applied field in demagnetising the sample. Thus, bumps essentially act as nucleation sites for reversal and pits act as pinning sites for reversal.

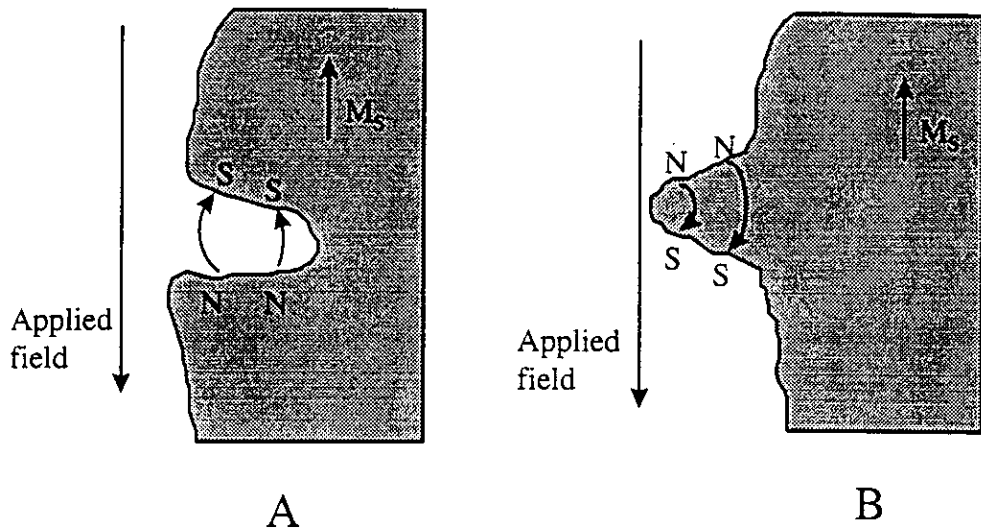


figure (6-18): The effect of localised fields near pits and bumps.

Using the *typical* $\gamma\text{-Fe}_2\text{O}_3$ particle parameters with the $\langle 110 \rangle$ cubic crystalline direction and an applied field direction of 1° the effect of different surface irregularities was investigated. The simulation's surface irregularity was defined by a normal distribution with a 10% standard deviation of the cubes original width. For a measure of the effect of different surface irregularities, 15 simulations were performed with the same standard deviation, but with a different set of random numbers.

A histogram of the switching field of these simulations was curve fitted with a Gaussian distribution and is given in figure (6-19). The width of this distribution, given as the particle consistency parameter σ/H_{MEAN} in chapter 3 allowed a direct comparison with the experimentally measured switching field distribution of sample 2.

The particle consistency parameter for the simulation results was calculated as 0.035. Its value was a factor of 4.1 smaller than that of the experimental results in chapter 3 for the $\gamma\text{-Fe}_2\text{O}_3$ particle of sample 2. This discrepancy could be attributed to either inaccurate modelling of the magnitude and type of surface irregularity or the imperfection free, single crystal nature of the model not being correct.

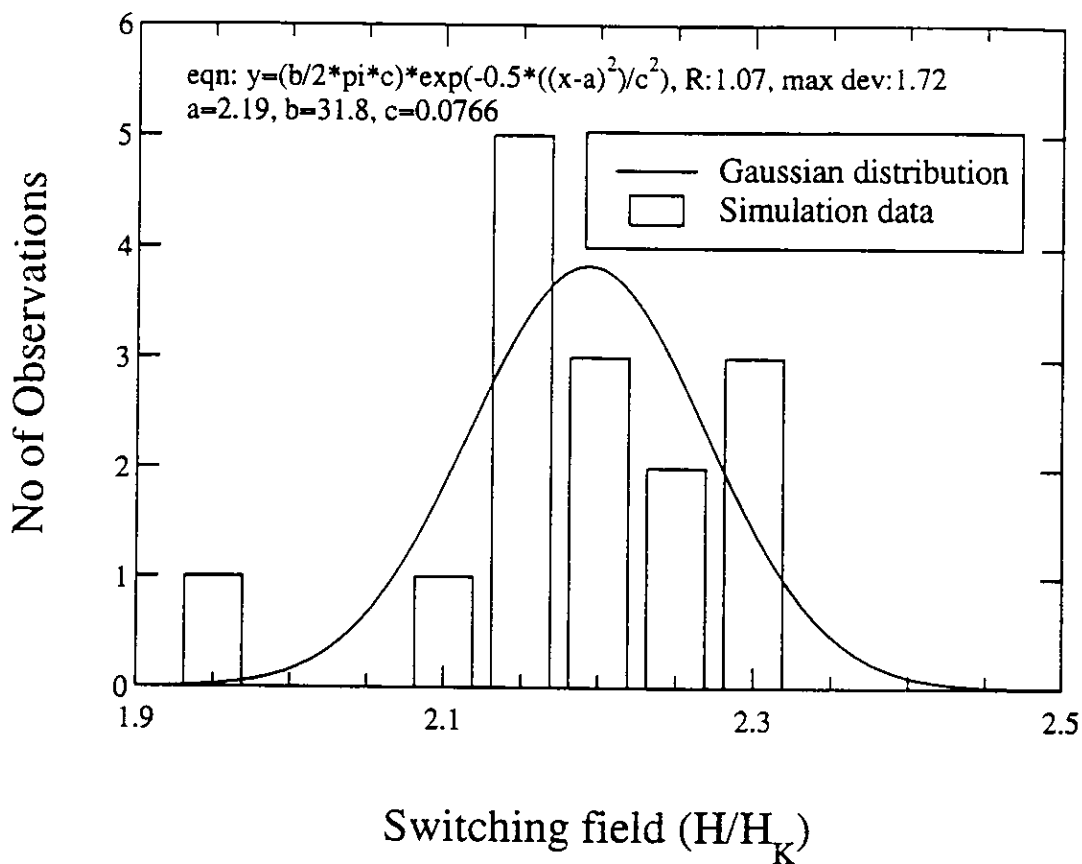


figure (6-19): Simulation switching field distribution for a normal distribution with a width standard deviation of 10% of the original width of a cube.

The effects of the magnitude of surface irregularities at different applied field angles were also investigated using the *typical* $\gamma\text{-Fe}_2\text{O}_3$ particle parameters with the $\langle 110 \rangle$ cubic crystalline direction. Simulations were performed with different surface irregularity magnitudes, defined by the magnitude of the standard deviation in the normal distribution. The results of these simulations, given in figure (6-20) indicate that as the magnitude of the surface irregularities increase, nucleation of the reversal mode occurs at lower applied fields. Thus, surface irregularities act as points of nucleation for reversal. It would also appear that the effect of surface irregularities at the different applied field angles was similar. This would seem to indicate that the different reversal mechanisms at the different applied field angles were affected by a similar amount by the surface irregularities.

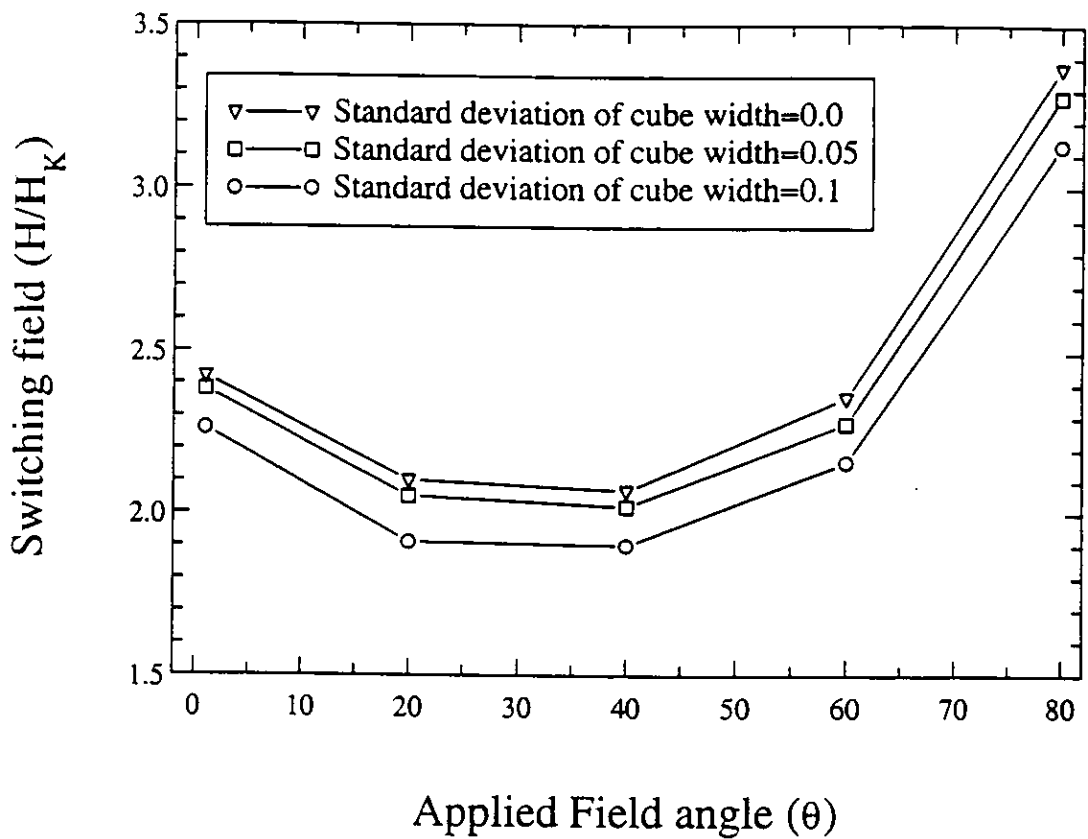


figure (6-20): The effect of the surface irregularity magnitude on switching field as a function of the applied field angle for the *typical* $\gamma\text{-Fe}_2\text{O}_3$ particle parameters with $\langle 110 \rangle$ cubic crystalline direction.

A model with no surface irregularities is unrealistic, as real particles are not purely symmetrical. This is emphasised by examining the reversal mechanism for a smooth regular model particle. The reversal mechanism within these models is initiated simultaneously from both ends of the particle. The reversal then sweeps through the model towards the centre. An example, of this type of reversal shown at coercivity, giving a symmetrical micromagnetic microstructure can be seen in figure (6-21). Coercivity of the same model with added surface irregularities can be seen in figure (6-22). A cursory examination of both micromagnetic microstructures shows the dramatic effect surface irregularities can have on the reversal mechanism within a model. The model with no surface irregularities appears to have a more coherent reversal mode, characterised as two coherent reversal layers, while the model with surface irregularities appears to have a more incoherent reversal model, characterised by a single vortex reversal structure.

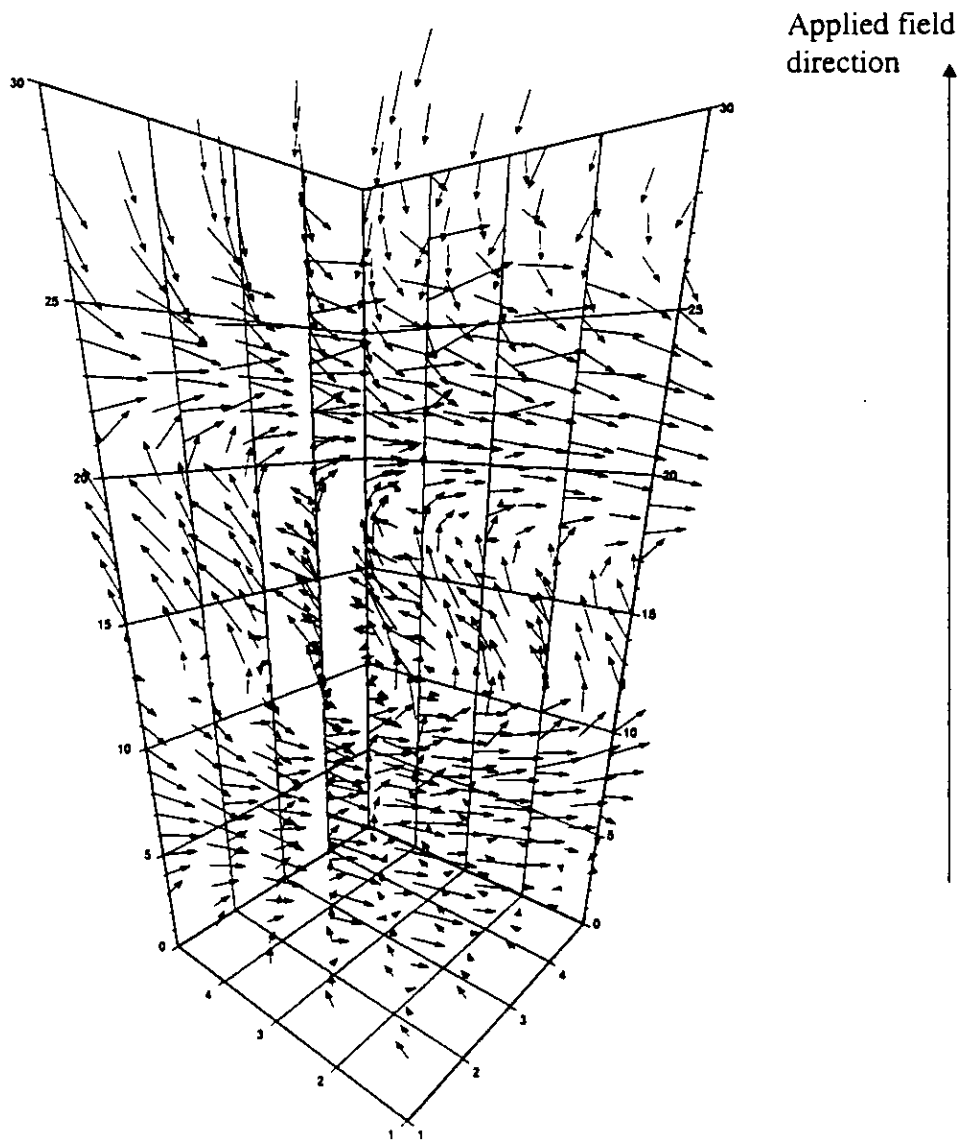


figure (6-21): Coercive state for an applied field direction of 1° with $\langle 110 \rangle$ cubic crystalline anisotropy and no surface irregularities.

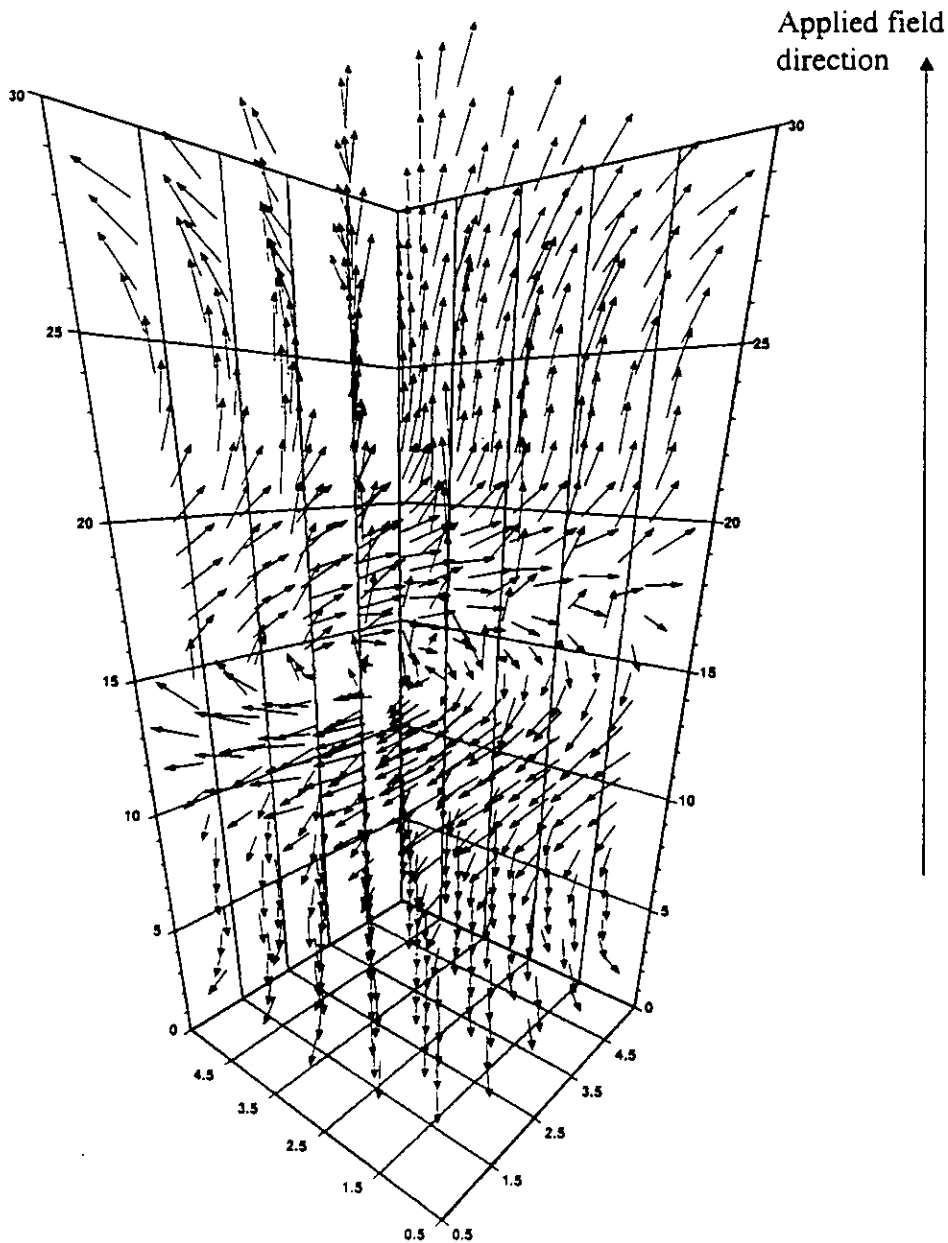


figure (6-22): Coercive state for an applied field direction of 1° with $\langle 110 \rangle$ cubic crystalline anisotropy and surface irregularities defined by a normal distribution with a standard deviation of 5% of the cube's original width.

The effect of symmetry within the developed model has been shown to create unrealistically symmetrical reversal mechanisms. As a consequence of this study all further investigations into the effect of different model parameters were performed on models with surface irregularities. Unfortunately, this led to a problem of different models having different surface irregularities, so the comparison of "like with like" was not exactly being performed. For example, when comparing models with different

aspect ratios it should be noted that their surface irregularities were different, although these surface irregularities had the same distribution width. Apart from this disadvantage, it was thought more appropriate to model more realistic reversal mechanisms and gain an insight into the general trends of the reversal mechanism when the structure of the model is changed.

In this study the effect of changes to A^* on the simulations results has been investigated. The parameter A^* as stated in section 6.4.3 defines the magnitude of the exchange coupling between adjacent cubes, the higher its value the greater the coupling and the greater the local moment alignment. Within the literature on the modelling of magnetic thin films and commercial magnetic particles the value of A^* has been proposed to be within the range 1.0-10.0pJ/m [3,5].

Simulations have been performed with the *typical* $\gamma\text{-Fe}_2\text{O}_3$ particle parameters of the previous section with the applied field direction of 1^0 and a cubic crystalline direction of $\langle 110 \rangle$. The results of these simulations are given in figure (6-23). They indicate that switching field and remanence are dependent on the exchange energy constant A^* . The switching field increased with A^* , although as A^* increased beyond 5.0pJ/m the switching field started to saturate. These characteristics are a result of a change in the reversal mechanism as a function of A^* . At low values of A^* ($<5.0\text{pJ/m}$) the magnetostatic energy was dominant and a vortex reversal mode was energetically favourable. As the value of A^* increased the exchange energy starts to dominate and a more coherent reversal mode becomes energetically favourable. With further increases in A^* the switching field saturates, indicating a coherent reversal mode. The results of the remanence as a function of the exchange energy constant indicated the effect of the demagnetising field. At low values of A^* ($<3.0\text{pJ/m}$) the demagnetising field was dominant creating a flowering state, reducing the remanence of the simulation.

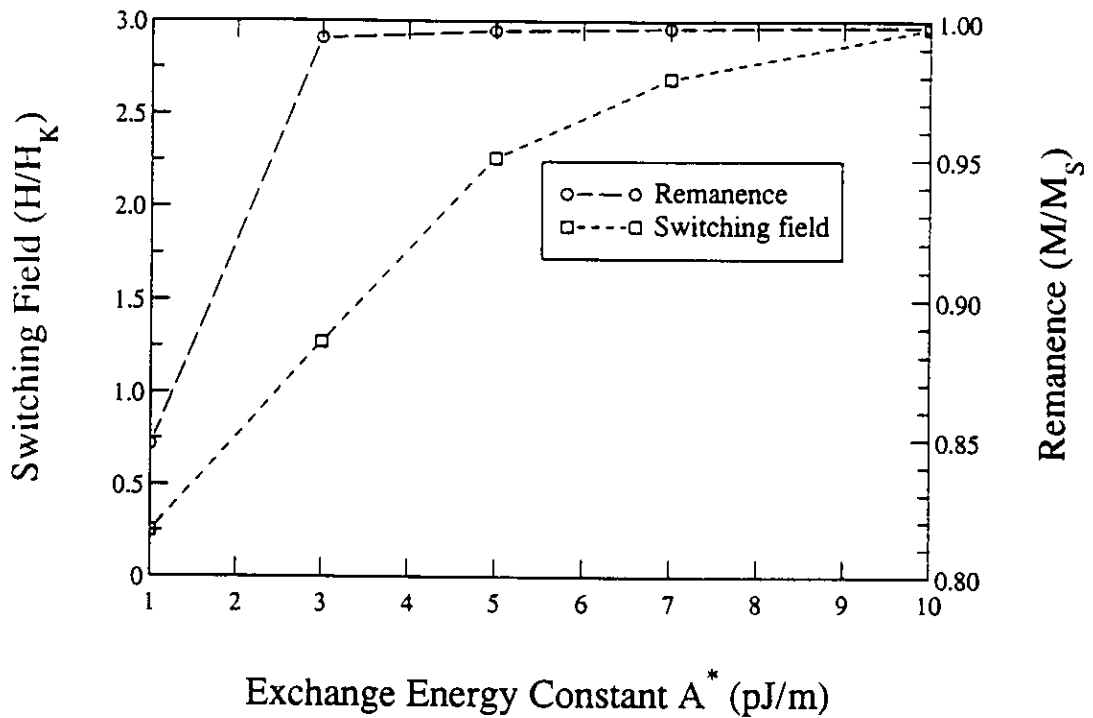


figure (6-23): Switching field and Remanence of a *typical* $\gamma\text{-Fe}_2\text{O}_3$ particle as a function of the exchange energy constant A^* .

The effect of changes in A^* on the switching field as a function of the applied field angle has also been investigated. Simulations for the *typical* $\gamma\text{-Fe}_2\text{O}_3$ particle parameters with exchange energy constants of 5.0 and 7.0 pJ/m are presented in figure (6-24). The results show that the switching field for $A^*=7.0\text{pJ/m}$ are consistently higher than for $A^*=5.0\text{pJ/m}$; this is particularly marked at low applied field angles. These results seem to indicate that an increase in A^* promotes a more coherent reversal mode at all applied field angles. At low applied field angles, the reversal modes are more incoherent, thus an increase in A^* had a more pronounced effect on its reversal mechanism and a more striking increase in the switching field was observed. At the higher applied field angles, a more coherent mode of reversal occurred and the effect of an increase in A^* was a slight increase in the coherent mode, identified by marginal increase in the switching field. At 40° the switching field for the simulation with the exchange energy constant of 5.0pJ/m was marginally higher than for the exchange energy of 7.0pJ/m. This result could explained by different reversal mechanisms which have different angular dependence occurring for the different exchange energy constants.

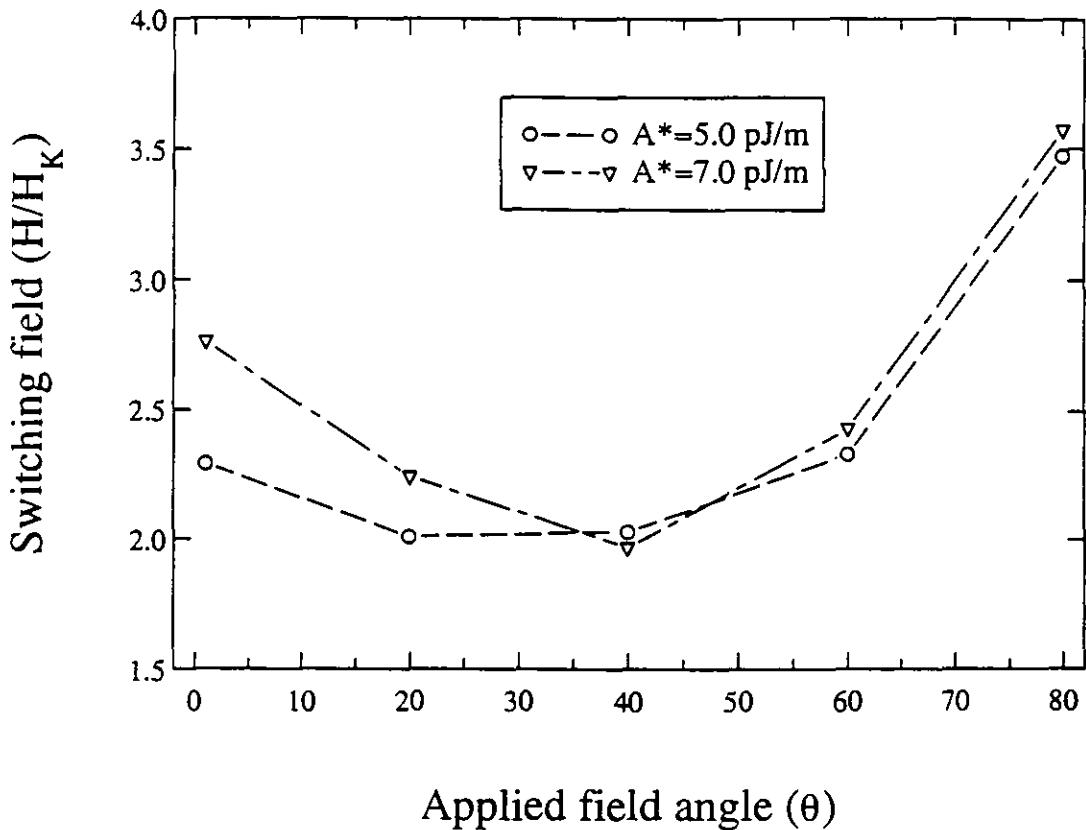


figure (6-24): Switching field as a function of the applied field for the *typical* $\gamma\text{-Fe}_2\text{O}_3$ particle parameters.

For understanding of the effect of changes in the aspect ratio, a number of simulations using the *typical* $\gamma\text{-Fe}_2\text{O}_3$ particle parameters with a $\langle 100 \rangle$ cubic crystalline direction and a length of $0.6\mu\text{m}$ were performed. The switching field as a function of the applied field angle for aspect ratios of 3:1, 4:1, 5:1 and 6:1 is presented in figure (6-25).

As the aspect ratio increased from 3:1 to 6:1, the volume of the model reduced by a factor of 4.1 and its demagnetising field reduced by a factor of 2.5. A smaller volume would suggest a reduced switching field assuming coherent reversal. A larger aspect ratio, reducing the demagnetising field would suggest an increased switching field. The results from the simulations showed that as the aspect ratio increased the switching field increased at all the applied field angles. These results would seem to imply the dominate effect the reduction in the demagnetising field can have on the reversal mechanism. In this case, reducing the demagnetising field aided coherent reversal at all the applied field angles.

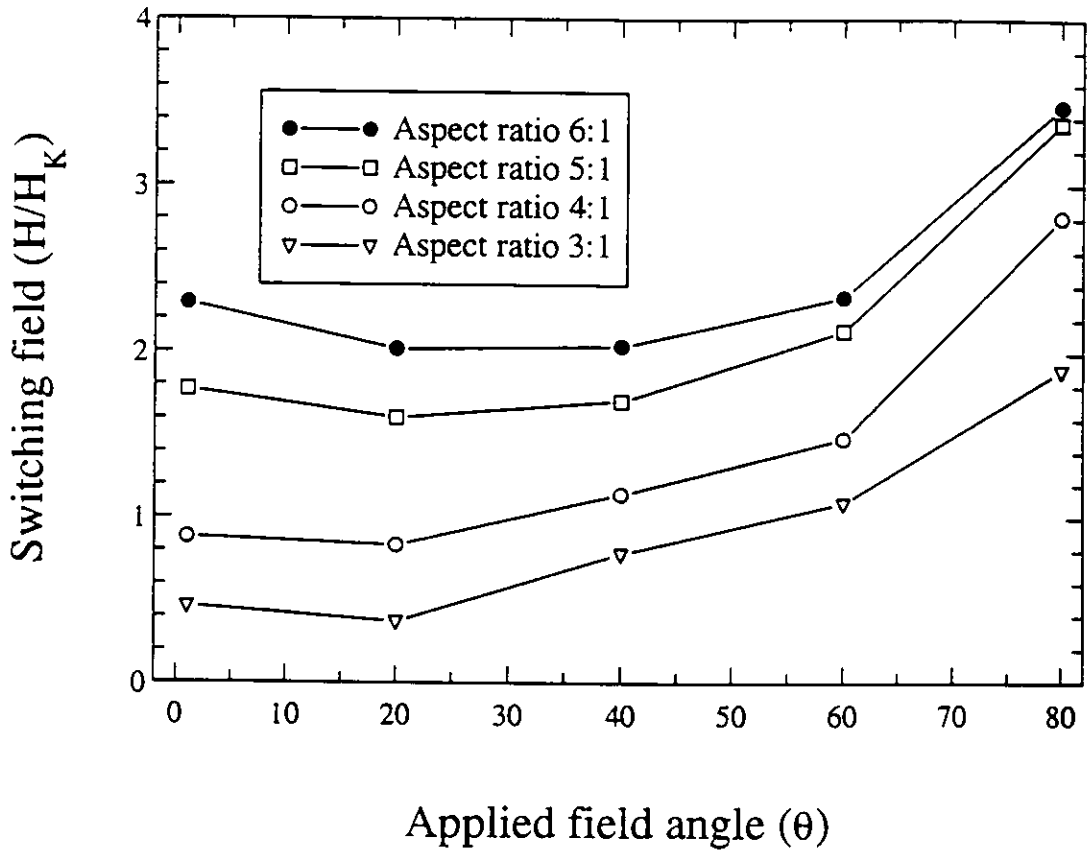


figure (6-25): Switching field for the *typical* $\gamma\text{-Fe}_2\text{O}_3$ particle with different aspect ratios as a function of the applied field angle.

Simulations using the *typical* $\gamma\text{-Fe}_2\text{O}_3$ particle parameters were also performed at the applied field angle of 1° for an extended range of aspect ratios. The results, given in figure (6-26), indicate a definite change in the reversal mechanism around an aspect ratio of 5.5:1. Examples of the reversal mechanism at coercivity for the aspect ratio 4:1 and 9:1 are presented in figure (6-27) and figure (6-28).

The reversal mechanism at coercivity for the simulation with an aspect ratio of 4:1 indicates the formation of two pronounced vortex structures. The formation of two reversing mechanisms within a particle was quite unusual in this numerical study, usually only one reversal mode was produced which then propagated through the particle. The reversal mechanism at coercivity for the 9:1 simulation indicated reversal by a coherent layer that propagated through the model reversing its micromagnetic moments.

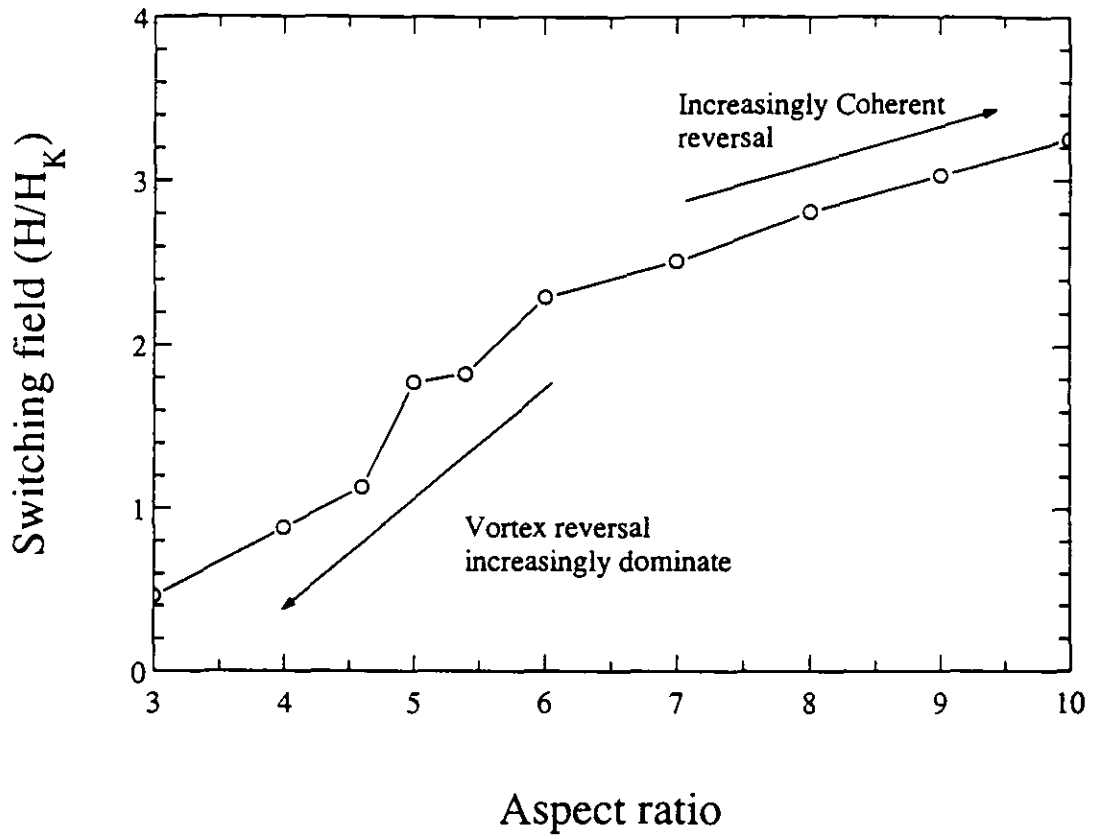


figure (6-26): Switching field as a function of aspect ratio using the typical $\gamma\text{-Fe}_2\text{O}_3$ particle parameters.

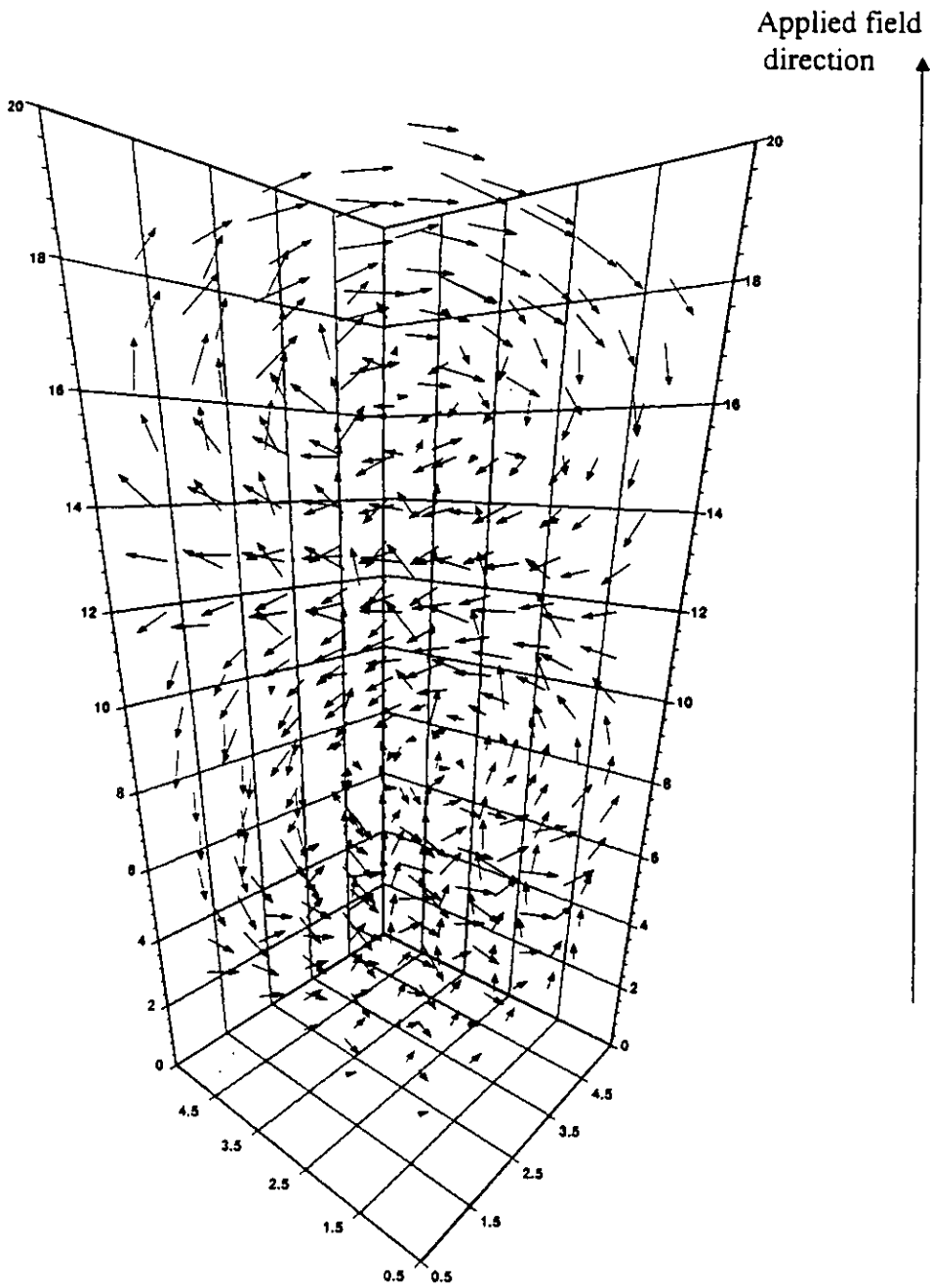


figure (6-27): The reversal mechanism at coercivity for the simulation with an aspect ratio of 4:1.

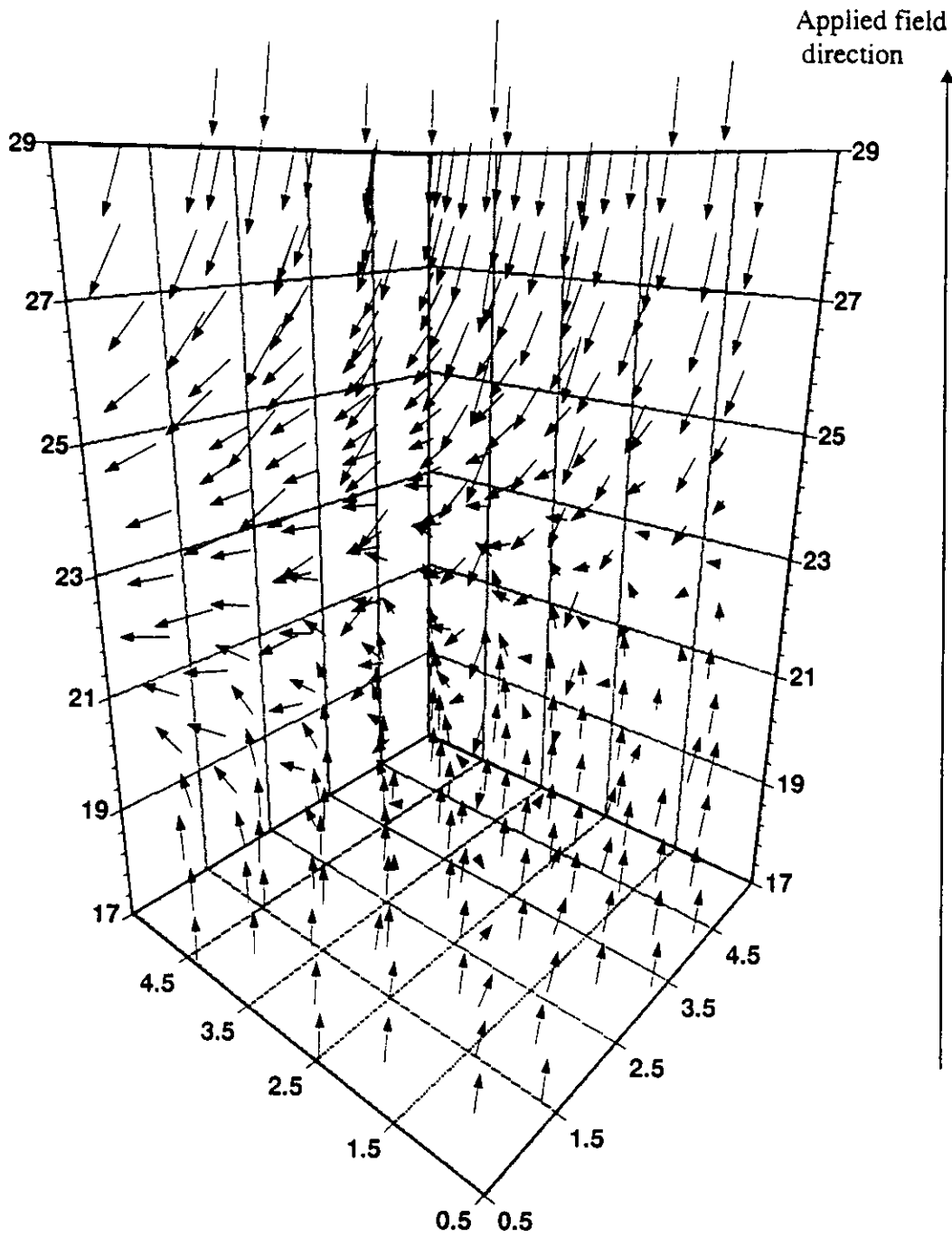


figure (6-28): The reversal mechanism at coercivity for the simulation with an aspect ratio of 9:1.

6.6.3 Simulations of a *typical* CrO₂ particle

Simulation parameters were derived to model the CrO₂ particles of sample 4. This sample was chosen as more of its particles were measured with the SEM than in sample 6 and so a more representative sample was obtained. Sample 5 was not chosen as its aspect ratio distribution was much broader than sample 4.

The *typical* particle chosen from sample 4 had an aspect ratio of 5:1 with a length of 0.6µm. This was represented by a 5x5x25 micromagnetic structure with pyramid ends and an irregular surface. Chromium dioxide particles are known to have a high degree of crystalline perfection with few surface imperfections [31,34]. As a consequence, the surface irregularities were described by a normal distribution with a narrow standard deviation width, 1% of the cubes original width.

The model parameters taken from the literature were saturation magnetisation $M_s=370\text{kA/m}$ [34,35], uniaxial crystalline anisotropy constant $K_1=-2.5\times 10^4\text{ J/m}^3$ [35] and an effective energy exchange constant $A^*=5.0\text{pJ/m}$ [3,5]. There is still uncertainty within the literature on the magnetocrystalline easy axis direction/directions within chromium dioxide particles. It has been reported by Cloud [36] that the directions of the easy magnetisation axes within Chromium dioxide lie in (100) planes at an angle of $\sim 40^\circ$ to a tetragonal axis. Other workers, Rodbell and Muller *et al.* [37,38] proposed that the chromium dioxide easy axis was parallel to its needle axis (c-axis). Due to computational time constraints, simulations were only performed with uniaxial anisotropy along the needle axis of the model.

For a direct comparison with the experimental switching field data of sample 4, simulations were performed at 5 different applied field angles 1° , 20° , 40° , 60° and 80° . From the simulated hysteresis loops, the switching field as a function of the applied field angle was generated and compared directly with two measured particles of sample 4, presented in figure (6-29).

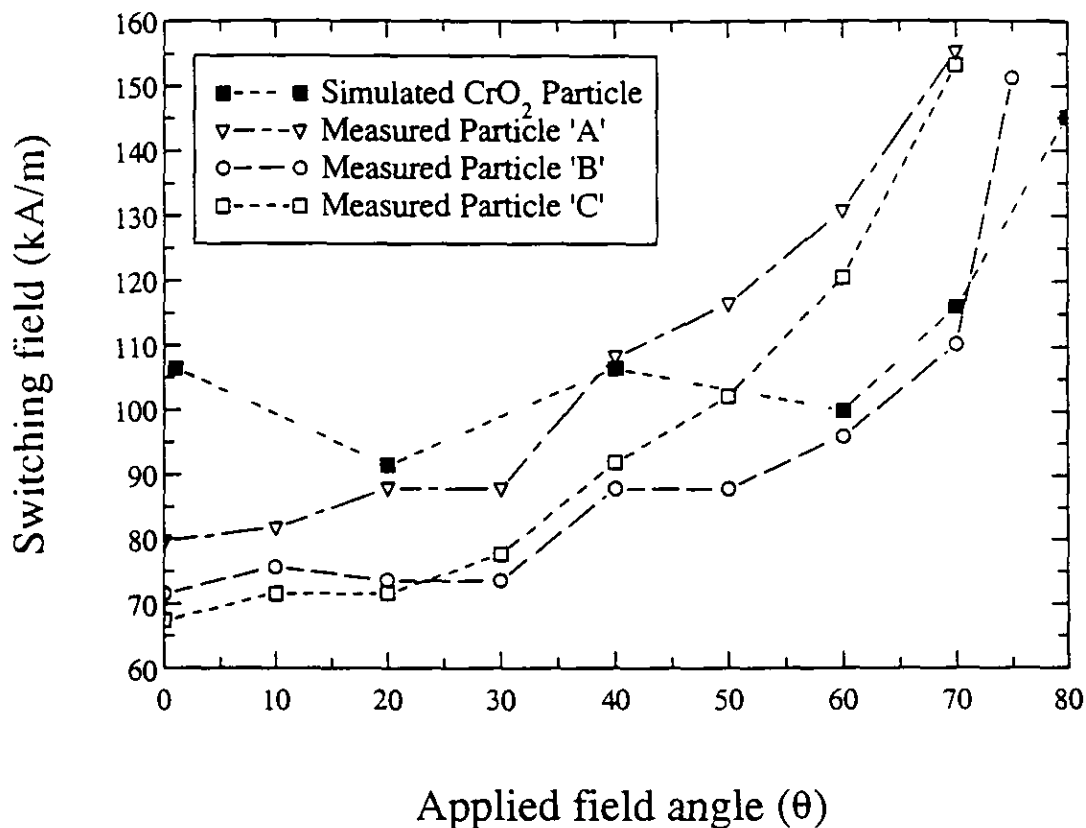


figure (6-29): Switching field as a function of the applied field angle.

The switching field angular dependence of the CrO_2 model showed some agreement with the measured particles characteristics. The models switching field at low applied field angles ($<20^\circ$) was significantly greater than that of the measured particles. At higher applied field angles 20° - 60° the models switching field remained approximately constant ($\sim 100\text{kA/m}$). At the large applied field angles ($>60^\circ$) the measured particles switching field increased markedly more than the switching field of the model. The discrepancies between the properties of the measured particles and the model might be attributed to an over simplified model shape, the presence of bulk crystalline imperfections or the correct degree of surface irregularities.

The reversal mechanisms within the CrO_2 particle simulations were characterised by having two coherent reversal layers at coercivity for applied field angles of less than and including 40° . Above 40° the reversal mechanism was similar at those angles to the mechanisms found in the $\gamma\text{-Fe}_2\text{O}_3$ particle model, where the reversal mechanism was tending towards coherent reversal.

An interesting point was that at low applied field angles ($<40^\circ$) two reversal layers were initiated in the CrO_2 particle model, while only one was initiated in the $\gamma\text{-Fe}_2\text{O}_3$ particle model. This could be attributed to the degree of surface irregularities within the respective models. A model with a low degree of surface irregularities might initiate reversal at both its ends at similar fields, while a model with a high degree of surface irregularities could initiate reversal from either end at quite different fields. So for models with a high degree of surface irregularities a race condition could occur, where reversal is initiated at one end, it then propagates through the model before reversal can be initiated at the other end.

Chapter Seven

7.1 Conclusions and further work

Interaction effects in recording media have been investigated by comparing the measured properties of isolated particles with the measured bulk properties of the media they constitute. It has been found that the interaction effects can significantly affect the characteristics of a medium.

The effect of interactions within the $\gamma\text{-Fe}_2\text{O}_3$ and the CrO_2 was in line with the findings of Knowles [1] and was consistent with the modified Henkel plots for these samples, which indicated demagnetising or negative interactions. These measurements and the analysis can be described by a mean field approximation which shifts the sample's coercivity and hence its SFD to lower fields. The results for the metal particle system, sample 7, were contrary to the mean field approximation, since the effect of interactions was to shift the SFD to higher field values. This indicates positive interactions, i.e. interactions that oppose demagnetisation. This result was contrary to the modified Henkel plot for this sample and the findings of other workers [2] who have investigated metal particle media. Thus, it was proposed that at a microscopic level local inter-particle interactions appear to enhance the switching field and dominate the behaviour of individual particles. At a macroscopic level, however, behaviour is still predominantly that of a system in which interactions are demagnetising. These findings appeared to be contradictory.

A suggestion for resolving this contradiction was found in the modelling study of Lyberatos and Wohlfarth [3]. In their study, chains of particles were introduced into a particulate system. This had the effect of increasing the system's coercivity; however, Henkel plots showed that interactions between adjacent chains dominated and exhibited an overall demagnetising behaviour. Only in very dilute systems did the interactions between particles in the chains start to dominate and produce positive interactions. It was therefore suggested that in the metal particle system studied there may be very

strong local alignment of particles which had the effect of increasing the system coercivity whilst not affecting the general negative interactions characteristic of all acicular particulate media.

The packing densities evaluated from the SFD means of the individual particles and the experimentally determined SFD means within the $\gamma\text{-Fe}_2\text{O}_3$ and CrO_2 particulate media were approximately 0.65 and 0.55 respectively. These calculated values are high for commercial particulate media, where the volumetric packing density is of the order of 0.4 [4,5]. This discrepancy might be attributed to the localised formation of agglomerations within the samples, effectively increasing the media's packing density and increasing the localised interaction field within an agglomeration.

Theoretical work by Coverdale *et al.* [6,7] and Satoh *et al.* [8] on fluid dispersions and on the microstructure of dried coatings supports these conclusions. Their investigations have indicated the presence of particle bundles and the formation of voids within the dried media. This would effectively increase the packing density of the media, increasing the localised interactions and thus reducing its coercivity.

As there is a general trend towards smaller particulates, MP^{++} for example, the microscopic technique utilised within this study has become inadequate to observe this new generation of particles. To further the research into the magnetic and physical properties of isolated particles an extension to the technique with the use of electron microscopy has to be employed. Lederman *et al.* [9,10] have already used this technique utilising electron microscopy in the investigation of experimental $\gamma\text{-Fe}_2\text{O}_3$ particles with very few surface imperfections. These particles exhibited a coherent reversal mechanism at large applied field but as the applied field angle θ approached zero, curling became the more probable reversal mechanism. These results are significantly different to the reversal mechanisms of the commercial particles examined in this study. This difference highlights the importance of continuing this work into the characterisation of the next generation of *commercial* particles.

Both an experimental and a modelling study of the effect of chaining of particles within metal particle media would be of interest, in particular studying the effect of chaining within the recording process. As chaining might effectively lock particles together magnetically, the minimum transition width within the media might increase

reducing its storage density. Another consequence of chaining might be an increased level of noise relating to the physical size of the magnetic structure created by the chains.

The study of chaining could be furthered by the production of aligned and random samples of particulate media which are susceptible to chaining. The characterisation of these samples, in particular the properties of the particles which constitute the media, their media's SFD and their noise characteristics would be insightful in investigating the presence and effect of chains within particulate media. It would also be interesting to investigate the presence of chains during the production of a medium. This investigation could explain at what stage chains are formed during the production process. The presence of chains within the dispersion could be identified with technique developed in this study. In essence, the presence of chains can be revealed by comparing the characteristics of the particles within the dispersion and the properties of medium produced from the dispersion.

A micromagnetic model was developed to simulate the reversal mechanisms within the commercial magnetic particles studied experimentally. The model represented the finite shape of a particle, its bulk magnetic properties and its surface irregularities. The model was used to simulate the hysteresis loop of a particle measured experimentally. From this loop, the switching field was obtained and compared directly with the experimentally measured switching fields for particles with similar physical dimensions. The effect of changes in model parameters on the results of the simulation was also investigated; in particular how the particle's shape affects its measured switching field.

The simulations representing *typical* $\gamma\text{-Fe}_2\text{O}_3$ particles indicated reasonable agreement at the lower applied field angles between the measured switching field of a particle and the switching field of the simulation representing the particle. As the applied field angle increased the measured switching field of the particles increased more markedly than the switching field of the simulation. This discrepancy between the switching field of the particles and the simulation increased with the applied field angle. It was believed that this was a consequence of assumptions and simplifications within

the model, particularly the absence of bulk crystalline imperfections and the effect of an oversimplified particle shape.

The simulations of $\gamma\text{-Fe}_2\text{O}_3$ with different surface irregularities showed the dramatic effect irregularities had on the reversal mechanism and the switching field of a model. The greater the degree of surface irregularities the lower the switching field of the model and the more incoherent its reversal mechanism. It was found that surface irregularities acted as nucleation sites for reversal, lowering the switching field of the model. The study of irregularities also highlighted the problems of models with symmetrical microstructures. These models generate purely symmetrical reversal mechanisms, which have a higher switching field than for models with surface irregularities. As the real particles used within the magnetic media industry are unlikely to be symmetric, models representing these commercial magnetic particles should contain surface irregularities, as in this study.

The exchange energy constant A^* was investigated for a model representing a $\gamma\text{-Fe}_2\text{O}_3$ particle. The results indicated that as A^* increased the exchange energy started to dominate the reversal mechanism and the reversal mechanism became more coherent.

The effect of aspect ratio on simulations representing $\gamma\text{-Fe}_2\text{O}_3$ particles was also investigated. The results indicated that as the aspect ratio of the model increased, the reversal mechanism became more coherent. This was the result of a reduced demagnetising field as the aspect ratio of the model increased.

The simulations representing a *typical* CrO_2 particle measured in chapter 3 indicated reasonable agreement at the higher applied field angles. At the lower applied field angles the switching field of the model was significantly higher than the switching field of the measured particle. This observation could be the result of assumptions and simplifications within the model, particularly the absence of bulk crystalline imperfections, the degree of surface imperfections and the effect of an oversimplified particle shape.

Overall, the model developed in this study can be considered as a success. It modelled, within expectable errors, the properties of *typical* $\gamma\text{-Fe}_2\text{O}_3$ and CrO_2 particles. It also indicated the effect of surface irregularities on the properties of real particles, in particular how surface irregularities can act as points of nucleation for reversal and how

they can broaden the switching field distribution for an ensemble of particles. The investigation of aspect ratio and particle size on the properties indicated qualitative results similar to those of other workers [11,12].

As with most micromagnetic simulations improvements could be made by increasing the number of elements in the model. Other improvements could include an exact calculation of the magnetostatic field instead of the point dipole approximation, an accurate representation of the particles surface irregularities and a representation of bulk crystalline imperfections. As crystalline imperfections are likely to be of the order of the atomic structure it is impracticable to model them accurately at the present time. However, a three dimensional irregular shaped model with each segment having its own easy axes directions would be a step forward. This would further avoid any symmetry effect and make the model more realistic.

Bibliography

8.1 References for chapter 1

- [1] J. Crangle. *Solid State Magnetism*, Anonymous Edward Arnald, 1991.
- [2] D. Jiles. *Introduction to magnetism and magnetic materials*, Anonymous London: Chapman and Hall, 1989.
- [3] P. C. Scholten, Which SI? *J. Magn. Magn. Mater.* vol. 149, pp. 57-59, 1995.
- [4] P. Weiss, *J. de Phys.* vol. 6, pp. 661-1907.
- [5] P. Langevin, *Annelles de Chem . et. Phys*, vol. 5, pp. 701-905.
- [6] P. Weiss, *Physical review*, vol. 74, pp. 1493-1948.
- [7] B. D. Cullity. *Introduction to magnetic materials*, Anonymous Addison-Wesley, 1972.
- [8] F. Bloch, *Z. Physik*, vol. 74, pp. 295-1932.
- [9] E. C. Stoner and E. P. Wohlfarth, A mechanism of magnetic hysteresis in heterogeneous alloys *Royal Society Philosophical Trans*, vol. 1947.
- [10] I. S. Jacobs and C. P. Bean, An approach to elongated fine-particle magnets *Physical review*, vol. 100, pp. 1060-1067, 1955.
- [11] E. H. Frei, S. Shtrikman, and D. Treves, Critical size and nucleation field of ideal ferromagnetic particles *Physical review*, vol. 106, pp. 446-455, 1957.
- [12] L. He, W. D. Doyle, and H. Fujiwara, High speed coherent switching below the Stoner Wohlfarth limit *IEEE Trans. Magn.* vol. 30, pp. 4086-4088, 1994.
- [13] W. D. Doyle, L. He, and P. J. Flanders, Measurement of the Switching Speed Limit in High Coercivity Magnetic Media *IEEE Trans. Magn.* vol. 29, pp. 3634-3636, 1993.
- [14] J. O. Artman, C. Alexander, J. C. Cates, and M. R. Parker, Estimation of ultimate switching speeds in hard magnetic recording media by ferromagnetic-resonance linewidth measurements *J. Magn. Magn. Mater.* vol. 104, pp. 977-978, 1992.

- [15] C. D. Mee and E. D. Daniel. *Magnetic recording*, Anonymous McGraw-Hill book company, 1987.
- [16] F. Luborsky, E. Development of elongated particle magnets *J. Appl. Phys.* vol. 32, pp. 171s-183s, 1961.
- [17]. L. Neel. *Compt Rend.*, vol 234 pp.1150 1947.
- [18] J. E. Knowles, Measurements on single magnetic particles *IEEE Trans. Magn.* vol. 14, pp. 858-860, 1978.
- [19] J. E. Knowles, Coercivity and packing density in acicular particles *J. Magn. Magn. Mater.* vol. 25, pp. 105-112, 1981.
- [19]. H.N. Bertram, M.K. Stafford, D.R. Mills. "The print-through phenomenon," *J Audio Eng, Soc.*, vol 28 pp.690-705, 1997.
- [21] M. P. Sharrock, Time dependence of switching fields in magnetic recording media (invited) *J. Appl. Phys.* vol. 76, pp. 6413-6418, 1994.
- [22] M. P. Sharrock and R. E. Bodnar, Magnetic-materials for recording - an overview with special emphasis on particles *J. Appl. Phys.* vol. 57, pp. 3919-3924, 1985.
- [23] M. P. Sharrock, Particulate magnetic recording media - a review *IEEE Trans. Magn.* vol. 25, pp. 4374-4389, 1989.
- [24] G. Bate, Magnetic recording materials since 1975 *J. Magn. Magn. Mater.* vol. 100, pp. 413-424, 1991.
- [25] S. J. Andress, A. Benedetti, A. R. Corradi, and G. Fagherazzi, The microstructure of gamma- Fe_2O_3 and its effects on the magnetization properties *IEEE Trans. Magn.* vol. 22, pp. 1341-1348, 1986.
- [26] A. E. Berkowitz, Some materials considerations in particulate media *IEEE Trans. Magn.* vol. 22, pp. 466-471, 1986.
- [27] A. E. Berkowitz, R. P. Goehner, E. L. Hall, and P. J. Flanders, Microstructure, relaxation, and print-through in gamma- Fe_2O_3 particles *J. Appl. Phys.* vol. 57, pp. 3928-3930, 1985.
- [28] J. C. Slonczewski, Origin of magnetic anisotropy in cobalt substituted magnetite *Physical review*, vol. 110, pp. 1341-1348, 1958.
- [29] M. Tachiki, Origin of the magnetic energy of cobalt ferrite *Prog. Theoret. Phys.* vol. 23, pp. 1055-1072, 1960.

- [30] S. Umeki, S. Saitoh, and Y. Imaoka, A new high coercivity magnetic particle for recording tape *IEEE Trans. Magn.* vol. MAG-10, pp. 655-656, 1974.
- [31] Y. Imaoka, S. Umeki, J. Kubota, and T. Tokuoka, Characteristics of cobalt adsorbed gamma Fe₂O₃ particles *IEEE Trans. Magn.* vol. MAG-14, pp. 649-654, 1978.
- [32] U. Kullmann, E. Koster, and B. Meyer, Magnetic-anisotropy of ir-doped cro₂ *IEEE Trans. Magn.* vol. 20, pp. 742-744, 1984.
- [33] P. Maestro, D. Andriamandroso, G. Demazeau, M. Pouchard, and P. Hagenmuller, New improvements of cro₂-related magnetic recording materials *IEEE Trans. Magn.* vol. 18, pp. 1000-1003, 1982.
- [34] D. S. Rodell, Magnetocrystalline anisotropy of single crystal CrO₂ *J. Phys. Soc. Japan*, vol. 21, pp. 1224-1225, 1966.
- [35] W. H. Cloud, D. S. Schreiber, and K. R. Babcock, X-ray and magnetic studies of CrO₂ single crystals *J. Appl. Phys.* vol. 33, pp. 1193-1194, 1962.
- [36] J. E. Knowles, Magnetic properties of individual acicular particles *IEEE Trans. Magn.* vol. 17, pp. 3008-3012, 1981.
- [37] O. Kubo, T. Ido, and H. Yokoyama, Properties of ba ferrite particles for perpendicular magnetic recording media *IEEE Trans. Magn.* vol. 18, pp. 1122-1124, 1982.
- [38] T. Onuki and Y. Toda, Optimal-design of hybrid magnet in maglev system with both permanent and electromagnets *IEEE Trans. Magn.* vol. 29, pp. 1783-1786, 1993.
- [39] K. O'Grady, R. G. Gilson, and P. C. Hobby, Magnetic pigment dispersions (a tutorial review) *J. Magn. Magn. Mater.* vol. 95, pp. 341-355, 1991.

8.2 References for chapter 2

- [1]. J.E. Knowles. "Measurements on single magnetic particles," *IEEE Trans Magn.*, vol 14 (5) pp.858-860, 1978.
- [2]. J.E. Knowles. "The measurement of the anisotropy-field of single tape particles," *IEEE Trans Magn.*, vol 20 pp.84-86, 1984.
- [3]. J.E. Knowles. "Magnetic measurements on single acicular particles of gamma ferric oxide," *IEEE Trans Magn.*, vol 16 (1) pp.62-67, 1980.
- [4]. W. Burrells. *Microscope technique*. vol 2nd London: Fountain press, book, 1977.

- [5]. R. Oldfield. Light microscopy. Wolfe , book, 1993.
- [6]. D.C. Baird. An introduction to measurement theory and experiment design. Prentice-Hall, book, 1962.

8.3 References for chapter 3

- [1]. J.E. Knowles. "Measurements on single magnetic particles," *IEEE Trans Magn.*, vol 14 (5) pp.858-860, 1978.
- [2]. E.C. Stoner, E.P. Wohlfarth. "A mechanism of magnetic hysteresis in heterogeneous alloys," *Royal Society Philosophical Trans*, 1947.
- [3]. I.S. Jacobs, C.P. Bean. "An approach to elongated fine-particle magnets," *Physical review.*, vol 100 (4) pp.1060-1067, 1955.
- [4]. Y.D. Yan, E. Della Torre. "Reversal modes in fine particles," *J de Phys.*, vol 49 pp.1813-1814, 1988.
- [5]. M.E. Schabes, H.N. Bertram. "Ferromagnetic switching in elongated gamma-Fe₂O₃ particles," *J Appl Phys.*, vol 64 pp.5832-5834, 1988.
- [6]. M. Lederman, S. Schultz, M. Ozaki. "Measurement of the dynamics of the magnetisation reversal in individual single domain ferromagnetic particles," *physical review letters.*, vol 73 (14) pp.1986-1989, 1994.
- [7]. J.E. Knowles. "Magnetic properties of individual acicular particles," *IEEE Trans Magn.*, vol 17 (6) pp.3008-3012, 1981.
- [8]. Y.S. Luo, J.G. Zhu. "Switching field characteristics of individual iron particles by MFM," *IEEE Trans Magn.*, vol 30 pp.4080-4082, 1994.
- [9]. C. Salling, R. O'barr, S. Schultz, I. Mcfadyen, M. Osaki. "Investigation of the magnetization reversal mode for individual ellipsoidal single-domain particles of gamma ferric oxide," *J Appl Phys.*, vol 75 (12) pp.7989-7992, 1994.
- [10]. M. Lederman, G.A. Gibson, S. Schultz. "Observation of thermal switching of a single ferromagnetic particle," *J Appl Phys.*, vol 73 pp.6961-6963, 1993.
- [11]. M. Ozaki, E. Matijevic. "Preparation and Magnetic Properties of Monodispersed Spindle-type gamma-Fe₂O₃ Particles," *Journal of Colloid and Interface Science.*, vol 107 (1) pp.199-203, 1985.
- [12]. A.E. Berkowitz, R.P. Goehner, E.L. Hall, P.J. Flanders. "Microstructure, relaxation, and print-through in gamma-Fe₂O₃ particles," *J Appl Phys.*, vol 57 pp.3928-3930, 1985.

- [13]. M.P. Sharrock, R.E. Bodnar. "Magnetic-materials for recording - an overview with special emphasis on particles," *J Appl Phys.*, vol 57 pp.3919-3924, 1985.
- [14]. S.J. Andress, A. Benedetti, A.R. Corradi, G. Fagherazzi. "The microstructure of gamma-Fe₂O₃ and its effects on the magnetization properties," *IEEE Trans Magn.*, vol 22 pp.1341-1348, 1986.
- [15]. A.E. Berkowitz, E.L. Hall, P.J. Flanders. "Microstructure of gamma ferric oxide particles: a response to Andress et al," *IEEE Trans Magn.*, vol mag-23 pp.3816-3819, 1987.
- [16]. M. Essig, M.W. Muller, E. Schwab. "Structural-analysis of the stabilization layer of chromium dioxide particles," *IEEE Trans Magn.*, vol 26 pp.69-71, 1990.
- [17]. H. Auweter, R. Feser, H. Jakusch, M.W. Muller, N. Muller, E. Schwab, R.J. Veitch. "Chromium dioxide particles for magnetic recording," *IEEE Trans Magn.*, vol 26 pp.66-68, 1990.
- [18]. H. Jachow, E. Schwab, R.J. Veitch. "Viscous magnetization of chromium-dioxide particles - effect of increased magnetocrystalline anisotropy," *IEEE Trans Magn.*, vol 27 pp.4672-4674, 1991.
- [19]. D.S. Rodell. "Magnetocrystalline anisotropy of single crystal CrO₂," *J Phys Soc Japan.*, vol 21 pp.1224-1225, 1966.
- [20]. W.H. Cloud, D.S. Schreiber, K.R. Babcock. "X-ray and magnetic studies of CrO₂ single crystals," *J Appl Phys.*, vol 33 (3) pp.1193-1194, 1962.
- [21]. M. Kishimoto, S. Kitahata, M. Amemiya. "Morphology and magnetic-properties of the iron-oxide layer formed on iron acicular particles," *IEEE Trans Magn.*, vol 22 pp.732-734, 1986.
- [22]. M.A. Hayat. Introduction to Biological Scanning Electron Microscopy. Baltimore: University Park Press, book, 1978.
- [23]. D. Kay. Techniques for Electron Microscopy. vol 2nd Oxford: Blackwell Scientific Publications Ltd, book, 1967.
- [24]. C.W. Oatley. The Scanning Electron Microscope. London: Cambridge University Press, book, 1972.
- [25]. P.R. Thornton. Scanning Electron Micoscope. London: Chapman and Hall Ltd, book, 1968.

8.4 References for chapter 4

- [1]. S. Foner. "Versatile and sensitive vibrating-sample magnetometer," *Rev Sci Instrum.*, vol 30 pp.548-557, 1959.
- [2]. O. Henkel. "Remanenzverhalten und Wechselwirkungen in hartmagnetischen Teilchenkollektiven," *Phys Status Solidi.*, vol 7 pp.919-929, 1964.
- [3]. P.M. Sillis, A. Hoare, A. Peters, T. Orth, P.R. Bissell, R.W. Chantrell, J. Pelzl. "Experimental and theoretical studies of transverse susceptibility in recording media," *IEEE Trans Magn.*, vol 28 pp.2695-2697, 1992.
- [4]. B.D. Cullity. Introduction to magnetic materials. Addison-Wesley, book, 1972.
- [5]. F. Schmidlin, P.R. Bissell, J.A. Gotaas. "Measurement of texture in magnetic recording media using a biaxial vibrating sample magnetometer," *J Appl Phys.*, vol 79 pp.4746-4748, 1996.
- [6]. D. Jiles. Introduction to magnetism and magnetic materials. vol 15th London: Chapman and Hall, book, 1989.
- [7]. E.C. Stoner, E.P. Wohlfarth. "A mechanism of magnetic hysteresis in heterogeneous alloys," *Royal Society Philosophical Trans*, 1947.
- [8]. D.E. Speliotis, K. Peter. "High Density Digital Recording on 4mm Metal Particle and Ba-Ferrite Tapes," *J Magn Magn Mater.*, vol 5(MRM '92) pp.28-32, 1992.
- [9]. D.E. Speliotis. "Performance of MP(++) and BaFe++ tapes in high density recording applications," *IEEE Trans Magn.*, vol 31 pp.2877-2882, 1995.
- [10]. M.P. Sharrock, R.E. Bodnar. "Magnetic-materials for recording - an overview with special emphasis on particles," *J Appl Phys.*, vol 57 pp.3919-3924, 1985.
- [11]. E.P. Wohlfarth. "Different methods of assessing switching field distributions of magnetic recording media," *IEEE Trans Magn.*, vol 20 pp.78-80, 1984.
- [12]. E. Koster. "Recommendation of a simple and universally applicable method for measuring the switching field distribution of magnetizing recording media," *IEEE Trans Magn.*, vol 20 pp.81-83, 1984.
- [13]. R.W. Chantrell, K. O'Grady. "Magnetic characterization of recording media," *J Phys D:Appl Phys.*, vol 25 pp.1-23, 1992.

- [14]. M. Walker, P.I. Mayo, K. O'Grady, S.W. Charles, R.W. Chantrell. "The magnetic properties of single domain particles with cubic anisotropy: II. Remanence curves," *J Phys :Condens Matter.*, vol 5 pp.2793-2808, 1993.
- [15]. E.P. Wohlfarth. "Relations between different modes of acquisition of the remanent magnetization of ferromagnetic particles" *J Appl Phys.*, vol 29 pp.595 1958.
- [16]. G.W.D. Spratt, P.R. Bissell, R.W. Chantrell, E.P. Wohlfarth. "Static and Dynamic Experimental Studies of Particulate Recording Media," *J Magn Magn Mater.*, vol 75 pp.309-318, 1988.
- [17]. X. He, C. Alexander, M.R. Parker. "Measurement of interaction fields in particulate tapes by linearization of the henkel plot," *IEEE Trans Magn.*, vol 28 pp.2683-2685, 1992.
- [18]. D.E. Speliotis, W. Lynch. "Magnetic-interactions in particulate and thin-film recording media," *J Appl Phys.*, vol 69 pp.4496-4498, 1991.
- [19]. P.I. Mayo, R.M. Erkkila, A. Bradbury, R.W. Chantrell. "Interaction effects in longitudinally oriented and nonoriented barium hexaferrite tapes," *IEEE Trans Magn.*, vol 26 pp.1894-1896, 1990.
- [20]. D. Richards, J.W. Harrell, M.R. Parker. "Remanence Studies of Interparticle Interactions in Ba-ferrite," *J Magn Magn Mater.*, vol 5(MRM '92) pp.164-166, 1992.
- [21]. P.E. Kelly, K. O'Grady, P.I. Mayo, R.W. Chantrell. "Switching mechanisms in cobalt-phosphorus thin-films," *IEEE Trans Magn.*, vol 25 pp.3880-3883, 1989.
- [22]. G. Bottoni, D. Candolfo, A. Cecchetti, F. Masoli. "Evolution of the interactions effects with co-doping of iron-oxide particles," *J Magn Magn Mater.*, vol 104 pp.975-976, 1992.
- [23]. P.I. Mayo, A. Bradbury, R.W. Chantrell, P.E. Kelly, H.E. Jones, P.R. Bissell. "Interaction effects in the remanence curves of CoTi-doped BaFe systems," *IEEE Trans Magn.*, vol 26 pp.228-230, 1990.
- [24]. G. Bottoni, D. Candolfo, A. Cecchetti, A.R. Corradi, F. Masoli. "Magnetization processes in iron particles for magnetic recording," *J Magn Magn Mater.*, vol 104 pp.961-962, 1992.
- [25]. A. Lyberatos, E.P. Wohlfarth. "A monte carlo simulation of the dependence of the coercive force of a fine particle assembly on the volume packing factor," *J Magn Magn Mater.*, vol 59 pp.L1-L4, 1986.

- [26]. A.R. Corradi, E.P. Wohlfarth. "Influence of densification on the remanence, the coercivities and the interaction field of elongated gamma-Fe₂O₃ powders," *IEEE Trans Magn.*, vol MAG-14 pp.861-863, 1978.
- [27]. P.J. Flanders, S. Shtrikman. "Experimental determination of the anisotropy distribution in ferromagnetic powders," *J Appl Phys.*, vol 33(1) pp.216-219, 1962.
- [28]. T.L. Templeton, A.S. Arrott, Y. Yoshida. "Angular dependence of magnetization in recording media," *IEEE Trans Magn.*, vol 30 pp.4263-4265, 1994.
- [29]. A. Aharoni, E.H. Frei, S. Shtrikman, D. Treves. "The reversible susceptibility tensor of the Stoner-Wohlfarth model," *Bul Res Counc of Israel.*, vol 6A pp.215-238, 1957.
- [30]. A. Hoare, R.W. Chantrell, W. Schmitt, A. Eiling. "The Reversible Transverse Susceptibility of Particulate Recording Media," *J Phys D:Appl Phys.*, vol 26(3) pp.461-468, 1993.
- [31]. D.V. Berkov, R.W. Chantrell. "Transverse susceptibility for the fanning mode of magnetization reversal," *J Magn Magn Mater.*, vol 120 pp.200-202, 1993.
- [32]. P.M. Sillis, P.R. Bissell. "A novel method for absolute magnetization measurement in longitudinal recording media using transverse susceptibility measurements," *J Phys D:Appl Phys.*, vol 24 pp.1891-1893, 1991.
- [33]. P.M. Sillis, P.R. Bissell, R.W. Chantrell. "The effects of texture and interactions on transverse susceptibility measurements of particulate media," *J Magn Magn Mater.*, vol 155 pp.123-125, 1996.
- [34]. P.M. Sillis. "Transverse Susceptibility Studies on Particulate Recording Media." University of Central Lancashire; Thesis, 1995.
- [35]. M.P. Sharrock. "Particulate magnetic recording media - a review," *IEEE Trans Magn.*, vol 25 pp.4374-4389, 1989.
- [36]. G. Bate. "Magnetic recording materials since 1975," *J Magn Magn Mater.*, vol 100 pp.413-424, 1991.
- [37]. C.D. Mee, E.D. Daniel. *Magnetic recording*. McGraw-Hill book company, book, 1987.
- [38]. J.E. Knowles, R.F. Pearson, A.D. Annis. "The angular distribution of the magnetization in magnetic recording tapes," *IEEE Trans Magn.*, vol MAG-16 pp.42-44, 1980.

8.5 References for chapter 5

- [1]. O. Henkel. "Remanenzverhalten und Wechselwirkungen in hartmagnetischen Teilchenkollektiven," *Phys Status Solidi.*, vol 7 pp.919-929, 1964.
- [2]. P.E. Kelly, K. O'Grady, P.I. Mayo, R.W. Chantrell. "Switching mechanisms in cobalt-phosphorus thin-films," *IEEE Trans Magn.*, vol 25 pp.3880-3883, 1989.
- [3]. G. Bottoni, D. Candolfo, A. Cecchetti, F. Masoli. "Evolution of the interactions effects with Co-doping of iron-oxide particles," *J Magn Mater.*, vol 104 pp.975-976, 1992.
- [4]. J.E. Knowles. "Magnetic measurements on single acicular particles of gamma ferric oxide," *IEEE Trans Magn.*, vol 16 (1) pp.62-67, 1980.
- [5]. G. Bate. "Particulate Recording Materials," *Proc IEEE.*, vol 74(11) pp.1513-1525, 1986.
- [6]. M.P. Sharrock. "Particulate magnetic recording media - a review," *IEEE Trans Magn.*, vol 25 pp.4374-4389, 1989.
- [7]. G.N. Coverdale, R.W. Chantrell, A. Hart, D. Parker. "A computer-simulation of the microstructure of a particulate dispersion," *J Appl Phys.*, vol 75 pp.5574-5576, 1994.
- [8]. A. Satoh, R.W. Chantrell, S. Kamiyama, G.N. Coverdale. "Three Dimensional Monte Carlo Simulation of Thick Chainlike Clusters Composed of Ferromagnetic Fine Particles." *Journal of Colloid and Interface Science.*, vol 181 pp.422-428, 1997.
- [9]. D.E. Speliotis, W. Lynch. "Magnetic-interactions in particulate and thin-film recording media," *J Appl Phys.*, vol 69 pp.4496-4498, 1991.
- [10]. A. Lyberatos, E.P. Wohlfarth. "A monte carlo simulation of the dependence of the coercive force of a fine particle assembly on the volume packing factor," *J Magn Mater.*, vol 59 pp.L1-L4, 1986.
- [11]. G. Bottoni, D. Candolfo, A. Cecchetti, A.R. Corradi, F. Masoli. "Magnetization processes in iron particles for magnetic recording," *J Magn Mater.*, vol 104 pp.961-962, 1992.

8.6 References for chapter 6

- [1]. E.C. Stoner, E.P. Wohlfarth. "A mechanism of magnetic hysteresis in heterogeneous alloys," *Royal Society Philosophical Trans*, 1947.
- [2]. I.S. Jacobs, C.P. Bean. "An approach to elongated fine-particle magnets," *Physical review.*, vol 100 (4) pp.1060-1067, 1955.
- [3]. M.E. Schabes, H.N. Bertram. "Ferromagnetic switching in elongated gamma-Fe₂O₃ particles," *J Appl Phys.*, vol 64 pp.5832-5834, 1988.
- [4]. M.E. Schabes, H.N. Bertram. "Magnetization reversal of cobalt-modified gamma-Fe₂O₃ particles," *J Appl Phys.*, vol 67 pp.5149-5151, 1990.
- [5]. Y.D. Yan, E. Della Torre. "Modeling of elongated fine ferromagnetic particles," *J Appl Phys.*, vol 66 (1) pp.320-327, 1989.
- [6]. M. Lederman, G.A. Gibson, S. Schultz. "Observation of thermal switching of a single ferromagnetic particle," *J Appl Phys.*, vol 73 pp.6961-6963, 1993.
- [7]. E. Della Torre. "Magnetization Calculation of Fine Particles (Invited)," *IEEE Trans Magn.*, vol MAG-22 (5) pp.484-477, 1986.
- [8]. C. Dean. "Micromagnetic Studies of metallic Thin Films," University of Central Lancashire; Thesis, 1993.
- [9]. J.E. Knowles. "Measurements on single magnetic particles," *IEEE Trans Magn.*, vol 14 (5) pp.858-860, 1978.
- [10]. J.E. Knowles. "Magnetic properties of individual acicular particles," *IEEE Trans Magn.*, vol 17 (6) pp.3008-3012, 1981.
- [11]. Y.S. Luo, J.G. Zhu. "Switching field characteristics of individual iron particles by MFM," *IEEE Trans Magn.*, vol 30 pp.4080-4082, 1994.
- [12]. J. Luine, K. Daly, R. Hu, A. Kain, A. Lee, H. Manasevit, C. Pettiettehall, R. Simon, D. Stjohn, M. Wagner. "10 GHz surface impedance measurements of (Y,Er)BaCuO films produced by mocvd, laser ablation, and sputtering," *IEEE Trans Magn.*, vol 27 pp.1528-1531, 1991.
- [13]. I.P. Nevirkovets, E.M. Rudenko. "Investigation of the wall effect in the long josephson-junctions," *IEEE Trans Magn.*, vol 27 pp.2751-2752, 1991.
- [14]. Y. Uesaka, Y. Nakatani, N. Hayashi. "Dynamic calculation of magnetization reversal in elongated particles," *J Appl Phys.*, vol 67 pp.5146-5148, 1990.

- [15]. Y. Kanai, T. Tsukamoto, Y. Saitoh, M. Miyakawa, T. Kashiwa. "Analysis of a hyperthermic treatment using a reentrant resonant cavity applicator for a heterogeneous model with blood flow," *IEEE Trans Magn.*, vol 33 pp.2175-2178, 1997.
- [16]. M.E. Schabes. "Micromagnetics of small Ferromagnetic Particles," University Of California San Diego; Thesis, 1989.
- [17]. Y.D. Yan, E. Della Torre. "Reversal modes in fine particles," *J de Phys.*, vol 49 pp.1813-1814, 1988.
- [18]. J.J. Miles, B.K. Middleton. "The role of microstructure in micromagnetic models of longitudinal thin-film magnetic media," *IEEE Trans Magn.*, vol 26 pp.2137-2139, 1990.
- [19]. J.J. Miles, B.K. Middleton. "A hierarchical micromagnetic model of longitudinal thin-film recording media," *J Magn Mater.*, vol 95 pp.99-108, 1991.
- [20]. R. Eisberg, R. Resnick. QUANTUM PHYSICS of Atoms, Molecules, Solids, Nuclei, and Particles. vol 21th Wiley, book, 1985.
- [21]. J.G. Zhu, H.N. Bertram. "Magnetization reversal in CoCr perpendicular thin films," *J Appl Phys.*, vol 66 (3) pp.1291-1307, 1989.
- [22]. J.G. Zhu, H.N. Bertram. "Micromagnetic studies of thin metallic-films," *J Appl Phys.*, vol 63 pp.3248-3253, 1988.
- [23]. R.H. Victora. "Micromagnetic predictions for magnetization reversal in CoNi films," *J Appl Phys.*, vol 62 (10) pp.4220-4225, 1987.
- [24]. M.E. Schabes, H.N. Bertram. "Magnetization processes in ferromagnetic cubes," *J Appl Phys.*, vol 64 (3) pp.1347-1357, 1988.
- [25]. W.H. Press, W.T. Vetterling, S.A. Teukolsky, B.P. Flannery. Numerical Recipes in Fortran. vol 2nd Cambridge University Press, book, 1992.
- [26]. L. He, W.D. Doyle, H. Fujiwara. "High speed coherent switching below the Stoner Wohlfarth limit," *IEEE Trans Magn.*, vol 30 pp.4086-4088, 1994.
- [27]. A.E. Berkowitz, R.P. Goehner, E.L. Hall, P.J. Flanders. "Microstructure, relaxation, and print-through in gamma-Fe₂O₃ particles," *J Appl Phys.*, vol 57 pp.3928-3930, 1985.
- [28]. G. Bate. "Particulate Recording Materials," *Proc IEEE.*, vol 74(11) pp.1513-1525, book, 1986.

- [29]. S.J. Andress, A. Benedetti, A.R. Corradi, G. Fagherazzi. "The microstructure of gamma-Fe₂O₃ and its effects on the magnetization properties," *IEEE Trans Magn.*, vol 22 pp.1341-1348, 1986.
- [30]. A.E. Berkowitz, E.L. Hall, P.J. Flanders. "Microstructure of gamma ferric oxide particles: a response to Andress et al," *IEEE Trans Magn.*, vol mag-23 pp.3816-3819, 1987.
- [31]. M. Essig, M.W. Muller, E. Schwab. "Structural-analysis of the stabilization layer of chromium dioxide particles," *IEEE Trans Magn.*, vol 26 pp.69-71, 1990.
- [32]. M.P. Sharrock, R.E. Bodnar. "Magnetic-materials for recording - an overview with special emphasis on particles," *J Appl Phys.*, vol 57 pp.3919-3924, 1985.
- [33]. J. Ensling, P. Gutlich, R. Klinger, W. Meisel, H. Jachow, E. Schwab. "Mossbauer study on the distribution of iron in high coercivity chromium dioxide particles," *IEEE Trans Magn.*, vol 28 pp.2680-2682, 1992.
- [34]. M.P. Sharrock. "Particulate magnetic recording media - a review," *IEEE Trans Magn.*, vol 25 pp.4374-4389, 1989.
- [35]. G. Bate. "Magnetic recording materials since 1975," *J Magn Magn Mater.*, vol 100 pp.413-424, 1991.
- [36]. W.H. Cloud, D.S. Schreiber, K.R. Babcock. "X-ray and magnetic studies of CrO₂ single crystals," *J Appl Phys.*, vol 33 (3) pp.1193-1194, 1962.
- [37]. D.S. Rodell. "Magnetocrystalline anisotropy of single crystal CrO₂," *J Phys Soc Japan.*, vol 21 pp.1224-1225, 1966.
- [38]. M.W. Muller, E. Schwab, R.J. Veitch. "Magnetic analysis of high coercivity chromium dioxide particles," *IEEE Trans Magn.*, vol 26 pp.1897-1899, 1990.

8.7 References for chapter 7

- [1] Knowles, J.E. , "Magnetic measurements on single acicular particles of gamma ferric oxide", IEEE Trans Magn, 1980, 16, {1}, p.62-67.
- [2] Speliotis, D.E., Lynch, W. , "Magnetic-interactions in particulate and thin-film recording media", J Appl Phys, 1991, 69, p.4496-4498.
- [3] Lyberatos, A., Wohlfarth, E.P. , "A monte carlo simulation of the dependence of the coercive force of a fine particle assembly on the volume packing factor", J Magn Magn Mater, 1986, 59, p.L1-L4.
- [4] Bate, G. , "Particulate Recording Materials", Proc IEEE, 1986, 74(11), p.1513-1525.
- [5] Sharrock, M.P. , "Particulate magnetic recording media - a review", IEEE Trans Magn, 1989, 25, p.4374-4389.
- [6] Coverdale, G.N., Chantrell, R.W., Hart, A., Parker, D. , "A computer-simulation of the microstructure of a particulate dispersion", J Appl Phys, 1994, 75, p.5574-5576.
- [7] Coverdale, G.N., Chantrell, R.W., Satoh, A., Vietch, R. , "Molecular dynamic model of the magnetic properties and microstructure of advanced metal particle dispersions.", J Appl Phys, 1997, 81, {8}, p.3818-3820.
- [8] Satoh, A., Chantrell, R.W., Kamiyama, S., Coverdale, G.N. , "Three Dimensional Monte Carlo Simulation of Thick Chainlike Clusters Composed of Ferromagnetic Fine Particles.", Journal of Colloid and Interface Science, 1997, 181, p.422-428.
- [9] Lederman, M., Gibson, G.A., Schultz, S. , "Observation of thermal switching of a single ferromagnetic particle", J Appl Phys, 1993, 73, p.6961-6963.
- [10] Lederman, M., Schultz, S., Ozaki, M. , "Measurement of the dynamics of the magnetisation reversal in individual single domain ferromagnetic particles", physical review letters, 1994, 73, {14}, p.1986-1989.
- [11] Yan, Y.D., Della Torre, E. , "Modeling of elongated fine ferromagnetic particles", J Appl Phys, 1989, 66, {1}, p.320-327.
- [12] Schabes, M.E., Bertram, H.N. , "Ferromagnetic switching in elongated gamma-Fe₂O₃ particles", J Appl Phys, 1988, 64, p.5832-5834.

Appendix A

9.1 Wohlfarth relationship.

The relationship between IRM remanent magnetisation and the DCD remanent magnetisation in a system of non-interacting magnetised bodies is linear. This relationship known as the Wohlfarth relationship given by

$$I_{DCD}(H) = 1 - 2I_{IRM}(H). \quad (1)$$

Here $I_{DCD}(H)$ and $I_{IRM}(H)$ are the DCD and IRM curves normalised to the appropriate saturated remanent magnetisation of the sample.

The relationship can be shown to be valid by examining the reversal process in a simple highly aligned particulate system, particle moments are either pointing up or pointing down. A schematic diagram indicating the reversal process within this simple system for the IRM and DCD curves can be found in figure blah.

The initial state of the IRM has half the moments pointing up and half pointing down, thus generating zero net magnetisation for the system. The initial state of the DCD curve has all its moments pointing down, generating a net normalised magnetisation of -1. From examining these values it can be seen that they conform to the Wohlfarth relationship. As an upward positive field is applied within the IRM and DCD curve measurements the moments begin to reverse into the upward field direction. As half of all the moments are already within the positive applied field direction in the IRM state then the magnitude of reversal in the DCD measurements are twice that of the IRM measurements. This again conforms to the Wohlfarth relationship. After complete reversal of the moments within the upward field direction the net remanent magnetisation of both the IRM and DCD curve are equal and equal to unity, conforming to the Wohlfarth relationship.

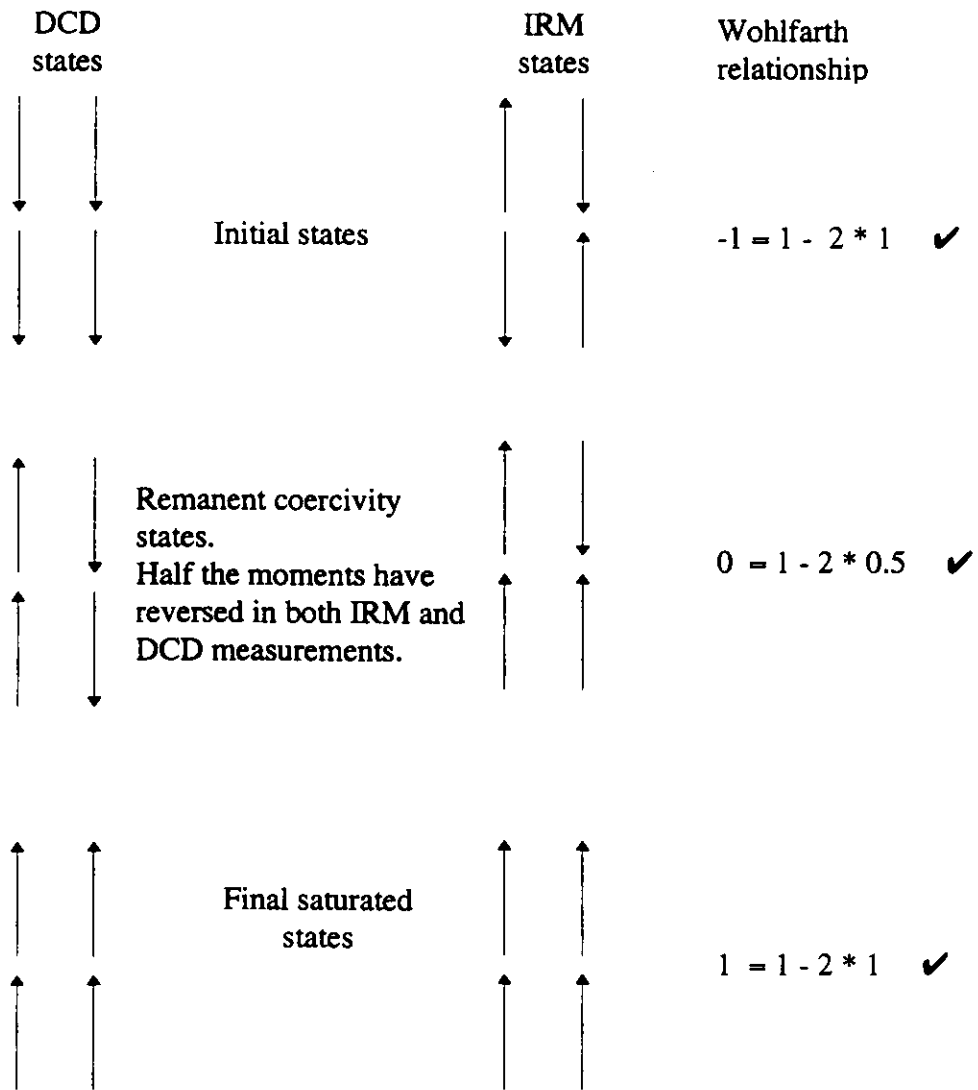


figure (9:1): Magnetic states within the IRM and DCD measurements of a highly simplified sample.

PUBLICATIONS



ELSEVIER

Interaction effects from reversal studies of single particles

S.R. McConochie^{*}, F. Schmidlin, P.R. Bissell, J.A. Gotaas, D.A. Parker

University of Central Lancashire, Preston, PR1 2HE, UK

Abstract

Interaction effects within particulate recording tapes have been investigated by comparing single particle behaviour with measured tape bulk properties. The particle systems were audio $\gamma\text{-Fe}_2\text{O}_3$ and 8 mm MP video tapes plus CrO_2 hand spreads. Interactions in the $\gamma\text{-Fe}_2\text{O}_3$ and CrO_2 systems were negative and consistent with mean field behaviour. However, the MP particle interactions were in the opposite sense, in contradiction to the Henkel plots. A model for this behaviour involving the creation of chains is suggested.

1. Introduction

We have investigated the interaction effects in recording particle systems by comparing the reversal properties of individual particles with bulk remanence of tapes or hand spreads. The angular switching field distribution (SFD) for an ensemble of isolated particles was determined combining measured switching field data and tape texture functions as indicated by their easy axis distributions. The SFD was compared with the differential of the isothermal remanence curve (IRM) for the corresponding tape. The difference between the two curves could be related to interaction effects. This paper reports on three systems: an audio $\gamma\text{-Fe}_2\text{O}_3$ tape, an 8 mm metal particle (MP) video tape, and an experimental CrO_2 hand spread.

2. Experimental method and results

The magnetisation reversal properties of isolated particles have been investigated using techniques developed by Knowles [1]. Isolated particles removed from the system were dispersed in a viscous liquid and viewed with an oil immersion objective microscope. Particles were aligned in a magnetic field of a few Oe. Field pulses of increasing magnitude were applied at an angle to the small aligning field until the particle was seen to rotate through 180° , which indicated that its moment had been switched.

With the pulsed field in the opposite direction to the aligning field, switching fields were measured for an ensemble of 50 isolated particles to generate an SFD for a non-interacting ensemble of particles. With such a small number of particles, the histogram was fairly coarse and so

it was assumed that the distribution for a large sample could be represented by a Gaussian curve fitted to the data. The measured histogram for 50 metal particles and a Gaussian curve fitted SFD are shown in Fig. 1.

The angular variation of switching for individual particles was determined by varying the angle between the pulsed field and the aligning field. The measured data can be represented by

$$H_\theta = H_0 + a \sin^b \theta \quad (1)$$

where a and b are curve fitting parameters. H_θ and H_0 are the switching fields at angles θ and 0 respectively. Typical measured data for a metal particle and a curve fit are presented in Fig. 2.

The easy axis distributions (in plane and out of plane) were measured for a recording tape or hand spread using a biaxial vibrating sample magnetometer [2]. For an in-plane

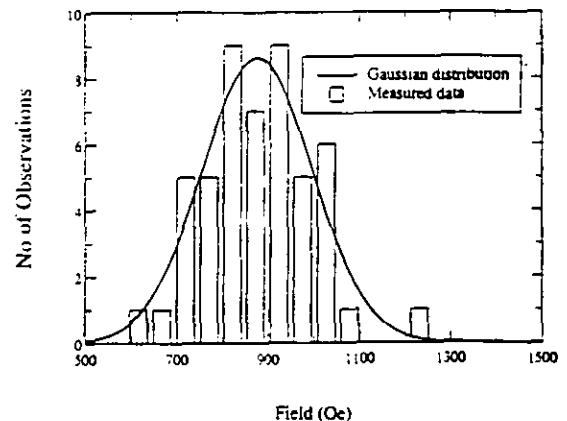


Fig. 1. Switching field distribution for an ensemble of isolated metal particles.

^{*}Corresponding author.

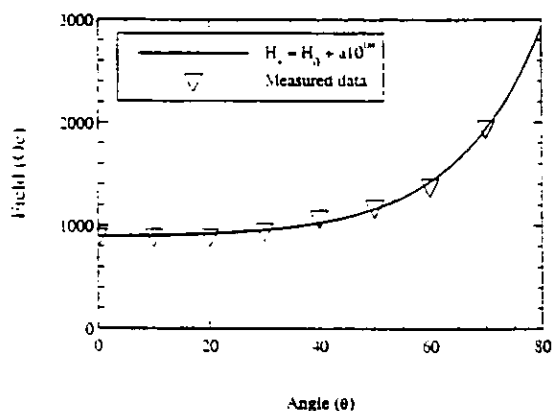


Fig. 2. Switching field as a function of angle for an isolated metal particle. For the curve fit $H_s = 384.6$, $a = 10.1$ and $b = 0.0288$.

determination, the sample was magnetically saturated at an angle θ to the sample orientation axis of the system. The remanent magnetisation was then measured in the applied field direction and orthogonal to it. The sample was then rotated through a small angle ($\delta\theta$) and again saturated. The change in remanence (treated as a vector) was then directly proportional to the particle moments with easy axes within an angle $\delta\theta$ at right angles to the field direction ($(\pi/2 - \theta)$ to the orientation axis). The procedure was repeated over a range $-\pi/2 < \theta < \pi/2$ to obtain the in plane easy axis distribution. The measurements were repeated out of plane, correcting for demagnetisation effects during the measurement using a technique similar to that described by Bernards and Cramer [3].

By numerically combining the Gaussian fitted SFD for an ensemble of particles and the angular variation of switching field with angle, both derived from the single particle measurements, with the measured easy axis distribution of the tape or hand spread, it was possible to generate SFDs and remanence curves for an assembly of

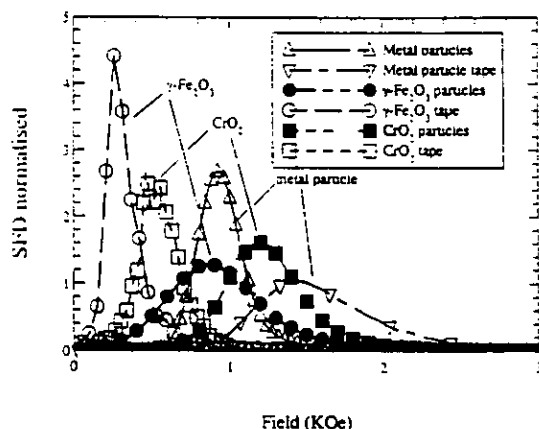


Fig. 3. Switching field distribution with and without interactions in the three tape systems.

particles matching the tape characteristics but with no interparticle interactions. These were compared with measured SFDs for the tapes and hand spreads obtained by differentiating the IRM curves. Fig. 3 shows the results obtained for the $\gamma\text{-Fe}_2\text{O}_3$ tape, CrO_2 hand spread and MP tape. It should be noted that the effects of interactions in the $\gamma\text{-Fe}_2\text{O}_3$ and the CrO_2 systems caused the switching field peak to shift to lower fields, whereas interactions in the metal particle system shifted the peak to higher fields.

Interaction effects were also investigated using the established Henkel plots [4]. In all three cases, the plots showed a tendency to demagnetising, or negative, interactions which are typical of all acicular particulate systems.

3. Discussion

The behaviour of the $\gamma\text{-Fe}_2\text{O}_3$ tape and CrO_2 hand spread is in line with the findings of Knowles [5] and is consistent with the Henkel plots which indicated demagnetising or negative interactions. These can be described by a mean field approximation which gives a shift in coercivity, and hence in the SFD, where the coercivity is related to packing by [6]

$$H_c(p) = H_0(1 - p), \quad (2)$$

where the coercivity $H_c(p)$ of a particulate system is directly dependent upon the packing fraction (p) of the particles within the system, and H_0 corresponds to $p = 0$.

The results for the metal particle system were very surprising and were contrary to a mean field approximation, since the effect of interactions was to shift the SFD to higher field values. This indicates interactions which oppose demagnetisation (positive interactions), which is contrary to the Henkel plot for this tape and the findings of other workers [7] for MP tapes. Thus, at a microscopic level, local interparticle interactions appear to enhance the switching field and dominate the behaviour of individual particles. However, at a macroscopic level, the behaviour is still predominantly that of a system in which interactions are demagnetising. These findings appear to be contradictory.

We have considered a number of possible explanations for this contradiction. Generally these would introduce a shift in the wrong direction and enhance the negative interaction effects. One possibility which must be considered is that the measured single particles were not representative of the distribution in the tape, or were damaged during removal and subsequent dispersion. The latter is unlikely since particles were removed by dissolving the binder system and dispersed using an ultrasonic bath. We do not believe that this process could be responsible for breaking or damaging particles. However, the experiment is 'selective' since many agglomerates were observed but ignored in the measurements, which can only be applied to single domain particles in the dispersion identified by their mode of reversal (rotation through 180°). There is a possi-

bility, albeit unlikely, that the particles which form agglomerates are different than those which remain isolated. Any multidomain particles will also be ignored in the measurements.

An alternative explanation for this contradiction may be found in a modelling study of Lyberatos and Wohlfarth [8]. Chains of particles were introduced into a particulate system. This had the effect of increasing the coercivity. However, Henkel plots showed that interactions between adjacent chains dominated and exhibited an overall demagnetising behaviour. Only if the system was very dilute did the interactions between particles in the chains start to dominate and produce positive interactions. We therefore suggest that in the metal particle system studied, there may be a very strong local alignment of particles which has the effect of increasing the system coercivity, whilst not affecting the general negative interactions characteristic of all acicular particle media. This investigation is continuing.

4. Conclusions

Interaction effects in recording media have been investigated by comparing single particle properties and bulk

media measurements. Different interaction effects have been found in the three systems studied. For the $\gamma\text{-Fe}_2\text{O}_3$ audio tape and the experimental CrO_2 hand spread, interactions were consistent with a mean field approach. However, for the metal particle system the interactions derived from single particle measurements were in the opposite sense to those indicated by Henkel plots. This suggests that the metal particle tape contained strong local alignment which enhanced the coercivity without effecting the overall demagnetising behaviour of the interactions.

References

- [1] J.E. Knowles, IEEE Trans. Magn. 14 (1978) 858.
- [2] M.P. Sharrock, IEEE Trans. Magn. 26 (1990) 225.
- [3] J.P.C. Bernardis and H.A.J. Cramer, J. Magn. Magn. Mater. 120 (1993) 221.
- [4] O. Henkel, Phys. Stat. Solidi 7 (1974) 919.
- [5] J.E. Knowles, IEEE Trans. Magn. 16 (1980) 62.
- [6] L. Néel, Compt. Rend. 234 (1947) 1150.
- [7] D.E. Speliotis and W. Lynch, J. Appl. Phys. 69 (1991) 4496.
- [8] A. Lyberatos and E.P. Wohlfarth, J. Magn. Magn. Mater. 59 (1986) L1.

Angular Dependence of Magnetization Reversal in $\gamma\text{-Fe}_2\text{O}_3$ Single Particles: an Experimental and Modelling Study.

S.R. McConochie, P.R. Bissell, D.A. Parker and J.A. Gotaas

Department of Physics, Astronomy and Mathematics, University of Central Lancashire, Preston PR1 2HE, UK

Abstract—The switching field for isolated $\gamma\text{-Fe}_2\text{O}_3$ magnetic particles has been investigated as a function of the applied field angle both experimentally and numerically. Micromagnetic simulations for a typical measured particle with cubic crystalline directions of $\langle 100 \rangle$ and $\langle 110 \rangle$ with respect to its long axis were compared directly with experimental results. At large applied field angles, the agreement between experimental results and numerical simulations was poor. However, at the smaller applied field angles the simulations gave reasonable agreement with the experimental results.

I. INTRODUCTION

The switching field as a function of angle has been investigated for individual $\gamma\text{-Fe}_2\text{O}_3$ particles removed from commercial audio recording tape. Results have been compared with those of a micromagnetic simulation of the particle incorporating typical parameters, such as length and aspect ratio, as measured by electron microscopy and magnetic properties of $\gamma\text{-Fe}_2\text{O}_3$ particles published in the literature. The simulations also incorporated a degree of surface irregularity to give a more realistic representation of a particle.

II. EXPERIMENTAL MEASUREMENTS

The switching field as a function of the applied field angle of an isolated $\gamma\text{-Fe}_2\text{O}_3$ particle was investigated using the technique developed by Knowles [1] and described in more detail elsewhere [2]. Particles were removed from audio tape using appropriate solvents and dispersed in a viscous resin. The dispersion was placed in a micro-slide tube and mounted on a modified microscope table fitted with pulsed magnetic field coils. A small dc field generated by permanent magnets was used to align the particles, which were then subjected to a magnetic field pulse of increasing amplitude until the moment of a particle was switched, after which it was observed to rotate slowly back to its original moment orientation in the small aligning field. The process was repeated for different directions of the pulse field so that switching field as a function of angle (θ) could be determined. Typical results for two particles 'A' and 'B', together with numerical results, are shown in Fig. 1. To establish the typicality of a particle, its switching field at $\theta=0^\circ$ for an ensemble of 50 aligned particles. A histogram of this ensemble is shown in Fig. 2 and the positions of particles, 'A' and 'B' are indicated.

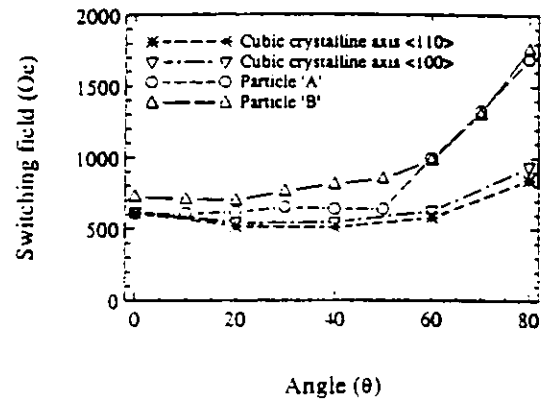


Fig. 1. Switching field as a function of the applied field angle.

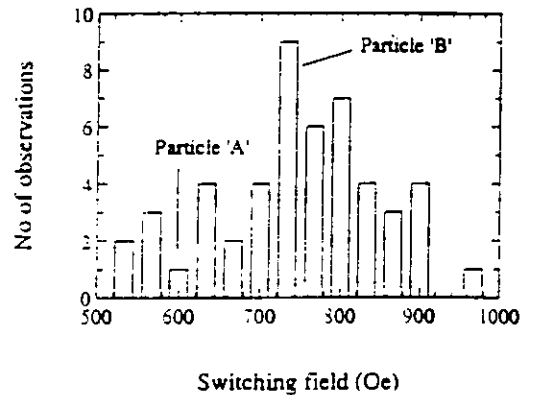


Fig. 2. Histogram of the switching field for an ensemble of 50 particles.

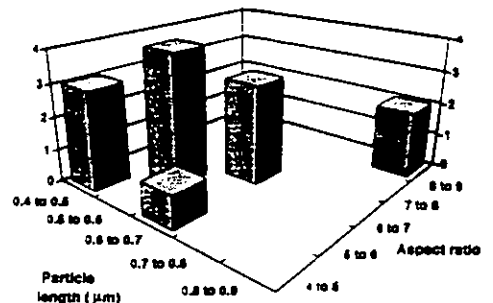


Fig. 3. Histogram of particle length and aspect ratio

Manuscript received January 20, 1997. S. R. McConochie, +44-1772-893579.
fax +44-1772-892903, s.r.mcconochie@uclan.ac.uk

For a comparison between experimental and numerical results, it is necessary to know the physical characteristics of the particles investigated. These characteristics were determined using Scanning Electron Microscopy (S.E.M.). Images obtained for samples of the $\gamma\text{-Fe}_2\text{O}_3$ particles were analysed for particle length and aspect ratio, a histogram of which is presented in Fig. 3. From this analysis a typical particle was identified as having an aspect ratio of 6:1 and a length of 0.6 μm . The S.E.M. images were of insufficient clarity to identify other features such as surface irregularities.

III. COMPUTER MODEL

A numerical model was developed to simulate the typical particle with dimensions determined by S.E.M. and theoretical bulk magnetic properties of $\gamma\text{-Fe}_2\text{O}_3$. The model represents the particle as a single crystal with an aspect ratio of 6:1 by an array of $5 \times 5 \times 30$ cuboids in a cubic lattice. For a more realistic model the lattice had tapered ends and an irregular surface formed by allowing the outside of external cuboids to be expanded/contracted by an amount chosen from an overall normal distribution. An arbitrary value of 10% of the cuboid's original width was chosen as the standard deviation for the normal distribution. An example of a typical model lattice with the same degree of surface irregularity is indicated in Fig. 4.

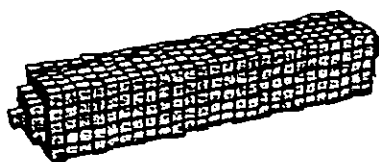


Fig. 4. Cuboid model

The effective field \vec{H}_{EFF} at the centre of each cuboid was determined by summing the individual contributions (magnetostatic \vec{H}_{MAG} , exchange \vec{H}_{EXC} , cubic anisotropy \vec{H}_{ANI} and applied field \vec{H}_{APP}).

$$\vec{H}_{EFF} = \vec{H}_{MAG} + \vec{H}_{EXC} + \vec{H}_{ANI} + \vec{H}_{APP} \quad (1)$$

The magnetostatic field at the centre of a given cuboid i was calculated, assuming a dipole approximation using

$$\vec{H}_{MAG} = \sum_j \frac{V_j}{r_{ij}^3} (3\vec{M}_j \cdot \hat{r}_{ij}\hat{r}_{ij} - \vec{M}_j), \quad (2)$$

where V_j is the volume of cuboid j , \vec{M}_j is its magnetization and \hat{r}_{ij} is the position vector from i to j . The exchange field was determined by

$$\vec{H}_{EXC} = \frac{C'}{M_s} \sum_{nn} \vec{M}_n, \quad (3)$$

where nn is the number of nearest neighbours of cuboid i , M_s is the saturation magnetization, K_1 is the anisotropy constant and $H_K = \frac{2K_1}{M_s}$ is the anisotropy field. The parameter C' is the inter-cuboid exchange constant defined by

$$C' = \frac{A^*}{K_1 a^2}, \quad (4)$$

where A^* is the effective energy exchange constant and a is inter-cuboid separation. The exchange constant C' is uniform within the bulk of the particle but varies at its surface. This is a consequence of the surface irregularity varying the position of the point dipole moment and thus changing the separation between point dipoles, parameter a .

The cubic anisotropy energy for a cuboid is given by

$$\vec{H}_{ANI} = - \frac{\partial (K_1 (M_x^2 M_z^2 + M_y^2 M_z^2 - M_x^2 M_y^2))}{\partial \vec{M}}, \quad (4)$$

The reduced effective field at a cuboid i is determined by normalising the effective field by the anisotropy field

$$\vec{h}_{EFF} = \frac{\vec{H}_{EFF}}{H_K}. \quad (5)$$

The model used a Jacobi technique discussed by Della Torre *et al.* (3) to determine the equilibrium magnetization state for each cuboid within the model. The magnetization state for a cuboid was calculated using a Runge-Kutta routine to integrate the reduced Landau-Lifshitz equation (4)

$$\frac{d\vec{m}_i}{dt} = (\vec{m}_i \times \vec{h}_{EFF}) - \alpha \vec{m}_i \times (\dot{\vec{m}}_i \times \vec{h}_{EFF}), \quad i=1,2,\dots,N. \quad (6)$$

The reduced damping constant α was chosen as 1.0 and the Runge-Kutta step size was set at 0.01 for all the simulations performed. The minimisation at a field step within the model was identified at the point where no moments rotated by more than 0.01° . Calculations carried out for the typical $\gamma\text{-Fe}_2\text{O}_3$ particle were similar to those of Schabes *et al.* (5) and Yan *et al.* (6). The model parameters were: $M_s = 340 \text{ emu/cm}^3$; $K_1 = 4.6 \times 10^4 \text{ erg/cm}^3$; the cubic crystalline direction was $\langle 110 \rangle$ with respect to the long axis of the particle; and $A^* = 5 \times 10^7 \text{ erg/cm}$. Similar micromagnetic simulations were performed with the cubic crystalline anisotropy in the $\langle 100 \rangle$ direction with respect to the particle long axis. Results of the simulations are shown together with experimentally measured results in Fig. 1. An example of the

coercive state for the model with an applied field direction of 1° with a cubic crystalline direction of $\langle 100 \rangle$ is presented in Fig. 5. The state indicates a typical reversal mechanism found in this study. This mechanism is characteristic of a vortex state reversal process, as described by Schabes *et al.* [7]. In this example, the reversal process is initiated at the particle's end, layer 1, and proceeds to sweep through the particle, indicated at layers 14-17.

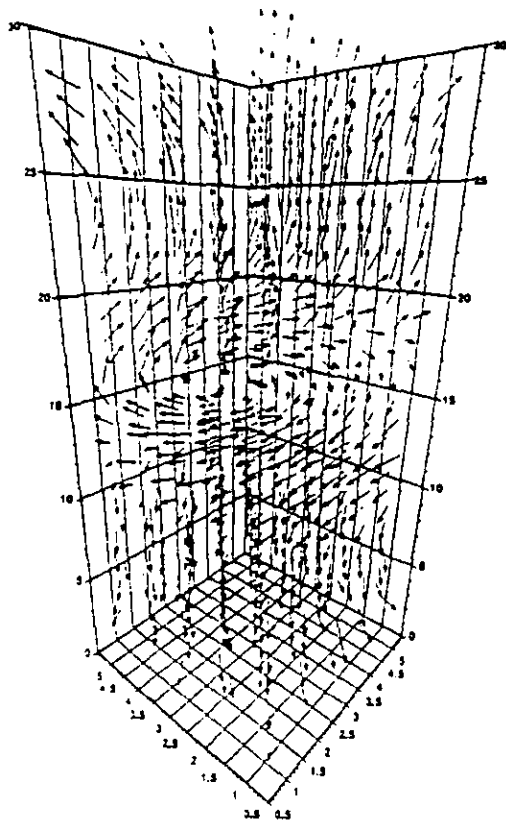


Fig. 5. Coercive state for 1° applied field direction with $\langle 100 \rangle$ cubic crystalline anisotropy.

IV. DISCUSSION

For aligned particles ($\theta=0^{\circ}$), numerical simulations of particles consisting of cuboids with cubic crystalline axes in the $\langle 100 \rangle$ and $\langle 110 \rangle$ directions are consistent with the experimentally measured switching field. As a function of the applied angle, the measured switching field characteristics are marginally more consistent with those modelled when the cubic crystalline axis was in the $\langle 100 \rangle$ direction rather than in the $\langle 110 \rangle$ direction. Real $\gamma\text{-Fe}_2\text{O}_3$ particles are likely to have predominately $\langle 110 \rangle$ cubic crystalline axis with respect to the particle's long axis [8].

The reversal mechanism as a function of the applied field angle has been investigated. As the applied field direction increases past 20° for both $\langle 110 \rangle$ and $\langle 100 \rangle$ cubic crystalline directions, the reversal mechanism becomes increasingly coherent. The crossover from an incoherent to a coherent reversal occurs through the transformation of the vortex state. As the applied field angle increases the vortex enlarges until a point is reached where the vortex state can no longer be supported and coherent reversal is initiated. In the coherent reversal regime, the model predicts a switching field which is consistent with a Stoner Wohlfarth particle [9].

Experimental measurements indicate a much larger switching field at angles approaching 90° . However, these particles are likely to have bulk crystalline imperfections which may act as pinning sites and enhance the particle switching field. This would appear to have a more dominant effect on the coherent reversal.

V. CONCLUSIONS

The switching field of $\gamma\text{-Fe}_2\text{O}_3$ particles has been measured experimentally as a function of the applied field angle. The reversal mechanism of these particles has been simulated by a micromagnetic model. The results from the simulations gave a reasonable agreement with the experimental results for small applied field angles. However, at larger angles of the applied field the agreement between the numerical and experimental results became poor. It is believed that this is a consequence of assumptions and simplifications within the model, particularly the absence of bulk crystal imperfections and the effect of an oversimplified particle shape. Further improvements to the model could include a representation of bulk imperfections by a distribution of cubic crystalline directions around the $\langle 110 \rangle$ direction together with a distribution of the magnitudes of the anisotropy constant.

REFERENCES

- [1] J.E. Knowles, "Measurements on single magnetic particles," *IEEE Trans. Magn.*, 14, No. 5, pp. 858-860, September 1978.
- [2] S.R. McConochie, F. Schrädlin, P.R. Bissell, J.A. Gotsis, D.A. Parker, "Interaction effects from reversal studies of single particles," *J. Magn. Magn. Mater.*, 155, pp. 89-91, 1996.
- [3] E. Della Torre, "Magnetization calculation of fine particles (invited)," *IEEE Trans. Magn.*, vol. 22, No. 5, 484-477, September 1986.
- [4] J.G. Zhu, H.N. Berrum, "Magnetization reversal in CoCr perpendicular thin films," *J. Appl. Phys.*, 66, 1291-1307, August 1989.
- [5] M.E. Schabes, H.N. Berrum, "Ferromagnetic switching in elongated $\gamma\text{-Fe}_2\text{O}_3$ particles," *J. Appl. Phys.*, 64, 5832-5834, November 1988.
- [6] Y.D. Yan, E. Della Torre, "Modeling of elongated fine ferromagnetic particles," *J. Appl. Phys.*, 66 (1), 320-327, July 1989.
- [7] M.E. Schabes, H.N. Berrum, "Magnetization processes in ferromagnetic cubes," *J. Appl. Phys.*, 64, 1347-1357, August 1988.
- [8] C.D. Mee, E.D. Daniel, "Magnetic Recording vol. 1," McGraw-Hill 1987.
- [9] M. Lederman, D.R. Fredkin, R. O'Barr and S. Schultz, "Measurement of thermal switching of the magnetization of single domain particles (invited)," *J. Appl. Phys.*, 75, 6217-6222, May 1994.